Innovative Approaches for Preclinical Development of Biotherapeutics

ARTICLE COLLECTION

Sponsored by:

WILEY | CURRENT PROTOCOLS A Wiley Brand | SARTORIUS

Label Free. Stress Free.

Minimize Cost, Maintain Quality in Biopharma

Octet® Bio-Layer Interferometry (BLI) systems are used throughout biotherapeutic discovery, development, manufacturing, and quality control to simplify and streamline the measurement of process and product attributes. The fluidic-free BLI design is an excellent alternative to assays performed using time- and labor-intensive methods such as ELISA and HPLC. Learn how to increase productivity, reduce costs, and shorten timelines.

Explore more at **www.sartorius.com/octet-bli**

Simplifying Progress

SARTORIUS

Contents

Introduction

In recent decades, biotherapeutic drugs have revolutionized modern medicine, treating complex diseases and disorders and impacting the lives of millions of patients. This class of drugs provides a more targeted and personalized approach to medicine, overcoming many of the challenges that have impeded the development of small molecules. Biotherapeutics entail many types of biological agents, but they largely consist of antibodies. In the last 35 years, over 100 monoclonal antibodies (mAbs) have been designated as drugs by the FDA. Available mAbs are directed against a large number of antigens and used for the treatment of immunological conditions, reversal of drug effects, cancer therapy, inflammatory diseases, and infectious diseases (such as COVID-19). With hundreds of additional entities in preclinical development, these biological agents will dramatically impact human health in the years to come.

As these agents are biological in nature, the manner in which they interact with the body can dramatically affect their safety and efficacy. Particularly, immunogenic responses have impeded the development of some biotherapeutic candidates. It is imperative, therefore, to perform extensive preclinical research to understand the mechanism of action, the pharmacokinetics (PK) and pharmacodynamics (PD), safety and toxicity, and dosing of biotherapeutic candidates.

In this article collection, we highlight five recent publications that cover aspects of biotherapeutic preclinical development. First, Vasudevan et al. (2017) determined the potency of inactivated H7 influenza vaccines using mAb-based biolayer interferometry assays and ELISA, showing that these assays are viable alternative methods for potency evaluation. Next, Rossotti et al. (2021) analyzed and reviewed the available evidence on immunogenicity of single-domain antibodies. They also discussed strategies to reduce the risk of immunogenicity by humanization. Following these articles, Gibbs et al. (2020) review physiologically based pharmacokinetic (PBPK) models in the context of describing the PK of bispecific antibodies. Additionally, they discuss the integration of PD models and PBPK models and provide perspectives on building dual PBPK-PD models to help guide the development of bispecific antibodies. Next, Teal et al. (2022) identified highly specific, low affinity affibody binding partners for insulin-like growth factor-1 (IGF-1) and pigment epithelium-derived factor (PEDF) to independently control protein release rates. They examined protein-affibody binding interactions using BLI and tested the system *in vivo*. Their work demonstrated a new approach to tune the release of therapeutic proteins both independently and simultaneously, paving the way for precise control over the delivery of multicomponent biological therapies. Finally, Marcion et al. (2021) studied Nanofitins as antibody alternatives for colorectal cancer. Particularly, they examined the binding of Nanofitins to heat shock protein 110 (HSP110) using BLI and characterized the ability of Nanofitins to inhibit HSP110 both *in vitro* and *in vivo*. They found that Nanofitins can modulate the tumor microenvironment and induce an anticancer immune response, leading to a decrease in tumor growth, suggesting that Nanofitins may be viable immunotherapies for cancer.

Through this research article collection, researchers will be educated on important considerations and strategies to enhance the preclinical development of biotherapeutic agents. Readers of this article collection will gain a deeper appreciation for the utility and role of label-free approaches, like biolayer interferometry, in the preclinical development of biotherapeutics.

Emily E. Frieben, Ph.D.
Associate Editor, *Wiley Interdisciplinary Reviews*

References

Vasudevan, A., Woerner, A., Schmeisser, F., Verma, S., Williams, O., Weir, J.P. Potency determination of inactivated H7 influenza vaccines using monoclonal antibody-based ELISA and biolayer interferometry assays. *Influenza Other Respi Viruses.* 2018, 12, 250-258. https://doi.org/10.1111/irv.12528

Rossotti, M.A., Bélanger, K., Henry, K.A. and Tanha, J. Immunogenicity and humanization of single-domain antibodies. *FEBS J.* 2022, 289, 4304-4327. https://doi.org/10.1111/febs.15809

Gibbs, J.P., Yuraszeck, T., Biesdorf, C., Xu, Y. and Kasichayanula, S. Informing development of bispecific antibodies using physiologically based pharmacokinetic-pharmacodynamic models: Current capabilities and future opportunities. *J. Clin. Pharmacol.*, 2020, 60, S132-S146. https://doi.org/10.1002/jcph.1706

Teal, C. J., Hettiaratchi, M. H., Ho, M. T., Ortin-Martinez, A., Ganesh, A. N., Pickering, A. J., Golinski, A. W., Hackel, B. J., Wallace, V. A., Shoichet, M. S., Directed evolution enables simultaneous controlled release of multiple therapeutic proteins from biopolymer-based hydrogels. *Adv. Mater.* 2022, 34, 2202612. https://doi.org/10.1002/adma.202202612

Marcion, G., Hermetet, F., Neiers, F., et al. Nanofitins targeting heat shock protein 110: An innovative immunotherapeutic modality in cancer. *Int. J. Cancer.* 2021, 148, 3019–3031. https://doi.org/10.1002/ijc.33485

Accepted: 13 November 2017

DOI: 10.1111/irv.12528

ORIGINAL ARTICLE

WILEY

Potency determination of inactivated H7 influenza vaccines using monoclonal antibody-based ELISA and biolayer interferometry assays

Anupama Vasudevan | **Amy Woerner** | **Falko Schmeisser** | **Swati Verma** | **Ollie Williams** | **Jerry P. Weir**

Division of Viral Products, Center for Biologics Evaluation and Research, Food and Drug Administration, Silver Spring, MD, USA

Correspondence
Jerry P. Weir, Division of Viral Products, Center for Biologics Evaluation and Research, Food and Drug Administration, Silver Spring, MD, USA.
Email: jerry.weir@fda.hhs.gov

Funding information
Biomedical Advanced Research and Development Authority (BARDA), Department of Health and Human Services

Background: The single radial immunodiffusion (SRID) assay, the accepted method for determining potency of inactivated influenza vaccines, measures an immunogenic form of the influenza hemagglutinin. Nevertheless, alternative methods for measuring vaccine potency have been explored to address some of the weaknesses of the SRID assay, including limited sensitivity and the requirement for large amounts of standardized reagents. Monoclonal antibody (mAb)-based potency assays also have the ability to detect and measure relevant immunogenic forms of HA.

Objectives: The objective of this study was to continue evaluation of mAb-based alternative methods for measuring the potency of inactivated influenza vaccines, focusing on A(H7N9) pandemic influenza vaccines.

Methods: Several murine mAbs that recognize different epitopes on the H7 hemagglutinin (HA) were identified and characterized. These mAbs were evaluated in both a mAb-capture ELISA and a mAb-based biolayer interferometry (BLI) assay.

Results: Results indicated that potency of inactivated A(H7N9) vaccines, including vaccine samples that were stressed by heat treatment, measured by either alternative method correlated well with potency determined by the traditional SRID potency assay.

Conclusions: The availability of multiple H7 mAbs, directed to different HA epitopes, provides needed redundancy in the potency analysis as A(H7N9) viruses continue to evolve antigenically and suggests the importance of having a broad, well-characterized panel of mAbs available for development of vaccines against influenza strains with pandemic potential. In addition, the results highlight the potential of mAb-based platform such as ELISA and BLI for development as alternative methods for determining the potency of inactivated influenza vaccines.

KEYWORDS
A(H7N9), influenza, potency assay

1 | INTRODUCTION

Traditionally, the potency of inactivated influenza vaccines has been determined using the single radial immunodiffusion (SRID) assay, an agarose gel-based format that uses strain-specific polyclonal antibody reagents to quantify the amount of influenza hemagglutinin (HA) present in a vaccine sample by comparison with the assigned HA value of a reference antigen standard.[1-3] The SRID assay is relatively simple and practical, strain-specific, and has acceptable accuracy and robustness for current vaccines. However, the dynamic range of the SRID is limited, the assay may not be ideal for newer types of influenza vaccines, and the assay requires large amounts of calibrated reagents that must be produced in a timely manner to support vaccine manufacturing. The latter issue is always a concern, both in the context of seasonal influenza vaccine manufacturing, as well as in the response to the emergence of a pandemic influenza strain.[4] Indeed, difficulties were encountered in the preparation of the SRID potency antisera for the A(H1N1)pdm09 pandemic vaccine and for candidate vaccines made in response to the emergence of the A(H7N9) virus in China in 2013.[5]

In an attempt to address some of the limitations of the SRID, several newer methods have been explored in recent years as possible alternative potency assays for inactivated influenza vaccines.[6-13] Several of these assays rely on the use of strain-specific monoclonal antibodies (mAbs) to capture and quantify HA in vaccine samples. Although the initial reports describing mAb-based alternative potency assays are promising and demonstrate the general feasibility for further development, there are unanswered questions concerning the identification and selection of the appropriate antibodies and how such antibody reagents can be generated in the time frame required for vaccine manufacture. These issues are especially concerning in the time frame of pandemic influenza vaccine manufacturing.

The goal of this study was to continue evaluation of mAb-based alternative methods for measuring the potency of inactivated influenza vaccines, focusing on A(H7N9) pandemic influenza vaccines produced following the emergence of novel A(H7N9) viruses in China in 2013 that resulted in hundreds of human fatalities.[14,15] Several mAbs, recognizing different epitopes on the H7 HA, were identified, characterized, and evaluated in both a mAb-capture ELISA and a mAb-based biolayer interferometry (BLI) assay. The results indicated that potency of inactivated A(H7N9) vaccines, including vaccine samples that were stressed by heat treatment, measured by either alternative method correlated well with potency determined by the traditional SRID potency assay and suggested the value and feasibility of having a broad, well-characterized panel of mAbs available for development of vaccines against influenza strains with pandemic potential. Overall, the results indicate the potential of mAb-based ELISA and BLI platforms for continued development as alternative methods for determining the potency of inactivated influenza vaccines.

2 | MATERIALS AND METHODS

2.1 | Cells and viruses

The A(H7N9) A/Shanghai/2/2013 virus used in these studies is a reassortant candidate vaccine virus (RG32A) prepared by and obtained from the Centers for Disease Control and Prevention (Atlanta, GA, USA). Influenza viruses were propagated in 9-day-old specific pathogen-free embryonated chicken eggs. Selection and characterization of A(H7N9) escape viruses were performed in Madin-Darby canine kidney (MDCK) cells. Mammalian virus-like particles (VLPs) containing the HA of the A(H7N9) A/Shanghai/2/2013 virus were prepared by modified vaccinia virus Ankara (MVA) vector infection of Vero cells and purified as previously described.[16] All virus and VLP work was approved by the FDA's Institutional Biosafety Committee. Reference antigens for the A(H7N9) influenza vaccine virus were produced by the Center for Biologics Evaluation and Research (CBER)/FDA. All cells were maintained in Dulbecco's modified Eagle medium supplemented with 10% FBS (HyClone, Logan, UT, USA), 2 mM L-glutamine, and 50 μg/mL gentamicin.

2.2 | Production of influenza H7 monoclonal antibodies

Purified murine mAbs to A/Shanghai/2/2013 HA were prepared as previously described,[17] using VLPs containing the HA from A/Shanghai/2/2013 as the immunogen. To select for mAbs directed to epitopes other than antigenic site A in HA, VLPs were prepared as immunogens from two modified MVA vectors that expressed either the H7 HA with a glycosylation site motif introduced at amino acid 123-125 (amino acid numbering throughout the text refers to the mature H7 HA, excluding the HA N-terminus signal peptide), or an H7 antigenic site A mutation at amino acid position 131 (R131G). Targeted mutations were introduced into the MVA plasmid insertion vectors using QuickChange Lightning® Site-Directed Mutagenesis Kit (Agilent Technologies, Santa Clara, CA, USA). Hybridoma clones secreting mAbs to influenza H7 HA were screened by ELISA using inactivated A/Shanghai2/2013 reference antigen as a capture antigen.

2.3 | Selection of escape mutants

The selection of A(H7N9) escape virus mutants[18] was performed by incubating A/Shanghai/2/2013 virus with H7 mAbs over a range of concentrations from 40 to 0.156 μg/mL, selecting resistant virus, and repeating the process for up to 2 more rounds of selection. Escape mutants were sequenced and tested for reduced inhibition of neutralization by the mAb compared to the parent virus.

2.4 | Measurement of potency by mAb ELISA

Potency ELISAs were performed as previously described.[12] Purified capture mAbs were used at a concentration of 2-4 μg/mL (determined empirically for each mAb to optimize antigen capture and minimize

non-specific background). Reference antigen and vaccine samples were treated with 1% Zwittergent 3-14 for 30 minutes, diluted in PBS/Tween/10% FBS (minimum 10-fold additional dilution) before being added to the Immulon 2HB plate. The primary detection antibody was a purified rabbit polyclonal IgG, generated by the immunization of rabbits with plasmid DNA vectors expressing A/Shanghai/2/2013 HA and boosted with mammalian-derived VLPs containing the same H7 HA. The secondary detection antibody was a goat anti-rabbit IgG conjugated with HRP. A 1:1 mix of ABTS:H_2O_2 was used as enzyme substrate. The HA concentration was determined by parallel line analysis of the four-parameter regression fits of vaccine samples to that of the standard (the reference antigen) on each plate. Replicates were included on each plate, and assays were repeated on different days.

2.5 | Measurement of potency by single radial immunodiffusion

The SRID assay was performed as previously described.[19,20] Vaccine potency was calculated using the parallel line bioassay method, which uses reference and test vaccine dose-response curves (log antigen dilution versus log zone diameter). Replicates were included in each SRID assay, and assays were repeated on different days.

2.6 | Biolayer interferometry

Epitope binning and vaccine potency determination by BLI were performed on an Octet Red-384 system (Pall ForteBio, Menlo Park, CA USA). For epitope binning, recombinant H7 (rHA) A/Anhui/01/2013 (Protein Sciences, Meriden, CT, USA) in PBS was biotinylated using an EZ-Link NHS-PEG_4 Biotinylation kit (Thermo Fisher, Rockford, IL, USA). A/Anhui/01/2013 is an A/Shanghai/2/2013-like A(H7N9) virus with the same HA as A/Shanghai/2/2013.

Binning was performed in 96-well microplates (Pall ForteBio) and used High Precision Streptavidin-coated (SAX) biosensors (Pall ForteBio) loaded with the biotinylated A/Anhui rHA at 5 μg/mL (determined empirically to generate a response signal of ~0.5). H7 antibodies were loaded into adjacent wells at a concentration of 50 μg/mL for initial saturating binding to HA and also loaded into a second set of wells at a concentration of 25 μg/mL to be used as the competing Ab in the assay. Loading time for the biotinylated rHA onto the SAX biosensors was 600 seconds; loading times for antibody 1 (saturating Ab) and antibody 2 (competing Ab) were 300 seconds. The binning experiments were designed so that every antibody was used for saturation and competition against all of the other antibodies. Data Analysis HT 9.0 software (Pall ForteBio) was used to analyze the results, which were presented in a matrix format to indicate antibody combinations that were either blocking or non-blocking.

Biolayer interferometry vaccine potency determination experiments used Dip and Read Anti-Mouse IgG Fc Capture (AMC) biosensors (Pall ForteBio) in a 384-well plate format (tilted-bottom microplates, Pall ForteBio) with a baseline buffer consisting of Kinetics Buffer (Pall ForteBio) with 0.1% Tween 20/0.1% BSA. Each mAb concentration was optimized by initially diluting the mAb to 10 μg/mL followed by twofold serial dilution before loading onto the AMC biosensor. Reference antigen, diluted to 30 μg/mL, was bound to the different concentrations of mAb, and the optimal mAb binding concentration was determined by selecting the highest mAb concentration at which the binding curves were not overlapping. For mAbs 1E9, 7B5, and 98, the optimal mAb concentration was determined to be 0.3 μg/mL. For mAb 5A6, an optimal concentration of 0.128 μg/mL was determined.

For vaccine potency determination, the AMC biosensors were dipped into buffer (baseline step) for 60 seconds, followed by loading the optimized mAb concentration for 300 seconds (load step). The biosensors were then dipped into the baseline buffer again, followed by the reference standard for 300 seconds (association step). A separate set of biosensors was used to repeat this process, except that the association steps used vaccine samples. The reference antigen and vaccine samples were prepared as a twofold dilution series with a starting concentration of approximately 30 μg/mL. All steps were performed at 23°C at a shake speed of 400 rpm. The HA concentration of vaccine samples was calculated by comparing the standard curve of the reference antigen to the standard curve generated for each vaccine sample. The same read time was used for both the reference and the vaccine sample being compared (20-300 seconds), and an unweighted dose-response 4PL curve was used for both the reference and the vaccine samples. Three replicates of standards and unknowns were included on each plate, and each assay repeated a minimum of two times on different days.

3 | RESULTS

3.1 | Isolation and characterization of monoclonal antibodies to the influenza H7 hemagglutinin

In a previous study, we described the isolation and characterization of murine mAbs to the H7 HA of the recently emerged A(H7N9) viruses in China,[17] but interestingly, all of the mAbs isolated in that study were directed to antigenic site A. In order to broaden the H7 HA epitope representation of our mAbs, we generated and characterized additional panels of mAbs using approaches designed to select for mAbs directed to epitopes other than antigenic site A. In addition, we evaluated some existing mAbs (mAbs 62 and 98) developed to an older H7N1 strain to determine how well these mAbs would bind the more recent A(H7N9) hemagglutinins.[21,22] Monoclonal antibodies were assessed for binding to HA in an ELISA using inactivated A(H7N9) A/Shanghai/2/2013 virus. Several mAbs that bound H7 HA well were identified and selected for further characterization, including testing for hemagglutination inhibition and binding in Western blot under reducing and non-reducing conditions (Table 1).

3.2 | Epitope analysis of influenza A(H7N9) monoclonal antibodies

Biolayer interferometry was used to perform epitope binning of the H7 A/Shanghai mAbs using biotinylated H7 A/Anhui/1/2013

TABLE 1 Characterization of H7 monoclonal antibodies

Antibody	Binding titer by ELISA[a]	Hemagglutination inhibition titer[b]	Western blot reducing/ non-reducing[c]
1A10	12 821K	3238	+/+
1E9	3226K	481	-/+
5A6	1587K	241	-/+
7B5	6250K	3851	-/+
7E3	3226K	1925	+/+
62	1587K	6476	-/+
98	1587K	4579	-/+

[a]Endpoint titer—highest dilution of antibody (initial concentration of 4 mg/mL) giving an absorbance value (405 nm) >0.050 and greater than the highest dilution of a matched dilution of control antibody of the same isotype; K = 1000; antigens for capture (inactivated whole influenza A/Shanghai/2/2013 virus used at 10 μg/mL).
[b]GMT of the antibody inhibition of A/Shanghai/2/2013 hemagglutination of chicken red blood cells; initial mAb concentration 0.8 mg/mL.
[c]mAb binding of A/Shanghai/2/2013 HA in Western blot analysis under reducing and non-reducing conditions.

rHA. Each mAb was captured separately to saturation, and all other mAbs were used as competing antibodies in order to examine competitive binding. As shown in Table 2, three of the mAbs (7B5, 7E3, and 1A10) grouped in one antigenic "bin" that did not include the other four mAbs (1E9, 98, 5A6, and 62). Of these other four mAbs, 1E9, 98, and 5A6 clearly grouped into a second antigenic "bin", as using any of these mAbs as saturating antibody blocked binding of itself and the other mAbs. The results for mAb 62 were not as clear-cut, but suggested that mAb 62 is also likely part of the second "bin." Although mAb 62 competed somewhat with saturating 1E9, 98, and 5A6 mAbs, saturating mAb 62 completely blocked subsequent binding by itself as well as 1E9, 98, and 5A6 (column 62).

Finer mapping of the epitopes recognized by the H7 mAbs was performed by generating virus escape mutants. Escape mutant viruses with single amino acid changes were obtained for mAbs 7B5 and 1A10 (G189E) and 1E9 (R247H). The G189 mutation is near antigenic site B, defined originally for influenza H3 HA;[23,24] the mutation at position 247 selected by mAb 1E9 is not in any of the previously defined antigenic sites for influenza H3. The locations of these escape mutations, as well as those for 5A6[17] (previously mapped to antigenic site A – R131G), are shown in Figure 1. Escape mutant viruses with amino acid changes at positions 119 (G119E) and 157 (K157E) have previously been reported for mAbs 98[22] and 62,[21] respectively. In several attempts at isolating escape mutants to these two mAbs, viruses with both amino acid changes (G119E and K157E) were always obtained. As shown in Figure 1, these two amino acids are located spatially adjacent to each other on the HA, suggesting that mAbs 62 and 98 probably recognize the same HA epitope.

Cross-neutralization experiments with the escape mutant viruses and the H7 mAbs were used to extend the epitope analysis of the H7 mAbs (Table 3). Initial experiments confirmed that mAbs 7B5, 1A10, and 7E3 shared a common epitope, as none of these mAbs were able to neutralize an escape virus with a G189E mutation (data not shown). In contrast, mAbs 5A6, 1E9, and 98 easily neutralized the G189E escape virus and mAb 7B5 easily neutralized the other three escape viruses. Although 5A6 and 1E9 grouped together in the BLI binning experiments, neutralization analysis indicated that the mAbs were different, as 5A6 was capable of neutralizing the 1E9 escape virus and 1E9 was capable of neutralizing the 5A6 escape virus. All escape viruses were neutralized well by mAb 98 indicating that the epitope recognized by this mAb differed from the other mAbs, including mAbs 5A6 and 1E9 which were grouped together with mAb 98 by BLI binning. The mAb 98 escape virus was not neutralized by mAb 1E9, however, suggesting that the 1E9 and 98 epitopes, although different, might be spatially close to

TABLE 2 Epitope binning of H7 monoclonal antibodies by biolayer interferometry

	Saturating mAb[b]							
mAb[a]	7B5	7E3	1A10	1E9	98	5A6	62	H5 2C6
7B5	0.0103	0.0133	0.0081	0.3313	0.3983	0.2563	0.1542	−0.0378
7E3	0.0097	0.0108	0.0085	0.3177	0.3918	0.2586	0.1542	−0.0368
1A10	−0.0022	−0.0013	0.0091	0.3324	0.404	0.2774	0.1763	−0.0271
1E9	0.2266	0.2311	0.2137	0.0176	0.0194	−0.0235	−0.0752	−0.1449
98	0.2775	0.278	0.2835	0.0551	0.0345	0.0211	−0.0629	−0.095
5A6	0.2009	0.1989	0.1799	0.0605	0.0686	0.014	−0.0752	−0.1967
62	0.288	0.2918	0.3048	0.1954	0.1578	0.1404	0.0142	−0.0544
H5 2C6	0.4263	0.4378	0.3934	0.3993	0.4355	0.3149	0.2337	−0.0039

[a]Competing mAb—Data presented is the raw nanometer shift caused by the binding of the competing antibody. To differentiate between competing antibodies that are blocked by the saturating antibody and those that are not, a threshold equal to the highest self-binding signal in the panel is set: 0.0345 (mAb 98). The threshold value is then used to color-code the matrix data in either red or green, to distinguish between competing antibodies that are or are not blocked by the saturating antibody.
[b]Saturating mAb—H7 antigen was captured onto the SAX sensor surface using biotin tag and the loaded sensor first exposed to the indicated saturating mAb.

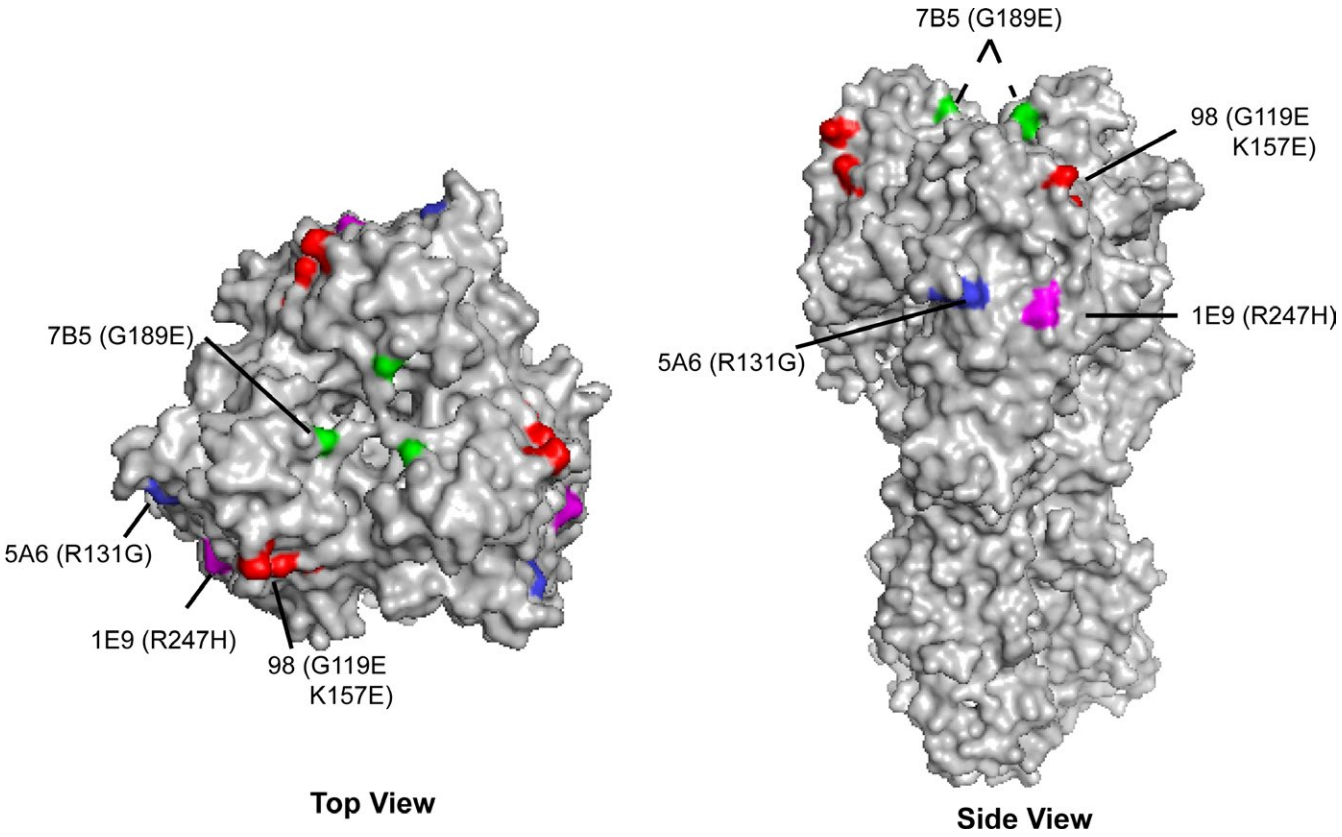

FIGURE 1 Location of HA amino acid changes in influenza A(H7N9) escape mutants. Antigenic structure of the A(H7N9) A/Shanghai/2/2013 HA trimer (PDB ID: 4LN6) and location of the escape mutations to mAbs 7B5 (green), 5A6 (blue), 1E9 (magenta), and 98 (red). A, Top view—the location of each escape mutation on one HA molecule of the trimer is indicated. B, Side view—the location of three escape mutations (5A6, 98, and 1E9) are shown on one HA monomer of the HA trimer; the location of the 7B5 mutation on the other two HA monomers is shown by dotted lines

TABLE 3 mAb neutralization of A/Shanghai/2/2013 escape mutants

	mAb[b]			
Virus[a]	5A6	7B5	1E9	98
A/Shanghai/2/2013	+++	+++	+++	+++
5A6v (R131G)	-	++	++	+++
7B5v (G189E)	++	-	++	+++
1E9v (R247H)	+	+++	-	+++
98v (G119E/K157E)	+	++	-	-

[a]Each virus was titrated and diluted to approximately 500 pfu/mL and incubated with mAb concentrations from 80 to 0.31 μg/mL for incubation with mAb.

[b](-) No virus neutralization at mAb >80 μg/mL; (+) neutralization at 20 μg/mL; (++) neutralization at 5 μg/mL; (+++) neutralization at mAb between 0.31 and 1.25 μg/mL.

each other on HA. Taken together, four distinct epitopes on the H7 HA were identified by the mAbs characterized in this study. Three epitopes, recognized by mAbs 5A6, 1E9, and 98, are located on the outer face of each HA monomer, whereas the fourth epitope recognized by mAb 7B5 is closer to the receptor-binding site of HA (Figure 1).

3.3 | Potency determination of A(H7N9) inactivated influenza vaccines by mAb-capture ELISA and biolayer interferometry

Monoclonal antibodies to H7 HA were used to develop a capture ELISA for quantifying the HA content of inactivated influenza A(H7N9) vaccines. The assay setup was similar to that previously described[12] and used four different H7-specific capture mAbs. ELISA potency values were determined by comparing the binding of HA in the vaccine samples relative to the binding of the reference antigen standard that has an assigned value in μg of HA. The measured ELISA potency values were compared to potency values determined concurrently by SRID assay. Two inactivated H7 vaccine samples from 2 different vaccine manufacturers were available for evaluation by SRID and mAb-capture ELISA.

The potency values obtained for Vaccine 1 using the ELISA-based potency assay were similar for mAbs 5A6, 98, and 1E9 (Figure 2A), ranging from 238 to 260 μg/mL, and similar to the SRID value of 248 μg/mL. However, the potency value obtained using mAb 7B5 was approximately 66% lower (85.1 μg/mL) than the average of the other three mAbs (250 μg/mL), suggesting that mAb 7B5 interacted differently with Vaccine 1 relative to binding of the reference antigen in the ELISA format. For Vaccine 2, the potency values determined using

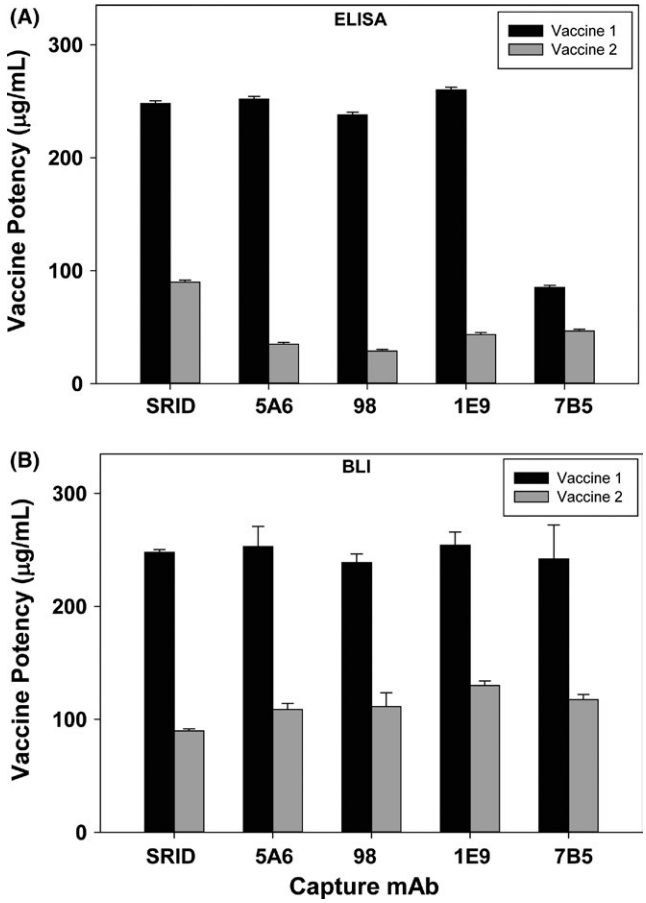

FIGURE 2 Potency values of two inactivated A(H7N9) vaccines determined by SRID, ELISA, and BLI. A, Potency and standard deviation of A/Shanghai/2/2013 A(H7N9) vaccines from two manufacturers were determined by traditional SRID analysis and ELISA using four H7-specific mAbs. B, Potency and standard deviation of A/Shanghai/2/2013 A(H7N9) vaccines from two manufacturers were determined by traditional SRID analysis and BLI using four H7-specific mAbs

all four mAbs were similar, averaging 38 µg/mL (Figure 2A), but was approximately 57% lower than the corresponding SRID potency value of 90 µg/mL, suggesting that the mAbs did not capture this vaccine as well as the reference antigen in the ELISA format.

In the mAb-capture ELISA potency assay, HA is quantified by comparing the total amount of HA in a vaccine and a reference standard bound by the capture mAbs. However, the rate of binding to the antibody should also be dependent on the concentration of HA in the sample and can be measured by techniques such as biolayer interferometry. We explored the development of a BLI assay as another alternative assay to quantify HA in vaccine samples in comparison with a reference standard using the four H7-specific mAbs described above. Preliminary experiments determined a loading concentration for each mAb and generated response curves to verify that the binding rate of reference antigen and vaccine samples to the mAb on the biosensor is concentration dependent (Materials and Methods).

Biolayer interferometry potency values were determined by generation of a binding rate response curve using dilutions of the reference

TABLE 4 Potency of A(H7N9) vaccine subjected to temperature stress at 56°C determined by SRID, ELISA, and BLI

		ELISA % Unstressed potency[a]					BLI % Unstressed potency				
Time at 56°C (h)	SRID	All mAbs[b]	mAb 1E9	mAb 7B5	mAb 5A6	mAb 98	All mAbs	mAb 1E9	mAb 7B5	mAb 5A6	mAb 98
0	100	100	100	100	100	100	100	100	100	100	100
0.25	18	26	19.7	44	22.7	19.2	3.4	3.4	5	2.4	2.6
1	10.9	3.2	2	5.6	3.1	2.1	1.2	1.2	1.3	1.0	1.2
4	5.6	0.9	0.92	1.4	0.4	0.76	N.D.	N.D.	N.D.	N.D.	N.D.
24	N.D.	N.D.	N.D.	N.D.	N.D.	N.D.	N.D.	N.D.	N.D.	N.D.	N.D.

[a]N.D.—Percent unstressed potency of vaccine relative to 4°C.
[b]N.D.—Average of all 4 mAb potency values.
N.D., Not detectable.

antigen (with an assigned value of HA in μg) to each H7 mAb and comparing that standard curve to a similar binding rate response curve for each of the two inactivated vaccine samples. The potency values obtained for Vaccine 1 using the BLI-based potency assay were consistent for the four mAbs, ranging from 238 μg/mL (mAb 98) to 254 μg/mL (mAb 1E9), and also correlated well with SRID value of 248 μg/mL for this vaccine sample (Figure 2B). Similarly, potency values obtained for Vaccine 2 were consistent for the four mAbs used in the assay, ranging from 109 μg/mL (mAb 5A6) to 130 μg/mL (mAb 1E9), and correlated well with the SRID value for Vaccine 2 of 90 μg/mL.

3.4 | Potency of temperature-stressed A(H7N9) A/Shanghai vaccine

To determine whether the mAb-based ELISA and BLI assays were able to distinguish subpotent A(H7N9) vaccine and accurately quantify loss of potency, we employed heat treatment at 56°C to accelerate the decline in potency and establish conditions under which potency was significantly reduced. Aliquots of A(H7N9) Vaccine 1 were incubated at 56°C for 15 minutes, 1, 4, and 24 hours and then were assayed by SRID, as well as ELISA and BLI using 1E9, 7B5, 5A6, and 98 H7 mAbs (Table 4). As measured by SRID, this vaccine exhibited a rapid loss of potency over time, with an 82% decline in potency after only 15 minutes at 56°C. The potency continued to decrease over time until the HA content was undetectable at 24 hours.

There was also a decline in potency as measured by ELISA and BLI using each H7 mAb. The relative potency decline measured by ELISA and BLI generally mirrored the decline in potency as measured by SRID, and the results obtained in both the ELISA and BLI analyses were similar for all four mAbs in each assay, indicating that all H7 mAbs were stability-indicating in these assays. The potency decline measured by ELISA or BLI appeared somewhat more rapid than that measured by SRID, particularly for the BLI analysis. For example, there was no detectable HA by the 4-hour time-point in the BLI analysis using any mAb. Taken together, the data show that similar heat-stressed declines in potency can be measured by all three assay platforms (SRID, ELISA, BLI) with all of the H7 mAbs and that all the platforms are capable of distinguishing temperature-stressed vaccines from unstressed vaccines.

4 | DISCUSSION

The SRID assay is the accepted standard for determining the potency of inactivated influenza vaccines. Importantly, the assay measures an immunogenic form of the HA antigen in the vaccine, and a link between SRID potency and vaccine immunogenicity and vaccine efficacy has been established. Nevertheless, the limitations of the SRID assay have spurred development of alternative methods to measure influenza vaccine potency. Monoclonal antibody-based potency assays also have the ability to detect and measure relevant immunogenic forms of HA, and several such promising assays have been described. However, there are at least two key issues that will have to be resolved during the development of mAb-based potency assays. One issue is the selection of the appropriate mAbs for the assay, including whether multiple antibodies are necessary to accurately assess the potency of the HA antigen in the vaccine. A second issue is whether, and how, suitable mAbs can be generated and characterized in the time frame of either seasonal or pandemic influenza vaccine manufacturing so that antibody production is not a potential bottleneck to timely vaccine manufacture.

In the current study, we began addressing these two issues in the context of mAb-based potency assays for pandemic H7 influenza vaccines that were developed following the A(H7N9) outbreak in China in 2013. Since the initial outbreak, waves of A(H7N9) virus infections in humans have reappeared each winter season, resulting in numerous human infections and deaths.[25] We generated and characterized several mAbs recognizing different epitopes on the H7 HA and evaluated these mAbs, as well as H7 mAbs (mAbs 62 and 98) that were developed several years prior to the A(H7N9) outbreak in China, for potency determination of A(H7N9) vaccines using two assay formats. Potency results from these assays were compared to the potency results obtained using the SRID potency assay. There was generally good correlation between the SRID potency values and potency values obtained using either the mAb-capture ELISA or BLI assay for most of the vaccine samples tested. However, as has been observed and discussed previously,[9,26] there are occasionally discrepancies in the actual values determined by SRID and any alternative potency assay, which may be at least partially related to the type of reference antigen used in the comparative analyses; additional work will be needed to better understand and resolve this issue. In the potency ELISA results reported here, one mAb (7B5) yielded potency results that were significantly lower for Vaccine 1 than the other tested mAbs. This difference in potency was not observed in the ELISA with the other vaccine sample, nor in the BLI assay with either Vaccine 1 or Vaccine 2, indicating that there are differences in the way individual mAbs interact with HA antigen in different vaccine formulations or assay formats. Although the fact that a particular mAb behaves differently in two assay formats may not be especially surprising, it does emphasize the importance of the issue of mAb redundancy and mAb selection and characterization, the criteria for which at this point in time remain mostly empirical. Importantly, however, mAbs such as mAb 98 that were generated to an earlier H7N1 strain, before the emergence of the A(H7N9) viruses in 2013, worked well in both assay formats to quantify HA in the available A(H7N9) vaccine samples. In addition, recent studies have indicated that some of the mAbs in the current panel of H7 mAbs, including 7B5 and 1E9, will capture HA from recent strains of A(H7N9) (e.g, A/A/Hong Kong/125/2017 and A/Guangdong/17SF003/2016) that are being developed as newer candidate vaccines (data not shown). Taken together, these results suggest the importance of evaluating multiple capture mAbs, including those directed to different HA epitopes, early in assay setup and development to increase the robustness of the assay, and the necessity of developing panels of mAbs to HAs of potential pandemic

influenza viruses, as well as for seasonal influenza strains, as a practical solution for implementation of a timely potency assay using mAbs.

Previous studies have shown that the ELISA-based mAb approach to determining the potency of vaccines can be used for a variety of vaccines and strains, although only a limited amount of development work has been performed for candidate pandemic vaccines. The ELISA approach as an alternative influenza vaccine potency assay has several attractive advantages. It is a relatively simple method commonly used in laboratories worldwide, requires greatly reduced amounts of standardized reagents, and is amenable to high-throughput automation. In addition, the ELISA method is more sensitive than the SRID and has a shorter assay time. The ELISA potency assay does require strain-specific antibodies, however, as well as characterized detection antibodies, and as shown in the current study and previous studies, the selection of the most appropriate antibodies for the assay is still empiric, and developmental work is necessary to set up the assay for a particular strain and vaccine formulation. For example, in addition to the poor capture of Vaccine 1 by mAb 7B5 in the ELISA format, other H7-specific mAbs such as 1A10 and 7E3 (Table 1) that recognize the same HA epitope as 7B5 did not capture H7 reference antigen very well in the ELISA setup (data not shown).

More recently, biolayer interferometry has emerged as an assay platform for protein quantification and its potential for determination of the potency of inactivated influenza vaccines has been proposed.[27] We used BLI to measure HA by comparing the binding of HA in vaccine samples to specific mAbs in comparison with a reference standard. In contrast to the ELISA, however, BLI measures rates of binding rather than total HA binding and does not require a detection antibody step. This method is of high throughput and is extremely fast, allowing for multiple samples and replicate assays to be run each day. Furthermore, fewer steps are required for the BLI assay compared to the ELISA method because no additional detection steps or reagents are required, although without an additional amplification step, the BLI method is less sensitive than the ELISA. We set up the BLI assay using anti-mouse IgG Fc biosensors to bind the H7 mAbs, but other biosensor presentations for the mAbs, as well as amplification steps, are possible. Although there is far less collective experience with a BLI-based assay than ELISA-based assays for vaccine potency determination, the initial studies are encouraging and the rapid turnaround time and high-throughput capability are particularly appealing. Further studies will be needed to determine whether this type of assay can be developed as an alternative potency assay for influenza vaccines.

Encouragingly, both alternative potency assay formats using H7-specific mAbs were capable of distinguishing heat-stressed vaccine samples from non-stressed samples. Both alternative assays measure fairly rapid declines in potency when vaccine was subjected to heat treatment at 56°C and were, in fact, somewhat more sensitive to the heat treatment than the SRID assay (e.g, 1- and 4-hour time-points). Future studies will be needed to further define the most appropriate methods for assessing the stability-indicating capabilities of alternative assays, and this will be an important component of the evaluation and selection of antibodies for any mAb-based assay.

In summary, the results of the current study broaden our understanding of the issues that must be resolved as development of mAb-based alternative potency assay for influenza vaccines progresses. Although the preparation and characterization of strain-specific mAbs will be a challenge, the results from this and other recent studies demonstrate that development and selection of cross-reactive mAbs is a realistic possibility. Advanced development and preparation of a well-characterized, diverse panel of mAbs that recognize different HA epitopes for influenza subtypes with pandemic potential, such as the H7 mAbs described in the present study, greatly increase the probability of having mAbs available for vaccine testing as influenza strains evolve.

ACKNOWLEDGEMENTS

This work was supported in part by the Biomedical Advanced Research and Development Authority (BARDA), Department of Health and Human Services. BARDA arranged for acquisition of A(H7N9) candidate vaccine samples. The Centers for Disease Control and Prevention (Dr. Ruben Donis) provided mAbs 62 and 98. Anupama Vasudevan and Swati Verma were participants of the Oak Ridge Institute for Science and Education program at CBER. We thank Drs. Vladimir Lugovtsev and Hongquan Wan for their thorough review of the manuscript.

ORCID

Jerry P. Weir http://orcid.org/0000-0002-0260-0996

REFERENCES

1. Williams MS. Single-radial-immunodiffusion as an in vitro potency assay for human inactivated viral vaccines. *Vet Microbiol*. 1993;37:253-262.
2. Williams MS, Mayner RE, Daniel NJ, et al. New developments in the measurement of the hemagglutinin content of influenza virus vaccines by single-radial-immunodiffusion. *J Biol Stand*. 1980;8:289-296.
3. Wood JM, Schild GC, Newman RW, Seagroatt V. An improved single-radial-immunodiffusion technique for the assay of influenza haemagglutinin antigen: application for potency determinations of inactivated whole virus and subunit vaccines. *J Biol Stand*. 1977;5:237-247.
4. Minor PD. Assaying the Potency of Influenza Vaccines. *Vaccines (Basel)*. 2015;3:90-104.
5. Schmeisser F, Jing X, Joshi M, et al. A novel approach for preparation of the antisera reagent for potency determination of inactivated A(H7N9) influenza vaccines. *Influenza Other Respir Viruses*. 2015;10:134-140.
6. Bodle J, Verity EE, Ong C, et al. Development of an enzyme-linked immunoassay for the quantitation of influenza haemagglutinin: an alternative method to single radial immunodiffusion. *Influenza Other Respir Viruses*. 2012;7:191-200.
7. Hashem AM, Gravel C, Farnsworth A, et al. A novel synthetic receptor-based immunoassay for influenza vaccine quantification. *PLoS ONE*. 2013;8:e55428.
8. Khurana S, King LR, Manischewitz J, Coyle EM, Golding H. Novel antibody-independent receptor-binding SPR-based assay

for rapid measurement of influenza vaccine potency. *Vaccine*. 2014;32:2188-2197.
9. Kuck LR, Sorensen M, Matthews E, Srivastava I, Cox MM, Rowlen KL. Titer on chip: new analytical tool for influenza vaccine potency determination. *PLoS ONE*. 2014;9:e109616.
10. Nilsson CE, Abbas S, Bennemo M, Larsson A, Hamalainen MD, Frostell-Karlsson A. A novel assay for influenza virus quantification using surface plasmon resonance. *Vaccine*. 2010;28:759-766.
11. Pierce CL, Williams TL, Moura H, et al. Quantification of immunoreactive viral influenza proteins by immunoaffinity capture and isotope-dilution liquid chromatography-tandem mass spectrometry. *Anal Chem*. 2011;83:4729-4737.
12. Schmeisser F, Vasudevan A, Soto J, Kumar A, Williams O, Weir JP. A monoclonal antibody-based immunoassay for measuring the potency of 2009 pandemic influenza H1N1 vaccines. *Influenza Other Respir Viruses*. 2014;8:587-595.
13. Wen Y, Han L, Palladino G, et al. Conformationally selective biophysical assay for influenza vaccine potency determination. *Vaccine*. 2015;33:5342-5349.
14. Gao R, Cao B, Hu Y, et al. Human infection with a novel avian-origin influenza A (A(H7N9)) virus. *N Engl J Med*. 2013;368:1888-1897.
15. Li Q, Zhou L, Zhou M, et al. Epidemiology of human infections with avian influenza A(A(H7N9)) virus in China. *N Engl J Med*. 2014;370:520-532.
16. Schmeisser F, Adamo JE, Blumberg B, et al. Production and characterization of mammalian virus-like particles from modified vaccinia virus Ankara vectors expressing influenza H5N1 hemagglutinin and neuraminidase. *Vaccine*. 2012;30:3413-3422.
17. Schmeisser F, Vasudevan A, Verma S, et al. Antibodies to antigenic site A of influenza H7 hemagglutinin provide protection against A(H7N9) challenge. *PLoS ONE*. 2015;10:e0117108.
18. Schmeisser F, Friedman R, Besho J, et al. Neutralizing and protective epitopes of the 2009 pandemic influenza H1N1 hemagglutinin. *Influenza Other Respir Viruses*. 2013;7:480-490.
19. Schmeisser F, Vodeiko GM, Lugovtsev VY, Stout RR, Weir JP. An alternative method for preparation of pandemic influenza strain-specific antibody for vaccine potency determination. *Vaccine*. 2010;28:2442-2449.
20. Vodeiko GM, Weir JP. Determination of H5N1 vaccine potency using reference antisera from heterologous strains of influenza. *Influenza Other Respir Viruses*. 2012;6:176-187.
21. He F, Kumar SR, Syed Khader SM, Tan Y, Prabakaran M, Kwang J. Effective intranasal therapeutics and prophylactics with monoclonal antibody against lethal infection of H7N7 influenza virus. *Antiviral Res*. 2013;100:207-214.
22. He F, Prabakaran M, Tan Y, Indira K, Kumar SR, Kwang J. Development of dual-function ELISA for effective antigen and antibody detection against H7 avian influenza virus. *BMC Microbiol*. 2013;13:219.
23. Wiley DC, Skehel JJ. The structure and function of the hemagglutinin membrane glycoprotein of influenza virus. *Annu Rev Biochem*. 1987;56:365-394.
24. Wiley DC, Wilson IA, Skehel JJ. Structural identification of the antibody-binding sites of Hong Kong influenza haemagglutinin and their involvement in antigenic variation. *Nature*. 1981;289:373-378.
25. Wang X, Jiang H, Wu P, et al. Epidemiology of avian influenza A A(H7N9) virus in human beings across five epidemics in mainland China, 2013-17: an epidemiological study of laboratory-confirmed case series. *Lancet Infect Dis*. 2017;17:822-832.
26. Verma S, Soto J, Vasudevan A, et al. Determination of influenza B identity and potency in quadrivalent inactivated influenza vaccines using lineage-specific monoclonal antibodies. *PLoS ONE*. 2017;12:e0175733.
27. Carvalho SB, Moleirinho MG, Wheatley D, et al. Universal label-free in-process quantification of influenza virus-like particles. *Biotechnol J*. 2017;12:1700031.

The FEBS Journal

FEBS PRESS science publishing by scientists

REVIEW ARTICLE

Immunogenicity and humanization of single-domain antibodies

Martin A. Rossotti[1], Kasandra Bélanger[1], Kevin A. Henry[1,2] and Jamshid Tanha[1,2]

1 Life Sciences Division, Human Health Therapeutics Research Centre, National Research Council Canada, Ottawa, Canada
2 Department of Biochemistry, Microbiology and Immunology, Faculty of Medicine, University of Ottawa, Canada

Keywords
humanization; immunogenicity; nanobody; single-domain antibody; therapeutic antibody; V_HH; V_{NAR}

Correspondence
J. Tanha, Human Health Therapeutics Research Centre, National Research Council Canada, 100 Sussex Drive, Ottawa, ON K1A 0R6, Canada
Tel: +1 613 990 7206
E-mail: jamshid.tanha@nrc-cnrc.gc.ca

(Received 4 February 2021, revised 26 February 2021, accepted 8 March 2021)

doi:10.1111/febs.15809

Single-domain antibodies (sdAbs), the autonomous variable domains of camelid and shark heavy-chain antibodies, have many desirable properties as components of biologic drugs. However, their sequences may increase the risk of immunogenicity and antidrug antibody (ADA) development in humans, and thus, sdAbs are routinely humanized during development. Here, we review and summarize the available evidence regarding the factors governing immunogenicity of sdAbs and our current state of knowledge of strategies to mitigate immunogenicity risks by humanization. While several sdAb properties, including high homology of camelid V_HHs with human IGHV3 gene products, favor low immunogenicity in humans, epitopes absent in the human repertoire including the exposed V_H:V_L interface may be intrinsically immunogenic. While most clinical trials have demonstrated minimal sdAb immunogenicity, two notable exceptions (the tetrameric DR5-specific V_HH TAS266 and the TNFR1-specific V_H GSK1995057) illustrate that special caution must be taken in identifying preexisting ADAs against highly potent sdAbs. Nonhuman sequence alone does not adequately explain sdAb immunogenicity, as some camelid V_HHs are nonimmunogenic while some fully human V_Hs elicit ADAs. The presence of preexisting ADAs directed against the exposed C-termini of some sdAbs in a significant proportion of individuals awaits a molecular explanation. Whether sdAb humanization reduces or promotes immunogenicity remains unclear: reduction of nonhuman sequence content at the expense of introducing low-level aggregation in humanized variants may be counterproductive. Further work will establish thresholds for V_HH and V_{NAR} humanization to maximize human sequence content while avoiding loss of binding affinity and/or immunogenicity resulting from aggregation or decreased stability.

Abbreviations
ADA, antidrug antibody; CD, cluster of differentiation; CD40L, CD40 ligand; CDR, complementarity-determining region; CEA, carcinoembryonic antigen; C_H, constant heavy-chain domain; C_L, constant light-chain domain; DC, dendritic cell; DR5, death receptor 5; EGFR, epidermal growth factor receptor; ELISA, enzyme-linked immunosorbent assay; EMA, European Medicines Agency; FDA, Food and Drug Administration; FR, framework region; GPL-1, glucagon-like peptide 1; HCAb, heavy chain-only antibody; HCV, hepatitis C virus; HLA, human leukocyte antigen; HV, hypervariable; IGHV, immunoglobulin heavy-chain variable gene; IgNAR, Ig new antigen receptor; IL, interleukin; K_D, equilibrium dissociation constant; MHC, major histocompatibility complex; MMR, macrophage mannose receptor; MUC1, mucin 1, cell surface-associated; PK/PD, pharmacokinetics/pharmacodynamics; RA, rheumatoid arthritis; sdAb, single-domain antibody; TCE, T-cell epitope; TNFR1, tumor necrosis factor receptor 1; TNF-α, tumor necrosis factor-α; VEGF, vascular endothelial growth factor; V_H, variable heavy-chain domain; V_HH, autonomous variable domain of camelid heavy chain-only antibody; V_L, variable light-chain domain; V_{NAR}, autonomous variable domain of shark Ig new antigen receptor.

Introduction

Conventional vertebrate immunoglobulins (Igs) are tetramers of two heavy and two light chains. The variable domains of each chain (V_H and V_L, respectively) assemble to form the antigen-binding site. In 1993, Hamers-Casterman *et al.* made an important discovery in the sera of camelid species (camels, llamas, and alpacas): in addition to conventional tetrameric antibodies, camelids produced homodimeric heavy chain-only antibodies (HCAbs) devoid of light chains [1] that arose through disruption of the 5′ splice site between the C_H1- and hinge-encoding exons [2]. HCAbs are thus composed of two identical heavy chains, each comprising two constant domains (C_H2 and C_H3), a hinge region and a variable V_HH domain responsible for antigen recognition (Fig. 1). Antigen binding by V_HH domains is mediated by only three hypervariable (HV) loops/complementarity-determining regions (CDRs) rather than the six loops of conventional antibodies, which are flanked by four relatively constant framework regions (FRs). The V_HH CDR3 loop is frequently long and extended, forming finger-like elongations, which in addition to the small footprint of

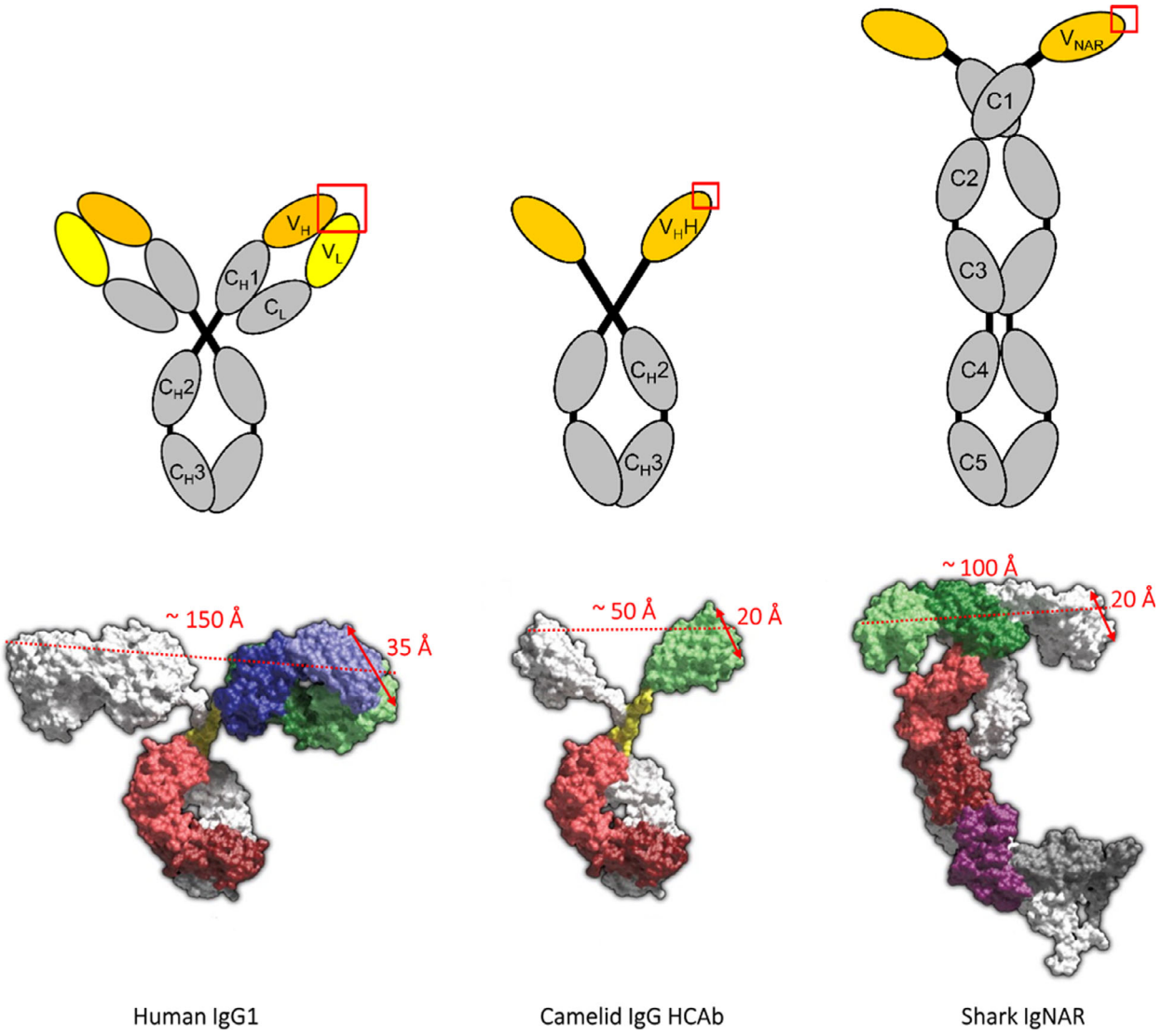

Fig. 1. Domain structures of conventional vertebrate tetrameric IgG1, camelid heavy chain-only IgG, and shark IgNAR. The variable domains of each antibody molecule are shown in yellow and the antigen-combining site is indicated by a red box. Structural models of all three types of antibodies are also shown below. Approximate paratope diameters and distances between antigen-combining sites are indicated. Figure reproduced from [4,7].

The FEBS Journal **289** (2022) 4304–4327 © 2021 Her Majesty the Queen in Right of Canada
The FEBS Journal © 2021 Federation of European Biochemical Societies.
Reproduced with the permission of the Minister of National Research Council Canada

V_HHs is partly responsible for their ability to bind concave epitopes such as the active sites of enzymes [3,4].

Two years after the discovery of camelid HCAbs, it was reported that sharks and other cartilaginous fish also produced HCAbs called Ig new antigen receptors (IgNARs) [5]. Thus, homodimeric antibodies lacking light chains have arisen multiple times by convergent evolution following the origin of conventional tetrameric antibodies in an ancestral vertebrate [6,7]. IgNARs are composed of two identical heavy chains, each comprising five constant domains and one variable V_{NAR} domain [8,9]. Compared with other Ig variable domains, $V_{NAR}s$ lack two β strands (C′ and C″), and consequently, CDR2 is absent; however, in addition to CDR1 and CDR3, loops connecting the C-D and D-E strands (HV2 and HV4, respectively) are involved in antigen recognition [10]. The autonomous variable domains of camelid HCAbs and shark IgNARs (V_HHs and $V_{NAR}s$) share several characteristics such as high stability and solubility, longer than average CDR3 loops, and presence of noncanonical disulfide linkages sculpting the binding site. However, since camelid species are generally easier to handle and access, generate stronger HCAb responses following immunization [11,12], and produce immunoglobulins sharing relatively high homology with human IGHV genes [13], V_HHs have attracted greater interest than $V_{NAR}s$ as biologic drugs.

Regardless of their species origin, single-domain antibodies (sdAbs) have important advantages over full-length conventional antibodies, which have been extensively reviewed in previous publications [10,14–16]. One major benefit of sdAbs is their small size (~ 15 kDa). While recombinant full-length Igs are costly to produce in mammalian cells, sdAbs are easily expressed in large quantities in economic production systems such as bacteria and yeast. In addition, their fast blood clearance

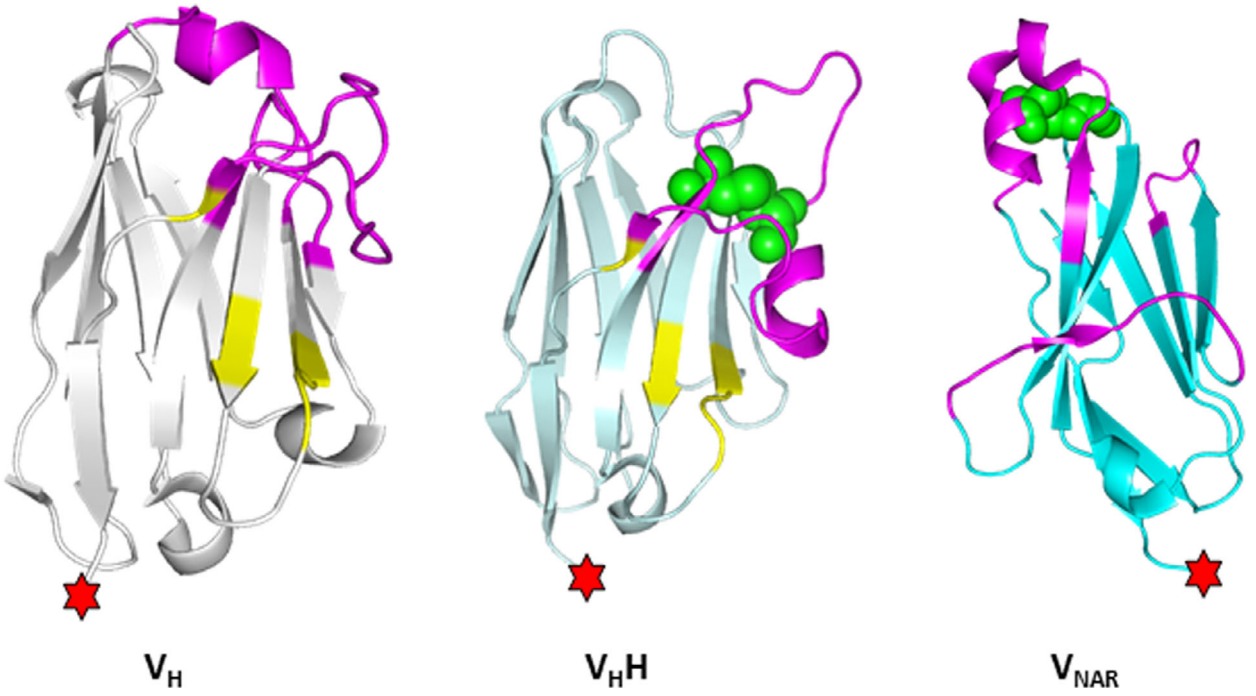

Fig. 2. Structures of human V_H (anti-MDM4, PDB ID: 2VYR), camelid V_HH (antilysozyme, PDB ID: 1JTT), and V_{NAR} (antilysozyme, PDB ID: 2I24) domains. Each domain is colored to indicate potential factors influencing immunogenicity. The FRs of fully human V_Hs/V_Ls contain no nonhuman sequences (white), while those of camelid V_HHs share up to 95% identity with human IGHV3 gene products (light cyan). By contrast, the FRs of shark $V_{NAR}s$ share little sequence homology with human products (cyan). In V_Hs/V_Ls and V_HHs, the interface with the absent V_L domain (yellow) is partially exposed. The CDR loops of sdAbs (magenta) may be immunogenic for several reasons: (a) in synthetic V_Hs/V_Ls, the CDRs may be prone to unusual amino acid composition including charged residues; (b) in camelid V_HHs, long CDR3 loops may take on unique conformations to fold over the V_L interface; and (c) in shark $V_{NAR}s$, CDR2 is absent but additional HV loops can make contacts with antigens. Both camelid V_HHs and shark $V_{NAR}s$ often contain noncanonical intradomain disulfide linkages (green) sculpting the binding site and potentially influencing Ig domain structure. Finally, the exposed C termini of some sdAbs may be inherently immunogenic, as Ig variable domains are naturally fused with C_H1 or C_L domains in human antibodies. Figure generated using PYMOL v 2.4.0 (Schrödinger, LLC, New York, NY, USA).

and effective tissue and tumor penetration make sdAbs particularly effective noninvasive imaging agents compared with conventional antibodies, which demonstrate limited biodistribution and extended half-life. If prolonged exposure is required (e.g., for the treatment of chronic diseases), the *in vivo* half-lives of sdAbs can be facilely improved via fusion to a serum albumin-binding moiety or the immunoglobulin Fc region [17–19]. Another important hallmark of sdAbs is their modularity: their strictly monomeric behavior makes sdAbs optimal building blocks for constructing multivalent and multispecific therapeutic and diagnostic molecules with improved functionality and potency [15,20–22]. Finally, the robust biophysical properties of sdAbs are sufficient for proper folding and antigen recognition under reducing intracellular conditions, enabling targeting of intracellular proteins in live cells that are otherwise inaccessible to conventional antibodies [23–25].

Immunogenicity of sdAbs

Despite their many desirable properties, the nonhuman origin of V_HHs and V_{NAR}s may increase the chance of triggering unwanted immune responses when administered as therapeutic agents. When considering immunogenicity risks, it is important to remember that although the transition from fully murine to chimeric (murine V_H/V_L, human constant domain) antibody therapy significantly reduced the frequency of antidrug antibody (ADA) development [26], subsequent advances (humanized and fully human antibodies) had comparatively minor impact on immunogenicity. Even fully human antibodies can elicit ADAs when administered parenterally at high dose [27]. However, some intrinsic features of sdAbs may favor low immunogenicity in humans: these include small size, which should decrease the number of potentially immunogenic epitopes, resistance to forming highly immunogenic aggregates, and for non-half-life-extended sdAbs, rapid blood clearance. Many of these features are shared with monomeric nonantibody scaffolds, which fall outside the scope of this review [28]. The high sequence identity of most V_HHs with human IGHV3 family gene products (up to 95% identity in FR sequences; [13]) is comparable to that of humanized murine V_H domains (e.g., trastuzumab) and would be expected to translate to low immunogenicity. V_{NAR}s, in contrast, share the classical Ig fold architecture, but their core frameworks are more distantly structurally related to human V_H and V_L domains [29], T-cell receptor variable domains [9], and other Ig-superfamily cell-surface receptors [30]. Because of the evolutionary distance separating sharks and humans, V_{NAR}s share little sequence identity with human V_H and V_L domains (~ 30% overall; [29]) and would thus be predicted to be the most immunogenic of all sdAbs.

Other general features of sdAbs, including fully human V_Hs and V_Ls, may be inherently immunogenic and even trigger the generation of novel types of ADAs (Fig. 2). Because the interface between the V_H and V_L domains of conventional antibodies is exposed in sdAbs (except for possibly V_{NAR}s, which may never have had a pairing partner that was subsequently lost during evolution), ADAs may be generated against it. While the CDR1 and CDR2 loops of V_HHs adopt similar canonical structures as human antibodies [13], their long CDR3 loops may adopt conformations absent in the human repertoire [31]. High levels of somatic hypermutation [32,33] of V_HH CDRs and FRs may serve to decrease their sequence homology with human IGHV3 gene products. Immunogenic conformational epitopes may also potentially be formed by subtle shifts in sdAb domain architecture arising from the presence of noncanonical disulfide linkage formation [34]. Anti-sdAb ADAs may also be more prone to neutralization than ADAs generated against full-size conventional IgGs, as by definition they must target epitopes in the variable domain including regions forming the antigen-binding site.

Preclinical assays of antibody immunogenicity

Prior to administration in humans, the immunogenicity of antibody therapeutics can be assessed in several ways. First, the presence of preexisting ADAs can be assessed using large and diverse panels of serum samples from animals or treatment-naïve human volunteers [35]. This method is simple but often requires design and validation of customized binding assays for individual antibodies, thus making comparisons of ADA incidence across different antibodies inexact. Second, *in silico* analyses (e.g., https://www.iedb.org/) can be used to predict antibody immunogenicity via the presence of CD4+ T-cell epitopes (TCEs), which are associated with sustained ADA production [36]. Such tools are often based on experimental datasets (peptide-MHC II binding assays [37] and T-cell stimulation assays [38]) but may still over-estimate the number of putative immunogenic regions and thus *in silico* TCE predictions should be corroborated using cell-based assays [39–41]. Third, *in vitro* immunoassays can help identify the presence of any TCEs. A variety of assays and screening platforms have been developed for this purpose including HLA peptide binding assays [37], T-cell epitope peptide screening assays [42], and whole protein *ex vivo* T-cell activation assays [43]. A

good illustration of the potential utility of these methods was provided by Harding *et al.* [41], who evaluated 15-mer peptides from the V_H and V_L domains of eight humanized or fully human therapeutic Abs in a cell-based assay using primary cells from almost 100 individuals and found that TCEs were largely present in CDRs and not FRs. Finally, immunogenicity can be assessed by dosing experimental animals (e.g., mice or nonhuman primates) although this is generally poorly predictive of human immunogenicity [44].

Immunogenicity of V_HHs

One of the pioneers in the clinical development of V_HHs was Ablynx, the Belgian biopharmaceutical company that was acquired by Sanofi in 2018. At the time of their acquisition, Ablynx had at least eight V_HH-based clinical programs and many others in late preclinical or earlier stages of development [45]. The bulk of clinical programs have been based around humanized V_HHs. To the best of our knowledge, no preclinical studies of the immunogenicity of V_HHs and their humanized derivatives using human serological panels or *in silico* studies have been published. The only preclinical study of the *in vitro* immunogenicity of V_HHs was carried out on two non-humanized ^{68}Ga-labeled anti-human epidermal growth factor receptor 2 (HER2) and anti-macrophage mannose receptor V_HHs, both of which are in phase II clinical trials for PET imaging of breast cancer and tumor-associated macrophages, respectively [46]. Both V_HHs were free of aggregates and were taken up by dendric cells (DCs) but failed to activate DCs or T cells in co-cultures (Table 1). Additionally, one study of a llama anti-epidermal growth factor receptor (EGFR) V_HH [47] found that amorphous aggregates (insoluble and disulfide-shuffled V_HHs) were immunogenic in mice while the soluble V_HH and heat-induced aggregates were not, even after six doses, illustrating that nonhuman sequence is not the only determinant of sdAb immunogenicity. While the pharmacokinetics/pharmacodynamics (PK/PD) profiles of monomeric and dimeric/trimeric half-life extended V_HHs showed no evidence of ADA development following a single injection in cynomolgus monkeys [48], ADAs were generated against vobarilizumab (ALX-0061, a bispecific antibody consisting of a humanized anti-interleukin 6 receptor V_HH fused to a humanized antiserum albumin V_HH for half-life extension) in at least half of monkeys after a single injection [49]. The consensus of more than 22 immunization studies of V_HHs in rodents and nonhuman primates was that ADAs were generated in 0–37% of animal, but were generally not neutralizing and did not impede interpretation of PK/PD or safety data [50].

As of 2020, at least 35 clinical trials of V_HH-based biologic drugs have been carried out involving more than 1000 patients and healthy volunteers [51]. Most trials have revealed no or minimal immunogenicity, comparable to that of fully human or humanized IgGs, with primarily transient treatment-emergent ADAs observed in 0–30% of subjects and neutralizing ADAs in < 3% of subjects [50]. In a phase I trial of a ^{68}Ga-labeled anti-HER2 dromedary V_HH for PET/CT imaging of breast cancer, none of 20 patients developed ADAs after a single injection [52]. A subsequent study found that 1/20 of these patients showed low levels of preexisting ADAs, which increased marginally over 3 months following the injection, albeit with no safety- and PK-related adverse effects [46]. A phase I study of ALX-0761 (a trimeric antibody consisting of humanized camelid anti-IL-17F, anti-IL-17A/F, and antiserum albumin V_HHs) showed that ~ 15% (5/33) psoriatic patients injected with multiple doses developed treatment-emergent ADAs that did not affect drug exposure [53]. A phase I study of ALX-0141 (a trimeric antibody consisting of two identical anti-RANKL humanized camelid V_HHs and one antiserum albumin humanized camelid V_HH) showed no evidence of ADAs in 42 healthy volunteers after a single subcutaneous injection [54]. No ADAs were detected in a 24-week phase I/II study of vobarilizumab (ALX-0061, bispecific humanized anti-interleukin 6 receptor and humanized antiserum albumin camelid V_HHs) in 37 patients with rheumatoid arthritis (RA) dosed every 4 or 8 weeks [55]; subsequent phase II and IIb trials in patients with RA and systemic lupus erythematosus identified treatment-emergent ADAs in similar proportions of drug-treated and placebo-treated patients [56,57]. Phase I and II studies of ALX-0171 (a trimeric antibody consisting of three identical anti-RSV humanized camelid V_HHs) administered in multiple doses by nebulization showed no evidence of treatment-emergent ADAs [58,59]. Phase I/II studies of ozoralizumab (ATN-103, a trimeric antibody consisting of two identical antitumor necrosis factor (TNF)-α humanized camelid V_HHs and one antiserum albumin humanized camelid V_HH) revealed < 3% incidence of neutralizing ADAs after long-term dosing of RA patients (< 3%; [60–62]). Phase I and 1b studies of caplacizumab (ALX-0081, a bivalent anti-von Willebrand factor humanized camelid V_HH) revealed no immune responses following single or multiple injections of the drug up to 1 month after the last dosing [63]. Larger subsequent phase II and phase III studies [64–66], treatment-emergent ADAs were identified in

Table 1. Summary of the results of sdAb immunogenicity assessments. aTTP, acquired thrombotic thrombocytogenic purpura; CD40L, CD40 ligand; DC, dendritic cell; GLP1R, glucagon-like peptide 1 receptor; HLE, half-life extension; IL, interleukin; MMR, macrophage mannose receptor; NR, not reported; RANKL, receptor activator of nuclear factor-κB ligand; RSV, respiratory syncytial virus; SA, serum albumin; SLE, systemic lupus erythematosus; TNFR1, tumor necrosis factor receptor 1; TNF-α, tumor necrosis factor-α; VEGF, vascular endothelial growth factor; vWF, von Willebrand factor.

Type of sdAb	Candidate	Target	Format	Humanization status	Stage	Immunogenicity assessment	Reference(s)
V_HH	Nb 3.49	MMR	Monomer	Not humanized	Preclinical (*in vitro*)	V_HH showed low capacity to activate DCs and induce T-cell proliferation in DC-T cell coculture assays	[46]
	7D12	EGFR	Monomer	Not humanized	Preclinical (mouse)	The soluble V_HH did not elicit ADAs following six injections, but amorphous V_HH aggregates were highly immunogenic	[47]
	Various	None (SA for HLE)	Monomer, dimer, trimer	NR	Preclinical (cynomolgus monkey)	PK/PD profiles suggested no ADA development following a single injection	[48]
	Vobarilizumab (ALX-0061)	IL-6, SA	Dimer	Humanized	Preclinical (cynomolgus monkey)	ADAs detected in at least 50% of monkeys following a single injection.	[49]
					Phase I/II	0/37 RA patients developed ADAs following multiple injections	[55]
					Phase II	Similar proportions of 250 ALX-0061-treated (103, 41%) and 62 placebo-treated (32, 52%) SLE patients showed treatment-emergent ADAs against ALX-0061	[57]
					Phase IIb	58/187 (31%) ALX-0061-treated RA patients developed treatment-emergent ADAs against ALX-0061	[56]
	2Rs15d	HER2	Monomer	Not humanized	Preclinical (*in vitro*)	V_HH showed low capacity to activate DCs and induce T-cell proliferation in DC-T cell coculture assays	[46]
					Phase I	In one study, 0/20 breast cancer patients showed ADAs before or after a single injection. In a subsequent study, one patient showed low levels of preexisting ADAs, which increased marginally over 3 months with no effect on drug exposure	[46,52]
	ALX-0761	IL-17A/F, SA	Trimer	Humanized	Phase I	5/33 (15%) of patients with psoriasis developed treatment-emergent ADAs following multiple doses that did not affect drug exposure	[53]
	ALX-0141	RANKL, SA	Trimer	Humanized	Phase I	0/42 healthy volunteers developed ADAs after a single injection	[54]
	ALX-0171	RSV fusion protein	Trimer	Humanized	Phase I	0/60 healthy volunteers developed ADAs following	[58]

Table 1. (Continued).

Type of sdAb	Candidate	Target	Format	Humanization status	Stage	Immunogenicity assessment	Reference(s)
						single or multiple doses of nebulized ALX-0171	
					Phase IIb	Similar proportions of 135 ALX-0171-treated (46, 34%) and 39 placebo-treated (10, 26%) RSV-infected children showed treatment-emergent ADAs against ALX-0171	[59]
	Ozoralizumab (ATN-103)	TNF-α, SA	Trimer	Humanized	Phase I/II	Treatment-emergent ADAs detected in < 3% of 266 RA patients receiving multiple doses	[60–62]
	Caplacizumab (ALX-0081)	vWF	Dimer	Humanized	Phase I/Ib	No immunogenicity detected after multiple dosing of 40 healthy volunteers and 24 patients with stable angina	[63]
					Phase II	Treatment-emergent ADAs detected in 3/36 (9%) of caplacizumab-treated aTTP patients after multiple doses that did not affect drug exposure	[64,65]
					Phase III	Treatment-emergent ADAs detected in 4/145 (3%) of caplacizumab-treated aTTP patients after multiple doses that did not affect drug exposure	[66]
	TAS266	DR5	Tetramer	Humanized	Phase I	Preexisting ADAs detected in 3/4 (75%) contributing to Grade ≥ 3 hepatotoxicity	[67]
V_{NAR}	E06	SA	Monomer	Nonhumanized and humanized	Preclinical (*in vitro*)	Shark and humanized V_{NAR}s showed minimal T-cell activation in a DC-T cell coculture assay compared with positive controls	[68]
	C4, D1	TNF-α, SA	Trimer, biparatopic Fc fusion	Nonhumanized	Preclinical (mouse)	After dosing mice, no ADAs were generated that interfered with TNF-α neutralization	[69]
V_H or V_L	BMS-986004	CD40L	Fc fusion	Fully human V_L	Preclinical (cynomolgus monkey)	PK/PD profiles suggested no clearing ADAs following single or multiple doses	[83]
	VEGF dual dAb	VEGF	Biparatopic Fc fusion	Fully human V_H and V_L	Preclinical (rabbit, cynomolgus monkey)	Clearing ADAs elicited in some animals following a single ocular injection	[84]
	Placalumab (PN0621, ART621, CEP-37247)	TNF-α	Fc fusion	Fully human V_L	Phase II	No ADAs detected following single or multiple dosing of 27 RA patients	[85,86]
					Phase I/II	No ADAs detected in sciatica patients following a single dose via the transforaminal epidural route	[87]
	GSK2374697	SA, (GLP1R)	Monomer	Fully human V_L	Phase I		[88]

Table 1. (Continued).

Type of sdAb	Candidate	Target	Format	Humanization status	Stage	Immunogenicity assessment	Reference(s)
						19/82 (23%) healthy individuals developed ADAs against the GLP1 agonist peptide after single or multiple dosing; 13/82 (16%) had weak preexisting ADAs against the V_L that did not impact drug exposure	
	GSK1995057	TNFR1	Monomer	Fully human V_H	Phase I	Preexisting anti-V_H ADAs were present in ~ 50% of drug-naïve subjects and caused cytokine release syndrome in at least 2/17 GSK1995057-treated healthy subjects	[89,90]
	GSK2862277	TNFR1	Monomer	Fully human V_H	Phase I	Preexisting anti-V_H ADAs were present in 7/46 (15%) of healthy subjects and caused cytokine release syndrome in at least one GSK2862277-treated subject	[91]

small number of patients (3–9%) but did not affect exposure. Caplacizumab was approved in 2018 by the EMA and in 2019 by the FDA for the treatment of thrombotic thrombocytopenic purpura and thrombosis.

In contrast with the minimal immunogenicity observed with most V_HHs, Papadopoulos *et al.* [67] described unexpected hepatotoxicity in a phase I safety and tolerability study of a tetravalent humanized camelid V_HH (TAS266) targeting death receptor 5 (DR5). TAS266 acted as a DR5 agonist and elicited superior antitumor efficacy compared with conventional anti-DR5 antibodies in preclinical studies. The trial was terminated early when three of four patients dosed with 3 $mg{\cdot}kg^{-1}$ TAS266 developed grade ≥ 3 hepatotoxicity attributable to the study drug. Preexisting ADAs were detected in the three patients who developed hepatotoxicity but not the one patient who did not. The authors suggested that preexisting ADAs might promote the formation of immune complexes that could accumulate in the liver, bind DR5, and induce apoptosis through activation of complement and inflammation. The case of TAS266 needs to be studied in more detail: the underlying mechanism of toxicity may not rely on preexisting ADAs and could instead reflect the ultra-high potency of the tetravalent antibody.

Immunogenicity of V_{NAR}s

Unlike camelid V_HHs, no clinical trials of shark V_{NAR}s have yet been conducted. In a preclinical study, Steven *et al.* [68] applied the ProImmune REVEAL® DC–T cell assay to a shark antiserum albumin V_{NAR} (E06) and found that the V_{NAR} had very low immunogenicity compared with positive controls (tuberculin and KLH). Recently, Ubah *et al.* [69] showed encouraging preclinical results for the future of V_{NAR}s as human therapeutics. The authors assessed the immunogenicity of V_{NAR}s in two different molecular formats: a tetravalent fusion of two different anti-TNF-α shark V_{NAR}s to IgG1 Fc, and a trimeric fusion of the same two anti-TNF-α V_{NAR}s with a humanized antiserum albumin V_{NAR}. After dosing mice with V_{NAR}-based proteins or the anti-TNF-α IgG adalimumab, ADAs were elicited against adalimumab that hindered its ability to neutralize cytokine in a cell-based assay while no neutralizing ADAs were detected against the V_{NAR} molecules.

Immunogenicity of human V_Hs and V_Ls

In view of limiting immunogenicity, there has been high interest in development of fully human sdAbs (V_Hs or V_Ls). Autonomous V_Hs/V_Ls do not exist naturally as part of the human antibody repertoire and must instead be engineered synthetically using a variety of technologies. *In vitro* display technologies, predominantly phage display, have been key platforms for discovery of all types of sdAbs, including synthetic/semi-synthetic fully human V_Hs and V_Ls [14,70–72]. Unlike V_HHs and V_{NAR}s, human V_Hs/V_Ls have the drawbacks of low solubility and high propensity to form aggregates, potentially leading to immunogenicity

despite their human FR sequences. Several remediating approaches have been developed [73,74], including transgenic mice/rats with knock-out endogenous antibody production and knock-in *igh* loci containing autonomous human V_H, D, and J_H gene segments and constant region genes lacking C_H1 exons [75–77], and have enabled the successful identification of nonaggregating and soluble human V_Hs and V_Ls against a wide range of antigens. However, three fundamental properties of human V_Hs and V_Ls may impact their immunogenicity: (a) with fully human FRs, these molecules depend entirely on their CDR sequences for both antigen binding, and for solubility, and solubility-enhancing CDRs may have unusual amino acid composition including over-representation of charged residues and histidine [73,78–80]; (b) despite their fully human sequences, the regions of V_Hs and V_Ls making up the interface between these two domains is not naturally exposed to the human immune system; and (c) as nonnatural antibodies, the CDR sequences of V_Hs and V_Ls are not screened by human central tolerance mechanisms [41,81]. With this in mind, another approach to building libraries based on autonomous human V_H and V_L scaffolds is to amplify naturally occurring CDR sequences from human repertoires [82], although it remains unclear whether this strategy is compatible with V_H/V_L solubility, stability, and antigen binding.

To the best of our knowledge, no preclinical studies of the immunogenicity of human V_Hs and V_Ls using human serum panels (apart from the case of GSK1995057, see below), *in silico* or *in vitro* studies have been published. The PK/PD profile of an Fc-fused anti-CD40L human V_H domain antibody (BMS-986004) in cynomolgus monkeys showed no indication of clearing ADAs after multiple doses [83]. By contrast, single ocular injection of a tetravalent fusion of two different anti-VEGF human V_H domains to IgG1 Fc, administered with hydrogel microparticles for sustained release, elicited clearing ADAs in rabbits and nonhuman primates [84].

The bulk of clinical development of human V_H and V_L domain antibodies has been led by the UK company Domantis, which was acquired by GSK in 2006. The first autonomous human V_H/V_L domain tested in a clinical trial was placulumab (PN0621/ART621/CEP-37247), an Fc-fused anti-TNF-α V_L domain: administration of single doses to healthy volunteers and multiple doses to RA patients [85,86] or patients with sciatic pain [87] did not elicit detectable ADAs according to the study sponsors. In a phase I study of single and multiple doses of GSK2374697 (an anti-serum albumin V_L domain fused to a GLP-1 receptor agonist peptide), 23% (19/82) of healthy individuals developed treatment-emergent ADAs that were specific to the peptide and not the V_L moiety [88]. A smaller group of subjects (16%) had weak preexisting ADAs targeting the V_L domain that did not affect drug exposure or lead to stronger treatment-emergent ADA responses. A surprising result was observed by Holland *et al.* [89] in a phase I clinical trial of GSK1995057, a TNFR1-specific V_H domain: preexisting ADAs were detected in roughly half of 28 healthy male subjects and single infusions of the V_H resulted in TNFR1-dependent cytokine release syndrome in some ADA-positive subjects, resulting in early termination of the trial. Based on these data, healthy subjects with preexisting ADAs were excluded from a phase I trial of nebulized GSK1995057 for treatment of acute lung injury [90]. In a subsequent study, Cordy *et al.* [91] mapped the specificity of ADAs elicited against GSK1995057 to multiple sites on the V_H, with the C terminus (and proline 14 by Kabat numbering, located near the C terminus in the three-dimensional structure) playing the largest role. Based on these data, a single alanine residue was added to the C terminus of the V_H, yielding a derivative V_H (GSK2862277) with dramatically reduced binding by GSK1995057-elicited ADAs. Hundreds of sera were negative for preexisting ADAs against GSK2862277, and in a phase I trial, preexisting ADAs were detected in a much smaller proportion of healthy men (15%, 7/46) receiving single or multiple doses of the drug. However, cytokine release syndrome occurred in one subject that was likely mediated by preexisting ADAs against GSK2862277. The explanation for the presence of preexisting ADAs against V_H FRs, and especially the exposed C terminus, remains a mystery.

Strategies to mitigate sdAb immunogenicity

Antibody drugs destined for human therapy often have sequences that are foreign to the human immune system and therefore potentially immunogenic, eliciting ADAs that adversely affect drug efficacy. Sequence modification-based strategies to reduce antibody immunogenicity during development include humanization, de-immunization, and tolerization. Only humanization, and not de-immunization and tolerization, has yet been applied to sdAbs (Fig. 3).

Humanization is defined as the replacement of xenogeneic sequences with human sequences in the antibody variable domain FRs. Since the first clinical approval of a therapeutic antibody in 1985 [92], several humanization approaches have been developed

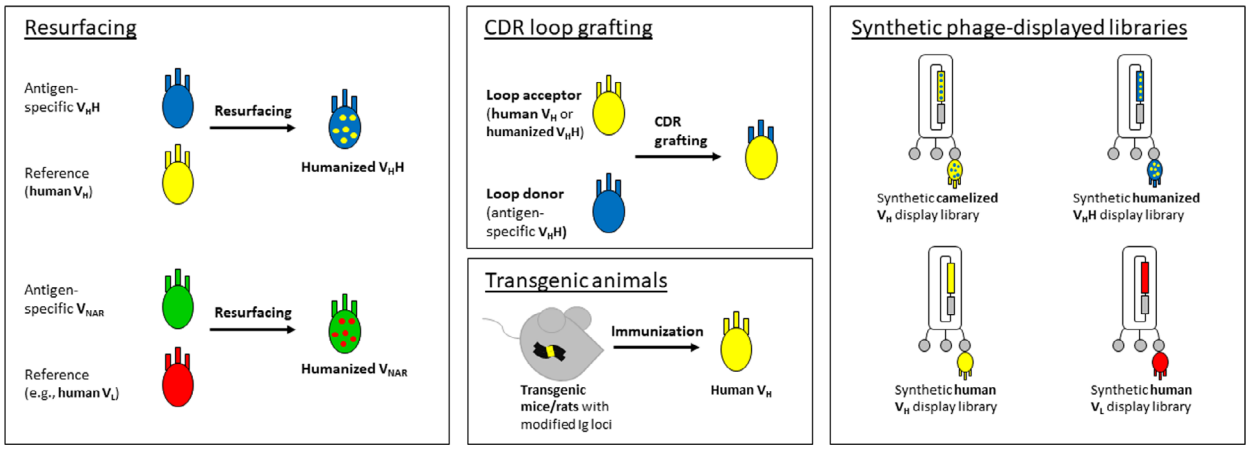

Fig. 3. Major strategies for mitigating the immunogenicity of sdAbs. Camelid V_HHs and shark $V_{NAR}s$ can be humanized by resurfacing/veneering using a homologous human variable domain as reference. V_HHs, and in principle $V_{NAR}s$, can also be humanized by grafting their CDRs onto a suitable acceptor scaffold (either a previously humanized V_HH/V_{NAR} or a fully human V_H followed by back mutation). Alternatives to humanization include use of phage display library technology and transgenic mice/rats with inactivated endogenous antibody production and knock-in *igh* loci containing autonomous V_H, D, and J_H gene segments and constant region genes lacking C_H1 exons.

including CDR grafting and resurfacing (also known as veneering). CDR grafting, the first method developed to humanize therapeutic antibodies, is the process whereby carefully selected CDRs from xenogeneic antibodies are grafted into human FRs. The design of the CDR-grafted antibody is essential to maintain the affinity and specificity of the parental antibody: choices of the CDR boundaries, of the human frameworks, and of back mutations in human FRs to the nonhuman antibody sequence are crucial to obtain the best possible outcome. Originally, CDR grafting strategies relied on the fixed FR sequences of a limited subset of well-characterized human IgGs [93,94]. However, over the years, evidence showed the importance of selecting FRs based on sequence homology with the parental nonhuman antibody [95,96]. The positions of back mutations are determined by sequence analysis and structural homology modeling. Delineation of CDR extent is crucially important and is based on a combination of CDR definitions to select only residues critical for binding. Resurfacing is defined as the replacement of only surface-exposed FR residues of nonhuman antibodies with corresponding residues from human antibody FRs [97–99]. Resurfacing is intended to have minimal effects on the properties of the parental antibody.

Despite progress in antibody humanization techniques, both humanized and fully human antibodies may still elicit ADAs [41]. While immunogenicity associated with antibodies depends on several factors such as aggregation, dose, and target antigen, the presence of CD4+ helper TCEs is a major determinant of sustained production of clearing ADAs. The identification and removal of CD4+ helper TCEs through immunological, molecular biological, and *in silico* techniques are referred to as de-immunization and have been successfully applied to several currently approved therapeutic antibodies [39]. By contrast with CD4+ helper TCEs, the presence of regulatory TCEs within the antibody backbone can minimize immunogenicity. The process of introducing tolerogenic regulatory TCEs into the antibody primary amino acid sequence to induce the expansion of regulatory T cells is called tolerization [39].

There is a consensus that despite the expected low immunogenicity of V_HHs and $V_{NAR}s$ [100,101], humanization is performed routinely as part of their development. The sdAb sequence is modified until finding a variant, with as high identity to human IGHV sequences as possible, that does not compromise the original properties of the parental sdAb. The current state of the art for humanization of a V_HH or V_{NAR} consists of several steps for CDR grafting or resurfacing the xenogeneic sdAb sequence to mimic human variable domains [102,103]. First, the sdAb sequence is aligned to a database of human germline IGHV genes (or in the case of $V_{NAR}s$, light-chain variable genes). The selected human germline V sequence is then used as a reference to modify amino acids in FRs at fixed positions that are least damaging to the robust properties of V_HHs and $V_{NAR}s$ [103]. Generally, two of the four germline encoded FR2

hydrophilic amino acids principally responsible for the solubility of V_HHs can be substituted (IMGT positions 49 and 50) without compromising the solubility or the monomeric behavior and function of the nonhuman antibodies [104–106]. The remaining two amino acids from the germline FR2 tetrad (IMGT positions 42 and 52) cannot be humanized as they are crucial to maintain the structural integrity of the V_HH and are essential for the proper conformation of the CDR3 loop [105,106]. Despite this restriction, humanized V_HHs have higher sequence identity with human IGHV gene products than humanized murine V_H domains (e.g., trastuzumab). Completely humanized V_HHs and $V_{NAR}s$ have sometimes been generated by introducing all amino acid exchanges (usually > 10 for V_HHs and dozens for $V_{NAR}s$) at once with variable detrimental effects on expression yield, aggregation behavior, and recognition of antigen. Alternatively, selected homologous human germline sequences can be used as acceptor scaffolds for the grafting of the CDR loops from V_HHs or $V_{NAR}s$, followed by back mutation of specific positions to restore sdAb properties. In both cases, the resulting variants are thoroughly characterized based on physicochemical and binding properties to select lead humanized sdAbs. Because some V_HHs use FR residues to make contacts with antigens [107], the effects of humanization may be inherently unpredictable.

Humanization of V_HHs

The first comprehensive report describing the humanization of V_HHs was by Vincke *et al.* [103], who proposed general systematic guidelines for accomplishing this goal. Prior to this, Saerens *et al.* explored the potential for CDR exchange between homologous V_HH scaffolds and identified a 'universal' dromedary V_HH framework (cAbBCII10) for CDR grafting while maintaining robust biophysical properties (expression, stability, and refoldability [102]). Vincke *et al.* chose NbHuL6, a V_HH specific for human lysozyme [108], and NbBcII10, a potent V_HH inhibitor of the BcII β-lactamase from *Bacillus cereus* [109], as test cases for humanization. Both V_HHs belonged to dromedary V_HH subfamily 2, representing more than 75% of isolated V_HHs in the literature [32]. Full humanization of NbHuL6 and NbBcII10 at the four key FR2 solubilizing residues (IMGT positions, 42, 49, 50, and 52), yielding NbHuL6$_{VGLW}$ and NbBcII10$_{VGLW}$, adversely affected V_HH expression yield, solubility, and antigen-binding affinity (45- and 2000-fold decreases in K_Ds, respectively). The authors went on to generate partially humanized variants of NbHuL6 to dissect the impact of each member of the germline FR2 tetrad on the V_HH's biochemical properties. They found that humanization of E49 and R50, yielding NbHuL6$_{FGLG}$, did not compromise expression yield or affinity and, furthermore, significantly increased stability as determined by measuring the free energy of unfolding (Table 2). These results were consistent with previous studies in which humanization of cAbAn33, a V_HH specific for the variant surface protein of trypanosomes, at positions 49 and 50 led to stability increases [105] and, conversely, camelization of human V_HHs at positions including 49 and 50 resulted in stability decreases [74]. Moreover, size exclusion chromatography experiments showed that the variant was monomeric although hints of decreased solubility, judged based on size exclusion chromatography peak tailing, were observed. Conversely, humanization of positions 42 and 52 (F42V and G52W) led to significant decreases in affinity as well as diminished stability. Humanization of position 42 played the most prominent role in affinity loss. Comparison of the co-crystal structures of NbHuL6 and its partially humanized variant, NbHuL6$_{FGLW}$, in complex with human lysozyme revealed similar CDR1 and CDR2 loop conformations for both V_HHs but a conformational shift in the NbHuL6$_{FGLW}$ CDR3 loop resulting from the G52W substitution, providing a structural explanation for the reduced affinities of NbHuL6 and NbBcII10 variants in which residue 52 was humanized.

In a subsequent set of experiments, Vincke *et al.* [103] humanized the complete framework of NbBcII10 by resurfacing (veneering). Using the human germline V_H DP47 (IGHV3-23) from the IGHV3 family as the reference [110,111], 11 solvent-exposed FR residues distributed over the entire V_HH outside of FR2 were substituted with human IGHV3 residues. The resulting resurfaced V_HH, h-NbBcII10, had similar affinity for BcII β-lactamase but decreased expression yield and thermal stability compared with the parental dromedary V_HH. The FR residues altered during resurfacing were previously shown to be important for the stability of monomeric llama V_HHs [112,113]. Further humanization of positions 49 and 50 of NbBcII10 and h-NbBcII10, yielding NbBcII10$_{FGLA}$ and h-NbBcII10$_{FGLA}$, respectively, resulted in improved thermostability without compromising solubility or antigen binding. By contrast, humanization of positions 49 and 50 of the NbHuL6 V_HH adversely affected solubility as determined by size exclusion chromatography analyses. Importantly, the maximally humanized V_HH, h-NbBcII10$_{FGLA}$, showed a complete loss of reversible folding and antigen binding following heat-induced denaturation, consequences which were collectively

Table 2. Summary of the results of sdAb humanization campaigns. MUC1, mucin 1; SA, serum albumin; VSG, variant surface glycoprotein.

Type of sdAb	Candidate	Target	Humanization technique	Acceptor or reference	Human FR identity (%)[a]	Reference
V_HH	cAbAn33	VSG	Resurfacing/veneering	IGHV3-23	83.5[b]	[105]
	NbHuL6	Lysozyme	Resurfacing/veneering	IGHV3-23	83.7	[103]
			CDR grafting	h-NbBcII10$_{FGLA}$	92.3	[103]
	NbBcII10	BcII β-lactamase	Resurfacing/veneering	IGHV3-23	92.3	[103]
	NbHSA	SA	CDR grafting	h-NbBcII10$_{FGLA}$	92.3	[103]
	NbAahII10	AahII scorpion toxin	CDR grafting	h-NbBcII10$_{FGLA}$	92.3	[117]
	Nb42	VEGF	Resurfacing/veneering	IGHV3-23	87.9[b]	[119]
	NRC-sdAb022	EGFR	Resurfacing/veneering	IGHV3-30	88.8–93.8	[120]
	NRC-sdAb028					
	NRC-sdAb032					
	NRC-sdAb033					
	NbCEA5	CEA	CDR grafting	h-NbBcII10$_{FGLA}$	92.3	[121]
	VHH6	CD7	CDR grafting	h-NbBcII10$_{FGLA}$	92.3[b]	[123]
	ER46	MUC1	CDR grafting	IGHV3-23	96.7[b]	[125]
	C21	CD16	CDR grafting	IGHV3-23	95.6[b]	[125]
	R11	SA	Resurfacing/veneering	IGHV3 consensus	82.4–92.3	[126]
	R28					
	M75					
	M79					
V_{NAR}	5A7	Lysozyme	Resurfacing/veneering	IGKV1-39	69.8	[29]
	E06	SA	Resurfacing/veneering	IGKV1-39	63.5	[29]
	E06	SA	Resurfacing/veneering	IGKV4-1	60–65	[68]

[a]Sequence identity was assessed in all framework regions (FR1-4) using IMGT FR definitions; [b]Humanization either significantly reduced stability and/or affinity for antigen, or these parameters were not assessed.

attributed to substitutions across the h-NbBcII10 domain, not just at positions 49 and 50. Comparison of the crystal structures of h-NbBcII10$_{FGLA}$ and NbBcII10 revealed that although substitutions distributed across the humanized V_HH induced minimal conformational changes, the structure of the humanized V_HH was distinct from that of the parental dromedary V_HH. Furthermore, superimposing the crystal structure of h-NbBcII10$_{FGLA}$ onto those of two human V_HHs of DP47 germline origin [114,115] revealed that except for two amino acids (S83 and V101), the remaining 11 humanized residues had identical spatial positioning, suggesting that the structural consequences of humanization were minimal.

Finally, Vincke *et al.* [103] employed CDR grafting as a second humanization approach to explore whether the humanized V_HH, h-NbBcII10$_{FGLA}$, could serve as a 'universal' acceptor scaffold for grafting CDR loops from donor V_HHs. Two CDR-grafted chimeric V_HHs were constructed: one containing the CDR loops from NbHuL6, a V_HH belonging to the same dromedary subfamily 2 as the NbBcII10$_{FGLA}$ scaffold, and another containing the CDR loops from a llama antiserum albumin V_HH, NbHSA, belonging to subgroup C [116]. Both CDR-grafted variants (h-NbBcII10$_{FGLA}$ L-L-L and h-NbBcII10$_{FGLA}$ S-S-S) had comparable expression levels and affinities as the parental CDR-donor V_HHs. While there was a slight decrease in thermodynamic stability of NbBcII10$_{FGLA}$ S-S-S compared with the donor NbHSA, the thermodynamic stability and the T_m of NbBcII10$_{FGLA}$ L-L-L were increased compared with the donor V_HH, NbHuL6. Furthermore, grafting of the NbHuL6 CDR loops was beneficial to the h-NbBcII10$_{FGLA}$ scaffold in terms of reversibility of thermal unfolding, underling the contribution of the CDRs to this property of V_HHs. Based on these findings, the authors proposed two general strategies for generating humanized V_HHs with optimal stability and affinity. The first option to consider is CDR grafting onto the 'universal' humanized V_HH scaffold, h-NbBcII10$_{FGLA}$, which often yields humanized V_HHs with good expression, stability, and solubility as well as preserved affinity and specificity. If this strategy leads to unacceptable affinity losses, the resurfacing approach, in which positions 49 and 50 are humanized but positions 42 and 52 are left unchanged due to their impact on stability and affinity, is a second option.

Following the resurfacing protocol of Vincke *et al.* [103], Ben Abderrazek *et al.* [117] humanized NbAahII10, a potent AahII scorpion toxin-neutralizing V_HH. Using h-NbBCII10$_{FGLA}$ as reference, NbAahII10 and a variant in which a CDR1 cysteine was

substituted with serine (NbAahII10 C/S) were humanized at 10 positions, yielding hu2NbAahII10$_{FERG}$ and hu2NbAahII10$_{FERG}$ C/S. Both partially humanized V_HHs maintained the camelid FR2 solubilizing residues at IMGT positions 42, 49, 50, and 52. From this starting point, maximally humanized versions hu3NbAahII10$_{FGLG}$ and hu3NbAahII10$_{FGLG}$ C/S were generated by humanizing positions 49 and 50. Humanization somewhat compromised V_HH expression, and although size exclusion chromatography experiments showed that the humanized variants appeared to be monomeric, progressive retardation of elution volume was observed with each humanization step. This finding reflected the propensity of the humanized V_HHs to interact with the column matrix because of hydrophobic changes in the V_L interface region, an effect seen with other FR2-humanized V_HHs as well [103,105]. Conversely, camelization of the same FR2 positions of aggregating human V_Hs leads to their solubilization [74]. In the study by Ben Abderrazek *et al.* [117] as in many others, humanized V_HH monomericity was assessed by size exclusion chromatography at relatively low protein concentrations, which may not be sufficiently sensitive to reveal aggregation at the high concentrations required for storage and administration of therapeutic antibodies. Humanization also led to decreases in the T_ms of all four humanized variants, although the T_m decrease was marginal for the maximally humanized V_HH. Importantly, humanization did not affect the affinity or the neutralization potency of NbAahII10.

Kazemi-Lomedasht *et al.* [118] applied a more conservative resurfacing approach to humanize a dromedary anti-VEGF V_HH, Nb42, altering its sequence at nine FR positions while maintaining all four key camelid solubility residues in FR2 [119]. Humanization did not significantly impact the ELISA binding or inhibitory function of the V_HH and was predicted to have little effect on domain structure based on homology modeling. The authors stated that humanization was predicted to lead to reduced immunogenicity based on *in silico* TCE predictions, although these data were not shown. Regrettably, the effects of humanization on important biophysical properties as solubility, expression yield, and stability were not explored.

Rossotti *et al.* [120] humanized four llama anti-EGFR V_HHs (NRC-sdAb022, NRC-sdAb028, NRC-sdAb032, and NRC-sdAb033) by veneering using human IGHV3-30 and IGHJ1 germline sequences as references. For each of the four V_HHs, three humanized versions (H1, H2, and H3) with increasing degrees of humanization were generated, but all variants maintained the parental camelid residues at IMGT positions 42 and 52. The H1 (minimal humanization) and H2 (intermediate humanization) variants had all other FR residues humanized except for those within five positions (H1) or two positions (H2) of a FR-CDR boundary, whereas the H3 (maximal humanization) variants had all other FR residues humanized. While humanization was unsuccessful for all variants of NRC-sdAb022 (H1 and H3 had low expression, while H2 aggregated and lost binding affinity), the H1 variants of the remaining three V_HHs as well as the H2 variant of NRC-sdAb033 displayed unimpaired solubility and binding. The humanized variants bore 89% (NRC-sdAb028-H1) to 94% (NRC-sdAb033-H2) FR sequence identity with human IGHV3-30. The remaining H2 and H3 variants either did not express, aggregated, or had compromised affinities. This is a clear example showing that the success and extent of V_HH humanization are sequence-specific; depending on the V_HH, not all amino acid could be substituted while maintaining a stable and active protein.

Vaneycken *et al.* [121] applied a CDR loop grafting approach using the 'universal' h-NbBcII10$_{FGLA}$ acceptor scaffold [103] to humanize NbCEA5, a dromedary V_HH specific to carcinoembryonic antigen (CEA) [122]. The CDR-grafted V_HH showed a 30-fold loss of affinity for CEA compared with the parental dromedary V_HH, although the affinity of the humanized V_HH was still high (K_D ~ 10 nM). Specific binding of the humanized V_HH to soluble and cell-displayed CEA was verified by ELISA and flow cytometry experiments, which also showed weaker binding compared with the parental V_HH. Competition binding assays confirmed binding specificity and indicated that both NbCEA5 and its humanized version recognized the same epitope. Furthermore, the CDR-grafted V_HH had essentially the same T_m as the acceptor scaffold (~ 74 °C), which was higher than that of NbCEA5 (70 °C). The humanized CEA5 V_HH could be labeled efficiently with ^{99m}Tc for imaging purposes without loss of binding and was shown to specifically target tumor cells *in vivo* similarly to the wild-type V_HH despite its significantly lower affinity.

h-NbBcII10$_{FGLA}$ was also used by Yu *et al.* [123] as the acceptor scaffold to graft the CDRs of a CD7-specific llama V_HH, VHH6 [124]. With the goal of using the humanized V_HH (huVHH6) for therapy of T-cell acute lymphoblastic leukemia, the authors constructed two immunotoxins consisting of a dimeric form of huVHH6 fused to two different *Pseudomonas* exotoxin A fragments. V_HH humanization did not alter the specificity of the immunotoxins, as shown by flow cytometry, and similar target cell-specific endocytosis was observed by laser scanning confocal microscopy for

the humanized and parental immunotoxins. Humanized immunotoxins also demonstrated selective cytotoxicity in *in vitro* assays, albeit less effectively than immunotoxins bearing the parental llama V_HH; this finding was attributed to reduced affinity resulting from humanization, although this was not explicitly tested. Further animal studies showed that one humanized immunotoxin format (dhuVHH6-PE38) prolonged the survival of tumor-bearing mice, although no benchmarking against immunotoxins comprising the parental llama V_HH was performed. Additionally, studies of the effect of humanization on the biophysical properties of VHH6, alone or in the context of immunotoxins, were not performed. However, all immunotoxins expressed in *Escherichia coli* with good yields (5 mg of purified protein per 1 L of bacterial culture).

Li *et al.* [125] reported a bispecific antibody, Muc-Bi-1, consisting of a first V_HH targeting MUC1 [126] connected through a short Gly-Ser linker to a second V_HH specific for the natural killer cell antigen CD16 [127]. A humanized version of the bispecific antibody, Muc-Bi-2, with 19 changes in the MUC16 V_HH FRs and 10 changes in the CD16 V_HH FRs, was generated by CDR loop grafting using the germline human V_H DP47 as the acceptor scaffold. Muc-Bi-2 had similar binding to Muc-Bi-1 in flow cytometry experiments. However, slight aggregation of Muc-Bi-2 was observed by size exclusion chromatography experiments, possibly because of full humanization of the four key FR2 solubility positions (42, 49, 50, and 52). No binding studies were performed to quantify the effect of humanization on the affinity of either V_HH arm of the bispecific antibody.

van Faassen *et al.* [128] reported the engineering, biophysical, and functional characterization of a series of humanized variants of four llama serum albumin-specific V_HHs (R11, R28, M75, and M79). To begin, the llama V_HH CDRs were grafted onto human IGHV3 consensus FRs (FR1–FR4), yielding fully humanized H0 variants with changes at 15 (R28-H0, M75-H0) or 19 (R11-H0 and M79-H0) FR positions. Full humanization included key FR2 solubility residues (IMGT positions 42, 49, 50, 52). From the H0 variants, an additional five (R28, M75, M79) or six (R11) variants (H1–H6) were designed with increasing numbers of back mutations (decreasing levels of humanization) at positions thought to have a role in antigen binding and/or solubility and stability. For all four V_HHs, full humanization (H0 variant) was detrimental to expression in *E. coli*. Significant expression was restored for M75 and R28 by back mutations at FR2 positions 42 and 52 (H1 variant), while additional back mutation of FR3 position 105 was required for expression of M79 (H2 variant). In addition to the above reversions, back mutation of positions 49 and 50 was required for expression of R11 (H3 variant). At these levels of humanization, the variants showed aggregation resistance status comparable to those of the parental llama V_HHs, although further back mutations were required to restore parental levels of thermostability (T_m). In terms of antigen binding, the H1 variant of M75 with back mutations at positions 42 and 52 (previously shown to be important in supporting the active conformation of the CDR3 loop [103]) had similar affinity to the parental llama V_HH. For the remaining three V_HHs, additional positions beyond 42 and 52 required back mutation to restore antigen-binding affinity. For M79, this was achieved in the H2 variant with an additional back mutation at position 105, which flanks and structurally supports the CDR3 loop. For R28, affinity was restored in the H4 variant with back mutations at key FR2 solubility/stability positions 49 and 50, at Vernier zone positions 1 and 54 that structurally support the CDR loop conformations, and at positions 83 and 85 in the FR3 D-E loop. For R11, affinity was restored in the H6 variant with back mutations at key FR2 solubility/stability positions 49 and 50, at position 105 flanking the CDR3 loop, at Vernier zone positions 1 and 54, at positions 83 and 87 in the FR3 D-E loop, and at positions 25 and 26 immediately preceding CDR1. Based on combined assessment of expression yield, solubility, stability, and antigen binding, M75-H1, M79-H2, R28-H5, and R11-H6 were chosen as leads and were subsequently shown to have similar *in vivo* serum half-life extension capabilities compared with the parental llama V_HHs. The results again emphasize the variability and sequence dependence of V_HH humanization.

Humanization of $V_{NAR}S$

HEL-5A7 (5A7) is a type I V_{NAR} that was isolated from an immune nurse shark phage display library. It specifically binds to hen egg white lysozyme with low nanomolar K_D and demonstrates considerable resistance to irreversible thermal denaturation [129]. In subsequent studies, attempts were made to humanize 5A7 by resurfacing using a human Vκ1 germline sequence (DPK9, IGKV1-39) as the structural template; of all human Ig variable domains, DPK9 was the most structurally similar to 5A7 [29]. Solvent-exposed residues in FR1, FR2, HV2, FR3b, and FR4 were exchanged for human DPK9/JK1 residues, leaving all six cysteine residues of the type I V_{NAR} scaffold intact. The resulting humanized V_{NAR} (5A7-IVabc) shared ~ 54% identity with the DPK9 V_L (~ 70% identity in FRs). Humanization did not compromise

the biophysical properties of 5A7-IVabc, as it expressed well in mammalian cells, showed no signs of aggregation as a monomer or Fc fusion, and retained full antigen-binding affinity (13.6 nM for 5A7 vs.14.8 nM for 5A7-IVabc).

The resurfacing approach was also extended to a second V_{NAR} (E06) for further validation [29]. E06 is a high-affinity (picomolar K_D) anti-human serum albumin V_{NAR} with cross-reactivity to mouse, rat, and monkey serum albumins and was isolated from an immune spiny dogfish phage display library [130]. E06 is a type IV V_{NAR} with < 30% sequence identity to human variable domains. Using 5A7-IVabc as the guide, a starting humanized variant of E06 was designed by replacing 30 of 103 residues with DPK9 residues (substitutions in FR1, FR2, FR3b, and FR4). The resulting molecule, huE06 v1.1, shared 63.5% identity with DPK9 in non-CDR sequences. Using huE06 v1.1 as the starting point, five additional humanized variants with changes in HV2, HV4, FR1, and FR3a (mostly toward the DPK9 consensus) were produced. No significant effect of humanization on expression yield of parental and humanized V_{NAR}-Fc fusions following transient transfection of COS-1 cells was observed. ELISA experiments using a panel of V_{NAR}s (E06, huE06 v1.1, huE06 v1.2, huE06 v1.3, huE06 v1.4, huE06 v1.5, huE06 v1.7) showed reduced binding of the humanized variants to serum albumin; loss of binding correlated with the extent of mutations in HV2 and HV4, with humanization of HV4 having the largest adverse effect on affinity (huE06 v1.4 and huE06 v1.5 showed no binding at all). Based on these results, the authors selected huE06 v1.1 and the parental E06 V_{NAR} for X-ray crystal structure determination. Structural data demonstrated that E06 N-terminal residues were involved in antigen binding and loss of binding in huE06 v1.4 was attributed at least partly to humanization of this region. Comparison of E06-albumin and huE06 v1.1-albumin co-crystal structures revealed the loss of one V_{NAR}:albumin contact following humanization. Thus, back mutations were introduced in huE06 v1.1 to replace three DPK9 residues with E06 V_{NAR} residues, yielding a new humanized variant, huE06 v1.10. ELISA showed that huE06 v1.10 had improved binding to serum albumin compared with huE06 v1.1, although binding was still significantly weaker compared with E06. No nonspecific binding of the humanized variants was observed against bovine serum albumin. The ELISA data were confirmed by surface plasmon resonance experiments showing that compared with E06, huE06 v1.1 and huE06 v1.10 had 85- and 34-fold weaker affinities, respectively, for human serum albumin.

Building on the efforts to obtain huE06 v1.10 (v1.10), Steven *et al.* [68] designed a second humanized version of E06 (v2.4) using the human V_K germline framework DPK24 (IGKV4-1) as the reference. These humanized V_{NAR}s, however, had significantly weaker binding affinity and undesirable biophysical properties compared with the parental E06 V_{NAR}. Thus, further studies were conducted to engineer humanized variants with improved biophysical properties and reduced immunogenicity. Random mutagenesis phage display libraries based on v1.10 and v2.4 were constructed and panned against human serum albumin to obtain variants with improved properties. Initial affinity and specificity screenings by ELISA identified tens of clones (49) from both libraries. Further stepwise screening of the clones expressed in HEK293 cells was performed based on antigen binding (ELISA), off-rate screening relative to E06 (surface plasmon resonance), ranking ELISA, and expression yield. This process identified four lead clones: BB10, BA11, and BB11 from the v1.10 library and 2G from the v2.4 library. These V_{NAR} variants typically had 1–2 mutations distributed randomly. These four humanized clones, similar to the parental E06 V_{NAR} and unlike v1.10, showed minimal tendency to aggregate. Immunogenicity screening using *in vitro* T-cell proliferation assays showed that while all wild-type and humanized versions were less immunogenic than positive controls, the humanized V_{NAR} 2G was the most immunogenic, followed by BB11. By contrast, BA11 and BB10 were slightly less immunogenic than the parental E06 V_{NAR}. All of the V_{NAR}s tested showed immunogenicity indexes similar to those of antibody therapeutics currently in the clinic. Size exclusion chromatography analyses showed that dimers and trimers of E06 and its humanized variants (BB11, BA11, and BB10) were nonaggregating, unlike dimers comprising v1.10. In this format, BA11 and BB11 extended serum half-life in rats to a similar extent as the parental E06 V_{NAR}. Finally, temperature- and pH-induced denaturation studies showed that humanization did not have a detrimental effect on the refolding of E06 following denaturation. BA11 was selected as the lead candidate, and in a follow-up study, a trimeric antibody consisting of humanized BA11 and shark anti-TNF-α V_{NAR}s was shown to potently neutralize TNF-α in various *in vitro* assays [131]. The trimeric V_{NAR} was less immunogenic than adalimumab in mice [69].

Alternatives to sdAb humanization

Because of the complexity and variable success of sdAb humanization, sometimes requiring multiple

attempts and engineering steps, several strategies have been developed to circumvent the need for humanization entirely. These technologies fall into three categories: (a) synthetic sdAb libraries constructed using humanized or fully human sdAb scaffolds, (b) attempts to bias V_HH isolation toward rare molecules with V_H-like sequence characteristics, and (c) transgenic animals producing HCAbs with fully human variable domains.

Synthetic humanized V_HH libraries

A synthetic phage display library of humanized V_HHs, NaLi-H1, with a complexity of 3×10^9, was described by Moutel *et al.* [132]. To construct the library, a consensus V_HH optimized for intracellular expression and stability (hs2dAb) was partially humanized at several positions in FR1–3 to mimic human IGHV3 sequences. The humanized hs2dAb maintained its camelid residues at IMGT positions 42, 49, 50, 52, and 103 (Gln). Using hs2dAb as the library scaffold, a synthetic phage display library of humanized V_HHs was constructed with diversity introduced through *in vitro* randomization of CDR1, CDR2, and CDR3. Selection and screening of the library yielded many functional and specific humanized V_HHs against intracellular and cell-surface protein targets, with some selected V_HHs having high affinities in the nM or pM range by surface plasmon resonance. However, these values may have been exaggerated due to potential contribution of avidity to binding because of aggregate contamination in the analytes. Using the same NaLi-H1 library, a family of six anti-tau V_HHs sharing the same CDR3 was selected [133] and showed K_Ds in the range of 0.7–4.5 μM. One representative V_HH (F8-2) fused to mCherry functioned as an intrabody, retaining its binding to tau when expressed in neuroblastoma cells. Affinity-optimized versions of the F8-2 V_HH in IgG Fc-fused formats were shown to detect tau in the brain tissues of transgenic mice. In another study, Crepin *et al.* [134] isolated five humanized follicle-stimulating hormone receptor V_HH inhibitors from the NaLi-H1 library. The dimeric, Fc-fused versions of the V_HHs were produced in *E. coli* cells expressing sulfhydryl oxidase and DsbC in functional form. Regrettably, in all three studies [132–134], data on biophysical attributes of humanized V_HHs such as expression yield, solubility, stability, and aggregation resistance were lacking.

From the same NaLi-Hi library, Galli *et al.* [135] generated a conformation-specific V_HH, dynab, showing preferential binding to the GTP hydrolytic state of dynamin-1 and thus allowing real-time monitoring of the enzymatic activity of dynamin *in vivo*. Utilizing dynab in live-cell intracellular imaging, the uncoupling of dynamin polymerization and GTPase activity was visualized. Experiments performed with eGFP-fused dynab demonstrated the V_HH's functionality as an intrabody. Mikhaylova *et al.* [136] reported the generation of an antitubulin V_HH (VHH#1) from the NaLi-H1 library. Using the V_HH (as well as a second immune llama V_HH, VHH#2, obtained from a different library) as the labeling agent, super-resolution imaging of microtubule bundles both *in vitro* and in various fixed cells was achieved, providing new insights into the mechanisms of microtubule organization. VHH#1 was reported to have good expression in *E. coli* (25 mg protein per liter of culture). However, no data on other important biophysical properties such as solubility, stability, and aggregation resistance were reported.

A similar CDR randomization approach was employed by Ju *et al.* [137] to generate a synthetic humanized V_HH phage display library based on the 'universal' humanized scaffold, $hNbBcll10_{FGLA}$, of Vincke *et al.* [103]. Several humanized V_HHs against each of three model antigens were identified by phage ELISA and DNA sequencing. However, no further steps were taken to characterize the humanized V_HHs, so the performance of the library with respect to binding affinity and biophysical properties including stability and solubility remains to be seen.

Naturally occurring camelid V_HHs

Approximately 10% of the camelid V_HH repertoire includes molecules with V_H sequence hallmarks, even at key positions in FR2 required for solubility [112,138,139]. Kastelic *et al.* applied a simple protocol which skipped the separation of V_H and V_HH domains during library cloning into a phagemid vector. Surprisingly, the authors claimed to have isolated camelid V_H domains with high affinity and good expression yields to multiple targets [140]. However, the binding data reported in this study were unconvincing, and thus, these domains may have had properties similar to those of rare human and murine autonomous V_H domains. A different approach was taken by Thanongsaksrikul *et al.* [141], who constructed a humanized naive V_H/V_HH phage display library from a nonimmunized dromedary. The authors used human V_H FR1- and FR4-specific primers in an attempt to increase the human sequence content of the cloned dromedary V_Hs/V_HHs. The degree of FR humanization of library members was variable but was significantly higher for V_Hs than V_HHs. Surprisingly, despite its unusually small size (1.6×10^5), the library yielded

binders in several screening attempts. The library yielded several humanized V_HHs specific for the light chain of type A botulinum toxin that efficiently neutralized the toxin, one of which had a K_D of ~ 12 nM. In subsequent screenings, the library yielded antigen-specific V_H/V_HHs that neutralized monocled cobra venom phospholipase A2 [142], inhibited hepatitis C virus (HCV) RNA-dependent RNA polymerase [143], inhibited the helicase activity of a C-terminal NS3 protein [144], inhibited HCV replication by binding to a HCV serine protease [145], neutralized the hemolytic activity of *Bordetella pertussis* CyaA hemolysin toxin [146], and inhibited the catalytic activity of the EGFR tyrosine kinase domain [147]. In none of these studies were important properties of the humanized V_H/V_HHs including expression, solubility, stability, and affinity assessed.

Synthetic humanized V_{NAR} libraries

To our knowledge, synthetic humanized V_{NAR} libraries have not been reported. However, given the difficulty in optimally humanizing V_{NAR} domains, we expect that such libraries might be useful for the development of V_{NAR} technology. Unfortunately, patents covering existing humanized V_{NAR} scaffolds restrict work in this area.

Synthetic fully human V_H/V_L libraries

Humanized, de-immunized, or tolerized antibodies are still not considered fully human since their origin was from a different species. Mitigation of immunogenicity is generally not attempted for therapeutic antibodies (at least conventional tetrameric IgGs) whose sequences are fully human in origin. The first fully human therapeutic antibody to be approved for clinical use, the antitumor necrosis factor-α IgG1 adalimumab, was isolated by phage display [148,149]. In this method, a library is constructed in which genetically engineered filamentous bacteriophages display human immune or naïve antibody repertoires. The library is then screened in repeated rounds of panning against a specific antigen to select binders. There are currently nine phage display-derived fully human conventional antibodies approved for therapy and many more being tested in the clinic [150,151]. However, application of *in vitro* display technology to discovery of fully human V_H and V_L sdAbs for human therapy has been more challenging for several reasons (see Section Immunogenicity of sdAbs above): (a) autonomous V_H and V_L domains do not exist naturally, so cannot be considered fully human, (b) since autonomous V_H and V_L domains rely entirely on their CDRs for solubility, stability, and antigen binding, molecules with optimal properties are extremely rare, and (c) clinical trial data have not shown that autonomous V_H and V_L domains are less immunogenic than camelid V_HHs. In an attempt to improve the properties of phage-displayed human V_H libraries, V_H camelization (introduction of solubilizing residues within FR2) was explored as an early strategy [74]. However, its effectiveness in solving the challenges listed above was unclear, and this strategy has been largely abandoned in favor of fully human V_H and V_L domains.

Transgenic animals

Transgenic animals whose endogenous immunoglobulin loci are inactivated and fully human antibody gene segments are inserted represent an interesting alternative to humanization methods. These promising technologies have led to the development of 19 antibody drugs currently on the market for the treatment of cancer, autoimmune, and inflammatory diseases [151]. Many years after the development of transgenic mice producing fully human conventional tetrameric antibody repertoires (e.g., Abgenix's XenoMouse™), it was discovered that inactivation of endogenous antibody production and knock-in of autonomous V_H gene segments along with constant region genes lacking the C_H1 exon [75–77] permitted the development of functional HCAb repertoires capable of binding a wide range of antigens. These technologies are proprietary and the mechanisms through which they have resolved the stability–diversity tradeoffs associated with synthetic fully human V_H/V_L libraries using the engine of *in vivo* VDJ recombination remains unclear. Importantly, while the starting material for these technologies (autonomous human V_H gene segments) may not contain nonhuman sequences, the final products may acquire autonomous folding (via VDJ recombination and/or somatic hypermutation) using sequence and structural patterns not found in the human repertoire. In addition, the resulting antibodies pass through a rodent and not a human tolerance system.

Conclusions

There are relatively limited data on immunogenicity of sdAbs compared with conventional antibodies. Long-term, high-dose sdAb treatment of chronic conditions may result in different immunogenicity outcomes. However, the available data suggest that the parameters governing sdAb immunogenicity are largely the same as those for conventional antibodies and include

sequence, dose, route of administration, target, and other factors. With two notable exceptions (TAS266 and GSK1995057), clinical trial data support the notion that sdAbs elicit limited ADAs with similar frequencies as humanized and fully human conventional antibodies. Clearly primary amino acid sequence alone is insufficient to fully explain sdAb immunogenicity, as shown by the lower *in vitro* immunogenicity of a shark V_{NAR} compared with humanized variants and the absence of ADA responses following administration of nonhumanized camelid V_HHs. The presence of preexisting ADAs against the C terminus of one fully human V_H domain (GSK1995057) in a large proportion of individuals has yet to be explained, but also shows that nonhuman sequence is not always the primary determinant of sdAb immunogenicity. Low-level aggregation induced following sdAb humanization may contribute to immunogenicity, and thus, the benefits of humanization are not totally clear, especially for V_HHs that naturally share high homology with human IGHV3 gene products. More work is needed to define optimal strategies for humanization of V_HHs and V_{NAR}s, so as to maximize human sequence content without compromising affinity, stability, or solubility in even minimal fashion, as subtle changes in these parameters may have unpredictable effects on immunogenicity.

Acknowledgements

This work was supported by funding from the National Research Council Canada.

Conflict of interest

The authors declare no conflict of interest.

Author contributions

KAH and JT conceived the manuscript. MAR, KB, KAH, and JT drafted the manuscript text. KB and KAH designed the figures. All authors read and approved the final manuscript.

References

1 Hamers-Casterman C, Atarhouch T, Muyldermans S, Robinson G, Hamers C, Songa EB, Bendahman N & Hamers R (1993) Naturally occurring antibodies devoid of light chains. *Nature* **363**, 446–448.
2 Nguyen VK, Hamers R, Wyns L & Muyldermans S (1999) Loss of splice consensus signal is responsible for the removal of the entire C_H1 domain of the functional camel IgG2A heavy-chain antibodies. *Mol Immunol* **36**, 515–524.
3 De Genst E, Silence K, Decanniere K, Conrath K, Loris R, Kinne J, Muyldermans S & Wyns L (2006) Molecular basis for the preferential cleft recognition by dromedary heavy-chain antibodies. *Proc Natl Acad Sci USA* **103**, 4586–4591.
4 Henry KA & MacKenzie CR (2018) Antigen recognition by single-domain antibodies: structural latitudes and constraints. *mAbs* **10**, 815–826.
5 Greenberg AS, Avila D, Hughes M, Hughes A, McKinney EC & Flajnik MF (1995) A new antigen receptor gene family that undergoes rearrangement and extensive somatic diversification in sharks. *Nature* **374**, 168–173.
6 Flajnik MF, Deschacht N & Muyldermans S (2011) A case of convergence: why did a simple alternative to canonical antibodies arise in sharks and camels? *PLoS Biol* **9**, e1001120.
7 Brooks CL, Rossotti MA & Henry KA (2018) Immunological functions and evolutionary emergence of heavy-chain antibodies. *Trends Immunol* **39**, 956–960.
8 Feige MJ, Grawert MA, Marcinowski M, Hennig J, Behnke J, Auslander D, Herold EM, Peschek J, Castro CD, Flajnik M *et al.* (2014) The structural analysis of shark IgNAR antibodies reveals evolutionary principles of immunoglobulins. *Proc Natl Acad Sci USA* **111**, 8155–8160.
9 Roux KH, Greenberg AS, Greene L, Strelets L, Avila D, McKinney EC & Flajnik MF (1998) Structural analysis of the nurse shark (new) antigen receptor (NAR): molecular convergence of NAR and unusual mammalian immunoglobulins. *Proc Natl Acad Sci USA* **95**, 11804–11809.
10 Barelle C & Porter A (2015) VNARs: an ancient and unique repertoire of molecules that deliver small, soluble, stable and high affinity binders of proteins. *Antibodies* **4**, 240–258.
11 Dooley H & Flajnik MF (2005) Shark immunity bites back: Affinity maturation and memory response in the nurse shark, *Ginglymostoma cirratum*. *Eur J Immunol* **35**, 936–945.
12 Crouch K, Smith LE, Williams R, Cao W, Lee M, Jensen A & Dooley H (2013) Humoral immune response of the small-spotted catshark, *Scyliorhinus canicula*. *Fish Shellfish Immunol* **34**, 1158–1169.
13 Klarenbeek A, El Mazouari K, Desmyter A, Blanchetot C, Hultberg A, de Jonge N, Roovers RC, Cambillau C, Spinelli S, Del-Favero J *et al.* (2015) Camelid Ig V genes reveal significant human homology not seen in therapeutic target genes, providing for a powerful therapeutic antibody platform. *mAbs* **7**, 693–706.
14 Muyldermans S (2013) Nanobodies: natural single-domain antibodies. *Annu Rev Biochem* **82**, 775–797.

15 Steeland S, Vandenbroucke RE & Libert C (2016) Nanobodies as therapeutics: big opportunities for small antibodies. *Drug Discov Today* **21**, 1076–1113.
16 Konning D, Zielonka S, Grzeschik J, Empting M, Valldorf B, Krah S, Schroter C, Sellmann C, Hock B & Kolmar H (2017) Camelid and shark single domain antibodies: structural features and therapeutic potential. *Curr Opin Struct Biol* **45**, 10–16.
17 Harmsen MM, Van Solt CB, Fijten HP & Van Setten MC (2005) Prolonged *in vivo* residence times of llama single-domain antibody fragments in pigs by binding to porcine immunoglobulins. *Vaccine* **23**, 4926–4934.
18 Kontermann RE (2011) Strategies for extended serum half-life of protein therapeutics. *Curr Opin Biotechnol* **22**, 868–876.
19 Henry KA, Tanha J & Hussack G (2015) Identification of cross-reactive single-domain antibodies against serum albumin using next-generation DNA sequencing. *Protein Eng Des Sel* **28**, 379–383.
20 Ubah OC, Buschhaus MJ, Ferguson L, Kovaleva M, Steven J, Porter AJ & Barelle CJ (2018) Next-generation flexible formats of VNAR domains expand the drug platform's utility and developability. *Biochem Soc Trans* **46**, 1559–1565.
21 Steeland S, Puimege L, Vandenbroucke RE, Van Hauwermeiren F, Haustraete J, Devoogdt N, Hulpiau P, Leroux-Roels G, Laukens D, Meuleman P *et al.* (2015) Generation and characterization of small single domain antibodies inhibiting human tumor necrosis factor receptor 1. *J Biol Chem* **290**, 4022–4037.
22 Riazi A, Strong PC, Coleman R, Chen W, Hirama T, van Faassen H, Henry M, Logan SM, Szymanski CM, Mackenzie R *et al.* (2013) Pentavalent single-domain antibodies reduce *Campylobacter jejuni* motility and colonization in chickens. *PLoS One* **8**, e83928.
23 Tanaka T, Lobato MN & Rabbitts TH (2003) Single domain intracellular antibodies: a minimal fragment for direct *in vivo* selection of antigen-specific intrabodies. *J Mol Biol* **331**, 1109–1120.
24 Rothbauer U, Zolghadr K, Tillib S, Nowak D, Schermelleh L, Gahl A, Backmann N, Conrath K, Muyldermans S, Cardoso MC *et al.* (2006) Targeting and tracing antigens in live cells with fluorescent nanobodies. *Nat Methods* **3**, 887–889.
25 Kaiser PD, Maier J, Traenkle B, Emele F & Rothbauer U (2014) Recent progress in generating intracellular functional antibody fragments to target and trace cellular components in living cells. *Biochim Biophys Acta* **1844**, 1933–1942.
26 Majidi J, Barar J, Baradaran B, Abdolalizadeh J & Omidi Y (2009) Target therapy of cancer: implementation of monoclonal antibodies and nanobodies. *Hum Antibodies* **18**, 81–100.
27 Getts DR, Getts MT, McCarthy DP, Chastain EM & Miller SD (2010) Have we overestimated the benefit of human(ized) antibodies? *mAbs* **2**, 682–694.
28 Vazquez-Lombardi R, Phan TG, Zimmermann C, Lowe D, Jermutus L & Christ D (2015) Challenges and opportunities for non-antibody scaffold drugs. *Drug Discov Today* **20**, 1271–1283.
29 Kovalenko OV, Olland A, Piche-Nicholas N, Godbole A, King D, Svenson K, Calabro V, Muller MR, Barelle CJ, Somers W *et al.* (2013) Atypical antigen recognition mode of a shark immunoglobulin new antigen receptor (IgNAR) variable domain characterized by humanization and structural analysis. *J Biol Chem* **288**, 17408–17419.
30 Streltsov VA, Varghese JN, Carmichael JA, Irving RA, Hudson PJ & Nuttall SD (2004) Structural evidence for evolution of shark Ig new antigen receptor variable domain antibodies from a cell-surface receptor. *Proc Natl Acad Sci USA* **101**, 12444–12449.
31 Mitchell LS & Colwell LJ (2018) Comparative analysis of nanobody sequence and structure data. *Proteins* **86**, 697–706.
32 Nguyen VK, Hamers R, Wyns L & Muyldermans S (2000) Camel heavy-chain antibodies: diverse germline V_HH and specific mechanisms enlarge the antigen-binding repertoire. *EMBO J* **19**, 921–930.
33 Henry KA, van Faassen H, Harcus D, Marcil A, Hill JJ, Muyldermans S & MacKenzie CR (2019) Llama peripheral B-cell populations producing conventional and heavy chain-only IgG subtypes are phenotypically indistinguishable but immunogenetically distinct. *Immunogenetics* **71**, 307–320.
34 Prabakaran P & Chowdhury PS (2020) Landscape of non-canonical cysteines in human V_H repertoire revealed by immunogenetic analysis. *Cell Rep* **31**, 107831.
35 Zhang D, Yang C, Chen X, Li X & Zhong D (2018) A bridging immunogenicity assay for monoclonal antibody: case study with SHR-1222. *Bioanalysis* **10**, 1115–1127.
36 Bartholdy C, Reedtz-Runge SL, Wang J, Hjerrild Zeuthen L, Gruhler A, Gudme CN & Lamberth K (2018) *In silico* and *in vitro* immunogenicity assessment of B-domain-modified recombinant factor VIII molecules. *Haemophilia* **24**, e354–e362.
37 Gfeller D & Bassani-Sternberg M (2018) Predicting antigen presentation – what could we learn from a million peptides? *Front Immunol* **9**, 1716.
38 Jawa V, Cousens LP, Awwad M, Wakshull E, Kropshofer H & De Groot AS (2013) T-cell dependent immunogenicity of protein therapeutics: preclinical assessment and mitigation. *Clin Immunol* **149**, 534–555.
39 De Groot AS, Terry F, Cousens L & Martin W (2013) Beyond humanization and de-immunization: tolerization as a method for reducing the

immunogenicity of biologics. *Expert Rev Clin Pharmacol* **6**, 651–662.
40 Groell F, Jordan O & Borchard G (2018) *In vitro* models for immunogenicity prediction of therapeutic proteins. *Eur J Pharm Biopharm* **130**, 128–142.
41 Harding FA, Stickler MM, Razo J & DuBridge RB (2010) The immunogenicity of humanized and fully human antibodies: residual immunogenicity resides in the CDR regions. *mAbs* **2**, 256–265.
42 Beissbarth T, Tye-Din JA, Smyth GK, Speed TP & Anderson RP (2005) A systematic approach for comprehensive T-cell epitope discovery using peptide libraries. *Bioinformatics* **21** (Suppl 1), i29–i37.
43 Jawa V, Terry F, Gokemeijer J, Mitra-Kaushik S, Roberts BJ, Tourdot S & De Groot AS (2020) T-cell dependent immunogenicity of protein therapeutics pre-clinical assessment and mitigation-updated consensus and review 2020. *Front Immunol* **11**, 1301.
44 van Meer PJ, Kooijman M, Brinks V, Gispen-de Wied CC, Silva-Lima B, Moors EH & Schellekens H (2013) Immunogenicity of mAbs in non-human primates during nonclinical safety assessment. *mAbs* **5**, 810–816.
45 Ablynx (2017) 2017 Annual Report. Ghent, Belgium. https://www.ablynx.com/uploads/pub/eng-4f6769aa-78ea-4bef-9f2e-bd5366f6619d-annualreportablynx2017.pdf
46 Ackaert C, Smiejkowska N, Xavier C, Sterckx YGJ, Denies S, Stijlemans B, Elkrim Y, Devoogdt N, Caveliers V, Lahoutte T *et al.* (2021) Immunogenicity risk profile of nanobodies. *Front Immunol* **12**. https://dx.doi.org/10.3389/fimmu.2021.632687
47 Kibria MG, Akazawa-Ogawa Y, Rahman N, Hagihara Y & Kuroda Y (2020) The immunogenicity of an anti-EGFR single domain antibody (V_HH) is enhanced by misfolded amorphous aggregation but not by heat-induced aggregation. *Eur J Pharm Biopharm* **152**, 164–174.
48 Hoefman S, Ottevaere I, Baumeister J & Sargentini-Maier ML (2015) Pre-clinical intravenous serum pharmacokinetics of albumin binding and non-half-life extended nanobodies. *Antibodies* **4**, 141–156.
49 Van Roy M, Ververken C, Beirnaert E, Hoefman S, Kolkman J, Vierboom M, Breedveld E, 't Hart B, Poelmans S, Bontinck L *et al.* (2015) The preclinical pharmacology of the high affinity anti-IL-6R nanobody ALX-0061 supports its clinical development in rheumatoid arthritis. *Arthritis Res Ther* **17**, 135.
50 Snoeck V (2013) Current experience in immunogenicity assessment of next generation biologics – nanobodies. *European Immunogenicity Symposium*, Munich, Germany.
51 Jovcevska I & Muyldermans S (2020) The therapeutic potential of nanobodies. *BioDrugs* **34**, 11–26.
52 Keyaerts M, Xavier C, Heemskerk J, Devoogdt N, Everaert H, Ackaert C, Vanhoeij M, Duhoux FP, Gevaert T, Simon P *et al.* (2016) Phase I study of ^{68}Ga-HER2-nanobody for PET/CT assessment of HER2 expression in breast carcinoma. *J Nucl Med* **57**, 27–33.
53 Svecova D, Lubell MW, Casset-Semanaz F, Mackenzie H, Grenningloh R & Krueger JG (2019) A randomized, double-blind, placebo-controlled phase 1 study of multiple ascending doses of subcutaneous M1095, an anti-interleukin 17A/F nanobody, in moderate-to-severe psoriasis. *J Am Acad Dermatol* **81**, 196–203.
54 Schoen P, Jacobs S, Verschueren K, Ottevaere I, Sobry S & Holz JB (2013) Anti-RANKL nanobody ALX-0141 shows sustained biomarker inhibition in a phase I study in healthy postmenopausal women. *European Calcified Tissue Society Congress*, Lisbon, Portugal.
55 Holz JB, Sargentini-Maier ML, De Bruyn S, Gachályi B, Udvaros I, Rojkovich B, Bruk S, Sramek P, Korkosz M, Krause K *et al.* (2014) Twenty-four weeks of treatment with a novel anti-IL-6 receptor nanobody (ALX-0061) resulted in 84% ACR20 improvement and 58% DAS28 remission in a phase I/II study in RA. *Ann Rheum Dis* **72**, A64.
56 NCT02287922 (2014) A phase IIb study for ALX-0061 monotherapy in subjects with rheumatoid arthritis. https://clinicaltrials.gov/ct2/show/NCT02287922
57 NCT02437890 (2015) A phase II study to evaluate safety and efficacy of ALX-0061 in subjects with systemic lupus erythematosus. https://clinicaltrials.gov/ct2/show/NCT02437890
58 De Bruyn S, De Smedt T, Allosery K, Crabbe P, De Brabandere V, Detalle L, Mortier K, Schoolmeester A, Wouters H, Stöhr T *et al.* (2015) ALX-0171: Safety and therapeutic potential of an inhaled anti-RSV nanobody. *Respiratory Drug Delivery Europe*, Antibes, France.
59 Cunningham S, Piedra PA, Martinon-Torres F, Szymanski H, Brackeva B, Dombrecht E, Detalle L & Fleurinck C (2021) Nebulised ALX-0171 for respiratory syncytial virus lower respiratory tract infection in hospitalised children: a double-blind, randomised, placebo-controlled, phase 2b trial. *Lancet Respir Med* **9**, 21–32.
60 NCT01007175 (2009) Study evaluating multiple ascending doses of ATN-103 in Japanese subjects with rheumatoid arthritis. https://clinicaltrials.gov/ct2/show/NCT01007175
61 NCT00959036 (2009) Study evaluating multiple doses of ATN-103 in subjects with active rheumatoid arthritis. https://clinicaltrials.gov/ct2/show/NCT00959036
62 NCT01063803 (2010) Study evaluating long-term safety of ATN-103 in subjects with rheumatoid arthritis. https://clinicaltrials.gov/ct2/show/NCT01063803
63 Bartunek J, Barbato E, Heyndrickx G, Vanderheyden M, Wijns W & Holz JB (2013) Novel antiplatelet

agents: ALX-0081, a nanobody directed towards von Willebrand factor. *J Cardiovasc Transl Res* **6**, 355–363.
64 Peyvandi F, Scully M, Kremer Hovinga JA, Cataland S, Knobl P, Wu H, Artoni A, Westwood JP, Mansouri Taleghani M, Jilma B *et al.* (2016) Caplacizumab for acquired thrombotic thrombocytopenic purpura. *N Engl J Med* **374**, 511–522.
65 Peyvandi F, Scully M, Kremer Hovinga JA, Knobl P, Cataland S, De Beuf K, Callewaert F, De Winter H & Zeldin RK (2017) Caplacizumab reduces the frequency of major thromboembolic events, exacerbations and death in patients with acquired thrombotic thrombocytopenic purpura. *J Thromb Haemost* **15**, 1448–1452.
66 Scully M, Cataland SR, Peyvandi F, Coppo P, Knobl P, Kremer Hovinga JA, Metjian A, de la Rubia J, Pavenski K, Callewaert F *et al.* (2019) Caplacizumab treatment for acquired thrombotic thrombocytopenic purpura. *N Engl J Med* **380**, 335–346.
67 Papadopoulos KP, Isaacs R, Bilic S, Kentsch K, Huet HA, Hofmann M, Rasco D, Kundamal N, Tang Z, Cooksey J *et al.* (2015) Unexpected hepatotoxicity in a phase I study of TAS266, a novel tetravalent agonistic nanobody targeting the DR5 receptor. *Cancer Chemother Pharmacol* **75**, 887–895.
68 Steven J, Muller MR, Carvalho MF, Ubah OC, Kovaleva M, Donohoe G, Baddeley T, Cornock D, Saunders K, Porter AJ *et al.* (2017) *In vitro* maturation of a humanized shark VNAR domain to improve its biophysical properties to facilitate clinical development. *Front Immunol* **8**, 1361.
69 Ubah OC, Porter AJ & Barelle CJ (2020) *In vitro* ELISA and cell-based assays confirm the low immunogenicity of VNAR therapeutic constructs in a mouse model of human RA: an encouraging milestone to further clinical drug development. *J Immunol Res* **2020**, 7283239.
70 Hoogenboom HR (2005) Selecting and screening recombinant antibody libraries. *Nat Biotechnol* **23**, 1105–1116.
71 Kovaleva M, Ferguson L, Steven J, Porter A & Barelle C (2014) Shark variable new antigen receptor biologics – a novel technology platform for therapeutic drug development. *Expert Opin Biol Ther* **14**, 1527–1539.
72 Zielonka S, Empting M, Grzeschik J, Konning D, Barelle CJ & Kolmar H (2015) Structural insights and biomedical potential of IgNAR scaffolds from sharks. *mAbs* **7**, 15–25.
73 Henry KA, Kim DY, Kandalaft H, Lowden MJ, Yang Q, Schrag JD, Hussack G, MacKenzie CR & Tanha J (2017) Stability-diversity tradeoffs impose fundamental constraints on selection of synthetic human V_H/V_L single-domain antibodies from *in vitro* display libraries. *Front Immunol* **8**, 1759.
74 Kim DY, Hussack G, Kandalaft H & Tanha J (2014) Mutational approaches to improve the biophysical properties of human single-domain antibodies. *Biochim Biophys Acta* **1844**, 1983–2001.
75 Drabek D, Janssens R, de Boer E, Rademaker R, Kloess J, Skehel J & Grosveld F (2016) Expression cloning and production of human heavy-chain-only antibodies from murine transgenic plasma cells. *Front Immunol* **7**, 619.
76 Clarke SC, Ma B, Trinklein ND, Schellenberger U, Osborn MJ, Ouisse LH, Boudreau A, Davison LM, Harris KE, Ugamraj HS *et al.* (2018) Multispecific antibody development platform based on human heavy chain antibodies. *Front Immunol* **9**, 3037.
77 Teng Y, Young JL, Edwards B, Hayes P, Thompson L, Johnston C, Edwards C, Sanders Y, Writer M, Pinto D *et al.* (2020) Diverse human V_H antibody fragments with bio-therapeutic properties from the Crescendo mouse. *N Biotechnol* **55**, 65–76.
78 Arbabi-Ghahroudi M, To R, Gaudette N, Hirama T, Ding W, MacKenzie R & Tanha J (2009) Aggregation-resistant V_Hs selected by *in vitro* evolution tend to have disulfide-bonded loops and acidic isoelectric points. *Protein Eng Des Sel* **22**, 59–66.
79 Dudgeon K, Rouet R, Kokmeijer I, Schofield P, Stolp J, Langley D, Stock D & Christ D (2012) General strategy for the generation of human antibody variable domains with increased aggregation resistance. *Proc Natl Acad Sci USA* **109**, 10879–10884.
80 Perchiacca JM, Lee CC & Tessier PM (2014) Optimal charged mutations in the complementarity-determining regions that prevent domain antibody aggregation are dependent on the antibody scaffold. *Protein Eng Des Sel* **27**, 29–39.
81 Chan CE, Lim AP, MacAry PA & Hanson BJ (2014) The role of phage display in therapeutic antibody discovery. *Int Immunol* **26**, 649–657.
82 Soderlind E, Strandberg L, Jirholt P, Kobayashi N, Alexeiva V, Aberg AM, Nilsson A, Jansson B, Ohlin M, Wingren C *et al.* (2000) Recombining germline-derived CDR sequences for creating diverse single-framework antibody libraries. *Nat Biotechnol* **18**, 852–856.
83 Kim SC, Wakwe W, Higginbotham LB, Mathews DV, Breeden CP, Stephenson AC, Jenkins J, Strobert E, Price K, Price L *et al.* (2017) Fc-silent anti-CD154 domain antibody effectively prevents nonhuman primate renal allograft rejection. *Am J Transplant* **17**, 1182–1192.
84 Adamson P, Wilde T, Dobrzynski E, Sychterz C, Polsky R, Kurali E, Haworth R, Tang CM, Korczynska J, Cook F *et al.* (2016) Single ocular injection of a sustained-release anti-VEGF delivers 6 months pharmacokinetics and efficacy in a primate laser CNV model. *J Control Release* **244**, 1–13.
85 NCT00854685 (2009) Dose optimisation study of ART621 in subjects diagnosed with rheumatoid

arthritis taking methotrexate. https://clinicaltrials.gov/ct2/show/NCT00854685
86 NCT00928317 (2009) Dose ranging study of ART621 in subjects diagnosed with rheumatoid arthritis taking methotrexate. https://clinicaltrials.gov/ct2/show/NCT00928317
87 NCT01240876 (2010) Study to evaluate the safety and efficacy of placulumab (CEP-37247) administered by the transforaminal epidural route for the treatment of patients with lumbosacral radicular pain associated with disk herniation. https://clinicaltrials.gov/ct2/show/NCT01240876
88 O'Connor-Semmes RL, Lin J, Hodge RJ, Andrews S, Chism J, Choudhury A & Nunez DJ (2014) GSK2374697, a novel albumin-binding domain antibody (AlbudAb), extends systemic exposure of exendin-4: first study in humans–PK/PD and safety. *Clin Pharmacol Ther* **96**, 704–712.
89 Holland MC, Wurthner JU, Morley PJ, Birchler MA, Lambert J, Albayaty M, Serone AP, Wilson R, Chen Y, Forrest RM *et al*. (2013) Autoantibodies to variable heavy (V_H) chain Ig sequences in humans impact the safety and clinical pharmacology of a VH domain antibody antagonist of TNF-α receptor 1. *J Clin Immunol* **33**, 1192–1203.
90 Proudfoot A, Bayliffe A, O'Kane CM, Wright T, Serone A, Bareille PJ, Brown V, Hamid UI, Chen Y, Wilson R *et al*. (2018) Novel anti-tumour necrosis factor receptor-1 (TNFR1) domain antibody prevents pulmonary inflammation in experimental acute lung injury. *Thorax* **73**, 723–730.
91 Cordy JC, Morley PJ, Wright TJ, Birchler MA, Lewis AP, Emmins R, Chen YZ, Powley WM, Bareille PJ, Wilson R *et al*. (2015) Specificity of human anti-variable heavy (V_H) chain autoantibodies and impact on the design and clinical testing of a V_H domain antibody antagonist of tumour necrosis factor-α receptor 1. *Clin Exp Immunol* **182**, 139–148.
92 Smith SL (1996) Ten years of orthoclone OKT3 (muromonab-CD3): a review. *J Transpl Coord* **6**, 109–119.
93 Jones PT, Dear PH, Foote J, Neuberger MS & Winter G (1986) Replacing the complementarity-determining regions in a human antibody with those from a mouse. *Nature* **321**, 522–525.
94 Riechmann L, Clark M, Waldmann H & Winter G (1988) Reshaping human antibodies for therapy. *Nature* **332**, 323–327.
95 Queen C, Schneider WP, Selick HE, Payne PW, Landolfi NF, Duncan JF, Avdalovic NM, Levitt M, Junghans RP & Waldmann TA (1989) A humanized antibody that binds to the interleukin 2 receptor. *Proc Natl Acad Sci USA* **86**, 10029–10033.
96 Graziano RF, Tempest PR, White P, Keler T, Deo Y, Ghebremariam H, Coleman K, Pfefferkorn LC, Fanger MW & Guyre PM (1995) Construction and characterization of a humanized anti-gamma-Ig receptor type I (Fc gamma RI) monoclonal antibody. *J Immunol* **155**, 4996–5002.
97 Padlan EA (1991) A possible procedure for reducing the immunogenicity of antibody variable domains while preserving their ligand-binding properties. *Mol Immunol* **28**, 489–498.
98 Roguska MA, Pedersen JT, Keddy CA, Henry AH, Searle SJ, Lambert JM, Goldmacher VS, Blattler WA, Rees AR & Guild BC (1994) Humanization of murine monoclonal antibodies through variable domain resurfacing. *Proc Natl Acad Sci USA* **91**, 969–973.
99 Norman RA, Ambrosetti F, Bonvin A, Colwell LJ, Kelm S, Kumar S & Krawczyk K (2020) Computational approaches to therapeutic antibody design: established methods and emerging trends. *Brief Bioinform* **21**, 1549–1567.
100 Nguyen VK, Muyldermans S & Hamers R (1998) The specific variable domain of camel heavy-chain antibodies is encoded in the germline. *J Mol Biol* **275**, 413–418.
101 Riechmann L & Muyldermans S (1999) Single domain antibodies: comparison of camel V_H and camelised human V_H domains. *J Immunol Methods* **231**, 25–38.
102 Saerens D, Pellis M, Loris R, Pardon E, Dumoulin M, Matagne A, Wyns L, Muyldermans S & Conrath K (2005) Identification of a universal V_HH framework to graft non-canonical antigen-binding loops of camel single-domain antibodies. *J Mol Biol* **352**, 597–607.
103 Vincke C, Loris R, Saerens D, Martinez-Rodriguez S, Muyldermans S & Conrath K (2009) General strategy to humanize a camelid single-domain antibody and identification of a universal humanized nanobody scaffold. *J Biol Chem* **284**, 3273–3284.
104 Davies J & Riechmann L (1994) 'Camelising' human antibody fragments: NMR studies on V_H domains. *FEBS Lett* **339**, 285–290.
105 Conrath K, Vincke C, Stijlemans B, Schymkowitz J, Decanniere K, Wyns L, Muyldermans S & Loris R (2005) Antigen binding and solubility effects upon the veneering of a camel VHH in framework-2 to mimic a VH. *J Mol Biol* **350**, 112–125.
106 Muyldermans S (2001) Single domain camel antibodies: current status. *J Biotechnol* **74**, 277–302.
107 Zavrtanik U, Lukan J, Loris R, Lah J & Hadzi S (2018) Structural basis of epitope recognition by heavy-chain camelid antibodies. *J Mol Biol* **430**, 4369–4386.
108 Dumoulin M, Conrath K, Van Meirhaeghe A, Meersman F, Heremans K, Frenken LG, Muyldermans S, Wyns L & Matagne A (2002) Single-domain antibody fragments with high conformational stability. *Protein Sci* **11**, 500–515.

109 Conrath KE, Lauwereys M, Galleni M, Matagne A, Frere JM, Kinne J, Wyns L & Muyldermans S (2001) β-lactamase inhibitors derived from single-domain antibody fragments elicited in the *Camelidae*. *Antimicrob Agents Chemother* **45**, 2807–2812.

110 Tomlinson IM, Walter G, Marks JD, Llewelyn MB & Winter G (1992) The repertoire of human germline V_H sequences reveals about fifty groups of V_H segments with different hypervariable loops. *J Mol Biol* **227**, 776–798.

111 Griffiths AD, Williams SC, Hartley O, Tomlinson IM, Waterhouse P, Crosby WL, Kontermann RE, Jones PT, Low NM, Allison TJ *et al.* (1994) Isolation of high affinity human antibodies directly from large synthetic repertoires. *EMBO J* **13**, 3245–3260.

112 Tanha J, Dubuc G, Hirama T, Narang SA & MacKenzie CR (2002) Selection by phage display of llama conventional V_H fragments with heavy chain antibody V_HH properties. *J Immunol Methods* **263**, 97–109.

113 Tanha J, Nguyen TD, Ng A, Ryan S, Ni F & Mackenzie R (2006) Improving solubility and refolding efficiency of human V_Hs by a novel mutational approach. *Protein Eng Des Sel* **19**, 503–509.

114 Barthelemy PA, Raab H, Appleton BA, Bond CJ, Wu P, Wiesmann C & Sidhu SS (2008) Comprehensive analysis of the factors contributing to the stability and solubility of autonomous human V_H domains. *J Biol Chem* **283**, 3639–3654.

115 Jespers L, Schon O, James LC, Veprintsev D & Winter G (2004) Crystal structure of HEL4, a soluble, refoldable human V_H single domain with a germ-line scaffold. *J Mol Biol* **337**, 893–903.

116 Achour I, Cavelier P, Tichit M, Bouchier C, Lafaye P & Rougeon F (2008) Tetrameric and homodimeric camelid IgGs originate from the same IgH locus. *J Immunol* **181**, 2001–2009.

117 Ben Abderrazek R, Vincke C, Hmila I, Saerens D, Abidi N, El Ayeb M, Muyldermans S & Bouhaouala-Zahar B (2011) Development of Cys38 knock-out and humanized version of NbAahII10 nanobody with improved neutralization of AahII scorpion toxin. *Protein Eng Des Sel* **24**, 727–735.

118 Kazemi-Lomedasht F, Behdani M, Bagheri KP, Habibi-Anbouhi M, Abolhassani M, Arezumand R, Shahbazzadeh D & Mirzahoseini H (2015) Inhibition of angiogenesis in human endothelial cell using VEGF specific nanobody. *Mol Immunol* **65**, 58–67.

119 Kazemi-Lomedasht F, Muyldermans S, Habibi-Anbouhi M & Behdani M (2018) Design of a humanized anti vascular endothelial growth factor nanobody and evaluation of its *in vitro* function. *Iran J Basic Med Sci* **21**, 260–266.

120 Rossotti MA, Henry KA, van Faassen H, Tanha J, Callaghan D, Hussack G, Arbabi-Ghahroudi M & MacKenzie CR (2019) Camelid single-domain antibodies raised by DNA immunization are potent inhibitors of EGFR signaling. *Biochem J* **476**, 39–50.

121 Vaneycken I, Govaert J, Vincke C, Caveliers V, Lahoutte T, De Baetselier P, Raes G, Bossuyt A, Muyldermans S & Devoogdt N (2010) *In vitro* analysis and *in vivo* tumor targeting of a humanized, grafted nanobody in mice using pinhole SPECT/micro-CT. *J Nucl Med* **51**, 1099–1106.

122 Cortez-Retamozo V, Backmann N, Senter PD, Wernery U, De Baetselier P, Muyldermans S & Revets H (2004) Efficient cancer therapy with a nanobody-based conjugate. *Cancer Res* **64**, 2853–2857.

123 Yu Y, Li J, Zhu X, Tang X, Bao Y, Sun X, Huang Y, Tian F, Liu X & Yang L (2017) Humanized CD7 nanobody-based immunotoxins exhibit promising anti-T-cell acute lymphoblastic leukemia potential. *Int J Nanomedicine* **12**, 1969–1983.

124 Tang J, Li J, Zhu X, Yu Y, Chen D, Yuan L, Gu Z, Zhang X, Qi L, Gong Z *et al.* (2016) Novel CD7-specific nanobody-based immunotoxins potently enhanced apoptosis of CD7-positive malignant cells. *Oncotarget* **7**, 34070–34083.

125 Li Y, Zhou C, Li J, Liu J, Lin L, Li L, Cao D, Li Q & Wang Z (2018) Single domain based bispecific antibody, Muc1-Bi-1, and its humanized form, Muc1-Bi-2, induce potent cancer cell killing in muc1 positive tumor cells. *PLoS One* **13**, e0191024.

126 Sadeqzadeh E, Rahbarizadeh F, Ahmadvand D, Rasaee MJ, Parhamifar L & Moghimi SM (2011) Combined MUC1-specific nanobody-tagged PEG-polyethylenimine polyplex targeting and transcriptional targeting of tBid transgene for directed killing of MUC1 over-expressing tumour cells. *J Control Release* **156**, 85–91.

127 Behar G, Siberil S, Groulet A, Chames P, Pugniere M, Boix C, Sautes-Fridman C, Teillaud JL & Baty D (2008) Isolation and characterization of anti-FcγRIII (CD16) llama single-domain antibodies that activate natural killer cells. *Protein Eng Des Sel* **21**, 1–10.

128 van Faassen H, Ryan S, Henry KA, Raphael S, Yang Q, Rossotti MA, Brunette E, Jiang S, Haqqani AS, Sulea T *et al.* (2020) Serum albumin-binding V_HHs with variable pH sensitivities enable tailored half-life extension of biologics. *FASEB J* **34**, 8155–8171.

129 Dooley H, Flajnik MF & Porter AJ (2003) Selection and characterization of naturally occurring single-domain (IgNAR) antibody fragments from immunized sharks by phage display. *Mol Immunol* **40**, 25–33.

130 Muller MR, Saunders K, Grace C, Jin M, Piche-Nicholas N, Steven J, O'Dwyer R, Wu L, Khetemenee L, Vugmeyster Y *et al.* (2012) Improving the pharmacokinetic properties of biologics by fusion to an anti-HSA shark VNAR domain. *mAbs* **4**, 673–685.

131 Ubah OC, Steven J, Kovaleva M, Ferguson L, Barelle C, Porter AJR & Barelle CJ (2017) Novel, anti-hTNF-α variable new antigen receptor formats with enhanced neutralizing potency and multifunctionality, generated for therapeutic development. *Front Immunol* **8**, 1780.
132 Moutel S, Bery N, Bernard V, Keller L, Lemesre E, de Marco A, Ligat L, Rain JC, Favre G, Olichon A *et al.* (2016) NaLi-H1: a universal synthetic library of humanized nanobodies providing highly functional antibodies and intrabodies. *Elife* **5**, e16228.
133 Dupre E, Danis C, Arrial A, Hanoulle X, Homa M, Cantrelle FX, Merzougui H, Colin M, Rain JC, Buee L *et al.* (2019) Single domain antibody fragments as new tools for the detection of neuronal tau protein in cells and in mice studies. *ACS Chem Neurosci* **10**, 3997–4006.
134 Crepin R, Veggiani G, Djender S, Beugnet A, Planeix F, Pichon C, Moutel S, Amigorena S, Perez F, Ghinea N *et al.* (2017) Whole-cell biopanning with a synthetic phage display library of nanobodies enabled the recovery of follicle-stimulating hormone receptor inhibitors. *Biochem Biophys Res Commun* **493**, 1567–1572.
135 Galli V, Sebastian R, Moutel S, Ecard J, Perez F & Roux A (2017) Uncoupling of dynamin polymerization and GTPase activity revealed by the conformation-specific nanobody dynab. *Elife* **6**, e25197.
136 Mikhaylova M, Cloin BM, Finan K, van den Berg R, Teeuw J, Kijanka MM, Sokolowski M, Katrukha EA, Maidorn M, Opazo F *et al.* (2015) Resolving bundled microtubules using anti-tubulin nanobodies. *Nat Commun* **6**, 7933.
137 Ju MS, Min SW, Lee SM, Kwon HS, Park JC, Lee JC & Jung ST (2017) A synthetic library for rapid isolation of humanized single-domain antibodies. *Biotechnol Bioprocess Eng* **22**, 239–247.
138 Deschacht N, De Groeve K, Vincke C, Raes G, De Baetselier P & Muyldermans S (2010) A novel promiscuous class of camelid single-domain antibody contributes to the antigen-binding repertoire. *J Immunol* **184**, 5696–5704.
139 Harmsen MM, Ruuls RC, Nijman IJ, Niewold TA, Frenken LG & de Geus B (2000) Llama heavy-chain V regions consist of at least four distinct subfamilies revealing novel sequence features. *Mol Immunol* **37**, 579–590.
140 Kastelic D, Frkovic-Grazio S, Baty D, Truan G, Komel R & Pompon D (2009) A single-step procedure of recombinant library construction for the selection of efficiently produced llama V_H binders directed against cancer markers. *J Immunol Methods* **350**, 54–62.
141 Thanongsaksrikul J, Srimanote P, Maneewatch S, Choowongkomon K, Tapchaisri P, Makino S, Kurazono H & Chaicumpa W (2010) A V_HH that neutralizes the zinc metalloproteinase activity of botulinum neurotoxin type A. *J Biol Chem* **285**, 9657–9666.
142 Chavanayarn C, Thanongsaksrikul J, Theung-in K, Bangphoomi K, Sookrung N & Chaicumpa W (2012) Humanized single domain antibodies (VH/VHH) that bound specifically to Naja kaouthia phospholipase A2 and neutralized the enzymatic activity. *Toxins* **4**, 554–567.
143 Thueng-in K, Thanongsaksrikul J, Srimanote P, Bangphoomi K, Poungpair O, Maneewatch S, Choowongkomon K & Chaicumpa W (2012) Cell penetrable humanized VH/VHH that inhibit RNA dependent RNA polymerase (NS5B) of HCV. *PLoS One* **7**, e49254.
144 Phalaphol A, Thueng-In K, Thanongsaksrikul J, Poungpair O, Bangphoomi K, Sookrung N, Srimanote P & Chaicumpa W (2013) Humanized VH/VHH that inhibit HCV replication by interfering with the virus helicase activity. *J Virol Methods* **194**, 289–299.
145 Jittavisutthikul S, Thanongsaksrikul J, Thueng-In K, Chulanetra M, Srimanote P, Seesuay W, Malik AA & Chaicumpa W (2015) Humanized V_HH transbodies that inhibit HCV protease and replication. *Viruses* **7**, 2030–2056.
146 Malik AA, Imtong C, Sookrung N, Katzenmeier G, Chaicumpa W & Angsuthanasombat C (2016) Structural characterization of humanized nanobodies with neutralizing activity against the *Bordetella pertussis* CyaA-hemolysin: implications for a potential epitope of toxin-protective antigen. *Toxins* **8**, 99.
147 Tabtimmai L, Suphakun P, Srisook P, Kiriwan D, Phanthong S, Kiatwuthinon P, Chaicumpa W & Choowongkomon K (2019) Cell-penetrable nanobodies (transbodies) that inhibit the tyrosine kinase activity of EGFR leading to the impediment of human lung adenocarcinoma cell motility and survival. *J Cell Biochem* **120**, 18077–18087.
148 Kempeni J (1999) Preliminary results of early clinical trials with the fully human anti-TNFα monoclonal antibody D2E7. *Ann Rheum Dis* **58** (Suppl 1), I70–I72.
149 Weinblatt ME, Keystone EC, Furst DE, Moreland LW, Weisman MH, Birbara CA, Teoh LA, Fischkoff SA & Chartash EK (2003) Adalimumab, a fully human anti-tumor necrosis factor α monoclonal antibody, for the treatment of rheumatoid arthritis in patients taking concomitant methotrexate: the ARMADA trial. *Arthritis Rheum* **48**, 35–45.
150 Frenzel A, Schirrmann T & Hust M (2016) Phage display-derived human antibodies in clinical development and therapy. *mAbs* **8**, 1177–1194.
151 Lu RM, Hwang YC, Liu IJ, Lee CC, Tsai HZ, Li HJ & Wu HC (2020) Development of therapeutic antibodies for the treatment of diseases. *J Biomed Sci* **27**, 1.

The Journal of Clinical Pharmacology
2020, 60(S1) S132–S146

DOI: 10.1002/jcph.1706

Informing Development of Bispecific Antibodies Using Physiologically Based Pharmacokinetic-Pharmacodynamic Models: Current Capabilities and Future Opportunities

John P. Gibbs, PhD[1], Theresa Yuraszeck, PhD[2], Carla Biesdorf, PhD[3], Yang Xu, PhD[4], and Sreeneeranj Kasichayanula, PhD[5]

Abstract

Antibody therapeutics continue to represent a significant portion of the biotherapeutic pipeline, with growing promise for bispecific antibodies (BsAbs). BsAbs can target 2 different antigens at the same time, such as simultaneously binding tumor-cell receptors and recruiting cytotoxic immune cells. This simultaneous engagement of 2 targets can be potentially advantageous, as it may overcome disadvantages posed by a monotherapy approach, like the development of resistance to treatment. Combination therapy approaches that modulate 2 targets simultaneously offer similar advantages, but BsAbs are more efficient to develop. Unlike combination approaches, BsAbs can facilitate spatial proximity of targets that may be necessary to induce the desired effect. Successful development of BsAbs requires understanding antibody formatting and optimizing activity for both targets prior to clinical trials. To realize maximal efficacy, special attention is required to fully define pharmacokinetic (PK)/pharmacodynamic (PD) relationships enabling selection of dose and regimen. The application of physiologically based pharmacokinetics (PBPK) has been evolving to inform the development of novel treatment modalities such as bispecifics owing to the increase in our understanding of pharmacology, utility of multiscale models, and emerging clinical data. In this review, we discuss components of PBPK models to describe the PK characteristics of BsAbs and expand the discussion to integration of PBPK and PD models to inform development of BsAbs. A framework that can be adopted to build PBPK-PD models to inform the development of BsAbs is also proposed. We conclude with examples that highlight the application of PBPK-PD and share perspectives on future opportunities for this emerging quantitative tool.

Keywords

biologics, bispecific antibody, PBPK

In recent years, novel biologic therapies have made unprecedented progress in bringing highly specific treatments to the fight against multiple types of diseases. These novel biologic treatments bring increased efficacy while minimizing adverse side effects in patients. Bispecific antibodies (BsAbs) are some of the most promising formats of biologics in development. Although emerging data suggest application of BsAb therapies in nononcology disease areas such as asthma and other immunologic disorders, the biggest strides have been made in using BsAbs to treat hematological malignancies.[1] With the approval of Blincyto for acute lymphoid leukemia and several trials in immunotherapy and immunology underway, BsAbs represent a proven and valuable alternative in the armamentarium to fight against deadly diseases.

Clinical success of this approach has been possible largely for 2 reasons: (1) our improved understanding of antibody structure and antigen-antibody interactions, namely, lock and key, induced fit, and conformational selection; and (2) enhancements in molecular biological understanding of disease progression and treatment-resistance mechanisms. Antibody formats that include mutations that impact FcRn binding can have a significant impact on pharmacokinetics and thereby on dosing regimens of new antibodies. Similarly, fun-

[1]Quantitative Clinical Pharmacology, Millennium Pharmaceuticals, Inc., Cambridge, Massachusetts, USA
[2]Clinical Pharmacology, CSL Behring, King of Prussia, Pennsylvania, USA
[3]Clinical Pharmacology and Pharmacometrics, AbbVie, North Chicago, Illinois, USA
[4]Clinical Pharmacology, Ascentage Pharma Group Inc., Rockville, Maryland, USA
[5]Clinical Pharmacology and Pharmacometrics, AbbVie Biotherapeutics, Redwood City, California, USA

Submitted for publication 7 May 2020; accepted 6 July 2020.

Corresponding Author:
John P. Gibbs, PhD, Quantitative Clinical Pharmacology, Takeda Pharmaceuticals, 40 Landsdowne Street, Cambridge, MA 02139
Email: John.gibbs@takeda.com

damental physicochemical properties including shape, size, hydrophobicity, and charge also have a significant impact on pharmacokinetics (PK), antigen-antibody interactions, and biological activity.[2] The complex interplay between the therapeutic antibody and the interaction with the target and its ultimate effect on clinical outcome can be elucidated using our fundamental understanding of factors affecting pharmacokinetics, pharmacology, and disease pathophysiology.

The emerging science of physiologically based pharmacokinetic (PBPK) modeling has made significant progress because of the continued impact on decision-making across the drug development continuum and resulting rapid uptake in academia, industry, and regulatory organizations. Because PBPK models explicitly describe processes that account for drug disposition, it is possible to obtain a quantitative characterization of pharmacokinetics in blood and other tissue compartments representing major organs in the body. Such prediction is of therapeutic relevance because it enables the estimation of drug exposure not only in plasma, but also at the site of action, which may be nearly impossible to measure via experimental methods. Because drug development decisions are rarely made only based on PK considerations, accounting for pharmacodynamic (PD) changes such as blood pressure reduction, tumor size reduction, or target receptor occupancy modulation can have a direct benefit in clinical efficacy decision-making when the relationship between PD changes and clinical outcome is known. PBPK models offer a mechanistic framework to quantify the PD effect of a drug by representing free drug concentrations at the site of action or in other tissues of relevance; in some cases, it may even be possible to link PK to clinical end points. Understanding tissue PK is particularly important in the case of large molecules like bispecific antibodies for which blood or plasma PK may not always be reflective of tissue concentrations because of various nonlinear processes.[3] Hence, PBPK-PD models provide a valuable framework for disease or toxicity modeling to inform important questions during drug development such as target and dose selection.[4]

The aim of this review is to (1) highlight the importance of BsAb therapies, (2) describe the applications of PBPK-PD models in development of BsAbs, (3) propose a PBPK-PD framework that can be implemented in informing the development of BsAbs, and (4) illustrate some of the future applications of BsAbs and the utility of PBPK-PD models in decision-making.

Mechanistically, BsAbs are designed to bind to 2 targets and can provide more robust and tailored immunogenic targeting than what is possible with natural antibodies.[5] BsAbs are engineered artificial antibodies capable of recognizing 2 epitopes of an antigen or 2 antigens. The targets may be 2 soluble targets, 2 cell-based receptor targets, a soluble target and a cell-based target, or 2 membrane-bound targets on the same cell (Figure 1). The diversity of bispecific formats and their biological and pharmacological properties make it possible to consider BsAbs as promising agents for use in various therapeutic areas and diseases, from recruiting cytotoxic T cells to targeting cancer cells for oncology treatments to anti-interleukin therapy to treat asthma and fibrosis.

Therapeutic antibodies use variable regions of heavy and light chains to bind to specific antigens through the Fab domain. Antibodies can bind to antigens with variable affinity and specificity with a diversity of 108 to 1010 different variants for each antigen-binding site.[5] The Fc region of the antibody can bind to receptors of the host immune system such as Fcγ receptors (FcγRs), C1q, and neonatal Fc receptor (FcRn) to initiate distinct effector functions. Small differences in the amino acid sequence and glycosylation pattern on the Fc domain can have significant impact on key properties such as immunoglobulin G (IgG) thermal stability, FcγR-binding effectiveness, and serum half-life.

Through decades of research and development of BsAbs and their derivatives, there are 2 common formats of BsAbs currently being explored: the single-chain variable fragment-based (no Fc fragment) antibody and the full-length IgG-based antibody. There are several approaches to improving the design of novel BsAbs such as antibody linker engineering, quadroma technology,[6] knobs-into-holes technology,[7] common light chain,[8] CrossMAb technology,[9] and protein engineering. These and other approaches have all been extensively investigated and make up the principal knowledge base of this fast-growing and diverse field.

Defining PBPK-PD Modeling

PBPK modeling is an approach to characterizing the absorption, distribution, metabolism, and elimination characteristics of a compound in humans or animal species. It also allows the evaluation of the effect of intrinsic (eg, organ dysfunction, age, genetics) and extrinsic (eg, drug-drug interactions) factors, alone or in combination, on drug exposure.[10,11] A PBPK model platform includes 3 key components: physiological framework (system parameters), computational framework, and drug properties.[12]

The physiological framework comprises a compartmentalized representation of the different organs, with each compartment described by a specific tissue volume and blood flow rate, which communicate with the blood (venous and arterial). The computational framework includes the program code, model structure, and

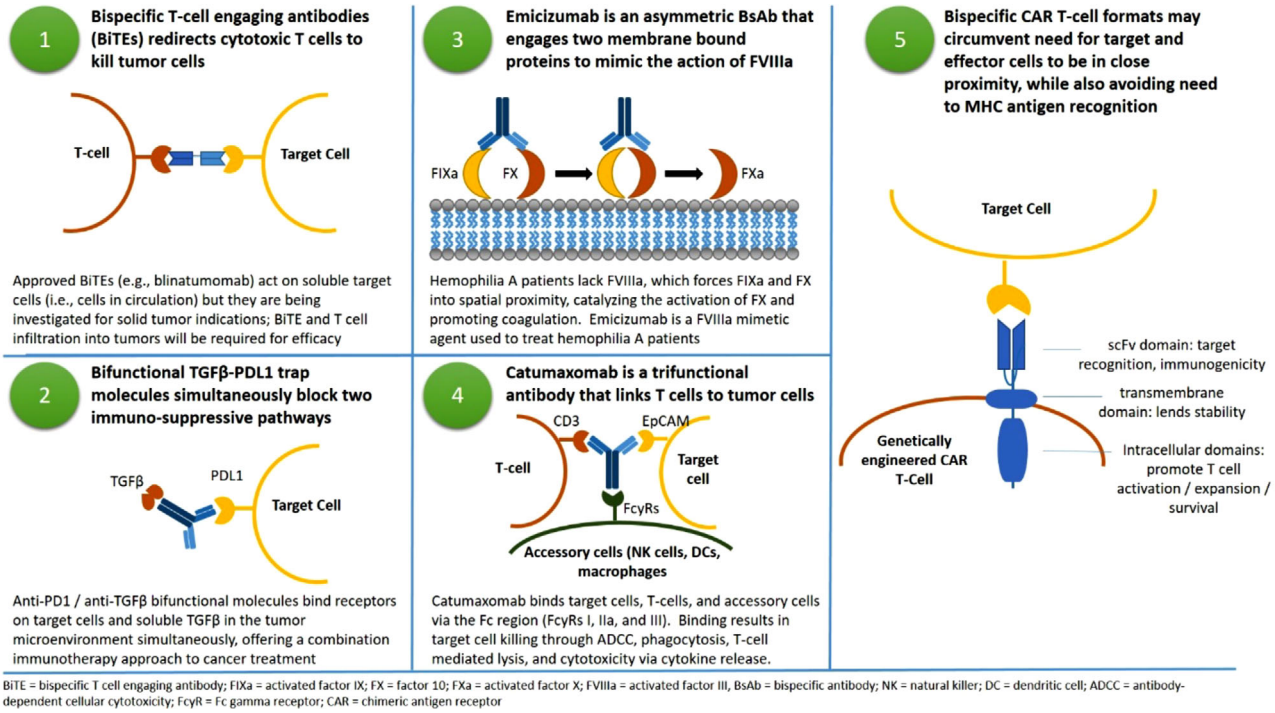

Figure 1. Mechanism of action of various formats of bispecific antibody therapies under development or currently approved.

mathematical equations used to represent the physiological framework. The system parameters are population specific and account for population variability and correlation between parameters. The drug model component of the PBPK platform comprises drug-dependent parameters including, but not limited to, molecular weight, hydrodynamic radius, and dissociation constant for binding to FcRn. The PBPK model is extended to include PD by describing the mechanism of action of the drug and its effects on the target biological pathway. These effects, which could include on-target effects that lead to efficacy or off-target effects that lead to toxicity, are dependent on binding affinity and avidity. Study design and formulation parameters are also part of the building blocks in an attempt to describe the PK in plasma as well as individual tissues/organs.[12,13]

Whole-Body Versus Minimal PBPK Modeling

The complexity of a PBPK model can vary, going from a minimal PBPK model to a full whole-body PBPK model. Although in the full model all the distribution organs and tissues are represented as separate perfused compartments, in the minimal model tissues with similar kinetics are lumped together.[14-16] The reduced complexity in a minimal PBPK model still allows for the openness of mechanistic characterization in only the organs/tissues of interest, whereas one advantage of full PBPK modeling is the ability to simulate the exposure of a drug in specific tissues that are not accessible to clinical sampling.[11]

PBPK-PD Versus Population Modeling and Quantitative Systems Pharmacology

Different modeling methods have been used to quantitatively describe the PKPD of drugs, with some of them incorporating more mechanistic approaches that describe disease pathophysiology and the complexity of drug action. Here we describe some differences and/or similarities between modeling approaches such as population PK, PK/PD, PBPK-PD, and quantitative system pharmacology (QSP) and the ways in which these approaches complement each other and can be integrated to provide a comprehensive understanding of the BsAbs and their action.

Population PK modeling applies statistical approaches and involves fitting of the model parameters to a clinically observed plasma concentration-time profile and/or urine data of a drug following dose administration. In this top-down approach, the main objectives are to build a model that describes observed data, estimates parameters means and their intersubject variability, and to identifies significant covariates of PK parameters.[12,17]

In a PK/PD model, the relationship between the pharmacokinetics (PK) of a therapeutic intervention and the resulting pharmacodynamic (PD) effect is demonstrated.[18,19] This approach can be empirical or can incorporate more mechanistic components with respect to either PK (in which a PBPK model would be used) or PD (in which case an empirical, semimechanistic, or QSP model can be employed), which facilitate

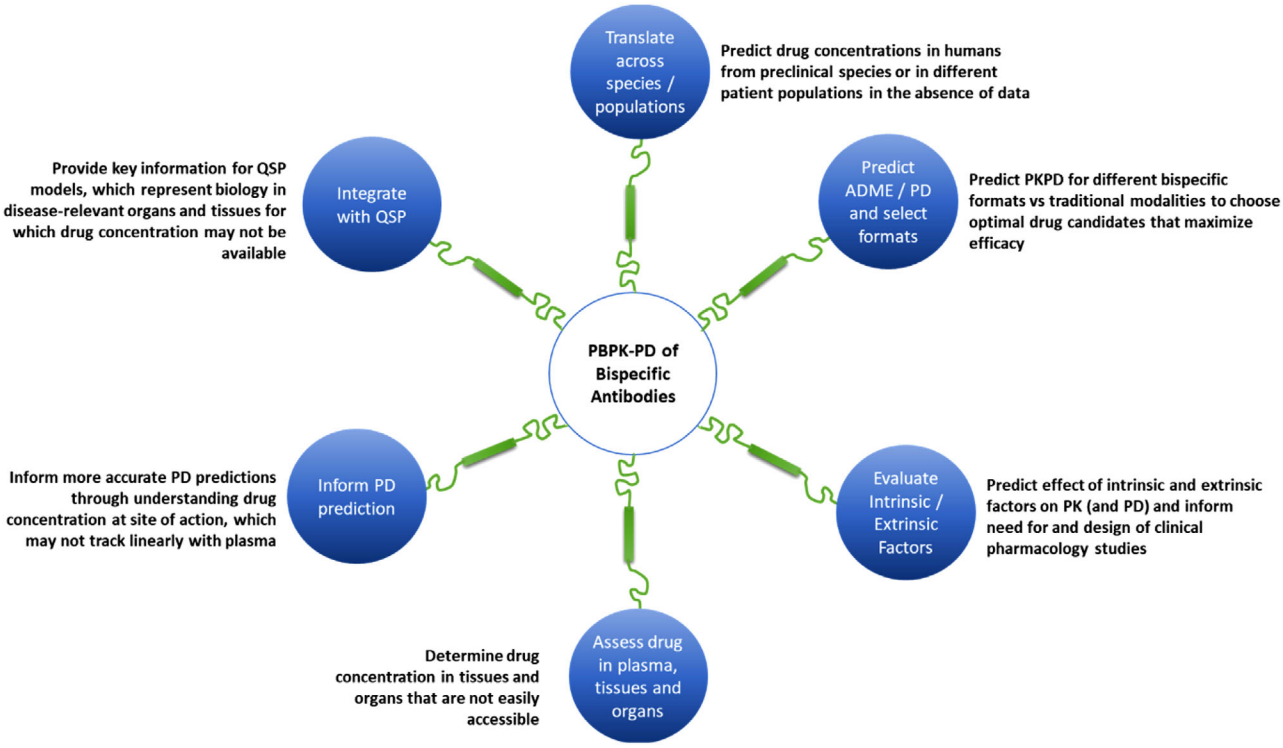

Figure 2. Application of PBPK-PD modeling in informing development of bispecific antibodies.

biology-driven translations across species and/or between different patient populations.[20,21] In some cases, the separation of mechanistic PK/PD from QSP models is not obvious, but certainly the mechanistic details, scientific questions, and technical aspects addressed by PK/PD and QSP models may differ.[21]

PBPK models have significant mechanistic detail and rely on physiological and drug-dependent parameters. The main advantage of PBPK models is that they can be used to extrapolate outside the studied population and experimental conditions.[10,14] This approach focuses predominantly on absorption, distribution, metabolism, excretion, and PK questions, but their value can be exponentially increased by combining them with PD models (empirical, semimechanistic, or QSP) to develop a PBPK-PD model that spans from dose to exposure (PBPK models) to response (PD models).[4,10]

The distinction between PBPK and other QSP models can become vague when considering local kinetics in tissues, which may be represented in great mechanistic detail. However, it is the PBPK models that focus on how the body handles the drugs rather than the more holistic view of QSP that defines the way drugs affects the body,[22] which differentiate PBPK and QSP models. The ultimate goal of PBPK modeling is to quantitatively determine drug distribution throughout the body, whereas the ultimate goal of QSP is to mechanistically and quantitatively understand a biological, toxicological, or disease process in response to therapeutic modulation.[23] The extension of PBPK to PBPK-PD may leverage QSP models to the understanding of the way the body handles the drug and the way the drug affects the body or may leverage more conventional PD modeling approaches. It is important to remember, however, that either of the modeling approaches should focus on the mechanistic basis of drug action and not explain all the biological processes involved.[24] The decision to develop a PBPK-QSP versus a PBPK-PD model is driven by the clinical question of interest (and has the same considerations for developing a QSP model that is not intended for integration with a PBPK model).

Advantages of PBPK-PD Modeling

PBPK-PD models can be used to address PK or PD questions throughout development (Figure 2). PBPK models were initially developed to determine the drug concentrations in plasma and specific tissues that are not easily accessible to clinical sampling. This can be particularly important if the pharmacological or toxicological effects are driven by the concentrations in that tissue.[9] Because PBPK, and PBPK-PD models allow separation of the parameters pertaining to the physiology and disease pathophysiology from that of the drug and the study design, they can be used to extrapolate PK/PD properties in various healthy and patient populations in the absence of clinical data. This

ability to predict and extrapolate beyond the initial data used to develop the models is a major advantage of modern PBPK-PD models and is a general limitation of data-driven models. This is a paradigm shift from the classical "learn-confirm" to a "predict-learn-confirm-apply" cycle. With respect to PK understanding, this change is largely because of combining in vitro-in vivo extrapolation (IVIVE) approaches with PBPK models.[25] Moreover, the separation of drug-specific and physiologic parameters within the model can allow a more mechanistic understanding of the sources of interindividual variability than can be provided by population and compartmental modeling techniques.[14] However, one caveat is that detailed understanding of physiologic variables in the population of interest is required but not always available, which can hinder the use of PBPK modeling in special populations.[26] PBPK-PD modeling allows extrapolation of pharmacodynamic effects across species and populations and has been facilitated by the use of mechanistic and QSP modeling.

General Applications and Challenges in Building a PBPK-PD Model

Advancements in computer science and physiologically based mathematical models have led to the expansion of the applications of PBPK-PD modeling. PBPK models have been recently used to support discovery and development of biologics including BsAbs. Case studies on the application of PBPK-PD in BsAbs are covered in the latter part of this article.

In the past 10 years, PBPK modeling has become increasingly accepted by regulatory agencies as a means of informing clinical study strategy, and it has become a useful tool in drug development. In addition, a number of drug labels are informed by simulation results generated using PBPK models.[26] The simulation results are mainly related to drug-drug interaction (DDI) risk assessments and genotype-related PK parameter estimates in a rare disease population. These cases show that either the simulations are used in lieu of conducting clinical studies or have informed the drug label that otherwise would have been silent in some specific situations.

Despite the increasing use of PBPK-PD modeling, there are many challenges that limit the utility of PBPK-PD modeling and simulation. Perhaps, the biggest challenge in further expansion of PBPK-PD models is the lack of adequate and reliable systems or physiological data. In general, IVIVE using PBPK-PD models requires considerably more experimental and in silico data than static models. because of the large number of parameters required for PBPK-PD modeling and the limited availability of in vivo data to verify individual parameters, model predictions can be confounded by lack of confidence in individual parameters.[26]

Systems data, such as the abundance and activity of non-CYP enzymes and transporters in various tissues, and absorption-related data and how these are changing by age/disease status are generally lacking. For example, the application of PBPK modeling to predict the pharmacokinetics in disease populations is hindered by lack of in vivo data in patient populations, poor understanding of the physiologic changes that occur in certain populations, and limited knowledge of tissue-specific changes in enzyme and transporter expression.[11,26] Similarly, in case of special populations (eg, pregnancy, elderly, and pediatric populations), although there have been tremendous interest and application of PBPK models, there are several factors that need further refinement and elucidation to reliably inform the ontogeny functions.[27]

Some of the challenges are even bigger when developing mechanistic PBPK-PD models for biologics and/or models that aim to provide mechanistic insights into drug efficacy and safety. In developing PBPK models for biologics, limited data on target expression and changes in disease populations result in the risk for overparameterization with PBPK models, and thus, there is an effort to move toward reduced PBPK models for therapeutic proteins.[28,29] These challenges are magnified when combining PBPK models with mechanistic models that allow for extrapolation of pharmacodynamic effects and assessment of clinical efficacy, like QSP models. The modeler faces the need to acquire all the data needed to inform a PBPK model for biologics, including target expression data and the data needed to inform a mechanistic or QSP model to predict PBPK-PD, a not inconsiderable challenge to surmount.

Another challenge in the PBPK-PD modeling field is determining how to assess model quality. In this regard, recent European Medicines Agency (EMA) and US Food and Drug Administration guidelines regarding PBPK analyses and reporting provide a significant milestone for this field and pave the way for a broader application of PBPK-PD modeling,[30,31] and perspectives from drug developers have made some impact and resulted in more clarity in the final guidance issued by the regulators.[12]

One of the significant applications of PBPK modeling for large molecules is to account for pharmacokinetics of tissue and in circulation. Ectodomain shedding is a common phenomenon that is noticed for some membrane-bound antigens in which the extracellular domain of the receptor is cleaved and released into circulation. This can have a significant impact on large-molecule pharmacokinetics, especially when targeting membrane-bound targets. Li et al previously

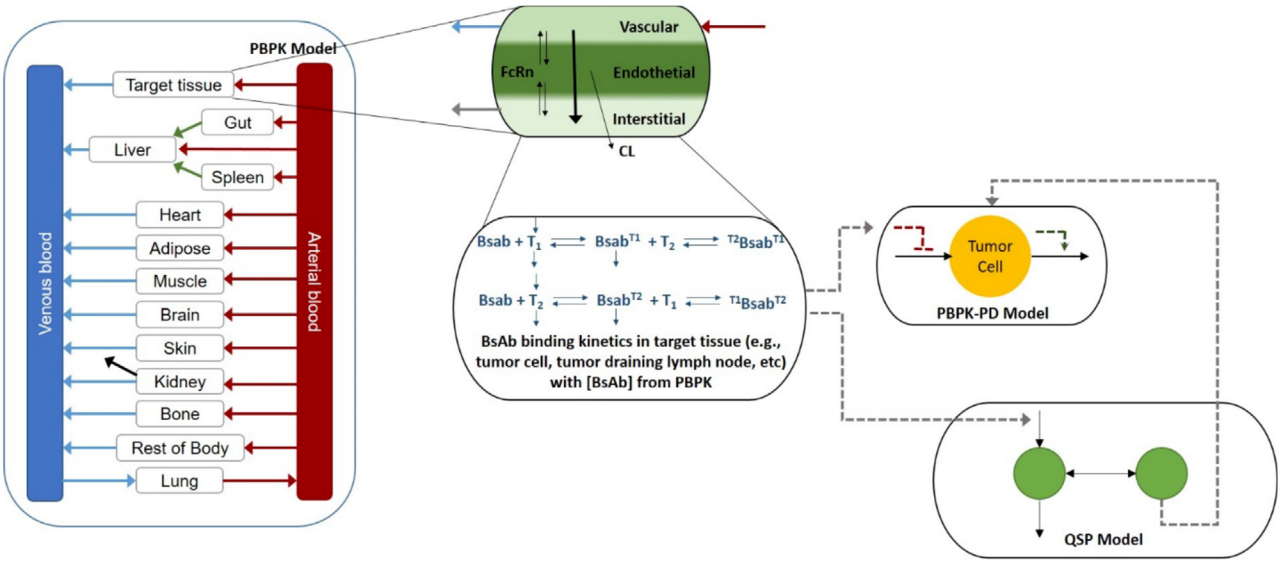

Figure 3. Proposed framework of core components to implement PBPK-PD-based decision-making in development of bispecific antibodies.

showed the application of minimal PBPK modeling to illustrate the impact of trough concentrations and clearance of trastuzumab with varying levels of its target antigen, human epidermal growth factor receptor 2.[32]

A Framework for Building PBPK-PD Models for BSAB

The understanding of BsAb PK and factors that can affect it is critical for the development of safe and efficacious drugs. Bridging PK to PD effects and clinical efficacy "closes the development loop," allowing for the selection of optimal doses and regimens that deliver the maximum benefit to patients. We propose a general framework to accomplish this goal that integrates PBPK modeling with conventional, semimechanistic, and/or QSP models to characterize BsAb PKPD across species and populations and effectively guide development (Figure 3). In this framework, a conventional PBPK model that describes distribution throughout the body is extended to describe BsAb binding to multiple targets, both of which potentially facilitate target mediated drug disposition (TMDD) mechanistic models with some feedback to describe the action of immune-modulatory agents on cytokine release. The particular details, especially with respect to PD, must be driven by the individual mechanism of action of the BsAbs under development, but this framework provides a guide for the modeler to extend these ideas into any therapeutic area to describe disease pathophysiology in general. In many cases, it will be possible to leverage publicly available models, to which much value can be added through integration.

PBPK modeling is an approach that has been used to characterize the in vivo behavior of drugs. A recent review[33] focused on PBPK modeling of monoclonal antibodies (mAbs), highlighting the key PK process and parameters to be considered and suggested potential extension of these PBPK models to predict the behavior of the next generation of antibody therapeutics as BsAbs.

PBPK models consist of many compartments linked via rate constant compartments and are realized as a set of ordinary differential equations. Each compartment represents certain organs and tissues in the body and is parameterized using known tissue physiology (ie, volume or weight). The rate constants governing transport between these compartments are parameterized according to known tissue- or organ-specific blood and lymph flows.

Several PBPK models/platforms for mAbs are available,[34-37] and a similar model structure can be used to model BsAbs. In general, it consists of organs/tissues connected through blood and lymph flow to systemic circulation. Each tissue is subdivided into spaces representing the vascular, interstitial, and cellular spaces. It also includes an endosomal space, where lysosomal degradation and high-affinity FcRn binding are located.

During subcutaneous absorption, antibodies are usually well absorbed (bioavailability of 50% to 100%), and this process has been simply described through administration of mAbs to the interstitial space of the skin in published PBPK models, mainly because there is low confidence in parameters as rate of fluid flows from injection site through the lymphatics to the circulation and the expression of FcRn in cells present in the lymphatics and lymph nodes[33] as it is generally accepted that the predominant route of absorption of antibody

therapeutics following subcutaneous administration is via the lymphatics.[38]

Understanding of determinants of BsAb disposition is crucial for the development of PBPK models. The primary route of distribution of antibodies to the tissues is via convective transport, which depends on the size of pores relative to the size of the antibody molecule and on the rate of fluid movement into tissue and has been mathematically described as a function of lymph flow and the vascular reflection coefficient, representing the fraction of mAbs in plasma that is unable to pass through paracellular pores.[33] In addition, "2-pore formalism"[39] has been used in some models[35,37] to describe the transcapillary exchange of the antibody between plasma and the interstitial space in each organ across the endothelial layer via convection through large pores and fluid circulation through small pores.

The elimination of antibodies is mainly via catabolism following endocytosis and transport to the lysosome, with the binding to FcRn playing a role as a protective pathway from degradation and recycling. In PBPK models, FcRn-mediated protection of IgG is typically described as occurring within the endosomes of the vascular endothelium and requires data describing FcRn expression and the rate of uptake into endothelial cells.[33] TMDD can happen because of the high-affinity interaction between antibody and target, and parameters such as target expression, target turnover, and target accessibility are also needed.

To account for differences in the structure of the model for BsAbs, TMDD should be extended to incorporate sequential binding to 2 targets at tissue sites of action to anticipate systemic and local BsAb concentrations and target suppression, which have been described,[40-42] and it has been shown that tissue-site target density, target-binding affinity, and type of target (soluble versus membrane-bound ligand) are major determinants governing BsAb disposition.[40] A mechanistic model[43] (extended from a mAb model[44]) to guide affinity optimization against soluble and membrane-bound targets for BsAbs has also been proposed to predict the optimum K_D for the 2 arms of the BsAbs given the target properties and to elucidate the effect of relative target expression and rate of target internalization on final target occupancy. It is crucial to incorporate target internalization rates into the analysis. If the receptor internalization rate is very high, resulting in TMDD, then the tighter bound compound (low K_D) may clear out faster through internalization than it would have with a higher K_D. This effect can be even more critical in the case of BsAbs than for monospecific ones. Because 2 membrane-bound targets create an opportunity for 2 TMDD sinks, it is particularly important to understand this property for both targets.

In the case of T-cell-engaging bispecific antibodies (T-BsAbs), a class of BsAbs that simultaneously binds to CD3 on T cells and a tumor-associated antigen on tumor cells,[45] the rapid and uncontrolled induction of T-cell-mediated cytokine release that leads to dose-limiting adverse events[46] should to be taken into account in the model to predict the optimal dosing regimen. A semimechanistic PK/PD model has been proposed,[47] and this framework could be integrated to a PBPK platform, resulting in a PBPK-PD approach to efficiently inform optimal dosing regimens for T-BsABs. A PBPK model to evaluate the effect caused by BsAbs of transient elevation of cytokines, particularly interleukin (IL)-6, on cytochrome P450 suppression has also been described.[48]

To inform model parameters, determination of baseline levels of a target and its levels of expression are often difficult and in cases when such data are not available at least an understanding of relative changes between healthy and disease physiological levels can help to guide preliminary simulations. For example, to account for faster clearance of infliximab in individuals with severe inflammation possibly because of higher tumor necrosis factor (TNF)-α concentrations and vascular hyperpermeability, a global 2-fold[49-52] and a local 3-fold increase in TNF-α concentration in inflamed organs[53,54] was applied in the PBPK model.[55] An increase in pore size was also applied to incorporate hyperpermeability in inflamed organs, in accordance with previous minimal PBPK models of inflammatory conditions that observed the requirement for lower vascular reflection coefficients in inflamed organs.[56-58] Another study also showed that inflammatory diseases such as inflammatory bowel disease (IBD) can increase vascular permeability and change mAb disposition[59] and confirmed a previous suggestion that convection and lymph drainage are the dominant pathways for biologic uptake and removal from tissues.[57,60] The study also demonstrated higher TNF-α production in inflamed colon and higher mAb distribution to inflamed tissue, with the reflection coefficient for colon in IBD mice estimated to be significantly lower than that in non-IBD mice. All these exemplify disease-related physiological parameters that can be incorporated into the PBPK model.

Another case is the elevation of the proinflammatory cytokine IL-6 in patients with various systemic inflammatory diseases including psoriasis and rheumatoid arthritis (RA)[61,62] and patients with certain types of cancer.[63] As IL-6 modulates drug-metabolizing enzymes such as cytochrome P450s (CYPs), resulting in alteration in biotransformation and elimination of small-molecule substrates of the affected CYPs,[64] it can lead to disease-mediated therapeutic protein–drug interactions. An example in which these physiological

changes were included in PBPK models to predict DDI liabilities is also available.[65]

Examples of PBPK-PD Modeling of BsAbs

Examples of PBPK models being used to support discovery and development of BsAbs over the past few years have been summarized (Table 1, Figure 1). These case studies cover a broad range of categories, including optimal design of a BsAb, optimization of clinical dosing, and management of a risk:benefit profile. Each example is presented with a brief description of the theme, key questions being addressed, and a summary of the potential implications and impact.

Design of Bispecific Antibody

To aid in the optimal design of BsAbs for the treatment of cancer, Van Steeg et al developed a mathematical modeling approach that accounted for in vitro target binding of BsAbs.[66] The model was an extension of earlier efforts and included heterogeneous bivalent binding as a function of the BsAb concentration, receptor expression, binding constants with an avidity factor, and consideration of spatial limitations. Spatial limitations dictate that a second binding interaction can occur only when the second receptor is in the vicinity of the first receptor. The model also considered other nontumor cells that could express the target serving as "decoy" receptors that might limit bivalent binding of the BsAb to the tumor cell. In vitro binding data for monovalent and BsAb constructs against epidermal growth factor receptor (EGFR) and insulin-like growth factor 1 receptor in 3 cell lines were used to verify the model after adjusting the reaction volume in the model. The model was used to design a new anti-EGFR bispecific targeting different epitopes for a case in which receptor density is high in the tumor and low in other tissues such as skin and liver. Results from the simulations predicted that low-affinity EGFR binding (750 nM) would yield high tumor receptor occupancy with minimal receptor occupancy in skin and liver (~20%). This example shows how PK/PD modeling of in vitro data can be used to help guide the selection of potency targets for early discovery efforts.

An alternate modeling approach to address spatial limitations for BsAb binding to cell membrane targets was proposed by Sengers et al.[67] The binding of anti-CD4/CD70 DuetMab was evaluated in cells that expressed both targets or just 1. Additional variants were prepared with reduced affinity for CD4 relative to the parent DuetMab, which had high affinity for CD4 (K_d = 0.9 nM) and low affinity for CD70 (K_d = 25 nM). Two binding models were considered based on ordinary differential equations and a Monte Carlo approach that was based on a computational biology model of processes involving diffusion and chemical reactions. Both models considered the diffusion-limited association rate constant for surface-bound reactants, which leads to cross-linked membrane targets. The mechanistic binding model may be useful for designing novel candidates by providing insights into bivalent ligand interaction for 2 cell-membrane receptors.

In a third example, a model for hypothetical BsAbs was developed to consider the relative impact of biodistribution into tissues and target-mediated elimination on predicted receptor occupancy for 2 cases.[40] The model included binding terms for 2 targets with production and degradation rates for the targets, elimination of the drug-target complex, and physiological representation of biodistribution of the antibody from plasma to a representative tissue compartment. A local sensitivity analysis was conducted to identify the impact of key model parameters on the antibody concentration-time profile in plasma and tissue as well as the concentration-time profile of free ligand or receptor. Overall, the authors showed how a mechanistic model of a bispecific could be used to evaluate drug-target interactions at the site of action to identify optimal binding affinities for 2 targets.

Informing Clinical Dose and Regimen

The first example in this category dealt with the projection of first-in-human (FIH) dose for a bispecific immunomodulatory antibody (P-cadherin LP-dual-affinity retargeting [DART]) based on the DART scaffold.[68] A minimal anticipated biological effect level (MABEL) approach was applied to project the FIH dose because of its immune agonistic properties. The pharmacological activity of P-cadherin LP-DART is driven by binding to both P-cadherin on the tumor cells and CD3 on T cells. A mechanistic PK/PD-driven approach was explored to understand the exposure-response relationship based on the trimolecular synapse concentration to project the MABEL dose. Orthogonal approaches including PK-driven and receptor occupancy calculations were also investigated for comparison. The PK/PD and PK-driven approaches suggest comparable doses, whereas receptor occupancy approach yields much higher doses. The advantage of the PK/PD method is that in using the synapse concentration as the exposure driver for pharmacology, the predicted dose is independent of experimental conditions. This study showcases the application of PK/PD modeling in immuno-oncology and could potentially be implemented for other bispecific biotherapeutics.

In the second example, a translational QSP model was constructed to quantify and predict efficacy across species.[69] The model considered T-cell activation, which is driven by the formation of a trimolecular complex between drugs, T cells, and tumor cells, and incorporated

Table 1. Key Examples of Modeling and Simulation of BsAbs and Their Impact on Drug Discovery and Development

Category	Key Theme	Key Question(s)	Brief Description	Implications/Impact	Reference
Optimal design of BsAbs	Properties of bispecific binding systems that would maximize binding efficiency for a BsAb. Optimal design of a BsAb.	Is the avidity hypothesis universally true, or are there conditions under which bispecifics are only as good as (or even worse than) combination antibodies?	A mathematical model was developed for the binding of BsAbs to their targets that accounts for the spatial distribution of the binding receptors and the kinetics of binding and is scalable for increasing valency. Results show that the affinity of bispecific arms must be optimized for maximum binding potency to be superior in their binding potency to a combination of antibodies.	This tool can be used for the design and development of the next generation of anticancer bispecific compounds.	van Steeg TJ et al, 2016[66]
	Role of surface diffusion in the binding of a BsAb to 2 membrane targets.	Can we use models to predict how the bispecific mAb interacts with the 2 cell-surface antigens?	A mathematical framework has been developed to describe a bispecific monoclonal antibody interaction with 2 independent membrane-bound targets that are expressed on the same cell surface. The BsAb in solution binds either of the 2 targets first and then cross-links with the second one while on the cell surface, subject to rate-limiting lateral diffusion step within the lifetime of the monovalently engaged antibody-antigen complex. The authors validated this approach against an independently published anti-CD4/CD70 DuetMab experimental data set.	The work can be useful for pharmacokinetic and pharmacodynamic modeling of novel drug candidates and targets, as well as understanding bivalent ligand interaction with 2 cell membrane receptors in general. It is also useful for comparing the advantages and disadvantages of applying a combination of monospecific mAbs versus respective bispecific variants in the case of cell surface-expressed targets.	Sengers et al, 2016[67]
	Simulations of site-specific target-mediated pharmacokinetic models for guiding the development of BsAbs	What are the differences in the disposition of BsAbs in plasma and possible sites of action in humans?	Although the biophysical properties of BsAbs are well studied, limited information is available outlining the determinants of their plasma and/or tissue disposition. This work extended the general TMDD modeling approach to incorporate sequential binding to 2 targets at tissue sites of action to anticipate systemic and local BsAb concentrations and target suppression.	Plasma kinetics alone is not sufficient to predict target-site kinetics and dynamics of an BsAb. Mathematical models can be used to define relationships among inaccessible system variables and provide projections of drug and target temporal profiles at the site of action.	Chudasama et al, 2015[40]
Clinical dose and regimen	PBPK modeling to elucidate the lack of benefit from using a bifunctional antibody (BFA) over a traditional approach.	How to optimize the design of bifunctional antibodies to enhance therapy?	Tumor-killing lymphocytes cannot reach the tumor cells in sufficient quantity to keep the tumor in check. Recently, the use of BFA has been proposed as a way to direct immune cells to the tumor, which has shown limited success. A PBPK model was developed that accounted for interactions between all relevant species in the various organs and tumor.	The design of the BFA is critical, and the binding constants of the antigen- and lymphocyte-binding epitopes need to be optimized for successful therapy.	Friedrich et al, 2002[70]
	Selection of first-in-human (FIH) dose for bispecific immune-oncology biotherapeutics.	How to project FIH dose for bispecific biotherapeutics using a mechanistic PK/PD model?	A minimal anticipated biological effect level (MABEL) approach was applied to project the FIH dose for a bispecific immunomodulatory molecule (P-cadherin LP-DART) because of its immune agonistic properties. The pharmacological activity of P-cadherin LP-DART is driven by binding to both P-cadherin on the tumor cells and CD3 on T cells. A mechanistic PK/PD-driven approach was explored to understand the exposure-response relationship based on the trimolecular synapse concentration to project the MABEL dose.	This study showcases the application of PK/PD modeling in projection of first-in-human dose for bispecific biotherapeutics.	Chen et al, 2016, CPT[68]

(*Continued*)

Table 1. Continued

Category	Key Theme	Key Question(s)	Brief Description	Implications/Impact	Reference
	Integration of the kinetics of T-cell, biologic, and effector cells under a unified mechanistic model structure.	How to extrapolate in vitro and in vivo data to inform clinical dosing of BsAbs?	A target-cell biologic-effector cell (TBE) complex-based cell-killing model was developed using in vitro and in vivo data, which incorporate information on binding affinities of BsAbs to CD3 and target receptors, expression of CD3 and target receptors, concentrations of effector and target cells, and the respective physiological parameters. The approach was successfully applied to blinatumomab as validation.	The TBE model can be used to extrapolate drug-specific parameters of the BsAbs to inform clinical dose selection. Next steps were proposed to include minimal PBPK model structure to guide dose and regimen selection.	Jiang et al (mAbs 2018)[72]
	A translational quantitative systems pharmacology (QSP) model to quantify and predict efficacy across species.	How to construct a model to integrate in silico, in vitro, and in vivo data to quantify T-cell-mediated tumor cell killing and translate it to the clinic?	CD3 BsAb constructs recruit cytolytic T cells to kill tumor cells. T-cell activation is driven by the formation of a trimolecular complex between drugs, T cells, and tumor cells, mimicking an immune synapse. A translational QSP model is proposed for CD3-bispecific molecules capable of predicting trimer concentration and linking it to tumor cell killing. The model was used to quantify the pharmacokinetic (PK)/pharmacodynamic (PD) relationship of a CD3-bispecific-targeting P-cadherin.	The mechanistic PK/PD model can be translated to the clinic for human PK/PD predictions and sensitivity analysis to determine important parameters driving efficacy. The model can be applied at early stages to aid in the design of CD3-bispecific constructs and to select molecules with optimal properties.	Betts et al, 2019[69]
	PBPK modeling to predict the dose of emicizumab for a pediatric population.	How to support dose projection for a pediatric population in the absence of observed data?	A PBPK model was developed to investigate whether a more mechanistic description of age-related differences could improve the confidence in PK projections.	Modeling and simulation activities led to the approval of emicizumab in all age groups by EMA, even with no clinical data available.	Retout et al, 2020[74]
	TMDD model for BsAbs and optimal dosing strategy.	How to develop the general target-mediated drug disposition model for BsAb and compute an optimal dose that immediately creates and maintains maximal possible ternary complex (TC) concentration?	BsAbs exert their cytotoxic effect by bridging effector T cells and target cells to form immunological TCs, driving the pharmacodynamics. Currently, there are no generalized mathematical models and no quasiequilibrium approximation characterizing the relationship between dose and TC formation, which is essential for successful discovery, development, and clinical translation.	A developed BsAb model can help in optimizing the design of BsAbs and selection of targets. In addition, the BsAb model/approximation can be used to select an optimal dosing strategy.	Schropp et al, 2019[42]
Management of risk:benefit	PD of drug-mediated drug interaction.	Is transient cytokine elevation resulting from the immunotherapy blinatumomab likely to result in clinically meaningful DDIs?	Blinatumomab immunotherapy mediates transient cytokine elevation. Cytokine elevation may affect CYP activity. A PBPK model was established to evaluate the effect of transient cytokine elevation on CYP activities. Transient cytokine elevation observed during blinatumomab treatment has a low DDI potential.	No DDI study was planned or performed by the sponsor. A dedicated DDI study was not requested by the regulatory agencies.	Xu et al, 2015[48]
	Optimize clinical dosing strategies for T-BsAbs by avoiding CRS.	How can we efficiently determine optimal dosing regimen for T-BsAbs and to assess cytokine release on T-cell-engaging BsAb treatment?	CRS is a common dose-limiting adverse event for T-BsAbs. A "priming" dose strategy (ie, a lower initial dose followed by a higher maintenance dose) has been implemented in the clinic to mitigate CRS and to achieve efficacious doses with T-BsAbs. So far, the selection of the optimal priming dosing regimen is largely empirical. A semimechanistic cytokine model was developed to simulate cytokine profiles following various dosing regimens.	The model may assist the design of clinical dosing strategies for T-BsAbs programs and thus enable the conduct of more efficient clinical trials.	Chen et al, 2019[47]

T-cell distribution to the tumor, proliferation, and contraction. The model was used to quantify the PK/PD relationship of a CD3 bispecific targeting P-cadherin (PF-06671008). A tumor stasis concentration was calculated as an estimate of minimum efficacious trimer concentration. The model was translated to the clinic and used to predict the disposition of PF-06671008 in patients. This example showed the utility of a translational QSP model for CD3-bispecific molecules, which integrates in silico, in vitro, and in vivo data in a mechanistic framework to quantify and predict efficacy across species.

The third example[42] illustrated the application of the TMDD model for BsAbs to characterize the relationship between dose and immunological ternary complex (TC) formation that drives the pharmacodynamics and to identify an optimal dose that maximizes formation of TCs. The model includes 4 different binding events for BsAbs, turnover of the targets, and internalization of the complexes. To reduce the number of model parameters, the quasiequilibrium approximation was constructed based on the fundamental assumption of rapid binding during all 4 binding events. The model was further used to investigate the kinetics of BsAb and TC concentrations, and the analysis showed that larger doses of BsAbs may delay the buildup of the TC. Developed BsAb model/approximation can be used to select an optimal dosing strategy. In addition, the BsAb model can aid in optimizing the design of BsAbs and selection of targets.

A PBPK model of lymphocytes was optimized to gain insights into T-cell BsAbs that targeted CD3 on T cells and a tumor antigen in mice.[70] A whole-body PBPK model described the distribution and retargeting of a BsAb, and an effector cell model captured processes controlling lymphocytes in blood, tissues, and tumor compartments.[71] Comparisons between model predictions and experimental data indicated reasonable agreement between lymphocyte AUC values, with highest levels in the tumor, spleen, lymph node, and skin. The results indicated that the lymphocyte trafficking dominated the system and strongly influenced the biodistribution of the BsAb. Sensitivity analysis of the therapeutic index using AUC_{tumor}/AUC_{plasma} ratio showed that adhesion-site density in the tumor vasculature was a critical parameter determining the therapeutic index. Overall, this work shows how to integrate T-cell trafficking into a physiologic model of a bispecific to guide dose and regimen.

The activity of T-cell-redirecting BsAbs is dependent on multiple interrelated factors, and the identification of the desired target product profiles remains a difficult task. A mechanistic PK/PD modeling framework for T-cell-redirecting bispecifics was developed[72] to assist the development of T-cell-redirecting BsAbs. A target-cell biologic-effector cell (TBE) complex-based cell-killing model was developed using in vitro and in vivo data, which incorporates information on binding affinities of BsAbs to CD3 and target receptors, expression of CD3 and target receptors, and concentrations of effector and target cells, as well as the respective physiological parameters. This TBE model can simultaneously evaluate the effect of multiple system-specific and drug-specific factors on the T-cell-redirecting BsAb exposure-response relationship on a physiological basis; it reasonably captured multiple reported in vitro cytotoxicity data and successfully predicted the effect of some key factors on in vitro cytotoxicity assays and the efficacious dose of blinatumomab in humans. The model can be expanded to guide target selection, candidate selection, and clinical dosing regimen projection.

PBPK modeling has been employed to support dose projection for pediatric population of emicizumab, a bispecific humanized mAb that binds activated factor (F) IXa and FX to activate FX, mimicking the function of missing or defective FVIIIa in patients with hemophilia A (PwHA).[73] In this example,[74] the PBPK simulations were carried out to investigate whether a more mechanistic description of age-related differences could improve the confidence in PK projections. Although the predictions remained highly uncertain because of the lack of validation of the PBPK approach for mAbs in pediatrics and the absence of data for the ontogeny of key mechanisms (eg, FcRn), the predictions were provided to the EMA,[75] highlighting that the methodology was not robust enough yet to confidently extrapolate PK in infants. The leverage of different modeling approaches (ie, popPK, PBPK, and exposure-response), together with literature data, led to approval of emicizumab in PwHA with FVIII inhibitors in all age groups in the European Union countries, and EMA acknowledges that modeling and simulation activities were decisive in the approval for patients < 1 year old, even when no clinical data were available.

Management of Risk:Benefit Profile

Of the 2 cases in the category of better managing risk:benefit using PBPK models, both are related to cytokine release syndrome (CRS) on T-cell-engaging BsAb treatment, such as blinatumomab. One case specifically assessed the risk of drug interaction mediated by the pharmacodynamics (ie, transient elevations in cytokine levels) of blinatumomab.[48] This case is of interest because it relates to a drug interaction mediated by therapeutic proteins by downregulation of CYPs as a result of cytokine release, especially of IL-6. Currently, there is limited information on clinical DDIs related to cytokine elevation, as well as relevant PBPK models to predict them. In this case, the potential for cytokine-mediated DDI was predicted based on

data from in vitro hepatocytes incubated with blinatumomab or cytokines and the clinical cytokine profiles. The model predicted little potential for DDI, and as a result of this prediction, no clinical DDI studies were conducted. PBPK modeling has thus proven useful in the development of blinatumomab. A similar modeling approach was successfully applied to understanding the relationship among an inflammation-driven disease rheumatoid arthritis, IL-6, and CYP3A4 activity, suggesting a general utility of PBPK modeling for risk assessment of cytokine-mediated drug interactions.[76]

The other example deals with how to minimize CRS toxicities in the clinic by designing the optimal priming dosing regimen.[47] A "fit-for-purpose" semimechanistic PK/PD model was developed to characterize the cytokine release profiles on T-BsAb treatment, including the priming effect observed with repeated dosing. The model was tailored to account for differences in tumor regression between hematological malignancies and solid tumors to reflect the impact of tumor-cell killing on cytokine release. The model captures the key features of cytokine kinetics with T-BsAb treatment, including the priming effect in which cytokine release was attenuated following repeated doses. It reasonably described the cytokine data for blinatumomab in patients and for P-cadherin LP DART in cynomolgus monkey. The model can be applied in determining optimal dosing strategies for T-BsAb programs to balance risk and benefit.

Emerging Applications of PBPK-PD Modeling in BsAb Development

Intratumoral Biodistribution for Understanding Target Engagement and Predicting Efficacy

Biologics with immunomodulatory potential that alter the immune cells have revolutionized cancer therapy.[77] Major challenges remain in understanding the optimal dose and target receptor occupancy for optimal biological activity, especially in solid tumors. One of the significant challenges is systemic administration, which is the preferred option, but may not be the optimal route of administration. Locoregional delivery of therapeutics by direct intratumoral injection has been proposed as a strategy to bypass the reticuloendothelial system and tumor vasculature barriers. This option could benefit a subset of patients with cancers that spread locally or regionally rather than systemically by treating the primary tumor site to control local cancer invasion. Furthermore, the most therapeutically meaningful sites of action are on the surface of lymphocytes in the lymph nodes closer to already infiltrating the tumor or present in the tumor microenvironment.

Several BsAbs in development are currently being considered in solid tumors with limited yet promising results.[78] For example, catumaxomab, a triomab cotargeting EpCAM/CD3, was approved for the intraperitoneal treatment of malignant ascites in patients with EpCAM-positive cancers.[79]

Determination of the recommended phase 2 dose in oncology immunotherapy is usually not just based on maximum tolerated dose but is usually informed via the totality of data such as pharmacodynamics, safety biomarkers, and efficacy. The advantage of PBPK-PD modeling is that it can potentially aid in the selection of optimal biological dose by accounting for not only drug exposure but also the temporal relationship between PK and biomarkers such as tumoral receptor occupancy and cytokine and T-cell activation data in blood, lymph node, and tumor.

Informing Drug Discovery and Novel Platforms

Novel discoveries and clinical successes pave the way for expanding therapeutic applications in other diseases that had little success. For example, as neuroinflammation becomes ever more deeply implicated in Alzheimer's disease, bispecific therapies targeting this process have entered into clinical trials. For example, Roche recently developed a bispecific transferrin receptor-engineered version of gantenerumab called the brain shuttle.[80] Experimental studies revealed that the effector function of the BsAb is camouflaged when the BsAb is bound to transferrin receptor but fully active when it binds to amyloid, its central nervous system target.

Another novel application of bispecific antibodies that has recently been reported is the clinical efficacy and safety data on faricimab, a novel bispecific antibody targeting angiopoietin and vascular endothelial growth factor-A (VEGF-A) in patients with diabetic macular edema.[81] The bispecific antibody is specifically designed for intraocular use and binds both VEGF-A and angiopoietin-2 with high affinity and specificity. The antibody is engineered to abolish binding interactions to the Fc gamma receptor and FcRn for reduced effector function and faster systemic clearance, providing evidence for the impact of antibody engineering to result in the desired effect on pharmacology of bispecific antibodies.[82]

Chimeric antigen receptor (CAR) T cells, T cells that have been genetically engineered to express a receptor that recognizes a specific antigen, have given rise to breakthroughs in treating hematological malignancies. However, their success in treating solid tumors has been limited. The unique challenges posed to CAR T-cell therapy by solid tumors can be described in 3 steps: finding, entering, and surviving in the tumor. The use of dual CAR designs that recognize multiple antigens at once and local administration of CAR T cells are both strategies that have been used to overcome the

hurdle of localization to the tumor.[83] Application of the PBPK-PD model was very elegantly shown by Singh et al. The authors used the PBPK-PD model to quantitatively inform the CAR-T development by predicting tumor growth inhibition for various CAR-T targets. The authors proposed the translational framework to inform the selection of lead CAR-T constructs and platforms.[84]

Conclusions

Therapeutic applications of BsAbs have evolved significantly in the recent past with significant promise toward future clinical approvals in various therapeutic areas. Here we have attempted to illustrate the available literature evidence of successes in using PBPK-PD modeling in BsAb development and provide a framework for future application of this emerging tool. The application of PBPK-PD modeling is an evolving field and when combined with the growing experience in the development of BsAbs will be a valuable asset to inform the development of BsAbs.

Conflicts of Interest

J.P.G. is an employee of Takeda and owns company stock. T.Y. is an employee of CSL Behring and owns company stock. C.B. is an employee of AbbVie. Y.X. is an employee of Ascentage Pharma Group. S.K. is an employee of AbbVie and owns company stock.

References

1. Raghu G, Richeldi L, Crestani B, et al. SAR156597 in idiopathic pulmonary fibrosis: a phase 2 placebo-controlled study (DRI11772). *Eur Respir J*. 2018;52(6):1801130.
2. Boswell CA, Tesar DB, Mukhyala K, Theil FP, Fielder PJ, Khawli LA. Effects of charge on antibody tissue distribution and pharmacokinetics. *Bioconjug Chem*. 2010;21(12):2153-2163.
3. Ovacik M, Lin K. Tutorial on monoclonal antibody pharmacokinetics and its considerations in early development. *Clin Transl Sci*. 2018;11(6):540-552.
4. Kuepfer L, Niederalt C, Wendl T, et al. Applied concepts in pbpk modeling: how to build a PBPK/PD model. *CPT Pharmacometrics Syst Pharmacol*. 2016;5(10):516-531.
5. Wang Q, Chen Y, Park J, et al. Design and production of bispecific antibodies. *Antibodies (Basel)*. 2019;8(3):43.
6. Zhang X, Yang Y, Fan D, Xiong D. The development of bispecific antibodies and their applications in tumor immune escape. *Exp Hematol Oncol*. 2017;6:12.
7. Ridgway JB, Presta LG, Carter P. "Knobs-into-holes" engineering of antibody CH3 domains for heavy chain heterodimerization. *Protein Eng*. 1996;9(7):617-621.
8. De Nardis C, Hendriks LJA, Poirier E, et al. A new approach for generating bispecific antibodies based on a common light chain format and the stable architecture of human immunoglobulin G1. *J Biol Chem*. 2017;292(35):14706-14717.
9. Klein C, Schaefer W, Regula JT, et al. Engineering therapeutic bispecific antibodies using CrossMab technology. *Methods*. 2019;154:21-31.
10. Jones HM, Rowland-Yeo K. Basic concepts in physiologically based pharmacokinetic modeling in drug discovery and development. *CPT Pharmacometrics Syst Pharmacol*. 2013;2(8):e63.
11. Sager JE, Yu J, Ragueneau-Majlessi I, Isoherranen N. Physiologically based pharmacokinetic (PBPK) modeling and simulation approaches: a systematic review of published models, applications, and model verification. *Drug Metab Dispos*. 2015;43(11):1823-1837.
12. Shebley M, Sandhu P, Emami Riedmaier A, et al. Physiologically based pharmacokinetic model qualification and reporting procedures for regulatory submissions: a consortium perspective. *Clin Pharmacol Ther*. 2018;104(1):88-110.
13. Krüger A, Maltarollo VG, Wenger C, Kronenberger T. ADME profiling in drug discovery and a new path paved on silica. In: Gaitonde V, Karmakar P, Trivedi A, eds. *Drug Discovery Development — New Advances*. London, UK: IntechOpen; 2020.
14. Tsamandouras N, Rostami-Hodjegan A, Aarons L. Combining the 'bottom up' and 'top down' approaches in pharmacokinetic modelling: fitting PBPK models to observed clinical data. *Br J Clin Pharmacol*. 2015;79(1):48-55.
15. Cao Y, Jusko WJ. Applications of minimal physiologically-based pharmacokinetic models. *J Pharmacokinet Pharmacodyn*. 2012;39(6):711-723.
16. Pilari S, Huisinga W. Lumping of physiologically-based pharmacokinetic models and a mechanistic derivation of classical compartmental models. *J Pharmacokinet Pharmacodyn*. 2010;37(4):365-405.
17. Mould DR, Upton RN. Basic concepts in population modeling, simulation, and model-based drug development. *CPT Pharmacometrics Syst Pharmacol*. 2012;1(9):e6.
18. Chen B, Dong JQ, Pan WJ, Ruiz A. Pharmacokinetics/pharmacodynamics model-supported early drug development. *Curr Pharm Biotechnol*. 2012;13(7):1360-1375.
19. Lave T, Caruso A, Parrott N, Walz A. Translational PK/PD modeling to increase probability of success in drug discovery and early development. *Drug Discov Today Technol*. 2016;21-22:27-34.
20. Wong H, Bohnert T, Damian-Iordache V, et al. Translational pharmacokinetic-pharmacodynamic analysis in the pharmaceutical industry: an IQ Consortium PK-PD Discussion Group perspective. *Drug Discov Today*. 2017;22(10):1447-1459.
21. Bradshaw EL, Spilker ME, Zang R, et al. Applications of quantitative systems pharmacology in model-informed drug discovery: perspective on impact and opportunities. *CPT Pharmacometrics Syst Pharmacol*. 2019;8(11):777-791.
22. Rostami-Hodjegan A. Reverse translation in PBPK and QSP: going backwards in order to go forward with confidence. *Clin Pharmacol Ther*. 2018;103(2):224-232.
23. Sorger PK, Allerheiligen SRB, Abernethy DR. Quantitative and systems pharmacology in the post-genomic era: new approaches to discovering drugs and understanding therapeutic mechanisms. An NIH white paper by the QSP workshop group. *NIH Bethesda*. 2011:1-48.
24. van der Graaf PH, Benson N. The role of quantitative systems pharmacology in the design of first-in-human trials. *Clin Pharmacol Ther*. 2018;104(5):797.
25. Jamei M. Where do PBPK models stand in pharmacometrics and systems pharmacology?. *CPT Pharmacometrics Syst Pharmacol*. 2020;9(2):75-76.
26. Jamei M. Recent advances in development and application of physiologically-based pharmacokinetic (PBPK) models: a transition from academic curiosity to regulatory acceptance. *Curr Pharmacol Rep*. 2016;2(3):161-169.

27. Ince I, Solodenko J, Frechen S, et al. Predictive pediatric modeling and simulation using ontogeny information. *J Clin Pharmacol*. 2019;59(Suppl 1):S95-S103.
28. Chetty M, Li L, Rose R, et al. Prediction of the pharmacokinetics, pharmacodynamics, and efficacy of a monoclonal antibody, using a physiologically based pharmacokinetic fcrn model. *Front Immunol*. 2014;5:670.
29. Diao L, Meibohm B. Tools for predicting the PK/PD of therapeutic proteins. *Expert Opin Drug Metab Toxicol* 2015;11(7):1-11.
30. EMA. *Guideline on the Reporting of Physiologically Based Pharmacokinetic (Pbpk) Modelling and Simulation*. Amsterdam, Netherlands: European Medicines Agency; 2018.
31. FDA. *Guidance for Industry: Physiologically Based Pharmacokinetic Analyses—Format and Content*. Silver Spring, Maryland: Food and Drug Administration; 2018.
32. Li L, Gardner I, Rose R, Jamei M. Incorporating target shedding into a minimal PBPK-TMDD model for monoclonal antibodies. *CPT Pharmacometrics Syst Pharmacol*. 2014;3(1):e96.
33. Glassman PM, Balthasar JP. Physiologically-based modeling of monoclonal antibody pharmacokinetics in drug discovery and development. *Drug Metab Pharmacokinet*. 2019;34(1):3-13.
34. Glassman PM, Balthasar JP. Physiologically-based pharmacokinetic modeling to predict the clinical pharmacokinetics of monoclonal antibodies. *J Pharmacokinet Pharmacodyn*. 2016;43(4):427-446.
35. Niederalt C, Kuepfer L, Solodenko J, et al. A generic whole body physiologically based pharmacokinetic model for therapeutic proteins in PK-Sim. *J Pharmacokinet Pharmacodyn*. 2018;45(2):235-257.
36. Shah DK, Betts AM. Towards a platform PBPK model to characterize the plasma and tissue disposition of monoclonal antibodies in preclinical species and human. *J Pharmacokinet Pharmacodyn*. 2012;39(1):67-86.
37. Wong H, Chow TW. Physiologically based pharmacokinetic modeling of therapeutic proteins. *J Pharm Sci*. 2017;106(9):2270-2275.
38. Richter WF, Bhansali SG, Morris ME. Mechanistic determinants of biotherapeutics absorption following SC administration. *AAPS J*. 2012;14(3):559-570.
39. Rippe B, Haraldsson B. Transport of macromolecules across microvascular walls: the two-pore theory. *Physiological Rev*. 1994;74(1):163-219.
40. Chudasama VL, Zutshi A, Singh P, Abraham AK, Mager DE, Harrold JM. Simulations of site-specific target-mediated pharmacokinetic models for guiding the development of bispecific antibodies. *J Pharmacokinet Pharmacodyn*. 2015;42(1):1-18.
41. Rhoden JJ, Dyas GL, Wroblewski VJ. A modeling and experimental investigation of the effects of antigen density, binding affinity, and antigen expression ratio on bispecific antibody binding to cell surface targets. *J Biol Chem*. 2016;291(21):11337-11347.
42. Schropp J, Khot A, Shah DK, Koch G. Target-mediated drug disposition model for bispecific antibodies: properties, approximation, and optimal dosing strategy. *CPT Pharmacometrics Syst Pharmacol*. 2019;8(3):177-187.
43. Kareva I, Zutshi A, Kabilan S. Guiding principles for mechanistic modeling of bispecific antibodies. *Prog Biophys Mol Biol*. 2018;139:59-72.
44. Tiwari A, Abraham AK, Harrold JM, Zutshi A, Singh P. Optimal affinity of a monoclonal antibody: guiding principles using mechanistic modeling. *AAPS J*. 2017;19(2):510-519.
45. Wu Z, Cheung NV. T cell engaging bispecific antibody (T-BsAb): from technology to therapeutics. *Pharmacol Ther*. 2018;182:161-175.
46. Lee DW, Gardner R, Mackall CL. Current concepts in the diagnosis and management of cytokine release syndrome. *Blood*. 2014;124(2):188-195.
47. Chen X, Kamperschroer C, Wong G, Xuan D. A modeling framework to characterize cytokine release upon t-cell-engaging bispecific antibody treatment: methodology and opportunities. *Clin Transl Sci*. 2019;12(6):600-608.
48. Xu Y, Hijazi Y, Wolf A, Wu B, Sun YN, Zhu M. Physiologically based pharmacokinetic model to assess the influence of blinatumomab-mediated cytokine elevations on cytochrome P450 enzyme activity. *CPT Pharmacometrics Syst Pharmacol*. 2015;4(9):507-515.
49. Manicourt D, Triki R, Fukuda K, Devogelaer J, Deuxchaisnes C, Thonar E. Levels of circulating tumor necrosis factor alpha and interleukin-6 in patients with rheumatoid arthritis. Relationship to serum levels of hyaluronan and antigenic keratan sulfate. *Arthritis Rheum*. 1993;36(4):490-499.
50. Bal A, Unlu E, Bahar G, Aydog E, Eksioglu E, Yorgancioglu R. Comparison of serum IL-1 beta, sIL-2R, IL-6, and TNF-alpha levels with disease activity parameters in ankylosing spondylitis. *Clin Rheumatol*. 2007;26(2):211-215.
51. Korolkova OY, Myers JN, Pellom ST, Wang L, M'Koma AE. Characterization of serum cytokine profile in predominantly colonic inflammatory bowel disease to delineate ulcerative and crohn's colitides. *Clin Med Insights Gastroenterol*. 2015;8:29-44.
52. Arican O, Aral M, Sasmaz S, Ciragil P. Serum levels of TNF-alpha, IFN-gamma, IL-6, IL-8, IL-12, IL-17, and IL-18 in patients with active psoriasis and correlation with disease severity. *Mediators Inflamm*. 2005;2005(5):273-279.
53. Olsen T, Goll R, Cui G, et al. Tissue levels of tumor necrosis factor-alpha correlates with grade of inflammation in untreated ulcerative colitis. *Scand J Gastroenterol*. 2007;42(11):1312-1320.
54. Olszewski WL, Pazdur J, Kubasiewicz E, Zaleska M, Cooke C, Miller N. Lymph draining from foot joints in rheumatoid arthritis provides insight into local cytokine and chemokine production and transport to lymph nodes. *Arthritis Rheumatism*. 2001;44(3):541-549.
55. Malik PRV, Edginton AN. Physiologically-based pharmacokinetic modeling vs. allometric scaling for the prediction of infliximab pharmacokinetics in pediatric patients. *CPT Pharmacometrics Syst Pharmacol*. 2019;8(11):835-844.
56. Chen X, DuBois DC, Almon RR, Jusko WJ. Biodistribution of etanercept to tissues and sites of inflammation in arthritic rats. *Drug Metab Dispos*. 2015;43(6):898-907.
57. Chen X, Jiang X, Jusko WJ, Zhou H, Wang W. Minimal physiologically-based pharmacokinetic (mPBPK) model for a monoclonal antibody against interleukin-6 in mice with collagen-induced arthritis. *J Pharmacokinet Pharmacodyn*. 2016;43(3):291-304.
58. Li X, Jusko WJ, Cao Y. Role of interstitial fluid turnover on target suppression by therapeutic biologics using a minimal physiologically based pharmacokinetic model. *J Pharmacol Exp Ther*. 2018;367(1):1-8.
59. Zheng S. Characterizing colon tnfα suppression and treatment effects of an anti-Tnfα monoclonal antibody in a mouse inflammatory bowel disease model: questions and solutions for a next generation pharmacometrician. ASCPT Webinar Series (Systems Pharmacology and Early Career Communities). https://www.ascpt.org/Portals/28/docs/Membership/Networks%20and%20Communities/Early%20Career/EC%20SP%20Jan%20Webinar%20Slides.pdf?ver=2020-02-05-071152-167. Accessed March 2020.
60. Chen X, Jiang X, Doddareddy R, et al. Development and translational application of a minimal physiologically based pharmacokinetic model for a monoclonal antibody against

interleukin 23 (IL-23) in IL-23-induced psoriasis-like mice. *J Pharmacol Exp Ther*. 2018;365(1):140-155.
61. Dowlatshahi EA, van der Voort EA, Arends LR, Nijsten T. Markers of systemic inflammation in psoriasis: a systematic review and meta-analysis. *Br J Dermatol*. 2013;169(2):266-282.
62. Kishimoto T. IL-6: from its discovery to clinical applications. *Int Immunol*. 2010;22(5):347-352.
63. Gao SP, Mark KG, Leslie K, et al. Mutations in the EGFR kinase domain mediate STAT3 activation via IL-6 production in human lung adenocarcinomas. *J Clin Invest*. 2007;117(12):3846-3856.
64. Morgan ET. Impact of infectious and inflammatory disease on cytochrome P450-mediated drug metabolism and pharmacokinetics. *Clin Pharmacol Ther*. 2009;85(4):434-438.
65. Jiang X, Zhuang Y, Xu Z, Wang W, Zhou H. Development of a physiologically based pharmacokinetic model to predict disease-mediated therapeutic protein-drug interactions: modulation of multiple cytochrome P450 enzymes by interleukin-6. *AAPS J*. 2016;18(3):767-776.
66. van Steeg TJ, Bergmann KR, Dimasi N, Sachsenmeier KF, Agoram B. The application of mathematical modelling to the design of bispecific monoclonal antibodies. *MAbs*. 2016;8(3):585-592.
67. Sengers BG, McGinty S, Nouri FZ, et al. Modeling bispecific monoclonal antibody interaction with two cell membrane targets indicates the importance of surface diffusion. *MAbs*. 2016;8(5):905-915.
68. Chen X, Haddish-Berhane N, Moore P, et al. Mechanistic projection of first-in-human dose for bispecific immunomodulatory P-Cadherin LP-DART: an integrated PK/PD modeling approach. *Clin Pharmacol Ther*. 2016;100(3):232-241.
69. Betts A, Haddish-Berhane N, Shah DK, et al. A translational quantitative systems pharmacology model for CD3 bispecific molecules: application to quantify t cell-mediated tumor cell killing by P-Cadherin LP DART((R)). *AAPS J*. 2019;21(4):66.
70. Friedrich SW, Lin SC, Stoll BR, Baxter LT, Munn LL, Jain RK. Antibody-directed effector cell therapy of tumors: analysis and optimization using a physiologically based pharmacokinetic model. *Neoplasia*. 2002;4(5):449-463.
71. Zhu H, Melder RJ, Baxter LT, Jain RK. Physiologically based kinetic model of effector cell biodistribution in mammals: implications for adoptive immunotherapy. *Cancer Res*. 1996;56(16):3771-3781.
72. Jiang X, Chen X, Carpenter TJ, et al. Development of a Target cell-Biologics-Effector cell (TBE) complex-based cell killing model to characterize target cell depletion by T cell redirecting bispecific agents. *MAbs*. 2018;10(6):876-889.
73. Shima M, Hanabusa H, Taki M, et al. Factor VIII-mimetic function of humanized bispecific antibody in hemophilia A. *N Engl J Med*. 2016;374(21):2044-2053.
74. Retout S, Grimm H-P, Petry C, Schmitt C, Frey N. A model-based extrapolation enabled labelling of emicizumab in haemophilia A paediatric patients <1 year old despite lack of clinical data. https://www.page-meeting.org/default.asp?abstract=9089. Accessed April 7, 2020.
75. EMA. Assessment report. EMA/88475/2018. 2018; Procedure No. EMEA/H/C/004406/0000. https://www.ema.europa.eu/en/documents/assessment-report/hemlibra-epar-public-assessment-report_en.pdf. Accessed March 2020.
76. Machavaram KK, Almond LM, Rostami-Hodjegan A, et al. A physiologically based pharmacokinetic modeling approach to predict disease-drug interactions: suppression of CYP3A by IL-6. *Clin Pharmacol Ther*. 2013;94(2):260-268.
77. Sharma P, Allison JP. The future ofimmune checkpoint therapy. *Cancer Immunol Immunotherapy*. 2015;348(6230):56-61.
78. Yu S, Li A, Liu Q, et al. Recent advances of bispecific antibodies in solid tumors. *J Hematol Oncol*. 2017;10(1):155.
79. Goere D, Flament C, Rusakiewicz S, et al. Potent immunomodulatory effects of the trifunctional antibody catumaxomab. *Cancer Res*. 2013;73(15):4663-4673.
80. Niewoehner J, Bohrmann B, Collin L, et al. Increased brain penetration and potency of a therapeutic antibody using a monovalent molecular shuttle. *Neuron*. 2014;81(1):49-60.
81. Sahni J, Patel SS, Dugel PU, et al. Simultaneous inhibition of angiopoietin-2 and vascular endothelial growth factor-A with faricimab in diabetic macular edema: BOULEVARD Phase 2 Randomized Trial. *Ophthalmology*. 2019;126(8):1155-1170.
82. Regula JT, Lundh von Leithner P, Foxton R, et al. Targeting key angiogenic pathways with a bispecific CrossMAb optimized for neovascular eye diseases. *EMBO Mol Med*. 2016;8(11):1265-1288.
83. Martinez M, Moon EK. CAR T cells for solid tumors: new strategies for finding, infiltrating, and surviving in the tumor microenvironment. *Front Immunol*. 2019;10:128.
84. Singh AP, Zheng X, Lin-Schmidt X, et al. Development of a quantitative relationship between CAR-affinity, antigen abundance, tumor cell depletion and CAR-T cell expansion using a multiscale systems PK-PD model. *MAbs*. 2020;12(1):1688616.

ADVANCED MATERIALS
www.advmat.de

Directed Evolution Enables Simultaneous Controlled Release of Multiple Therapeutic Proteins from Biopolymer-Based Hydrogels

*Carter J. Teal, Marian H. Hettiaratchi, Margaret T. Ho, Arturo Ortin-Martinez, Ahil N. Ganesh, Andrew J. Pickering, Alex W. Golinski, Benjamin J. Hackel, Valerie A. Wallace, and Molly S. Shoichet**

With the advent of increasingly complex combination strategies of biologics, independent control over their delivery is the key to their efficacy; however, current approaches are hindered by the limited independent tunability of their release rates. To overcome these limitations, directed evolution is used to engineer highly specific, low affinity affibody binding partners to multiple therapeutic proteins to independently control protein release rates. As a proof-of-concept, specific affibody binding partners for two proteins with broad therapeutic utility: insulin-like growth factor-1 (IGF-1) and pigment epithelium-derived factor (PEDF) are identified. Protein–affibody binding interactions specific to these target proteins with equilibrium dissociation constants (K_D) between 10^{-7} and 10^{-8} M are discovered. The affibodies are covalently bound to the backbone of crosslinked hydrogels using click chemistry, enabling sustained, independent, and simultaneous release of bioactive IGF-1 and PEDF over 7 days. The system is tested with C57BL/6J mice in vivo, and the affibody-controlled release of IGF-1 results in sustained activity when compared to bolus IGF-1 delivery. This work demonstrates a new, broadly applicable approach to tune the release of therapeutic proteins simultaneously and independently and thus the way for precise control over the delivery of multicomponent therapies is paved.

1. Introduction

Therapeutic proteins offer significant advantages over small molecule drugs because they modulate biomolecular pathways to treat disease in ways that small molecules cannot. Sustained delivery of therapeutic proteins can improve patient compliance, minimize toxicity associated with high drug concentrations, and prolong their effect in the body. However, most controlled release strategies were developed for use with small molecule drugs and are not compatible with proteins. Encapsulation within nanoparticles typically involves exposure to high shear stresses and organic solvents, which result in protein denaturation.[1,2] Covalent tethering of therapeutic proteins to biomaterials may interfere with receptor binding interactions and mask catalytic sites required for bioactivity.[3,4] Strategies that rely on physical properties of a material to mediate protein releases, such as matrix

C. J. Teal, M. T. Ho, M. S. Shoichet
Institute of Biomedical Engineering
164 College Street, Toronto, ON M5S 3G9, Canada
E-mail: molly.shoichet@utoronto.ca

C. J. Teal, M. H. Hettiaratchi, M. T. Ho, A. N. Ganesh, A. J. Pickering, M. S. Shoichet
Terrence Donnelly Centre for Cellular and Biomolecular Research
University of Toronto
160 College Street, Toronto, ON M5S 3E1, Canada

M. H. Hettiaratchi, A. N. Ganesh, A. J. Pickering, M. S. Shoichet
Department of Chemical Engineering and Applied Chemistry
University of Toronto
200 College Street, Toronto, ON M5S 3E5, Canada

A. Ortin-Martinez, V. A. Wallace
Donald K. Johnson Eye Institute
Krembil Research Institute
University Health Network
399 Bathurst Street, Toronto, ON M5T 2S8, Canada

The ORCID identification number(s) for the author(s) of this article can be found under https://doi.org/10.1002/adma.202202612.

A. W. Golinski, B. J. Hackel
Department of Chemical Engineering and Materials Science
University of Minnesota–Twin Cities
421 Washington Avenue Southeast, 356 Amundson Hall, Minneapolis, MN 55455, USA

V. A. Wallace
Department of Laboratory Medicine and Pathobiology
University of Toronto
27 King's College Circle, Toronto, ON M5S 1A1, Canada

V. A. Wallace, M. S. Shoichet
Department of Ophthalmology and Vision Sciences
University of Toronto
340 College Street, Toronto, ON M5T 3A9, Canada

M. S. Shoichet
Department of Chemistry
University of Toronto
80 St. George Street, Toronto, ON M5S 3H6, Canada

DOI: 10.1002/adma.202202612

degradation or polymer crosslinking density, result in unpredictable, accelerated protein release in vivo.[1,5]

Affinity-controlled release strategies minimize protein degradation through incorporation of therapeutic proteins into biomaterials that modulate protein release through non-covalent, reversible interactions. Early affinity-controlled protein release strategies relied on native interactions with heparin and other extracellular matrix (ECM) molecules.[6] However, heparin–protein interactions are inherently non-specific, limited to select proteins, and difficult to modify to tune protein release rates.[7–9] As a result, synthetic affinity interactions have been engineered between proteins and materials to control the release of a broader range of therapeutics. For example, fusion proteins have been expressed with either ECM-binding domains in order to mimic naturally occurring affinity interactions[10–13] or with other small protein domains with affinity for known binding peptides (e.g., Src homology 3)[14,15] to facilitate controlled release from ECM-based or peptide-containing biomaterials. While these strategies enable tunable release of a wide range of proteins that do not have an inherent affinity for natural or synthetic biomaterials, they require challenging recombinant expression and do not allow independently tunable release of multiple proteins.

Combining multiple proteins into a single therapeutic strategy can offer significant advantages over single component therapies, but require sophisticated delivery systems. For example, sequential delivery of proteins has been achieved by combining different release mechanisms, through layer-by-layer degradation of a composite material, or use of stimuli responsive biomaterials.[16–20] Recent research has highlighted the importance of not only temporal control, but rate of protein release. For example, co-delivery of bone morphogenetic protein-2 (BMP-2) and platelet-derived growth factor (PDGF) with different release kinetics achieved robust bone regeneration only if the burst release of PDGF was followed by sustained release of BMP-2, but not if both therapeutics were released simultaneously or individually.[21] Moreover, Anderson and co-workers demonstrated improved axonal outgrowth across spinal cord lesions by the combined, staggered delivery of viral vectors before injury and recombinant proteins after injury.[22] Notably, the most effective treatment condition had all six therapeutic proteins delivered.

We were interested in co-delivery of two therapeutic proteins of broad interest: insulin-like growth factor-1 (IGF-1) and pigment epithelium-derived factor (PEDF). IGF-1 is a small, 7.6 kDa, positively-charged protein at physiological pH (pI = 7.76) whereas PEDF is a larger, 45 kDa, negatively-charged protein (pI = 5.97). IGF-1, a potent mitogenic protein, has shown promising results in pre-clinical trials by reducing lesion volumes after stroke[23] and improving cardiac function after congestive heart failure.[24] PEDF, an anti-angiogenic protein, has demonstrated success in treating a wide variety of cancers in pre-clinical studies through its ability to inhibit tumor blood vessel growth.[25–27] Moreover, IGF-1 and PEDF have significant therapeutic potential in retinal degenerative diseases,[28–31] and co-delivery of these factors together may have a synergistic therapeutic effect.

We wanted to create a system which enabled independently tunable and simultaneous controlled release of multiple therapeutic proteins. To achieve this, we utilized affibody proteins. Affibodies are derived from the B-domain of the immunoglobulin-binding region of staphylococcal protein A.[32] Affibodies have similar molecular recognition properties as antibodies, but are much smaller in size (less than 10 kDa vs over 150 kDa). Furthermore, they have greater specificity for target proteins than peptides and their bacterial origin enables high-yield expression and purification from *Escherichia coli*. Affibodies lack any native cysteine residues, enabling plasmid constructs to be engineered with N- or C-terminal cysteines for simple chemical modification via Michael-type addition.[32–34] Thus, affibodies are ideal for immobilization within a hydrogel drug delivery vehicle using click chemistry.

We used directed evolution to develop affibodies with low, but specific affinities for our target therapeutic proteins of interest. Similar to affinity maturation, in which B cells create antibodies with increasing affinity for a particular antigen,[35] directed evolution has enabled the development of affibodies with high affinities for target proteins through iterative rounds of affibody gene diversification and screening using display technologies. Each round of library diversification and screening yields increasingly stronger interactions between binding partners.[36] This approach previously enabled the discovery of an affibody protein with a picomolar ($K_D \approx 10^{-12}$ M) affinity to human epidermal growth factor receptor 2, a cancer marker, after five rounds of evolution.[37] Since we were interested in low affinity binding partners for controlled release, we limited our diversification and screening process to one round. We aimed to isolate affibody binding partners with dissociation constants between $K_D \approx 10^{-6}$ to 10^{-9} M, which is similar to affinities used in other controlled release systems.[6,14,38] There are several display platforms for protein engineering including tethering protein variants to ribosomes, mRNA, DNA, phages, bacteria, mammalian, or insect cells.[15] While these other techniques could be used to identify low affinity binding partners, yeast surface display has several advantages.[16] Most strikingly for the current work, yeast display enables fine affinity quantification and stratification by FACS, enabling recovery of affibody mutants with precise affinity to the target of interest.[17] Moreover, display of thousands of protein replicates per yeast along with multivalent target presentation (via bead immobilization[39] or avidin tetramerization of biotinylated target[40]) enables highly avid selections to enrich binders of moderate affinity for controlled release. Also, yeast are easy to manipulate compared to other eukaryotic display systems and can incorporate post-translational modifications into displayed proteins.

To demonstrate the broad utility of affibody-controlled release with different biomaterial matrices, we immobilized them into three different hydrogel drug delivery vehicles. We modified affibodies with a methyltetrazine (Tz) functional group and used inverse electron Diels–Alder (IEDDA) chemistry to immobilize them onto two different biopolymers (methylcellulose, MC, and hyaluronan, HA) with norbornene (Nb) functional groups. The IEDDA reaction occurs spontaneously under physiological conditions, minimizing protein denaturation. For our in vitro experiments, we then used the same tetrazine–norbornene click chemistry to produce crosslinked MCxMC and HAxHA hydrogels which are stable for at least 28 days.[41,42] For our in vivo experiments, we took our MC modified with affibodies and created

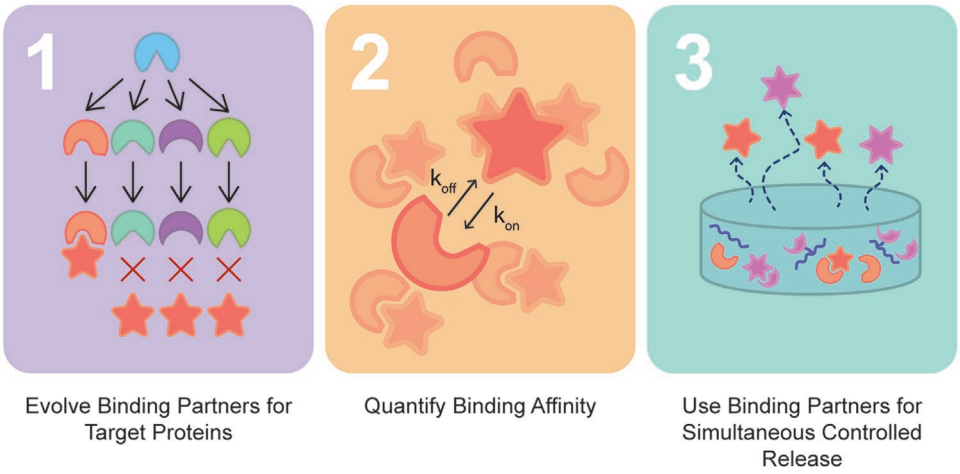

Figure 1. Pipeline for identifying affibody binding partners for controlled release. 1) An affibody library of 10^8 genetic variants was screened using yeast for binders to target therapeutic proteins. 2) Single yeast clones that bound to the target protein were isolated and the dissociation equilibrium constant was measured. 3) Binding partners were immobilized within hydrogels for independent, simultaneous controlled release of target therapeutic proteins.

a physical blend with HA to form our HAMC hydrogel, which forms physical crosslinks at physiological temperatures. HAMC has previously been shown to be biocompatible, and has been used deliver therapeutic proteins to the retina.[43] Thus, we demonstrate the versatility of our system for different applications.

In this work, we used directed evolution in a completely new way—that is to identify affibody binding partners to each of IGF-1 and PEDF, with low, but specific affinities for each target protein to enable controlled release. We evolved binding partners to our target proteins, quantified their binding affinities, and incorporated them into our hydrogel delivery vehicles (**Figure 1**). We then simultaneously and independently controlled the release of each of IGF-1 and PEDF and demonstrated bioactive release in vitro with both and in vivo with IGF-1.

2. Results

Magnetic activated cell sorting (MACS) was first used to enrich for affibody binding partners to either IGF-1 or PEDF. After four rounds of MACS, the enriched populations were sorted by fluorescence activated cell sorting (FACS). Yeast that were double positive for both expressed affibody and immobilized target protein were present in the top right quadrant (**Figure 2**A). Flow cytometry analysis showed 12.0% (Figure S1, Supporting Information) binding to IGF-1 and 14.4% (Figure S2, Supporting Information) binding to PEDF after normalizing to all yeast displaying affibodies on their surface. FACS was performed to select yeast cells that bound to the target protein with low affinity determined from target binding normalized by affibody expression (Figure S3, Supporting Information, red gates). Individual yeast clones that frequently occurred in each enriched population were isolated for further analysis. Analysis by flow cytometry demonstrated that each yeast clone displayed high specificity for its respective target protein. We identified two affibodies of interest from our initial library. The IGF-1-binding clone, AEAKYTKEWYAAALEIASLPNLTGYQKDAFNYALLNDPSQSSELLSEAKKLNDSQAPK, displayed high binding to IGF-1 (62.6% of yeast normalized to all yeast displaying affibodies bound to 1×10^{-6} M of IGF-1) (Figure 2B) and negligible binding to both the no target and PEDF controls (Figure 2C,D), demonstrating high specificity to IGF-1. Similarly, the PEDF-binding clone, AEAKYYKELDTAILSIWSLPNLTDSQVLAFVLALYDDPSQSSELLSEAKKLNDSQAPK, displayed high binding to PEDF (71.3% of yeast normalized to all yeast displaying affibodies bound to 1×10^{-6} M PEDF) (Figure 2E) and minimal binding to the no target and IGF-1 controls (Figure 2F,G), demonstrating high specificity to PEDF.

We characterized the affinity interactions between target proteins and soluble, recombinant-expressed affibodies. Genes coding for affibody proteins were ligated into pET28b+ plasmids and flanked by sequences coding for hexahistidine (H_6) and strep (WSHPQFEK) purification tags, as well as a C-terminal cysteine for downstream chemical modification (Figure S4A, Supporting Information). Affibodies expressed in *E. coli* were approximately 8.6 kDa, as indicated by SDS PAGE (Figure S4B, Supporting Information) and mass spectrometry (Figure S4C, Supporting Information). The C-terminal cysteine of the affibody was modified with methyltetrazine-maleimide for site-specific conjugation to MC-Nb and HA-Nb polymers. After modification with methyltetrazine-maleimide, affibody molecular weight increased from 8.6 to 9.1 kDa, confirming the addition of a single functional group (Figure S4D, Supporting Information). Importantly, the modified affibody maintained an alpha-helical structure, as determined by circular dichroism (CD; Figure S4E, Supporting Information). We used biolayer interferometry (BLI) to quantify binding interactions between affibodies that bind to either IGF-1 or PEDF (Figure 2H). The IGF-1-binding affibody bound to IGF-1 with a dissociation constant (K_D) of $2.94 \pm 0.39 \times 10^{-7}$ M, a binding constant (k_{on}) of $4.3 \pm 0.40 \times 10^4$ $M^{-1}s^{-1}$, and an unbinding constant (k_{off}) of $1.25 \pm 0.39 \times 10^{-2}$ s^{-1}, indicating fast on- and fast off-rates. The IGF-1-binding affibody bound to soluble IGF-1 (Figure 2I), with no significant binding to soluble PEDF (Figure 2J).The PEDF-binding affibody bound to PEDF with a K_D of $2.99 \pm 0.95 \times 10^{-8}$ M, k_{on} of $4.28 \pm 0.89 \times 10^3$ $M^{-1}s^{-1}$, and k_{off} of $1.22 \pm 0.21 \times 10^{-4}$ s^{-1},

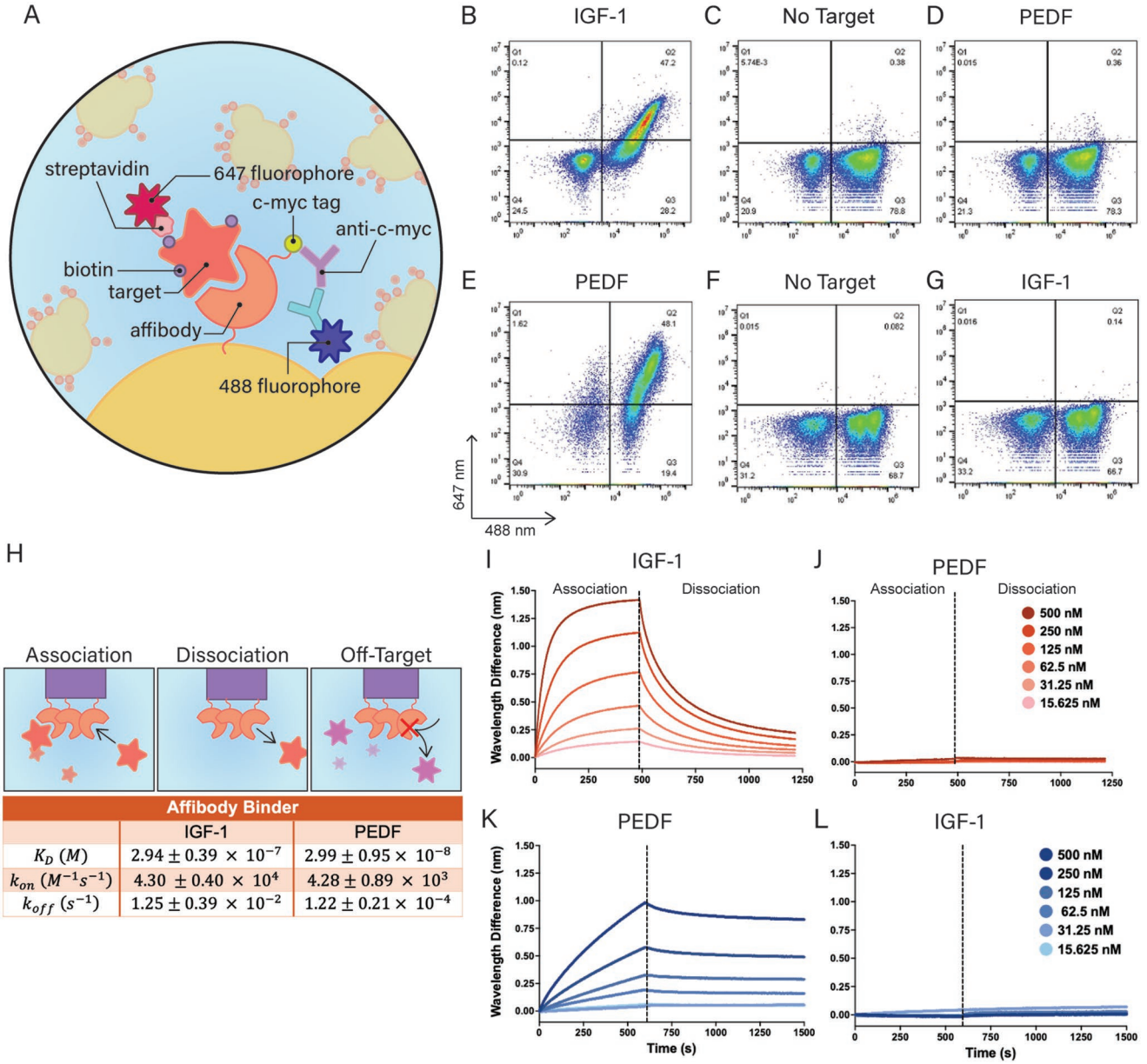

Affibody Binder		
	IGF-1	PEDF
K_D (M)	$2.94 \pm 0.39 \times 10^{-7}$	$2.99 \pm 0.95 \times 10^{-8}$
k_{on} $(M^{-1}s^{-1})$	$4.30 \pm 0.40 \times 10^{4}$	$4.28 \pm 0.89 \times 10^{3}$
k_{off} (s^{-1})	$1.25 \pm 0.39 \times 10^{-2}$	$1.22 \pm 0.21 \times 10^{-4}$

Figure 2. Directed evolution identifies unique affibody binding partners for IGF-1 and PEDF. A) Affibody proteins were expressed with a c-myc peptide tag at their C-terminus. Primary antibodies bound to the tag, ensuring full expression of the protein, followed by a secondary conjugated to Alexa Fluor 488. Target proteins were modified with biotin on their surface. After incubating the target protein with the yeast, a streptavidin conjugated to Alexa Fluor 647 bound to the biotin on the target. B–D) Yeast displaying 488-labeled-IGF-1 affibody incubated with 647-labeled-IGF-1 (B), no target protein (C), and 647-labeled-PEDF (D). E–G) Yeast displaying 488-labeled-PEDF affibody incubated with 647-labeled-PEDF (E), no target protein (F), and 488-labeled-IGF-1 (G). H) Biolayer interferometry measured association and dissociation between affibodies and their target proteins through changes in the interference pattern of reflected white light, enabling quantification of the equilibrium dissociation constant (K_D) that governs release. I,J) Target protein biolayer interferometry data of binding between 200×10^{-12} M of soluble IGF-1 affibody and 15.625 to 500×10^{-9} M of IGF-1 (I) or off-target 15.625 to 500×10^{-9} M of PEDF (J). K) Target protein biolayer interferometry of binding between 200×10^{-12} M of soluble PEDF affibody and 15.625 to 500×10^{-9} M of PEDF. L) Off-target biolayer interferometry of binding between 200×10^{-12} M of soluble PEDF affibody and 15.625 to 500×10^{-9} M of IGF-1.

indicating both slower binding and slower release than that observed with IGF-1 and its affibody binding partner. The PEDF-binding affibody bound to soluble PEDF (Figure 2K), but not to soluble IGF-1 (Figure 2L).

The substitution reactions of MC and HA with methyltetrazine and Nb were confirmed by ^{1}H NMR and UV–vis spectrophotometry. For MC, there were 0.12 mmol Nb per gram of MC and 0.09 mmol methyltetrazine per gram MC (Figure S5, Supporting Information). For HA, there were 1.61 mmol Nb per gram of HA and 1.17 mmol methyltetrazine per gram of HA (Figure S6, Supporting Information). While isomerism can impact the rate of reaction between tetrazine and Nb

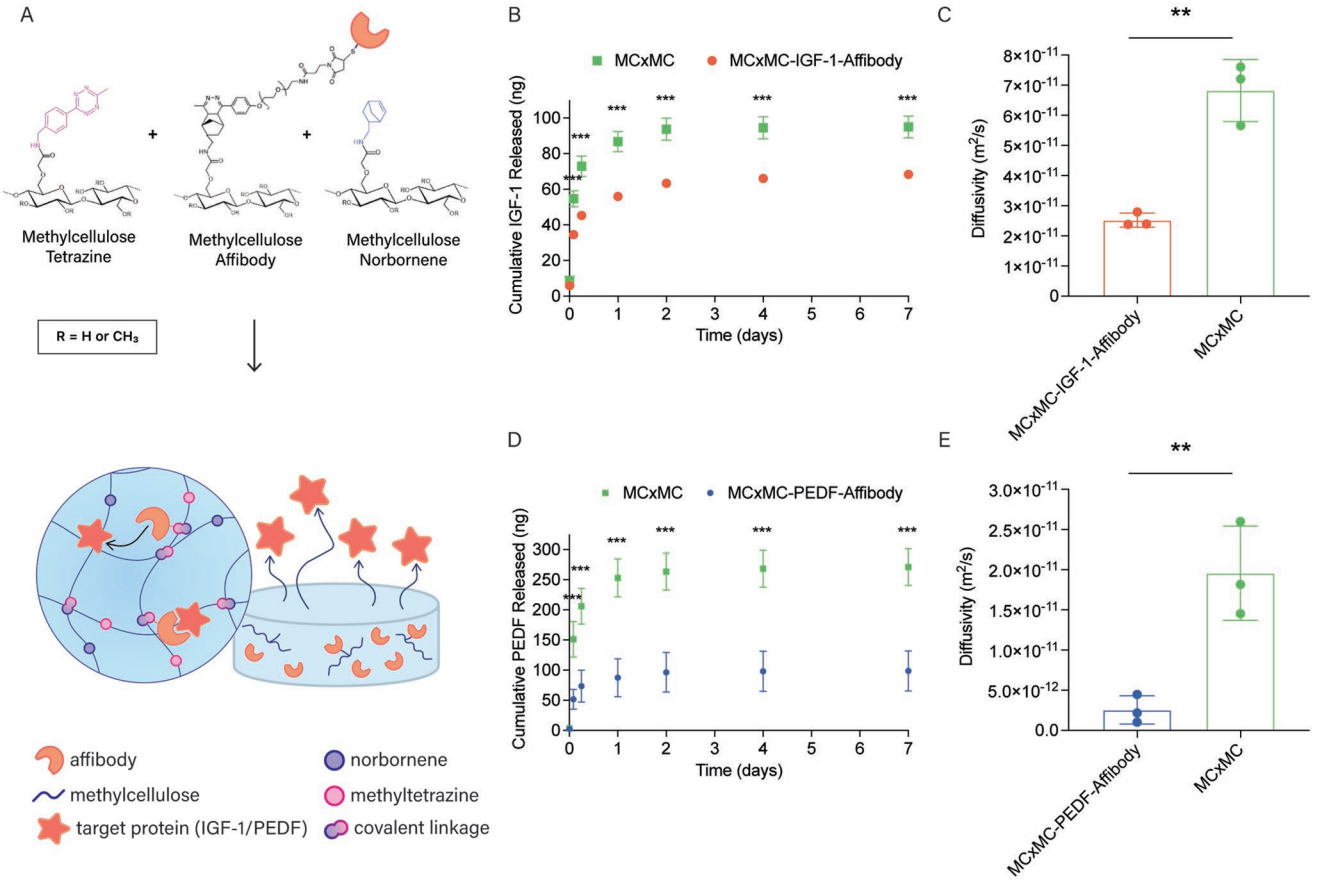

Figure 3. Affibody binding partners enable release of a single protein from hydrogels. A) 1% w/v MC hydrogels were synthesized from MC-norbornene, MC-methyltetrazine, and either MC-IGF1-affibody or MC-PEDF-affibody using IEDDA click chemistry. 12.5 pmol of either IGF-1 or PEDF and 1250 pmol (1.25 nmol) of either IGF-1 or PEDF affibodies were incorporated in each hydrogel. B) Release of IGF-1 over 7 days from MCxMC versus MCxMC-IGF1-affibody ($n = 3$, mean ± standard deviation (sd) plotted, two-way analysis of variance (ANOVA), Bonferroni's post-hoc test, $^{***}p < 0.001$). C) IGF-1 diffusivity through the hydrogel, calculated using the short-time approximation for Fickian diffusion from a thin polymer slab from (B) (unpaired, two-tailed, mean ± sd plotted, Student's *t*-test, $^{**}p < 0.01$). D) Release of PEDF over 7 days from MCxMC versus MCxMC-PEDF-affibody ($n = 3$, mean ± sd plotted, two-way ANOVA, Bonferroni's post-hoc test, $^{*}p < 0.05$, $^{**}p < 0.01$, $^{***}p < 0.001$). E) PEDF diffusivity through the hydrogel, calculated using the short-time approximation for Fickian diffusion from a thin polymer slab from (D) ($n = 3$, mean ± sd plotted, unpaired, two-tailed, Student's *t*-test, $^{**}p < 0.01$).

functional groups, these hydrogels have shown tunable gelation times and are minimally swelling and stable for at least 28 days in vitro.[41,42,44] Conjugation of affibodies to each of MC and HA resulted in 1.90 ± 0.41 nmol affibody mg^{-1} MC and 3.6 ± 1.8 nmol affibody mg^{-1} HA.

We first investigated the release of each of IGF-1 and PEDF from 1% w/v MCxMC hydrogels, using a 100-fold molar excess of immobilized affibody to protein. Specifically, MCxMC hydrogels had 1250 pmol of affibody immobilized to control the release of 12.5 pmol of each protein (96 ng IGF-1, 557 ng PEDF) (**Figure 3**A). The release profile of IGF-1 from MCxMC hydrogels modified with IGF1-affibodies (MCxMC-IGF1-affibody) was extended relative to unmodified MCxMC (Figure 3B). To compare the release rates, we calculated the effective diffusivity of the protein through the gel using a short-time approximation for unidirectional diffusion from a plane sheet. The diffusivity of IGF-1 from MCxMC of 6.82 ± 1.03 × 10^{-11} s^{-1} was significantly reduced in the presence of IGF-1 affibodies to 2.52 ± 2.34 × 10^{-11} s^{-1} (Figure 3C). Similarly, the release profiles of PEDF from unmodified MCxMC were slowed from MCxMC-PEDF-affibody hydrogels (Figure 3D); and the diffusivity of PEDF from MCxMC of 1.69 ± 0.56 × 10^{-11} m^2 s^{-1} was reduced to 2.55 ± 1.76 × 10^{-12} m^2 s^{-1} from MCxMC-PEDF-affibody hydrogels (Figure 3E).

To demonstrate the versatility and ultimate utility of our system, we next investigated the dual, simultaneous release of IGF-1 and PEDF from HAxHA hydrogels (**Figure 4**A). We confirmed that protein release from HAxHA hydrogels was only affected by the corresponding affibody (Figure 4B–F). IGF-1 release from HAxHA-IGF1-affibody hydrogels was attenuated with 100 times excess IGF-1 affibody binding partner, but not from HAxHA-PEDF-affibody hydrogels with 100 times excess of PEDF affibody binding partner. In fact, the release from the latter was like IGF-1 released from HAxHA hydrogels without binding partners (Figure S8, Supporting Information). For dual protein delivery, we tuned protein release rates by changing the amount of affibody in the hydrogel while keeping the amount of each protein constant at 12.5 pmol, such that five hydrogels were evaluated. Hydrogels with different ratios of affibodies for IGF-1 and PEDF displayed significantly

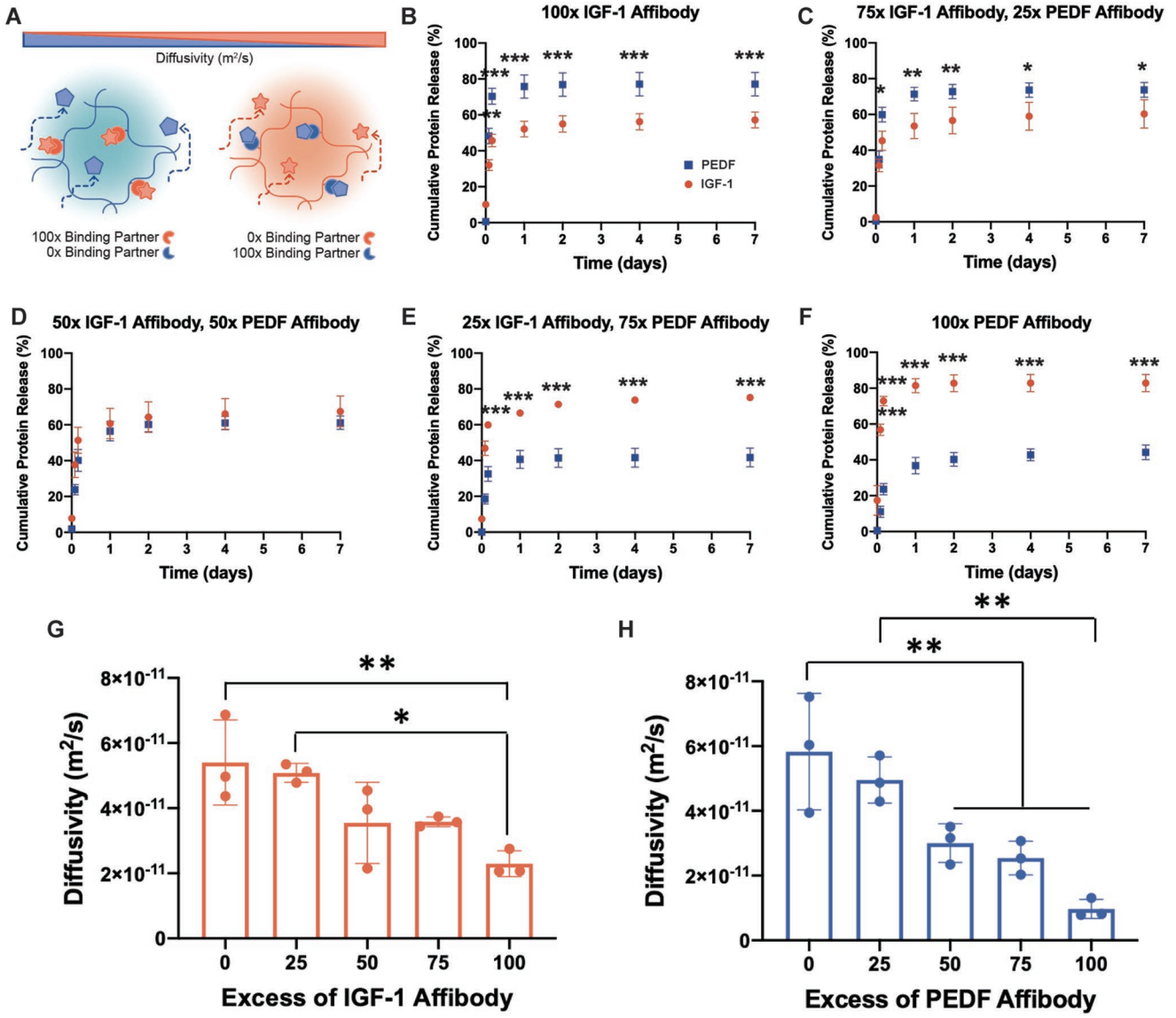

Figure 4. Affibody binding partners enable simultaneous, independent control over the release of multiple proteins from hydrogels. A) 0.75% w/v HAxHA hydrogels were synthesized from HA-norbornene, HA-methylphenyltetrazine, HA-IGF-1-affibody, and HA-PEDF-affibody using IEDDA click chemistry. 12.5 pmol of each protein was encapsulated in each hydrogel. Increasing or decreasing the respective binding partner changed the diffusivity of the protein through the gel. B–F) IGF-1 and PEDF release was measured by ELISA over 7 days from HAxHA hydrogels containing the following: B) 100 times excess IGF-1 affibody to IGF-1 (1.25 nmol), C) 75 times excess IGF-1 affibody to IGF-1 (0.94 nmol) and 25 times excess PEDF affibody to PEDF (0.31 nmol), D) 50 times excess IGF-1 affibody to IGF-1 (0.63 nmol) and 50 times excess PEDF affibody to PEDF (0.63 nmol), E) 25 times excess IGF-1 affibody to IGF-1 (0.31 nmol) and 75 times excess PEDF-affibody to PEDF (0.94 nmol), and F) 100 times excess PEDF-affibody to PEDF (1.25 nmol) ($n = 3$, mean ± sd plotted, two-way ANOVA, Bonferroni's post-hoc test, $^{*}p < 0.05$, $^{**}p < 0.01$, and $^{***}p < 0.001$). G) Diffusivity of IGF-1 decreases with increased IGF-1 affibody in hydrogel. H) Diffusivity of PEDF decreases with increased PEDF affibody in hydrogel ($n = 3$, mean ± sd plotted, one-way ordinary ANOVA, Tukey's post-hoc test, $^{*}p < 0.05$, $^{**}p < 0.01$).

different release profiles, while hydrogels with equal amounts of each binding partner displayed similar release profiles. Increasing the amount of affibodies for either IGF-1 or PEDF decreased the effective diffusivity of that protein from the hydrogel (Figure 4G,H). PEDF release in the presence of the 100 times excess PEDF-affibody (44.2 ± 4.1%) was lower than IGF-1 release in the presence of 100 times excess IGF-1-affibody (57.2 ± 4.5%), which may be due to the larger size of PEDF and higher binding affinity of PEDF to the PEDF binding affibody. An enzyme-linked immunosorbent assay (ELISA) for IGF-1 and PEDF detected negligible amounts of protein recovered from the mechanically disrupted gels after 7 days, preventing a mass balance from being completed (Figure S7, Supporting Information). This could be attributed to a combination of protein degradation and adsorption to the polymer matrix in vitro.[15,45,46] Importantly, we demonstrate that the extent of protein release can be switched from high PEDF and low IGF-1 release (Figure 4B) to the opposite of low PEDF and high IGF-1 release

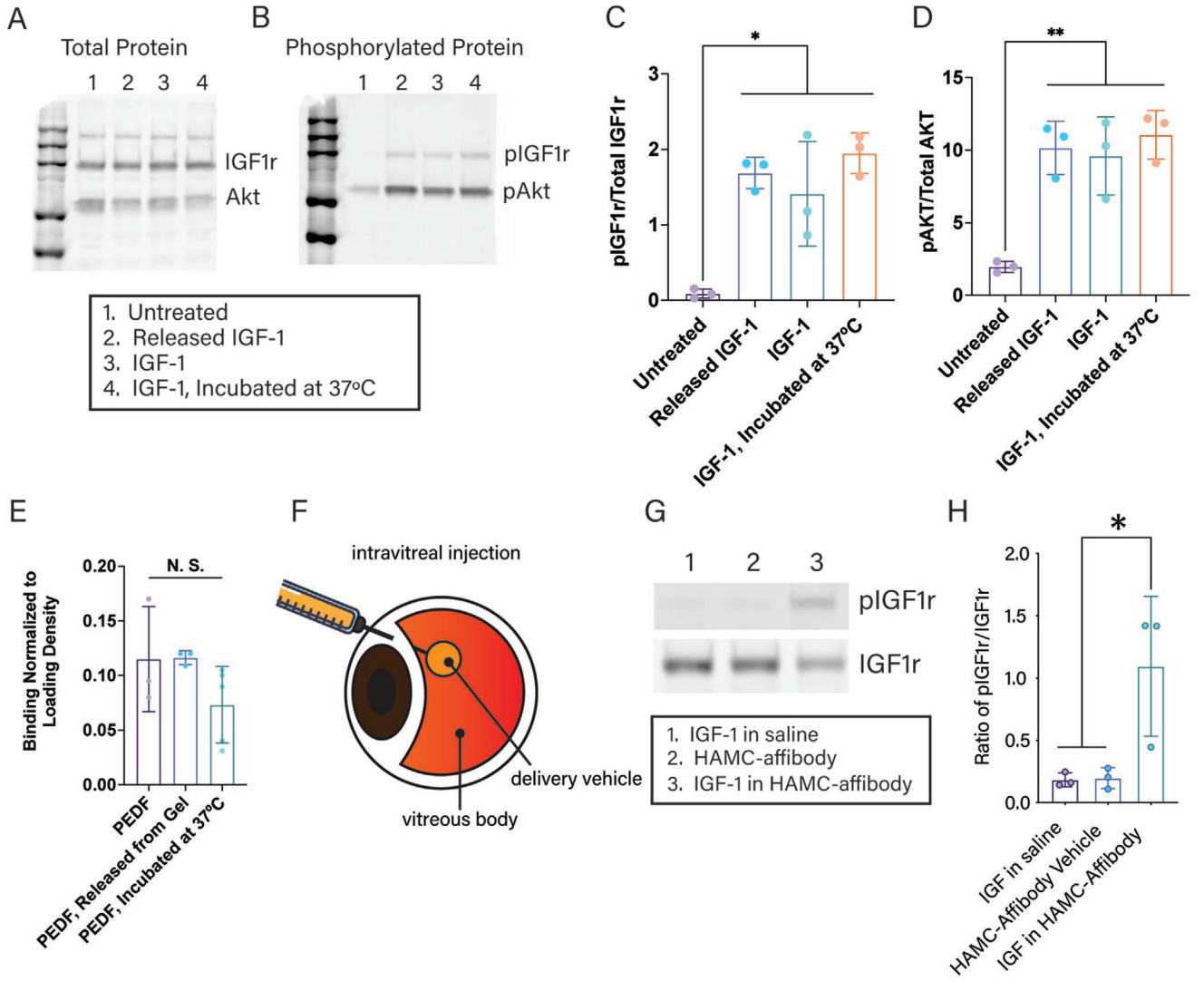

Figure 5. Released IGF-1 and PEDF are bioactive in vitro, and IGF-1 is bioactive in vivo. IGF-1 or PEDF were incorporated into a 0.75% w/v HAxHA hydrogel with 25× molar excess of their respective affibody binding partners, and released therefrom over 48 h. A) Western blot of total IGF1r and Akt and B) pAkt and pIGF1r after treating A549 lung carcinoma cells with: 1) media only; 2) IGF-1 released from the hydrogel vehicle, 3) fresh IGF-1 positive control, or 4) IGF-1 that was incubated at 37 °C for 48 h control. C,D) Quantification of phosphorylated IGF1r (C) and phosphorylated Akt (D) normalized to the total protein loaded ($n = 3$, mean ± sd plotted, one-way ANOVA, Tukey's post-hoc test, $^{*}p < 0.05$, $^{**}p < 0.01$). E) Binding response normalized to loading density for PEDF, PEDF released from the hydrogel vehicle, or PEDF that was incubated at 37 °C for 48 h ($n = 3$–5, mean ± sd plotted, one-way ANOVA, Tukey's post-hoc test, $^{*}p < 0.05$). F) Schematic demonstrating intravitreal injection of the drug-loaded delivery vehicle into the vitreous body of C57BL/6J mice. G) Western blot of wild type mouse retinal tissue for pIGF1r and total IGF1r 24 h after intravitreal injection of: 1) IGF-1 in saline; 2) hydrogel-(HAMC)-IGF1-affibody; or 3) IGF1 released from HAMC-IGF1-affibody. H) Quantification of IGF1r signaling. GAPDH was used as a loading control for all targets. Phosphorylated IGF1r was normalized to the total amount of IGF1r detected for all treatment groups ($n = 3$, mean ± sd plotted, one-way ANOVA, Tukey's post-hoc test, $^{*}p < 0.05$, $^{**}p < 0.01$, and $^{***}p < 0.001$).

(Figure 4F), simply by changing the binding partner immobilized in the hydrogel and without making any additional changes to the protein or hydrogel itself.

Since the bioactivity of biologics often diminishes when incorporated into delivery vehicles,[47] we investigated the bioactivity of released IGF-1 and PEDF. For IGF-1 bioactivity, we used HAxHA hydrogels modified with 25× molar excess of the IGF-1-affibody binding partner to release 255 ng of IGF-1. The IGF-1 receptor (IGF1r) is widely expressed on cancer cells,[48] and its phosphorylation is linked with the phosphorylation of protein kinase B (Akt),[49] a downstream protein associated with cell growth and proliferation.[50] We used A549 human lung adenocarcinoma cells to measure the bioactivity of released IGF-1 relative to equal amounts of fresh IGF-1 versus IGF-1 incubated at 37 °C IGF-1 for 48 h. Western blot analyses of IGF1r and Akt total protein (**Figure 5**A) and phosphorylated protein (Figure 5B) showed no significant differences between treatment groups (Figure 5C,D), indicating that the released IGF-1 is bioactive.

For PEDF bioactivity, we used the same HAxHA hydrogel but modified with 25× molar excess of the PEDF-affibody binding partner to release 1.25 µg of PEDF. Bioactive PEDF

binds to collagen 1,[51,52] and the collagen 1 binding motif of PEDF has been implicated in its anti-angiogenic activity in vivo.[53] To determine the bioactivity of released PEDF, we used BLI to quantify the binding of PEDF to bovine collagen 1. PEDF immobilized to Ni-NTA probes bound to collagen 1 in a dose-dependent manner (Figure S9A, Supporting Information). To ensure the validity of this test, we chemically denaturated PEDF with 6 M guanidine, and observed significantly less denatured PEDF bound to soluble collagen 1 (Figure S9B,C, Supporting Information). To measure the bioactivity of released PEDF, we compared PEDF released from the gel to fresh PEDF and PEDF incubated at 37 °C for 48 h. All were immobilized and incubated with 100×10^{-9} M bovine collagen 1 for 10 min, and t he response between groups was normalized to loading density. The released PEDF was bioactive, with similar bioactivity to both fresh PEDF and 48 h-incubated PEDF, with no significant differences (Figure 5E).

We investigated whether the presence of either IGF-1 or PEDF impacted the activity of the other in vitro. The bioactivity of IGF-1 was the same with or without the addition of PEDF. Specifically, MCF-7 breast cancer cells proliferated to a similar extent when cultured with either IGF-1 or IGF-1 and PEDF, but neither with PEDF nor media alone (Figure S10, Supporting Information). Similarly, the activity of PEDF was the same with or without IGF-1. The binding activity of PEDF to collagen 1 was unaffected by the presence of IGF-1.

To gain further insight into the translational potential of this innovative delivery system, we delivered IGF-1 in vivo from a HA-methylcellulose-based hydrogel (HAMC). The MC polymer chains of HAMC were modified with IGF-1-affibody using the same IEDDA chemistry described for the MCxMC hydrogels. Each of the following formulations was injected into the vitreous of C57BL/6J mice (Figure 5F): 1 µg of IGF-1 loaded into the HAMC-IGF1-affibody vehicle, 1 µg of soluble IGF-1 alone in saline, and HAMC-affibody vehicle alone. Mice were sacrificed 24 h after injections, and the retinal tissue was extracted for western blot analysis of phosphorylated IGF1r. Interestingly, only the IGF-1 delivered from the HAMC-IGF1-affibody group resulted in significant IGF1r phosphorylation (Figure 5G), which was confirmed by densitometry (Figure 5H). IGF-1 delivered from the HAMC-affibody had two times as much phospho-IGF1r than IGF-1 delivered from saline. We hypothesize that the HAMC-IGF-1-affibody had a stabilizing effect on the delivered IGF-1, similar to how antibodies and antibody-like proteins bind to functional epitopes on antigens and stabilize their structures.[54,55]

3. Discussion

We demonstrate, for the first time, independent, simultaneous controlled release of multiple bioactive proteins from a single biomaterial matrix using distinct affinity interactions, thereby enabling tunable release rates. This system utilizes protein–protein interactions to modulate the release rates of two therapeutically-relevant proteins, IGF-1 and PEDF. While it is increasingly clear delivery of multiple therapeutic factors is necessary to see the greatest therapeutic outcome,[56] having fine precision control over the delivery of those factors will greatly enhance tissue repair speed and quality.[57] Many affinity-controlled release systems have been created since the initial development of heparin-based drug delivery systems, drastically expanding the types of proteins that could be delivered from localized depots in the body. However, these systems have been limited to controlling release of only one protein at a time. Conversely, our approach using affibodies offers an elegant and powerful tool to control the release of multiple biophysically and structurally diverse proteins simultaneously.

We prioritized the isolation of low affinity (vs the typical high affinity) binders to our target proteins for controlled release through yeast display. While most directed evolution strategies aim to increase binding affinity to a target protein, we aimed to find low affinity binding partners but maintain a high level of specificity. Our isolated affibodies controlled the release of IGF-1 and PEDF from three different hydrogel matrices. Diffusivity of both IGF-1 and PEDF was tunable with the inclusion of different concentrations of each corresponding affibody binding partner. Not only could this system prolong therapeutic concentrations of both proteins, it demonstrates the flexibility of this system to be incorporated into other biomaterial matrices for different applications. The major limitation with this approach is that competing amines, such as in gelatin or chitosan, could make modification of the matrix complex. However, tetrazine-Nb crosslinking chemistry has been used to form gelatin, alginate, and PEG-based hydrogels.[58–60] Our strategy is versatile and amenable to other water-based, click-crosslinking strategies that avoid both cross-reactivity and adverse outcomes in the local microenvironment.[61,62] Importantly, delivered IGF-1 was bioactive in vivo and both released IGF-1 and PEDF were independently controlled and bioactive in vitro, suggesting that we will be able to similarly achieve independent and controlled release of bioactive IGF-1 and PEDF in vivo.

4. Conclusion

This new way of identifying highly specific, low affinity binding partners opens the door to simultaneous delivery of numerous therapeutic proteins. This versatile approach to engineering protein–protein affinity interactions will pave the way for precise spatiotemporal control over the release of several proteins, and ultimately be useful for enhanced tissue regeneration.

5. Experimental Section

Materials: All chemical reagents were used directly as provided by the suppliers unless otherwise stated. pET28b+ vectors and gene inserts were purchased from Genscript (Piscataway, NJ, USA). Nuvia IMAC columns, Precision Plus Protein Dual Color Standard, and low-fluorescence PVDF membranes were purchased from BioRad (Hercules, CA, USA). The following reagents were purchased from Thermo Fisher Scientific (Waltham, Massachusetts, USA): anti-foam 204, EZ-Link NHS Biotin, Pierce Biotin Quantitation Kit, Pierce Streptavidin Magnetic Beads, Dynabeads M-270 Carboxylic Acid magnetic beads, goat-anti-mouse IgG Cross-Adsorbed Secondary Antibody Alexa Fluor 488, Streptavidin Alexa Fluor 647 conjugate, Exonuclease I, FastAP, Axygen Maximum Recovery microcentrifuge tubes, F12-K Nutrient Mixture cell culture medium, 12% tris-glycine acrylamide gels, SuperBlock (PBS) blocking

buffer, and Earle's Balanced Salt Solution (EBSS). Mouse anti-c-myc antibody was purchased from Biolegend (San Diego, CA, USA). Dialysis tubing (2 kDa molecular-weight cut-off (MWCO), 12–14 kDa MWCO, 100 kDa MWCO) was purchased from Spectrum Labs (New Brunswick, NJ, USA). The following reagents were purchased from The Bioshop (Burlington, ON, Canada): yeast nitrogen base, galactose, isopropyl β-D-1-thiogalactopyranoside, Tris HCl, NaCl, tris(2-carboxyethyl) phosphine hydrochloride salt, imidazole, Coomassie Brilliant Blue G-250 dye, lysogeny broth (LB), and terrific broth (TB). Bacto Casamino Acids, Technical were purchased from Becton, Dickinson, and Company (Sparks, MD, USA). SHuffleT7 competent *E. coli* were purchased from New England Biolabs (Ipswich, MA, USA). Easy Yeast Plasmid Isolation Kit and CloneAmp HiFi PCR Premix kits were purchased from Takara Bio USA (Mountainview, CA, USA). MC (300 kg mol^{-1}) was purchased from Shin Etsu (Tokyo, Japan). Sodium hyaluronate (200 kDa) was purchased from Lifecore Medical (Chaska, MN, USA). Pharmacological-grade high-molecular-weight sodium hyaluronate (HMW HA) (1.2–1.9 MDa) was purchased from NovaMatrix (Sandvika, Norway). The affibody library transfected with the affibody variants were a gift from the Hackel Lab. Bovine collagen 1 (Cat. No. 3442-050-01), IGF-1 (Cat. No. 291-G1), and PEDF (Cat. No. 1177-SF) proteins and corresponding Human IGF-1/IGF-1 Duoset ELISA and Human Serpin F1/PEDF DuoSet ELISA kits were purchased from R&D Systems (Minneapolis, MN, USA). PEDF (Cat. No. ab56289) was also purchased from Abcam (Cambridge, UK). The following reagents were purchased from Click Chemistry Tools (Scottsdale, AZ, USA): methyltetrazine-maleimide and methyltetrazine-amine HCl salt. 5-Norbornene-2-methylamine (mixture of isomers) and 4-(4,6-dimethoxy-1,3,5-triazin-2-yl)-4-methylmorpholinium chloride (DMTMM) was purchased from TCI America (Portland, OR, USA). Ketamine (Ketalean, Cat. No. 8KET004D) was purchased from Bimeda MTC Animal Health Inc. (Cambridge, ON, Canada). Medetomidine (Cepetor, Cat. No. 23615060) and atipamezole (Revertor, Cat. No. 236 1504 0) were purchased from Modern Veterinary Therapeutics LLC (Miami, FL, USA). Hypromellose (0.2% w/v) gel (Genteal Tears, Cat. No. 0078-0429-57) and tropicamide (1% w/v) solution (Mydiacyl, Cat. No. 0065-0355-03) was purchased from Alcon (Mississauga, ON, Canada). Sterile NaCl (0.9% w/v) solution (Cat. No. JB1300) was purchased from Baxter Corporation (Mississauga, ON, Canada). 96-well low binding black plates were purchased from Greiner Bio-one (Kremsmünster, Austria). Octet Super Streptavidin (SSA) biosensors and Octet Ni-NTA biosensors were purchased from Sartorius AG (Göttingen, Germany). 30-gauge sharp needles (Cat. No. 305136) were purchased from VWR International LLC (Mississauga, ON, Canada). 32-gauge blunt needles (Cat. 7762-05) were purchased from Hamilton Company (Montréal, QC, Canada). RealTime Glo MT Viability assay was purchased from Promega (Madison, WI, USA). All other solvents and reagents were purchased from MilliporeSigma (St. Louis, MO, USA).

Yeast Surface Display Library Culture: *Saccharomyces cerevisiae* (EBY100 strain) containing the pCT surface display vector with the gene for the affibody protein were stored at −80 °C in a solution of 15% v/v glycerol in growth media at a density of 20 times the theoretical diversity of the library (1.72×10^8 affibody variants). Yeast libraries were grown at 30 °C to a saturation density of ≈10^8 cells mL^{-1} in growth medium (57×10^{-3} M sodium citrate dihydrate, 20×10^{-3} M citric acid, 111×10^{-3} M dextrose, 12×10^{-3} M yeast nitrogen base, and 45×10^{-3} M Bacto Casamino Acids). Expression of the affibody was under the control of an inducible galactose promoter (Gal1-10), and yeast were grown in galactose-containing induction medium (38×10^{-3} M Na_2HPO_4-$7H_2O$, 62×10^{-3} M NaH_2PO_4-H_2O, 10×10^{-3} M galactose, 5.5 dextrose, 12×10^{-3} M yeast nitrogen base, and 45×10^{-3} M casamino acids) at an initial cell density of 10^7 cells mL^{-1} for 16 h at 30 °C to induce affibody surface expression.

Biotinylation of Target Proteins: For MACS with streptavidin beads, flow cytometry, and FACS, the lysines of target proteins (IGF-1, PEDF) were modified with biotin using biotin NHS ester (EZ-Link NHS Biotin), resulting in an average of 1 biotin per IGF-1 and 3 biotins per PEDF. Modification of IGF-1 or PEDF was verified using the Pierce Biotin Quantitation Kit, which detects the molar ratio of biotin to protein. Biotinylation was further verified using mass spectrometry to detect the shift in protein molecular weight compared to unmodified protein controls.

Streptavidin Magnetic Bead Preparation: To prepare the streptavidin-conjugated magnetic beads for MACS, 60 µL of Pierce Streptavidin Magnetic Beads were washed once with 1 mL of 0.1% v/v Tween 20 in TBS and three times with 1 mL of PBSA (1% w/v bovine serum albumin (BSA) in PBS). Beads were washed by hand-mixing, placing the tube on a magnet (DynaMag-2, Thermo Fisher Scientific, Waltham, USA), and carefully removing the supernatant. After washing, proteins were immobilized to the surface of the beads. Beads were resuspended in 1 mL of PBSA, 1 mL of PBSA with 5 µg of the biotinylated off-target protein, or 1 mL of PBSA with 5 µg of the target biotinylated protein. The beads were rotated at 4 °C for an hour before being washed with PBSA and resuspended in 200 µL of PBSA for distribution among six 2 mL tubes for cell sorting.

Carboxylic Acid Magnetic Bead Preparation: To prepare the carboxylic acid-conjugated magnetic beads for MACS, 60 µL of Dynabeads M-270 carboxylic acid were mixed with 600 µL of 0.01 M NaOH at room temperature for 10 min. The beads were then washed three times by placing the tube on the magnet, removing the supernatant, and adding 600 µL of distilled water. Beads were mixed with 600 µL of 50 mg mL^{-1} of 1-ethyl-3-(3-dimethylaminopropyl)carbodiimide (EDC) in distilled water at room temperature for 30 min, washed with distilled water, and resuspended in 600 µL of 100×10^{-3} M 2-ethanesulfonic acid. The beads were divided into six 2 mL tubes for protein immobilization. 33 pmol of BSA, off-target protein, or target protein were added to the beads and rotated at room temperature for 30 min. The tubes were then placed on the magnet, the supernatant was removed, and 500 µL of 0.05 M Tris at pH 7.4 was added to each tube. The tubes were placed on the magnet again, the supernatant was removed, and 500 µL of PBSA was added to each tube.

Magnetic-Activated Cell Sorting of Yeast Surface Display Library: Four rounds of MACS were performed, alternating between streptavidin-conjugated beads and carboxylic acid-functionalized beads, as previously described.[40] Before the first sort, the glycerol stock was thawed and expanded in growth media. A volume of cells, corresponding to 20× the initial diversity of the library, was transferred into induction media for 24 h, at an initial density of 10^7 cells mL^{-1}, shaking at 200 rpm in a 30 °C incubator. After induction, the cells were counted again and 20 times the theoretical library diversity was removed for sorting.

To select for yeast binding to the target protein of interest, two negative sorts and one positive sort were conducted using either the streptavidin- or carboxylic-acid-conjugated magnetic beads. The first negative sort consisted of identifying affibody proteins that bound to BSA. The second negative sort consisted of identifying affibody proteins that bound to the off-target protein. For the first sort, the total volume of cells was evenly distributed between the tubes with prepared magnetic beads with immobilized BSA. The cells were rotated with the prepared beads with immobilized BSA at 4 °C for at least 2 h, then placed on the magnet, and the supernatant with unbound cells was collected. The unbound cells were added to tubes containing magnetic beads with immobilized off-target protein. The cells were rotated with the prepared beads at 4 °C for at least 2 h, placed on the magnet, and the supernatant with unbound cells was collected. For the positive sort with the target protein, the unbound cells in the supernatant were incubated with the magnetic beads at 4 °C for at least 2 h. The beads were placed on the magnet and collected, and the supernatant with unbound cells was discarded. The beads were washed with PBSA to remove any loosely bound cells. The beads were resuspended in 20 mL of growth media and grown in a shaking incubator at 200 rpm at 30 °C for 48 h or until the cell density reached 10^8 cells mL^{-1}. The cells were diluted to 10^7 cells mL^{-1} in induction media and induced to express affibodies before proceeding with the next round of MACS.

Fluorescence-Activated Cell Sorting of Yeast Surface Display Library: FACS was performed on MACS-sorted yeast to further discriminate yeast displaying affibodies that bound to target proteins of interest. 20×10^6 cells induced to express protein were pelleted by centrifugation at 3000 rpm for 3 min and washed 3 times in 1 mL of PBSA. Biotinylated

target proteins were diluted to 20×10^{-6} M in PBSA. Cells were incubated with the target protein and mouse anti-c-myc antibodies on a tube rotator at 4 °C for 1 h. The cells were pelleted and washed with PBSA, before being incubated with streptavidin conjugated with a 647 nm excitable fluorophore and a goat-anti-mouse antibody conjugated with a 488 nm fluorophore 4 °C for 15 min. The cells were then washed and resuspended in 300 µL of PBSA, and sorted using a BD FACSAria III machine (BD Biosciences, San Jose, CA, USA). Cells that were double positive for bound target protein and displayed affibody were gated and sorted, as previously described.[40]

Sequencing Genes Coding for Affibody Proteins: FACS-sorted yeast were plated on YPD plates and grown for 48 h, and individual yeast colonies were selected from the plate and grown for 48 h in growth medium to a density of at least 10^7 cells mL^{-1}. The cells were pelleted, and 10 mg of yeast were removed. pCT plasmids were extracted using the Easy Yeast Plasmid Isolation Kit, and suspended in ultrapure distilled water. Due to the poor efficiency of plasmid extraction from yeast, the gene coding for the affibody was further amplified by PCR. Primers were synthesized by ACGT Corp. (Toronto, ON, Canada), and amplified using CloneAmp HiFi PCR Premix. PCR products were processed with a combination of Exonuclease I and FastAP Thermosensitive Alkaline Phosphatase to degrade excess primers and dephosphorylate DNA ends, respectively. Sanger sequencing was performed on the PCR products by ACGT Corp.

Expression and Purification of Affibody Proteins: Genes for affibodies that bound to IGF-1 or PEDF were inserted into a pET28b+ vector after the isopropyl β-D-1-thiogalactopyranoside (IPTG)-inducible T7 promoter. The protein was expressed from N-terminus to C-terminus starting with a strep (WSHPQFEK) tag, affibody protein, a hexahistidine (H_6), and a cysteine (C). Vectors were transformed into SHuffle T7 competent *E. coli* K12, and colonies were selected from kanamycin-containing plates. Transformed *E. coli* were grown in 20 mL of LB with 100 µg mL^{-1} of kanamycin for 16 h and used to inoculate large cultures of 1.8 L of TB containing 100 µg mL^{-1} kanamycin and 10 drops of anti-foam 204. TB cultures were grown at 37 °C in a LEX-10 bioreactor (Epiphyte3, Toronto, ON, Canada) with constant air sparging until $OD_{600} \geq 0.8$ was reached (≈4 h), upon which 0.5×10^{-3} M IPTG was added, and protein expression was induced for 16 h at 22 °C. TB cultures were centrifuged for 15 min at 6000 rpm and 4 °C using an Avanti JXN-26 centrifuge (Beckman Coulter, Brea, CA, USA). The cell pellets were resuspended in 30 mL of lysis buffer (50×10^{-3} M Tris pH 7.5, 500×10^{-3} M NaCl, 5×10^{-3} M imidazole, and 1×10^{-3} M tris(2-carboxyethyl)phosphine hydrochloride salt) and lysed using a 500 W sonicator (QSonica, Newtown, CT, SA) at 40% amplitude for 5 min at 10 s intervals. The soluble fraction of the cell lysate was collected, and nickel affinity chromatography was performed using a fast protein liquid chromatography (FPLC) instrument (NGC Quest 10 Chromatography System, BioRad Laboratories Inc., Hercules, CA, USA). The supernatant was applied to a 5 mL column pre-packed with Nuvia IMAC resin, which was pre-equilibrated with lysis buffer containing 1×10^{-3} M tris(2-carboxyethyl)phosphine. The column was washed with 7 CV (column volumes) of wash buffer (50×10^{-3} M Tris pH 7.5, 500×10^{-3} M NaCl, 30×10^{-3} M imidazole) with 1×10^{-3} M tris(2-carboxyethyl)phosphine, then 7 CV of wash buffer without 1×10^{-3} M tris(2-carboxyethyl)phosphine to remove the tris(2-carboxyethyl) phosphine for downstream chemical modification of the cysteines. The protein was eluted with 30 CV of elution buffer (50×10^{-3} M Tris pH 7.5, 500×10^{-3} M NaCl, 250×10^{-3} M imidazole), and 1 mL fractions corresponding to the 280 nm peak were collected and pooled.

Modification of Affibody with Methyltetrazine or Biotin: Affibody concentration was determined by 280 nm peak integration in ChromLab software (BioRad, version 6.0) after purification using FPLC. Methyltetrazine-maleimide or biotin-maleimide was dissolved into the protein solution in 2× molar excess to the affibody. DMSO was added to the solution at a final concentration of 10% v/v to improve the solubility of the hydrophobic methyltetrazine-maleimide or biotin-maleimide molecules. The solution was incubated at room temperature on a tube rotator for 1 h. The protein solution was dialyzed (MWCO 2 kDa) overnight against PBS. Protein was filtered using a 0.2 µm filter to remove aggregates, and the final concentration was determined by Pierce 660 nm Protein Assay Modified protein was stored at −80 °C.

Biolayer Interferometry for Affibody Proteins: The on-rates (k_{ON}), off-rates (k_{OFF}), and dissociation constants (K_D) of protein-affibody interactions were obtained through BLI using an Octet QK system (Pall Forté Bio, Fremont, CA, USA). 200 µL of samples or kinetics buffer (PBS with 0.1% w/v BSA and 0.002% v/v Tween-20) were dispensed into individual wells of a 96-well black plate. The operating temperature was maintained at 25 °C. Affibody proteins were diluted to 200×10^{-12} M into kinetics buffer. IGF-1 affibody was immobilized on Ni-NTA sensor tips. PEDF affibody was immobilized on Super Streptavidin sensor tips, because PEDF had naturally occurring histidine residues which contribute to significant non-specific binding. The target proteins were diluted with the same buffer into a range of different concentrations from 500 to 15.625×10^{-9} M. The raw data were processed by subtraction of values from reference wells which contained only kinetics buffer, and then aligned with associations. The binding interaction constants were obtained by fitting the processed data to a heterogeneous binding model (binding of 2 ligands to 1 receptor) in the Octet analysis software.

Biolayer Interferometry for Collagen 1: The binding of PEDF and bovine collagen 1 was obtained through BLI using an Octet QK system (Pall Forté Bio). 200 µL of sample were dispensed into individual wells of a 96-well low binding black plate. PEDF was diluted to 1 µg mL^{-1} in PBS and bovine collagen 1 was serially diluted from 100 to 3.25×10^{-9} M in SuperBlock (PBS) blocking solution to minimize non-specific binding with the Ni-NTA probes. PEDF was immobilized onto Ni-NTA probes via a 6× histidine tag at its c-terminus. The experiment was first conducted with the PEDF loaded probes, then performed immediately again without PEDF. The operating temperature was maintained at 25 °C. The raw data from each run (with or without PEDF) were first processed by subtracting values from the reference wells, which contained only SuperBlock blocking solution, to remove drift during the data collection. The processed data from run where PEDF was immobilized on the probe was then subtracted from the data where the probes were bare, to account for any non-specific binding of collagen 1. After subtraction, the binding data were flipped so all values reported were positive for ease of interpretation and compatibility with the Octet analysis software.

To measure diminished binding activity of PEDF after denaturation, the same experiment was conducted but only for the highest concentration of collagen 1 (100×10^{-9} M). After loading the probe with PEDF, the tips were incubated in 6 M guanidine hydrochloride for 30 s, before incubating with the collagen 1 solutions.

Synthesis of Methylcellulose-Methyltetrazine and Methylcellulose-Norbornene: MC-methyltetrazine and MC-Nb were synthesized as previously described.[42] Briefly, MC-carboxylate was dissolved in 2-ethanesulfonic acid (MES) buffer (pH 5.5) with stirring overnight at 4 °C until transparent. 0.125 g of 4-(4,6-dimethoxy-1,3,5-triazin-2-yl)-4-methyl-morpholinium chloride were added to activate carboxylic groups, followed by the addition of 0.125 g of methyltetrazine-amine (Click Chemistry Tools, Scottsdale, AZ, USA) or 77 µL of Nb-methylamine (mix of isomers, TCI Chemicals, Portland, OR, USA), which was allowed to react for 3 days. The polymer solution was dialyzed (100 kDa MWCO) for 1 day in PBS and 2 days in deionized water, changing the dialysis buffer 3 times per day and stirring at 4 °C. The dialyzed polymer solution was filter-sterilized, lyophilized, and stored at 4 °C.

The degree of substitution of MC-Nb was quantified using ^{1}H NMR (Agilent DD2-500 spectrometer). The lyophilized MC-Nb polymer was dissolved in deuterium oxide with maleic acid (TraceCERT) as an internal standard. To determine substitution of MC-Nb, the integral area of the Nb protons (2H(CH=CH) at 6.03–6.27 ppm) were compared to the protons of the maleic acid standard (2H, s, at 6.38 ppm). Substitution was calculated using the following equation:

$$A_{NORB} = \frac{n_{IC} \times I_{IC} \times m_{IC} \times 1000}{n_{norb} \times I_{norb} \times M_{IC} \times m_{norb}} \times P_{IC} \quad (1)$$

where A_{norb} is the amount of Nb groups per mass (mmol · g^{-1}); n_{IC} is the number of protons of internal calibrant; I_{IC} is the integral of the internal calibrant resonance signal; m_{IC} is the mass of internal calibrant in the sample; n_{norb} is the number of protons that give rise to the Nb resonance signal; I_{norb} is the integral of the Nb resonance signal; M_{IC} is

the molar mass of the internal calibrant; m_{norb} is the mass of MC-Nb in the sample; and P_{IC} is the purity of the internal calibrant.

The degree of substitution of MC-methyltetrazine was quantified using a spectrophotometer (Infinite M200 Pro Microplate Reader, Tecan, Männedorf, Switzerland). The lyophilized MC-methyltetrazine was dissolved in PBS at 5 mg mL^{-1}. Methyltetrazine-amine was dissolved at 500 µg mL^{-1} in 1 mL of PBS. The methyltetrazine-amine solution was used to produce a seven-point standard curve using twofold serial dilutions. Absorbance of the standard and polymer solutions was recorded at 525 nm. A four-parameter logistic curve was fit to the standard, and the substitution was determined through interpolation based on the absorbance.

Synthesis of Hyaluronan-Norbornene and Hyaluronan-Methyltetrazine: HA-tetrazine and HA-Nb were synthesized as previously described.[41] Briefly, HA (200 kDa) was dissolved in MES buffer (pH 5.5), stirring at room temperature until transparent. 1.03 g of DMT-MM were added to activate carboxylic acid groups and allowed to react for 30 min, stirring at room temperature. 30 mg of methyltetrazine-amine or 229.3 µL of Nb-methylamine was added to the activated HA solution and reacted for 3 days or 15 h, respectively, stirring at room temperature. The solutions were dialyzed (12–14 kDa MWCO) for 1 day in PBS and 2 day in deionized water, changing the dialysis buffer 3 times per day and stirring at room temperature. The solution was filter-sterilized, lyophilized, and stored at 4 °C. The degree of substitution was determined by ^{1}H NMR (Agilent DD2-500 spectrometer). The N-acetyl group of the HA (2 ppm) was used as a reference to calculate the substitution of Nb (2H(CH=CH) at 5.99–6.28 ppm) or methyltetrazine (4H (phenyl) at 7.5–8.48 ppm).

Synthesis of Methylcellulose or Hyaluronan Modified with Affibody Protein: To synthesize MC-Nb or HA-Nb modified with affibody, the polymer was dissolved at 10 mg mL^{-1} in PBS at 4 °C at a concentration of 10 mg mL^{-1} overnight on an orbital shaker. 5× molar excess of affibody-Tz to MC-Nb polymer or 2× molar excess affibody-Tz to HA-Nb polymer was added to the solution and allowed to react overnight, rotating at 4 °C. The solution was dialyzed (MWCO 100 kDa) for 2 days against PBS for 2 days followed by dialysis against 1 day in deionized water for 1 day, changing the buffer 3 times per day. The polymer was lyophilized and stored at 4 °C. To determine substitution of protein onto the polymer, modified polymer was reconstituted at 10 mg mL^{-1} in PBS at 4 °C overnight, and protein modification was quantified using Pierce 660 nm Protein Assay.

Protein Release from Affibody-Modified Hydrogels: MCxMC-affibody and HAxHA-affibody hydrogels were synthesized by the inverse electron demand Diels–Alder click reaction between polymer-methyltetrazine, polymer-Nb, and affibody-Nb functional groups. The hydrogel components were incorporated together such that the ratio of methyltetrazine to Nb functional groups was 1:1 in the MC hydrogels and 1:2 in the HA hydrogels. Hydrogels contained 1.25 nmol of recombinant human IGF-1 or recombinant human PEDF with either 0, 25, 50, 75, or 100 times molar excess of affibody. All components were pipetted into 2 mL microcentrifuge tubes with the total volume equal to 100 µL and mixed using a SpeedMixer (FlackTek Inc., Landrum, USA) at maximum speed for 30 s, followed by centrifugation in a swinging bucket centrifuge at 14 000 rpm to create a flat surface. The mixed polymer solution was left on a shaking platform at 37 °C overnight to form a gel. The next day, 900 µL of PBS with 0.1% BSA w/v was added to the surface of the gels. The supernatant carefully removed and replaced at 0, 2, and 6 h, and 1, 2, 4, and 7 days. IGF-1 or PEDF in the supernatant was quantified using enzyme-linked immunosorbent assays.

Calculation of Diffusivity: To compare protein release rates from the hydrogels and determine effective protein diffusivity, a short time approximation for unidirectional diffusion from a plane sheet was used (Equation (3)):

$$\frac{M_t}{M_\infty} = kt^{1/2} \tag{2}$$

where M_t is the mass of drug released at time t, M_∞ is the mass of drug released as time approaches infinity, and k is constant that is proportional to the apparent diffusivity of the protein within the gel. The ratio of M_t to $M_\infty$was plotted against the square root of time, and the slope of the linear region (k), indicative of Fickian diffusion, was determined. Diffusivity was then determined using the following equation:

$$k = 4 \times \left(\frac{D}{\pi l^2}\right)^{1/2} \tag{3}$$

where D is the diffusivity and l is the thickness of the gel.

Mass Spectrometry: Mass spectrometry was conducted at the Advanced Instrumentation for Molecular Structure core facility at the University of Toronto on purified and methyltetrazine modified affibody proteins. Proteins were ionized using electrospray ionization with positive polarity with the Agilent 6538 Q-TOF mass spectrometer (Agilent Technologies, Santa Clara, CA, USA).

SDS-PAGE of Affibody Proteins: To investigate the molecular weight of the purified proteins and purified proteins modified with methyltetrazine-modified proteins, 20 µg of protein were added to Laemmli buffer. Samples were boiled for 5 min. 10 µL of Precision Plus Protein Dual Color Standards and boiled samples were added to separate wells in a 12-well 10% w/v polyacrylamide gel. Gels were run under denaturing conditions at 120 V for 1 h. Gels were stained using Brilliant Blue dye for 45 min, and destained in destain buffer (10% v/v acetic acid, 30% v/v methanol, and 60% v/v deionized water) for 2 days before imaging.

Circular Dichroism: Far-UV CD was conducted using a JASCO J-810 CD spectrophotometer (JASCO, Easton, MD, USA). Briefly, affibodies were diluted into PBS at 0.2 mg mL^{-1}, and 200 µL of solution was pipetted into a glass cuvette with a path length of 1 cm. Spectra from 200 to 260 nm were obtained at room temperature and plotted to verify the presence of alpha-helical structure.

Bioactivity of IGF-1: To determine the bioactivity of released IGF-1 from the hydrogel vehicle, a release was performed as reported with some modifications. 255 ng of IGF-1 were incorporated into HAxHA (0.75% w/v) hydrogels with 25× molar excess of the corresponding affibody binding partner. Released protein was quantified by ELISA. All release samples were diluted to a concentration of 50 ng mL^{-1} for in vitro treatments.

A549 cells were seeded at 1×10^6 cells per well of a 6 well plate in maintenance media (F-12 media supplemented with 10% FBS and 1% penicillin–streptomycin) overnight. The media was replaced with serum free media for 24 h before treatment with the released IGF-1 samples. Release samples were diluted in media and treatment occurred for 20 min before lysis in ice-cold RIPA buffer. The lysates were sonicated at 30% amplitude for 10 s and centrifuged at 15 000 rcf for 20 min at 4 °C. Protein concentration was quantified using BCA. Lysates were stored at −80 °C for western blot analysis.

Bioactivity of IGF-1 in the Presence of PEDF: MCF-7 cells were seeded at 3000 cells per well in a white-walled 96-well plate in maintenance media (DMEM/F-12 with 20% v/v FBS, 1% v/v penicillin/streptomycin). The cells were incubated at 37 °C for 2 h, allowing them to adhere to the plate. The media was replaced with serum free media and incubated for 24 h before treatment. Cell proliferation was monitored with RealTime Glo MT Viability Assay. The NanoLuc Enzyme and MT cell viability substrates were diluted 1000-fold in serum free media, thoroughly mixed by vortexing, and filtered through a 0.22 µm syringe filter. The RealTime-Glo media was supplemented with one of: no protein, IGF-1 (20 ng mL^{-1} or 2.63×10^{-9} M), PEDF (118 ng mL^{-1} or 2.63×10^{-9} M), or IGF-1 and PEDF (both at 2.63×10^{-9} M). The serum free media was aspirated and replaced with RealTime-Glo supplemented media. Cells were equilibrated with the media for 2 h and luminescence was detected using a plate reader (Infinite M200 Pro Microplate Reader, Tecan, Männedorf, Switzerland). Cell proliferation was normalized to the reading after equilibration at 48 h.

Bioactivity of PEDF: To determine the bioactivity of released PEDF from the hydrogel vehicle, a release was performed as reported with some modifications. 1.52 µg of PEDF were incorporated into HAxHA (0.75% w/v) hydrogels with 25× molar excess of the corresponding affibody binding partner. Released protein was quantified by ELISA.

Collagen 1 was diluted to 100×10^{-9} M in SuperBlock (PBS) blocking buffer and dispensed into individual wells of a 96-well black plate. The operating temperature was maintained at 25 °C. PEDF, released PEDF, or PEDF incubated at 37 °C for 48 h were immobilized on Ni-NTA sensor tips. The experiment was conducted a second time without PEDF loaded onto the probes. The raw data from the first run were subtracted from parallel reference probes which performed the same experiment without PEDF loaded onto tips to remove any signal from non-specific binding, and then aligned with associations. The maximum change in the reflected wavelength was recorded and normalized to the amount of PEDF loaded onto the probe initially. Changes in the binding activity, and therefore bioactivity of the PEDF protein were compared.

Bioactivity of PEDF in the Presence of IGF-1: To assess binding interactions between PEDF and collagen 1 in the presence of IGF-1, collagen 1 and IGF-1 were diluted to 100×10^{-9} M in SuperBlock (PBS) blocking buffer and dispensed into individual wells of a 96-well black plate. The operating temperature was maintained at 25 °C. PEDF was immobilized on Ni–NTA sensor tips. Subsequently the PEDF loaded probes were incubated with 100×10^{-9} M of bovine collagen 1 and IGF-1. The experiment was conducted a second time without PEDF loaded onto the probes. The raw data from the first run were subtracted from parallel reference probes on which the same experiment was performed without PEDF loaded onto tips to remove any signal from non-specific binding, and then aligned with associations. The change in the reflected wavelength at 100 s was recorded, enabling comparison between the conditions.

Animals: All experiments were approved by the University Health Network Research Ethics Board and adhered to the guidelines of the Canadian Council on Animal Care. Animal husbandry was in accordance with the Association for Research in Vision and Ophthalmology (ARVO)

Statement for the Use of Animals in Ophthalmic and Vision Research: Animals were maintained under standard laboratory conditions and all procedures were performed in conformity with the University Health Network Animal Care Committee (protocol 3499.21). 27 C57BL/6 J mice (Charles River) of both sexes were used, all between 6 and 8 weeks old at the time of treatment.

In Vivo Delivery Vehicle Preparation: Sterile-filtered HA (HMW 1.2–1.9 MDa) and MC or modified affibody-MC were dissolved in EBSS at 0.5% w/v overnight at 4 °C. Gels were speed-mixed (DAC 150 FVZ, Siemens) for 30 s and centrifuged at 15 000 rcf for 5 min at 4 °C to eliminate bubbles. Prepared hydrogels were kept on ice prior to use. Animals were given an intravitreal injection of either 1 µg of IGF-1 reconstituted in EBSS, loaded onto the HAMC-affibody hydrogel, or injected with the empty HAMC hydrogel vehicle alone.

Intravitreal Injections: Animals were anesthetized using a mixture of ketamine (100 mg mL^{-1}, Ketalean) at 50 mg kg^{-1} and medetomidine (1 mg mL^{-1}, Cepetor) at 1 mg kg^{-1} in sterile NaCl solution (0.9% w/v) administered intraperitoneally. Pupils were dilated using 1% tropicamide (Mydriacyl) drops, followed by application of a 0.2% hypromellose gel (Genteal Tears) to maintain proper eye lubrication. For injections, the left eye was gently prolapsed and then immobilized using a customized latex dam to allow free blood circulation during the procedure. The retina fundus was visualized under a dissection microscope. A scleral incision was made in the dorso-temporal side, posterior to the limbus using a 30-gauge sharp needle. Next, using a Remote Infuse/Withdraw Pump 11 Elite Nanomite Programmable Syringe Pump (70-4507, Harvard Apparatus, Saint Laurent, QC, Canada) connected to a Compact Mouse and Rat Stereotaxic Instrument, Dual Manipulator (75-1827, Harvard Apparatus, Saint Laurent, QC, Canada), a blunt 32-gauge needle was inserted tangentially into the vitreal space avoiding the lens. The delivery rate of injection was 2 µL min^{-1}, and needle was held in place post-injection for 30 additional seconds to minimize reflux. After the injections, the anaesthesia was reversed using an intraperitoneal injection of 1 mg kg^{-1} atipamezole (5 mg mL^{-1} Revertor). Animals were placed on a heating pad and monitored until fully recovered.

Mice were euthanized 1 day after injection by carbon dioxide inhalation and retinas were collected for protein extraction. Three retinas were pooled per biological replicate and snap-frozen for western blot analysis.

Immunoblotting: RIPA lysis buffer was supplemented with fresh protease and phosphatase inhibitors prior to protein extraction. Lysates were then sonicated (Ultrasonic Liquid Processor VCX 130, Sonics and Materials Inc., Connecticut, USA) at 30% amplitude for 10 s. Samples were then centrifuged at 15 000*g* for 15 min at 4 °C. and protein concentration was quantified using BCA. A mass of 30 µg of protein from cell lysates or retinas were loaded onto a 12% tris-glycine gel. Gel electrophoresis was performed at 100 V constant voltage for 1 h. Low-fluorescence PVDF membranes were pre-activated in methanol and soaked in transfer buffer (48×10^{-3} M Tris, 39×10^{-3} M Glycine, 0.04% SDS, 20% methanol). Electrophoretic transfer was performed using the Trans-Blot TURBO (Biorad) at 15 V constant voltage for 20 min. Transferred membranes were blocked in 5% w/v BSA (in TBS for phosphorylated proteins, TBS with 0.1% Tween-20 for total protein blotting) for 1 h at room temperature. Blots were incubated with primary antibody diluted in blocking buffer overnight at 4 °C. After antibody incubation, three consecutive washes were performed in 10 min in TBS or TBST for phosphorylated blots and total protein blots, respectively. The blots were incubated with secondary antibody for 1 h at room temperature and washed before imaging on the Typhoon 9500 FLA (GE Healthcare Life Sciences). Quantification was performed using Fiji, where the band intensity of each target was normalized to GAPDH, and then the intensity of the phosphorylated protein blot was normalized to the total protein blot.

Statistical Analyses: All data are presented as mean ± standard deviation. Statistical analyses were performed using GraphPad Prism version 8 (GraphPad Software, San Diego, CA, USA). Equal variances across samples and normality of data were verified. Differences between groups were assessed using one-way or two-way ANOVA, as appropriate, followed by Bonferroni's or Tukey's post-hoc test where appropriate. p values are represented as $^{*}p < 0.05$, $^{**}p < 0.01$, and $^{***}p < 0.001$.

Supporting Information

Supporting Information is available from the Wiley Online Library or from the author.

Acknowledgements

The authors are grateful to members of the Shoichet lab for their thoughtful review. The authors are grateful to the following for partial funding of this research: NSERC (Discovery and Herzberg to M.S.S.; PGSD to C.J.T.; Vanier to M.T.H.; PDF to M.H.H.), CIHR (Foundation to M.S.S.) CFREF to Medicine by Design (to M.S.S.), and Vision Science Research Program (Scholarship to C.J.T. and M.T.H.).

Conflict of Interest

The authors declare no conflict of interest.

Author Contributions

C.J.T. and M.H.H. contributed equally to this work. C.J.T., M.H.H., and M.S.S. designed experiments, interpreted results, and wrote the manuscript. C.J.T. and M.H.H. performed most of the experiments. M.T.H. assessed the bioactivity of IGF-1 in vitro and in vivo. A.O.-M. assisted with in vivo experiments. V.W. provided animals and advice on related experiments. A.N.G. and A.J.P. assisted with yeast surface display and cell sorting. A.N.G. assisted with materials characterization and fabrication. A.W.G. aided in methodology for yeast display techniques. B.J.H. provided the affibody library and advice on related experiments.

Data Availability Statement

The data that support the findings of this study are available from the corresponding author upon reasonable request.

Keywords

affibodies, controlled release, directed evolution, yeast display

Received: March 21, 2022
Revised: June 28, 2022
Published online: July 24, 2022

[1] M. Ye, S. Kim, K. Park, *J. Controlled Release* **2010**, *146*, 241.
[2] S. Yang, W. Yuan, T. Jin, *Expert Opin. Drug Delivery* **2009**, *6*, 1123.
[3] O. M. Ba, M. Hindie, P. Marmey, O. Gallet, K. Anselme, A. Ponche, A. C. Duncan, *Colloids Surf., B* **2015**, *134*, 73.
[4] S. Reed, B. Wu, *Ann. Biomed. Eng.* **2014**, *42*, 1528.
[5] G. Jiang, B. H. Woo, F. Kang, J. Singh, P. P. DeLuca, *J. Controlled Release* **2002**, *79*, 137.
[6] S. E. Sakiyama-Elbert, *Acta Biomater.* **2014**, *10*, 1581.
[7] M. H. Hettiaratchi, M. S. Shoichet, *Tissue Eng., Part A* **2019**, *25*, 925.
[8] M. H. Hettiaratchi, C. Chou, N. Servies, J. M. Smeekens, A. Cheng, C. Esancy, R. Wu, T. C. McDevitt, R. E. Guldberg, L. Krishnan, *Tissue Eng., Part A* **2017**, *23*, 683.
[9] M. H. Hettiaratchi, T. Rouse, C. Chou, L. Krishnan, H. Y. Stevens, M.-T. A. Li, T. C. McDevitt, R. E. Guldberg, *Acta Biomater.* **2017**, *59*, 21.
[10] M. M. Martino, P. S. Briquez, E. Guc, F. Tortelli, W. W. Kilarski, S. Metzger, J. J. Rice, G. A. Kuhn, R. Muller, M. A. Swartz, J. A. Hubbell, *Science* **2014**, *343*, 885.
[11] M. M. Martino, F. Tortelli, M. Mochizuki, S. Traub, D. Ben-David, G. A. Kuhn, R. Müller, E. Livne, S. A. Eming, J. A. Hubbell, *Sci. Transl. Med.* **2011**, *3*, 100ra89.
[12] J. A. Andrades, B. Han, J. Becerra, N. Sorgente, F. L. Hall, M. E. Nimni, *Exp. Cell Res.* **1999**, *250*, 485.
[13] A. Mansurov, J. Ishihara, P. Hosseinchi, L. Potin, T. M. Marchell, A. Ishihara, J.-M. Williford, A. T. Alpar, M. M. Raczy, L. T. Gray, M. A. Swartz, J. A. Hubbell, *Nat. Biomed. Eng.* **2020**, *4*, 531.
[14] K. Vulic, M. S. Shoichet, *J. Am. Chem. Soc.* **2012**, *134*, 882.
[15] M. M. Pakulska, K. Vulic, M. S. Shoichet, *J. Controlled Release* **2013**, *171*, 11.
[16] T. P. Richardson, M. C. Peters, A. B. Ennett, D. J. Mooney, *Nat. Biotechnol.* **2001**, *19*, 1029.
[17] A. T. Raiche, D. A. Puleo, *Biomaterials* **2004**, *25*, 677.
[18] Y. Wang, M. J. Cooke, N. Sachewsky, C. M. Morshead, M. S. Shoichet, *J. Controlled Release* **2013**, *172*, 1.
[19] Z. Wei, E. Volkova, M. R. Blatchley, S. Gerecht, *Adv. Drug Delivery Rev.* **2019**, *149*, 95.
[20] J. A. Shadish, G. M. Benuska, C. A. DeForest, *Nat. Mater.* **2019**, *18*, 1005.
[21] P. S. Lienemann, Q. Vallmajo-Martin, P. Papageorgiou, U. Blache, S. Metzger, A.-S. Kiveliö, V. Milleret, A. Sala, S. Hoehnel, A. Roch, R. Reuten, M. Koch, O. Naveiras, F. E. Weber, W. Weber, M. P. Lutolf, M. Ehrbar, *Adv. Sci.* **2020**, *7*, 1903395.
[22] M. A. Anderson, T. M. O'Shea, J. E. Burda, Y. Ao, S. L. Barlatey, A. M. Bernstein, J. H. Kim, N. D. James, A. Rogers, B. Kato, A. L. Wollenberg, R. Kawaguchi, G. Coppola, C. Wang, T. J. Deming, Z. He, G. Courtine, M. V. Sofroniew, *Nature* **2018**, *561*, 396.
[23] S. Bake, A. Okoreeh, H. Khosravian, F. Sohrabji, *Exp. Neurol.* **2019**, *311*, 162.
[24] A. Serose, A. Salmon, B. Prudhon, M. Agnes Doyennette, M. Fiszman, Y. Fromes, *Mol. Ther.* **2004**, *9*, S353.
[25] F. R. Steele, G. J. Chader, L. V. Johnson, J. Tombran-Tink, *Proc. Natl. Acad. Sci. USA* **1993**, *90*, 1526.
[26] J. A. Doll, V. M. Stellmach, N. P. Bouck, A. R. Bergh, C. Lee, L. P. Abramson, M. L. Cornwell, M. R. Pins, J. Borensztajn, S. E. Crawford, *Nat. Med.* **2003**, *9*, 774.
[27] J. Yang, S. Chen, X. Huang, J. Han, Q. Wang, D. Shi, R. Cheng, G. Gao, X. Yang, *Cancer Biol. Ther.* **2010**, *9*, 967.
[28] J. Parker, N. Mitrousis, M. S. Shoichet, *Biomacromolecules* **2016**, *17*, 476.
[29] A. Hernández-Pinto, F. Polato, P. Subramanian, A. de la Rocha-Muñoz, S. Vitale, E. J. de la Rosa, S. P. Becerra, *Exp. Eye Res.* **2019**, *184*, 24.
[30] J. Bullock, S. P. Becerra, in *The Serpin Family: Proteins with Multiple Functions in Health and Disease* (Eds: M. Geiger, F. Wahlmüller, M. Furtmüller), Springer International Publishing, Cham, Switzerland **2015**, pp. 197–212.
[31] W. Zheng, Q. Meng, H. Wang, F. Yan, P. J. Little, X. Deng, S. Lin, *Mol. Neurobiol.* **2018**, *55*, 1915.
[32] J. Löfblom, J. Feldwisch, V. Tolmachev, J. Carlsson, S. Ståhl, F. Y. Frejd, *FEBS Lett.* **2010**, *584*, 2670.
[33] J. Cho, S. H. Kim, B. Yang, J. M. Jung, I. Kwon, D. S. Lee, *J. Controlled Release* **2020**, *324*, 532.
[34] H. Moon, Y. Bae, H. Kim, S. Kang, *Chem. Commun.* **2016**, *52*, 14051.
[35] L. M. F. Merlo, L. Mandik-Nayak, in *Cancer Immunotherapy*, 2nd ed., (Eds: G. C. Prendergast, E. M. Jaffee), Academic Press, San Diego, CA, USA **2013**, pp. 25–40.
[36] R. E. Cobb, R. Chao, H. Zhao, *AIChE J.* **2013**, *59*, 1432.
[37] A. Orlova, M. Magnusson, T. L. J. Eriksson, M. Nilsson, B. Larsson, I. Höidén-Guthenberg, C. Widström, J. Carlsson, V. Tolmachev, S. Ståhl, F. Y. Nilsson, *Cancer Res.* **2006**, *66*, 4339.
[38] T. Natsume, T. Koide, S. Yokota, K. Hirayoshi, K. Nagata, *J. Biol. Chem.* **1994**, *269*, 31224.
[39] M. Ackerman, D. Levary, G. Tobon, B. Hackel, K. D. Orcutt, K. D. Wittrup, *Biotechnol. Prog.* **2009**, *25*, 774.
[40] G. Chao, W. L. Lau, B. J. Hackel, S. L. Sazinsky, S. M. Lippow, K. D. Wittrup, *Nat. Protoc.* **2006**, *1*, 755.
[41] V. Delplace, P. E. B. Nickerson, A. Ortin-Martinez, A. E. G. Baker, V. A. Wallace, M. S. Shoichet, *Adv. Funct. Mater.* **2020**, *30*, 1903978.
[42] V. Delplace, A. J. Pickering, M. H. Hettiaratchi, S. Zhao, T. Kivijärvi, M. S. Shoichet, *Biomacromolecules* **2020**, *21*, 2421.
[43] V. Delplace, A. Ortin-Martinez, E. L. S. Tsai, A. N. Amin, V. Wallace, M. S. Shoichet, *J. Controlled Release* **2019**, *293*, 10.
[44] R. Sen, D. Gahtory, J. Escorihuela, J. Firet, S. P. Pujari, H. Zuilhof, *Chem. - Eur. J.* **2017**, *23*, 13015.
[45] L. E. Tellier, T. Miller, T. C. McDevitt, J. S. Temenoff, *J. Mater. Chem. B* **2015**, *3*, 8001.
[46] I. Freeman, A. Kedem, S. Cohen, *Biomaterials* **2008**, *29*, 3260.
[47] M. M. Pakulska, S. Miersch, M. S. Shoichet, *Science* **2016**, *351*, aac4750.
[48] N. Chapuis, J. Tamburini, P. Cornillet-Lefebvre, L. Gillot, V. Bardet, L. Willems, S. Park, A. S. Green, N. Ifrah, F. Dreyfus, P. Mayeux, C. Lacombe, D. Bouscary, *Haematologica* **2010**, *95*, 415.
[49] D. R. Alessi, M. Andjelkovic, B. Caudwell, P. Cron, N. Morrice, P. Cohen, B. A. Hemmings, *EMBO J.* **1996**, *15*, 6541.
[50] E. Paplomata, R. O'Regan, *Ther. Adv. Med. Oncol.* **2014**, *6*, 154.
[51] M. Cauble, P. Yang, U. Baumann, J. M. Gebauer, B. G. Orr, L. T. Duong, M. M. Banaszak Holl, *J. Struct. Biol.* **2017**, *199*, 132.
[52] C. Meyer, L. Notari, S. P. Becerra, *J. Biol. Chem.* **2002**, *277*, 45400.
[53] J. Hosomichi, N. Yasui, T. Koide, K. Soma, I. Morita, *Biochem. Biophys. Res. Commun.* **2005**, *335*, 756.
[54] A. Haque, J. N. Andersen, A. Salmeen, D. Barford, N. K. Tonks, *Cell* **2011**, *147*, 185.

[55] B.-H. Luo, K. Strokovich, T. Walz, T. A. Springer, J. Takagi, *J. Biol. Chem.* **2004**, *279*, 27466.
[56] X. Sun, S. Vilar, N. P. Tatonetti, *Sci. Transl. Med.* **2013**, *5*, 205rv1.
[57] K. J. Rambhia, P. X. Ma, *J. Controlled Release* **2015**, *219*, 119.
[58] R. M. Desai, S. T. Koshy, S. A. Hilderbrand, D. J. Mooney, N. S. Joshi, *Biomaterials* **2015**, *50*, 30.
[59] J. Carthew, J. E. Frith, J. S. Forsythe, V. X. Truong, *J. Mater. Chem. B* **2018**, *6*, 1394.
[60] D. L. Alge, M. A. Azagarsamy, D. F. Donohue, K. S. Anseth, *Biomacromolecules* **2013**, *14*, 949.
[61] R. Y. Tam, J. Yockell-Lelièvre, L. J. Smith, L. M. Julian, A. E. G. Baker, C. Choey, M. S. Hasim, J. Dimitroulakos, W. L. Stanford, M. S. Shoichet, *Adv. Mater.* **2019**, *31*, 1806214.
[62] A. E. G. Baker, L. C. Bahlmann, R. Y. Tam, J. C. Liu, A. N. Ganesh, N. Mitrousis, R. Marcellus, M. Spears, J. M. S. Bartlett, D. W. Cescon, G. D. Bader, M. S. Shoichet, *Adv. Mater.* **2019**, *31*, 1901166.

Received: 7 July 2020 | Revised: 23 November 2020 | Accepted: 4 January 2021

DOI: 10.1002/ijc.33485

CANCER THERAPY AND PREVENTION

IJC International Journal of Cancer

Nanofitins targeting heat shock protein 110: An innovative immunotherapeutic modality in cancer

Guillaume Marcion[1,2] | François Hermetet[1,2] | Fabrice Neiers[2,3] | Burhan Uyanik[1,2] | Lucile Dondaine[1,2] | Alexandre M. M. Dias[1,2] | Laurène Da Costa[2,4,5] | Mathieu Moreau[2,4,5] | Pierre-Simon Bellaye[5] | Bertrand Collin[4,5] | Jessica Gobbo[1,2,5] | Loïc Briand[2,3] | Renaud Seigneuric[1,2] | Olivier Kitten[6] | Mathieu Cinier[6] | Carmen Garrido[1,2,5]

[1]INSERM, UMR 1231, Label Ligue Nationale contre le Cancer and LipSTIC, Dijon, France

[2]Université Bourgogne Franche-Comté, Dijon, France

[3]Centre des Sciences du Goût et de l'Alimentation, INRA, Dijon, France

[4]ICMUB UMR 6302, Dijon, France

[5]Anticancer Center Georges François Leclerc, Dijon, 21000, France

[6]Affilogic SAS, Nantes, France

Correspondence
Carmen Garrido, INSERM, UMR 1231, University of Bourgogne Franche-Comté, Faculty of Medicine, 7 boulevard Jeanne d'Arc, 21079 Dijon, France.
Email: cgarrido@u-bourgogne.fr

Funding information
French Government grant managed by the French National Research Agency under the program "Investissements d'Avenir", Grant/Award Numbers: ANR-11-LABX-0021, ANR-15-IDEX-0003; Ligue Nationale contre le Cancer; Association pour la Recherche sur le Cancer; Conseil Régional de Bourgogne; Institut National du Cancer

Abstract

The presence of an inactivating heat shock protein 110 (HSP110) mutation in colorectal cancers has been correlated with an excellent prognosis and with the ability of HSP110 to favor the formation of tolerogenic (M2-like) macrophages. These clinical and experimental results suggest a potentially powerful new strategy against colorectal cancer: the inhibition of HSP110. In this work, as an alternative to neutralizing antibodies, Nanofitins (scaffold ~7 kDa proteins) targeting HSP110 were isolated from the screening of a synthetic Nanofitin library, and their capacity to bind (immunoprecipitation, biolayer interferometry) and to inhibit HSP110 was analyzed in vitro and in vivo. Three Nanofitins were found to inhibit HSP110 chaperone activity. Interestingly, they share a high degree of homology in their variable domain and target the peptide-binding domain of HSP110. In vitro, they inhibited the ability of HSP110 to favor M2-like macrophages. The Nanofitin with the highest affinity, A-C2, was studied in the CT26 colorectal cancer mice model. Our PET/scan experiments demonstrate that A-C2 may be localized within the tumor area, in accordance with the reported HSP110 abundance in the tumor microenvironment. A-C2 treatment reduced tumor growth and was associated with an increase in immune cells infiltrating the tumor and particularly cytotoxic macrophages. These results were confirmed in a chicken chorioallantoic membrane tumor model. Finally, we showed the complementarity between A-C2 and an anti-PD-L1 strategy in the in vivo and in ovo tumor models. Overall, Nanofitins appear to be promising new immunotherapeutic lead compounds.

KEYWORDS
anticancer-targeted therapy, HSP110, Nanofitins, small peptide molecules

Abbreviations: BLI, biolayer interferometry; BSA, bovine serum albumin; CAM, chorioallantoic membrane; FBS, fetal bovine serum; HSP, heat shock protein; ID, injected dose; iNF, irrelevant Nanofitin; NBD, nucleotide-binding domain; O/N, overnight; PBD, peptide-binding domain; RT-qPCR, quantitative real-time PCR; WT, wild type.

Guillaume Marcion and François Hermetet contributed equally to this work.

Mathieu Cinier and Carmen Garrido contributed to the co-direction of the work.

1 | INTRODUCTION

Heat shock protein 110 (HSP110 also called HSPH1 or HSP105) is a stress-inducible molecular chaperone with antiaggregation and

antiapoptotic properties, at least in vitro.[1,2] HSP110 has been shown to be overexpressed in different cancers and particularly in colorectal and gastric cancers where HSP110 expression has been correlated with poor prognosis.[3-5] In colorectal cancer, one multicenter study including more than 3000 patients demonstrated that the presence of a HSP110 inactivating mutation was associated with an excellent response to chemotherapy.[6] Despite its clinical relevance, the role(s) of HSP110 in cancer has been little studied compared to other HSPs. We recently demonstrated that HSP110 favored colon cancer cell proliferation through the activation of STAT3.[7] HSP110 has also been involved in cancer cell proliferation by disrupting the beta-catenin degradation mediated by its phosphorylation, thereby maintaining Wnt pathway activity.[8]

The role of HSP110 is not limited to its intracellular functions. Like many HSPs, HSP110 can be released into the extracellular medium. Extracellular HSPs are believed to act as danger signals that can affect immune response.[9,10] Most studies have associated extracellular HSP levels (in blood or plasma) with poor prognosis. For instance, HSP70, through the activation of myeloid-derived suppressor cells, and HSP27, through its effect in differentiating tolerogenic macrophages,[11,12] have been shown to block the development of an anticancer immune response. Concerning HSP110, it has been shown to induce immunosuppression by inhibiting the activation of dendritic cells through scavenger receptor binding.[13] More recently, in colorectal cancer patients, we showed that the correlation between HSP110 and poor prognosis was associated with the ability of the extracellular chaperone to favor the formation of protumor M2-like macrophages in the tumor microenvironment.[14] These M2-like macrophages are known to suppress the immune response by activating T-helper-2 cells and promoting tumor progression and angiogenesis.[15]

Over the last decade, HSP90 and HSP70 have gained increasing interest as therapeutic targets in oncology.[16-18] However, despite the recently reported clinical studies demonstrating the relevance of HSP110 in gastrointestinal cancers, notably in colorectal cancer, no inhibitors of HSP110 are currently in preclinical or clinical evaluation. Inhibitor compounds can be broadly divided into two classes: (small) chemical molecules and biologics.[10,19,20] Because we are focused on the second class of compound, we based our approach on the Nanofitin alternative binding scaffold (Supplementary Figure 1). Nanofitins are single chain, small (~7 kDa) and robust (high resistance to temperature and chemical stress) protein binders that can be engineered to address a target with high specificity and affinity.[21-24] In this work, Nanofitins targeting and inhibiting HSP110 were generated, yielding candidates with subnanomolar affinity straight out of the panning campaign. The Nanofitin with the highest affinity, dubbed A-C2, provided inhibition of the HSP110 chaperone and its protumor immune function in vitro and in vivo. We also showed the interest of A-C2 in combination with PD-L1 checkpoint inhibitors, which are a currently used targeted immunotherapy. Overall, these results indicate that A-C2 Nanofitin might be a novel therapeutic lead compound for cancer.

What's new?

Inactivating HSP110 mutations in colorectal cancers have been correlated with excellent prognosis and revealed the ability of HSP110 to favor the formation of tolerogenic macrophages. As an alternative to neutralizing antibodies, here the authors selected Nanofitins (scaffold ~7 kDa-proteins) able to target HSP110 with subnanomolar affinity. The highest-affinity Nanofitin, A-C2, was shown to accumulate within the tumor and reduce tumor growth in vivo through a mechanism involving macrophages. The results also demonstrated A-C2 complementarity with PD-L1 checkpoint inhibitors, an immunotherapeutic approach currently in use. Altogether, this work shows the potential of Nanofitins as therapeutic lead compounds.

2 | MATERIALS AND METHODS

2.1 | Cell cultures

SW480 (RRID: CVCL_0546), CT26 (RRID: CVCL_7254) and MDA-MB-231 (RRID: CVCL_0062) cells (provided by ATCC) were cultivated in RPMI or DMEM (for the last two), supplemented with 10% fetal bovine serum (FBS, Dutscher). All human cell lines have been authenticated using STR profiling within the last 3 years. All experiments were performed with mycoplasma-free cells.

2.2 | Plasmid constructions for the expression of HSP110

HSP110 and truncated HSP110 forms carrying either the nucleotide-binding domain (NBD-HSP110, amino acids 1-384) or the peptide-binding domain (PBD-HSP110, amino acids 385-858) C-terminus His-Tag were generated by gene synthesis performed by Geneart (Thermo Fisher) and cloned into a Pet21α, as previously described.[25] HSP110 was cloned using infusion into pCMV-HA.

2.3 | Cell transfection and immunoprecipitation

1.5×10^5 cells were seeded on 12-well plates, and HSP110-HA and/or Nanofitins-Flag were transfected with X-tremeGENE HP DNA Transfection Reagent (Roche) 48 hours before immunoprecipitation. Conditioned media were prepared from 2.5×10^5 cells cultured in a 12-well plate for 72 hours in DMEM supplemented with 10% FBS. The supernatant was then harvested and centrifuged at 450*g* for 5 minutes to remove residual cells, and then to 2000*g* for 20 minutes to remove cell debris. Cells were lysed in lysis buffer (50 mM Tris pH 7.4, 150 mM NaCl, 0.5% Triton X100, 2 mM EDTA) with

IJC International Journal of Cancer

cOmplete Protease Inhibitor Cocktail tablet (Roche) and phosphatase inhibitors (Sigma) for 30 minutes. Then lysates were centrifuged 16 000*g* for 15 minutes. Protein concentration was measured with a Lowry kit (Bio-Rad). 2 μg of Anti-Flag (F1804, Sigma) or Anti-GFP antibodies (G8965-07, Euromedex USbio) were incubated with protein G Dynabeads (Invitrogen) 4 hours at 4°C under rotation. For immunoprecipitation, 300 μg of all lysate or 1 μg of A-C2-GFP and recombinant HSP110 wild-type (WT), HSP110 peptide-binding domain (PBD) or HSP110 nucleotide-binding domain (NBD) proteins were incubated overnight (O/N) at 4°C before being incubated 40 minutes with prepared beads. Complexes were washed three times with lysis buffer and solubilized with 2x sample buffer (50 mM Tris pH 6.8, 8% v/v glycerol, 1.6% w/v SDS, 0.8% v/v 2-mercaptoethanol, bromophenol blue), heated to 95°C for 10 minutes and then processed by western blotting.

2.4 | Western blotting

Cultured cells were lysed in RIPA buffer supplemented with cOmplete Protease Inhibitors (Roche), 10 mM sodium fluoride, 1% v/v PMSF and Phosphatase Inhibitor Cocktail 2 (Sigma-Aldrich). Protein concentrations of cellular extracts were assessed using DC protein assay (Bio-Rad). SDS-PAGE was carried out and separated proteins were transferred to a polyvinylidene difluoride (PVDF) membrane. Membranes were blocked 1 hour with Tris-buffered saline (TBS)-Tween 0.1% (TBST), 3% w/v bovine serum albumin (BSA; Sigma-Aldrich), incubated with primary antibodies in TBST 3% BSA, O/N at 4°C. Primary antibodies used are Anti-HSP110 (1:1000, EPR4576 or EPR4577, Abcam), HSP70 (1:1000, ADI-SPA-810, Enzolife sciences), 14-3-3 (1:1000, sc732, Santa Cruz), β-actin-peroxidase (1:30′000, A3854, Sigma-Aldrich), GFP-labeled A-C2 (1 μg/mL), GFP (1:1000, #2956, Cell Signaling) and DDDDK tag/FLAG (1:5000, ab1162, Abcam). Membranes were incubated with HRP-conjugated secondary antibodies (1:10000, Jackson ImmunoResearch Laboratories) or with Clean-Blot Detection Reagent (HRP) (1:400, Thermo Scientific) (for immunoprecipitation analysis) when necessary and then revealed with ECL (Bio-Rad).

2.5 | Heat shock

For assessment of HSP induction by heat, monolayers of cells were exposed to 42°C- or 45°C-prewarmed cell culture media and incubated in circulating water bath (controlled so as to produce a temperature of 42°C or 45°C) for 1 hour or 15 minutes, respectively, followed by 4-hour recovery in an incubator at 37°C with fresh 37°C-prewarmed cell culture medium. Control cells remained cultured at 37°C.

2.6 | Macrophage differentiation

Monocytes from human peripheral blood were obtained from healthy donors with informed consent and purified using Ficoll and Percoll gradient. Monocytes (100 000/well) were incubated in a 6-well plate with macrophage colony-stimulating factor (M-CSF, 100 ng/mL, 130-096-492, Miltenyi Biotec) for 5 days, and then cells were polarized into M2 macrophages by incubation with interleukin-4 (IL-4, 20 ng/mL, 130-093-922, Miltenyi Biotec) for 48 hours. After morphological differentiation in M2, macrophages were incubated for 48 hours with 500 μL of SW480 colorectal cancer cell' supernatant diluted twice with OptiMEM to a final volume of 1 mL.

2.7 | Flow cytometry analysis

Macrophages were harvested, washed once in phosphate-buffered saline (PBS) and incubated for 20 minutes at 4°C with fluorescein-5-isothiocyanate (FITC) and V500-conjugated antibodies directed against CD206 (550889, BD Biosciences) and HLA-DR (561226, BD Biosciences), respectively. Cells were then washed twice in PBS and analyzed using a Canto flow cytometer (Becton Dickinson, Franklin Lakes, NJ).

2.8 | Immunofluorescence

Cells were seeded on a 12-well plate with coverslip for 48 hours. Then, cells were incubated 10 minutes in 4% paraformaldehyde, washed in TBS and incubated 10 minutes in 100% methanol at −20°C. After a wash in TBST, coverslips were saturated 30 minutes in 3% BSA-TBST and incubated O/N with 10 μg/mL GFP-labeled A-C2 or the control Nanofitin B-D1 and recombinant anti-Hsp105/HSP110 [EPR4576] (ab109624, Abcam) primary antibody at a dilution of 1:250 in 3% BSA-TBST at 4°C and then rinsed with PBS twice. Primary antibody was detected using Alexa Fluor 568-coupled secondary antibodies (1:500, Invitrogen), 30 minutes at room temperature (RT). Then, slides were mounted using DAPI-containing Prolong Gold antifade reagent (Life Technologies). Cells were observed using an Axio Imager 2 (Carl Zeiss Microscopy GmbH, Jena, Germany) equipped with an Apotome 2 module (Carl Zeiss GmbH). Images were acquired with an AxioCam MRm monochrome CCD camera (Carl Zeiss) and processed for colocalization studies (Fiji, NIH software).

2.9 | Quantitative real-time PCR

After mRNA isolation from macrophages with the TRIzol Reagent (Invitrogen), M-MLV reverse transcriptase (Promega) was used to synthesize cDNA according to the manufacturers' recommendations. The following primers were then used for quantitative PCR (qPCR): IL12 (forward: CATGGGCCTTCATGCTATTT; reverse: TGATGTACTTGC AGCCTTGC), IL10 (forward: TGGTGAAACCCCGTCTCTAC; reverse: CTGGAGTACAGGGGCATGAT) and actin (forward: GTTGTCGAC GACGAGCG; reverse GCACAGAGCCTCGCCTT). Samples were run in triplicate using the SYBR Green real-time PCR master mix (Life Technologies, Saint Aubin, France) and the ABI ViiA 7 real-time PCR system (Applied Biosystems, Foster City, CA). Thermal cycling for all qPC

R consisted in 95°C for 5 minutes followed by 40 cycles of 30 seconds at 95°C and 1 minute at 60°C. Data were normalized to human *Actin* using the $2^{-\Delta\Delta Ct}$ method.

2.10 | ELISA screening of the Nanofitins

Streptavidin (SA) (100 μL, 66 nM; Sigma-Aldrich) in TBS (Tris 20 mM, NaCl 150 mM pH 7.4) was immobilized in Maxisorp plate wells (Nunc) by O/N incubation at 4°C. Each of the following steps was run at room temperature, with shaking at 600 rpm for incubation steps. The wells were washed three times with 300 μL of TBS, then blocked with 300 μL of 0.5% BSA in TBS for 1 hour. The plate was flicked over and biotinylated HSP110 (100 μL, 40 nM) in TBS with 0.5% BSA being allowed to bind for 1 hour. Prior to each of the following incubation steps, the wells were washed three times with 300 μL of TBST. Nanofitins (1 μM, 100 μL, diluted in TBST) were applied to wells with and without immobilized antigen for 1 hour. Revelation was then carried out by the addition of 100 μL of RGS-His antibody HRP conjugate (Qiagen) diluted 1:4000 in TBST for 1 hour, followed by the addition of 100 μL of *o*-phenylenediamine dihydrochloride substrate (Sigma-Aldrich) solution at 1 mg/mL in revelation buffer (0.05 M citric acid, 0.05% hydrogen peroxide). Absorbance at 450 nm was measured using a Varioskan ELISA plate reader (Thermo Scientific).

2.11 | HSP110 antiaggregation activity

A concentration of 0.15 μM of Luciferase (Sigma-Aldrich) was incubated in the presence or not of 1.5 μM HSP110 and/or inhibitors at 42°C during 30 minutes in 25 mM Hepes, pH 7.6, 5 mM $MgCl_2$, 2 mM dithiothreitol and 2 mM ATP buffer. Then, denaturated luciferase was incubated with 60% reticulocyte lysate (Promega) at 30°C for 2 hours. Before activity measurement, luciferase was diluted 5-fold in 25 mM Hepes pH 7.6. Samples were loaded in half-area 96-well plates (PerkinElmer) and luminescence was measured after auto-injection of luciferase assay solution (Promega) with EnVision Multilabel Reader (PerkinElmer).

2.12 | Biolayer interferometry

Protein-protein interactions were determined by biolayer interferometry (BLI) on an Octet Red instrument (Pall, Fortébio, Menlo Park, CA).[26-28] Recombinant proteins (Nanofitins or HSP110) were labeled with NHS-PEG4-Biotin with a 1:3 ratio and then free biotin was removed using a desalting column (Thermo Scientific). Proteins were loaded on SA biosensor in PBS buffer and were incubated with various concentrations of analytes in running buffer (50 mM Tris, 0.01% BSA, 0.002% Tween 20) during 180 and 600 seconds for association and dissociation, respectively. Affinities were determined as described in previous studies. Experimental curves were background-corrected, smoothed with the Savitzky-Golay algorithm and fit using the OctetRED instrument software (ForteBio Data Analysis version 7.1.).

2.13 | Tumor growth analysis in mouse model

Tumors were induced subcutaneously by injecting 5×10^5 CT26 cells in 100 μL of serum-free RPMI 1640 into the right flank of female BALB/c mice (Charles River, France). Mice were treated every 2 days (i.p.) with A-C2, H4, B-D1 (20 mg/kg), PBS (vehicle) or with InVivoMAb anti-mouse PD-L1 (B7-H1) (10 mg/kg, clone 10F.9G2, BioXCell, BE0101), either alone or in combination. Every 2 days, tumor volumes were measured. The ethics committee for animal welfare of the University of Burgundy and the French Ministry of Higher Education, Research and Innovation approved all animal experiments performed for the purposes of this publication (under reference APAFIS#25224). Mice were treated according to the guidelines of this French ministry.

2.14 | Immunohistochemistry of intestine

Small intestines were collected, stripped of soft tissue, fixed in 10% buffered formalin for 24 hours, processed and embedded in paraffin. Four-μm-thick sections were cut from paraffin-embedded samples and were incubated with the anticleaved Caspase-3 primary antibody at 4°C O/N. Primary antibodies were detected using secondary antibodies and DAB (1:500, Invitrogen), 30 minutes at RT and tissue was stained using hematoxylin and eosin. Then, slides were mounted using mounting media (Life Technologies). Sections were observed using an Axio Imager 2 (Carl Zeiss Microscopy GmbH, Jena, Germany), and small intestine slice images were acquired with an AxioCam MRm monochrome CCD camera (Carl Zeiss).

2.15 | Peripheral blood analysis

After intracardiac peripheral blood sampling, hematopoietic cells were counted using a hemocytometer (SCIL Vet ABC+, Oostelbeers, the Netherlands).

2.16 | In vivo tumor targeting of HSP110 with ^{68}Ga radiolabeled Nanofitin

Female BALB/c mice-bearing CT26 tumors (300 mm^3) in the right shoulder were anesthetized through isoflurane inhalation for intravenous injection (tail vein) of 5 MBq of ^{68}Ga-Nanofitin or ^{68}Ga-EDTA right before imaging. Mice were then maintained under anesthesia and placed on the imaging heated bed inside BioPET-CT (BioScan). A tumor-centered CT scan was then obtained (150 μA, 45 kV, 240 projections, 8 shots/projection). Mice underwent 60-minute PET imaging of the same region (tumor-centered, right after CT scan acquisition). At the end of imaging, the mice were intraperitoneally injected with an overdose of pentobarbital for euthanasia and the organs were harvested for gamma counting (PerkinElmer, France). PET reconstructions were performed for the complete 60-minute scan. A region of

interest within the tumor was manually determined, and the percentage of injected dose per gram of tissue (%ID/g) of the tumor was measured. All experiments were approved by the ethics committee of the "Centre George François Leclerc" (Dijon, France).

2.17 | Immunohistochemistry of tumor infiltration

Immunofluorescence was performed on paraffin-fixed 5 μm section. Samples were incubated with the primary antibody at 4°C O/N. Specific markers of subtype macrophage and T-lymphocyte were used: M1-like, i-NOS (nitric oxide synthase 2, 1:200, ab178945, Abcam); M2-like, anti-CD206 (1:200, ab64693, Abcam), CD4 (1:500, ab183685, Abcam) and CD8 (1:500, ab217344, Abcam). Primary antibodies were detected using Alexa Fluor 488 or Alexa Fluor 568-coupled secondary antibodies (1:500, Invitrogen), 30 min at RT. Then, slides were mounted using DAPI-containing Prolong Gold antifade reagent (Life Technologies). Sections were observed using an Axio Imager 2 (Carl Zeiss Microscopy GmbH, Jena, Germany). Tumor slice images were acquired with an AxioCam MRm monochrome CCD camera (Carl Zeiss).

2.18 | Tumor growth analysis in chicken chorioallantoic membrane model

The tumor growth assay (Inovotion, Grenoble, France) was developed in chorioallantoic membrane (CAM) of embryonated chicken eggs (White Leghorn) from MDA-MB-231 cells. At Day 9 of development (E9), an inoculum of 100 μL of graft medium, corresponding to 50 μL DMEM (Thermo Fisher, France), 50 μL Matrigel (Corning, France), containing 1×10^6 cells was added on the CAM. Grafted eggs were treated with five injections (at E10, E12, E14, E15 and E17) of A-C2, (20 mg/kg), anti-PD-L1 Nanofitin (B11; 20 mg/kg), bispecific Nanofitin (A-C2-B11; 20 mg/kg), Keytruda (pembrolizumab, anti-PD-1 antibody, 2 mg/kg, Merck) or PBS (vehicle). At Day 9 post-engraftment (E18 of development), tumors were collected, fixed (PFA 4%), cleaned of normal CAM tissue and then weighed.

2.19 | Statistical analyses

Data are expressed as means ± SD or SEM, or presented as medians, first and third quartiles, and whiskers. The differences between experimental groups were assessed with two-tailed unpaired Student's *t*-tests (*t*-test). A one-way analysis of variance (ANOVA) has been used to correct for multiple testing. Statistics was performed using Prism 6 software (GraphPad). A *P* value of <.05 was considered statistically significant, and significance is indicated in the figures with the following symbols: **P* < .05; ***P* < .01; ****P* < .001; *****P* < .0001.

Additional methods can be found in the online Supplementary Materials and Methods.

3 | RESULTS

3.1 | Screening of Nanofitins targeting HSP110

Full-length, well-folded and highly pure (>95%) HSP110 was used as bait for the generation of anti-HSP110 Nanofitins. Purity and secondary structure were confirmed respectively by SDS-PAGE analysis and circular dichroism (Supplementary Figure 2A,B). The screening of the Nanofitin libraries was performed by ribosome display[21] over four rounds. Two Nanofitin libraries were screened independently (selection arms A and B, Supplementary Figure 3A). Positive hits targeting HSP110 were identified by ELISA using crude lysis supernatants from microcultures. At that stage, Nanofitins were expressed as a fusion with an N-terminal HIS-tag and a C-terminal GFP tag, the GFP serving as a reporter to (a) select clones in the correct open reading frame and (b) quantify the concentration of the Nanofitins in the lysis supernatant (details of the constructions used in our study are given in Supplementary Information). Ninety-five clones per selection arm were tested for HSP110 binding, resulting in a total 81 of positive hits showing an ELISA response on HSP110-coated wells at least twice that of the background signal in the absence of target (Supplementary Figure 3A). Sequence analysis made it possible to group the Nanofitins into four distinct families named A, B, C and D, and represented at 81, 15, 2 and 2% respectively (Supplementary Figure 3B). Among these groups, 20 different Nanofitin-binding site compositions could be identified. These 20 Nanofitin candidates were compared for their binding level in ELISA at a fixed concentration (1 μM, Figure 1A) as well as for their ability to inhibit HSP110 chaperone activity using a luciferase assay (Figure 1B). Although binding to HSP110 was confirmed in ELISA for all the Nanofitins at 1 μM, only three of them (A-C2, A-F12 and A-H3) significantly inhibited HSP110 chaperone activity when set at an equimolar concentration with HSP110. Based on this result, these three Nanofitins were characterized further with respect to their inhibition potential in a dose-dependent experiment ranging from one third (0.5 μM) to five (7.5 μM) molar equivalents of HSP110. B-D1 Nanofitin was also included in the experiment to serve as a non-inhibiting control. In agreement with our previous observation, Nanofitins A-C2, A-F12 and A-H3 inhibited HSP110 chaperone function in a dose-dependent manner, whereas B-D1 did not provide any inhibition even at the highest dose investigated (Figure 1C). BLI experiments were used to evaluate the Nanofitin-binding kinetics to HSP110, which revealed an affinity for A-C2, A-F12, A-H3 and B-D1 of 0.77, 1.45, 9.3 and 1400 nM, respectively (Figure 1D,E). The very low affinity of B-D1 might explain its noninhibition profile.

Since A-C2 was the Nanofitin with the highest affinity constant, it was selected for further experiments. Using HSP110 deletion mutants (Supplementary Figure 4A), we were able to show that A-C2 binds most probably the C-terminus domain of HSP110, which includes the peptide-binding domain (Supplementary Figure 4B). Kinetic measurement of the association of A-C2 with the HSP110 C-terminal domain demonstrated affinity constants similar to what was obtained when wild-type HSP110 was used (Supplementary Figure 4C,D).

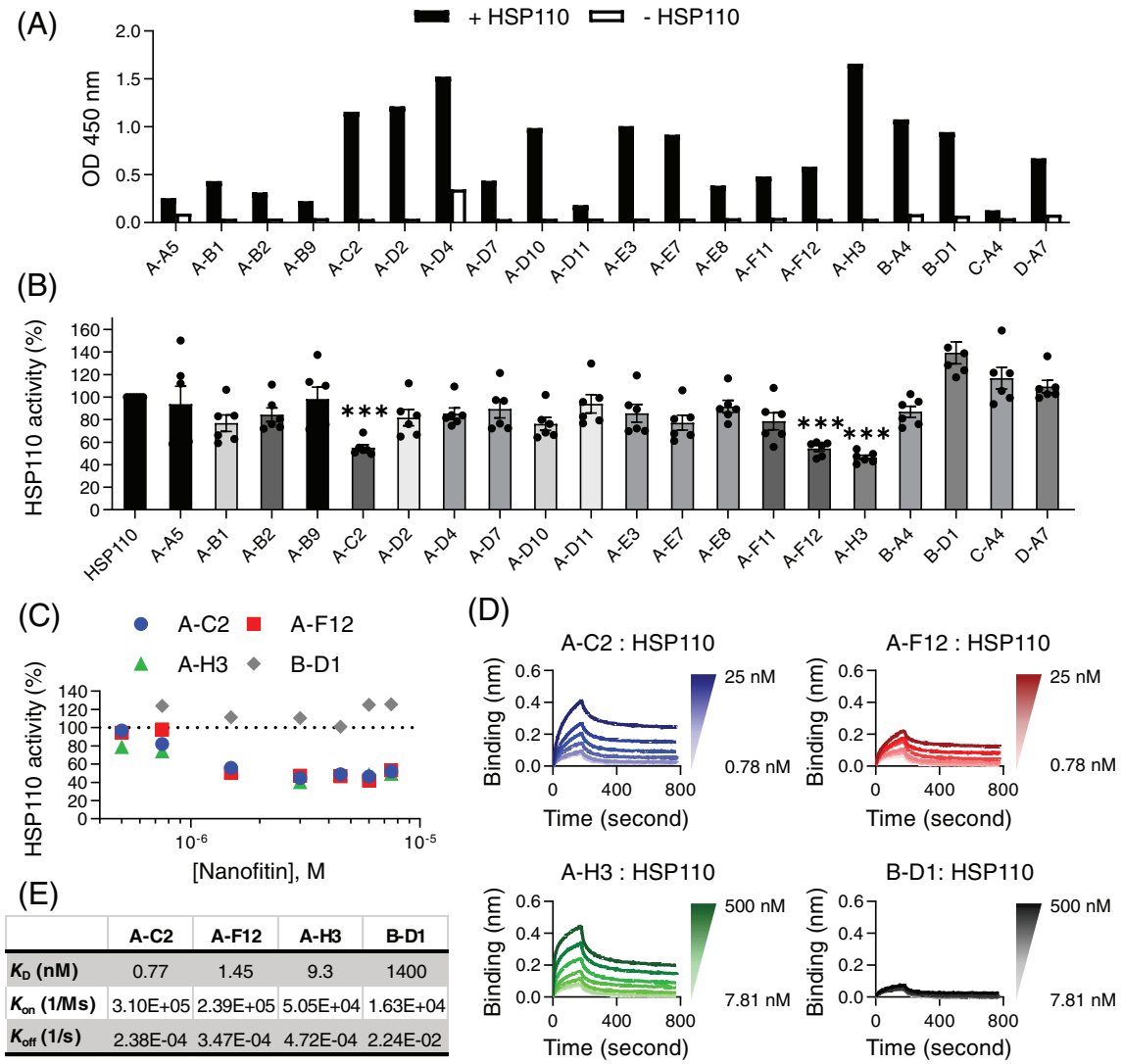

(E)

	A-C2	A-F12	A-H3	B-D1
K_D (nM)	0.77	1.45	9.3	1400
K_{on} (1/Ms)	3.10E+05	2.39E+05	5.05E+04	1.63E+04
K_{off} (1/s)	2.38E-04	3.47E-04	4.72E-04	2.24E-02

FIGURE 1 Nanofitin screen based on their association with HSP110 and its inhibition. A, After a selection by ribosome display, the level of GFP-tagged Nanofitins was screened by ELISA in HSP110-coated (+HSP110) or uncoated (−HSP110) wells. After the addition of RGS His antibody HRP conjugate and *o*-phenylenediamine dihydrochloride substrate, the optical density (OD450) was measured at 450 nm (B) antiaggregation HSP110 activity measurement in the presence of GFP-tagged Nanofitins by in vitro chaperone refolding assays using temperature-denatured luciferase as substrate. A-C2, A-H3 and A-F12 inhibit HSP110 chaperone activity. Percentage of HSP110 refolding activity normalized to luciferase-positive signal in the absence of Nanofitin. Data are expressed by mean ± SEM (one-way ANOVA; ***$P < .001$). C, HSP110 antiaggregating activity was measured in the presence of increasing concentrations of three anti-HSP110 GFP-tagged Nanofitins (A-C2, A-F12, A-H3) or a Nanofitin control (B-D1). A-C2, A-F12 and A-H3 associate and inhibit HSP110 in a dose-dependent manner. D, Sensorgrams showing dose-dependent association of GFP-tagged A-C2, A-F12 and A-H3 with GFP-tagged HSP110 immobilized in a streptavidin biosensor in comparison with B-D1 (negative control), determined by biolayer interferometry (BLI, Octet), and enabling the measure of (E) the HSP110 interaction affinity constants (equilibrium dissociation constant, K_D; association reaction, K_{on}; dissociation reaction, K_{off}) of the mentioned Nanofitins

3.2 | A-C2 Nanofitin as a HSP110 detection tool: binding to endogenous HSP110

To study the specificity of A-C2 in a cellular context, we used human colon cancer SW480 (Figure 2A) and murine colon cancer CT26 (Supplementary Figure 5) cells, before and after a heat shock, to increase the expression of HSPs and notably HSP110 and HSP70 (the most stress-inducible HSP). We then used the Nanofitin (GFP-tagged) as a primary revelation tool in a western blotting experiment to see which HSP could be detected. We found that only HSP110 (both the alpha and beta isoforms) was revealed by A-C2 but not any other protein including HSP70 (an HSP110-related chaperone), even though it was overexpressed after the heat shock (Figure 2A). To confirm the interaction between the Nanofitin and HSP110 within the cells, we performed immunoprecipitation experiments in cells transfected with a pCMV vector coding for either flag tagged A-C2 or a flag-tagged irrelevant Nanofitin, dubbed iNF, used as a negative control. As shown in Figure 2B, the two Nanofitins were expressed intracellularly and could be immunoprecipitated using the anti-

IJC International Journal of Cancer

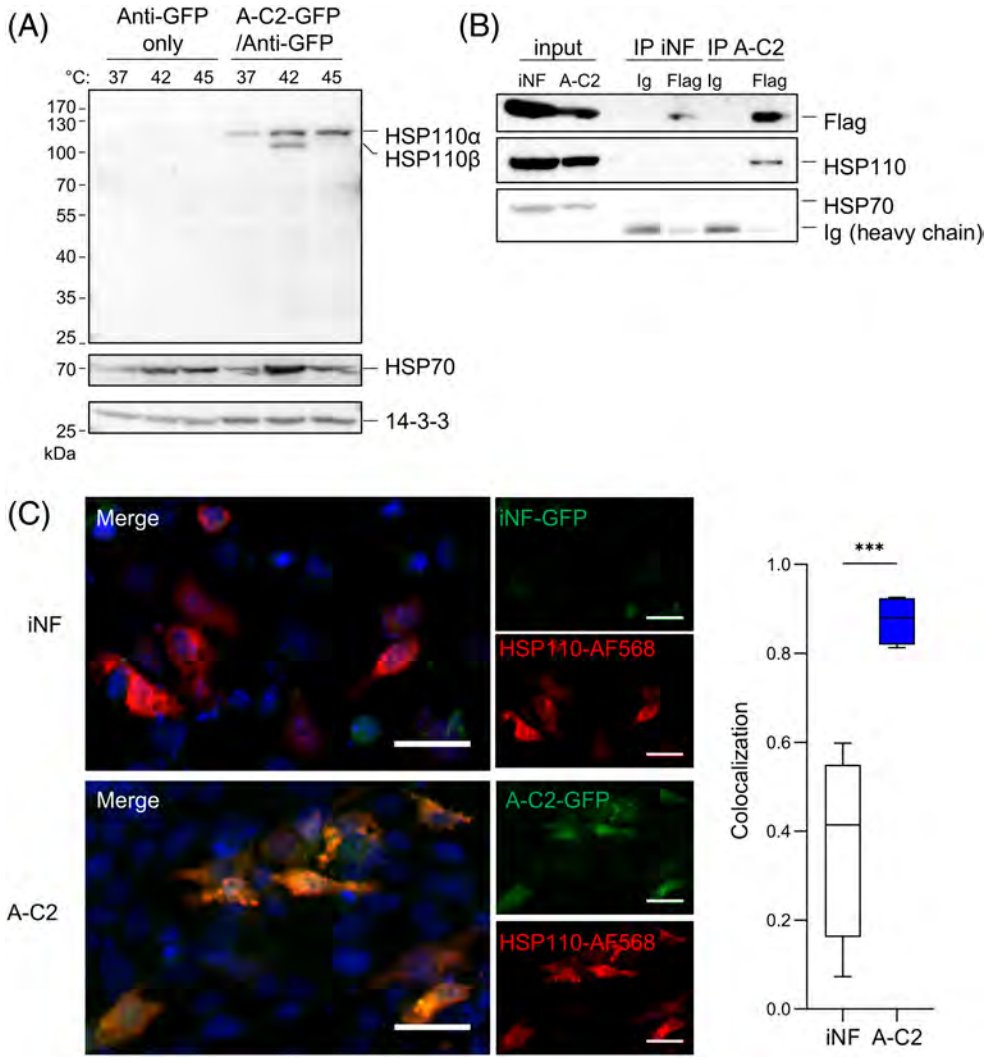

FIGURE 2 Specificity of the A-C2 Nanofitin for endogenous HSP110 in cancer cells. A, After a 42°C (1 h) or 45°C (15 minutes) heat shock, SW480 cells were lysed and analyzed by western blotting using the indicated GFP-tagged Nanofitins as antibodies. Nanofitins were revealed with anti-GFP antibody. HSP70 and 14-3-3 were used as controls for the efficiency of the heat shock and as a loading control, respectively. B, SW480 cells were transfected with a Flag-tagged A-C2 or Flag-tagged H4 (iNF, used as a negative control). Nanofitins were immunoprecipitated using Flag antibody, and HSP110 and HSP70 were revealed by immunoblotting. C, Immunofluorescence was performed to monitor colocalization of the Nanofitin A-C2 (in green) with endogenous HSP110 (in red). GFP-tagged H4 (iNF) was used as a negative control. White scale bars represent 30 μm. Statistics of the colocalization (Fiji, NIH Software) on SW480 cells (n > 30 cells) is shown on the right panel. Data are presented as median (central line), first and third quartiles (bottom and top of boxes, respectively), and whiskers (extreme values) (two-tailed unpaired Student's *t*-test; ***, $P < .001$)

flag tag antibody. HSP110 was co-immunoprecipitated with A-C2 but HSP70 was not (Figure 2B), demonstrating the ability of the Nanofitin to be expressed functionally and to engage its target within the cell. Further immunofluorescence experiments suggest GFP-tagged A-C2 and HSP110 colocalization within the cells (Figure 2C).

3.3 | A-C2 is able to inhibit the effect of HSP110 on tolerogenic macrophages

We and others have shown that secreted HSP110 is abundant in the tumor microenvironment and that it is involved in macrophage polarization toward a tolerogenic (M2-like) phenotype.[4,14] We tested the impact of A-C2 on this protumoral effect of HSP110. As already reported, the presence of HSP110 favors primary human monocyte polarization toward an M2-like phenotype, which is demonstrated by an increase in CD206 expression, while the expression of the M1 marker HLA-DR decreases (Figure 3A,B). The ability of HSP110 to increase CD206 and to decrease HLA-DR was inhibited in a dose-dependent manner by A-C2. In agreement with these results, and also in a dose-dependent manner, A-C2 inhibited an HSP110-mediated increase in M2-like cytokines such as IL-10 and an HSP110-mediated decrease in M1-like cytokines such as IL-12 (Figure 3C,D).

3.4 | A-C2 localizes in the tumor area after intravenous injection

To investigate the potential of A-C2 as a novel immunomodulatory modality for the treatment colorectal cancers, we first performed biodistribution experiments to determine A-C2 localization within the tumor area after systemic administration. BALB/c mice were subcutaneously injected with the colorectal cancer cell line CT26. When the tumor reached 300 mm^3, ^{68}Ga-labeled A-C2 was injected intravenously and PET/CT scans were performed. At 1 hour postinjection, we observed an accumulation of ^{68}Ga-labeled A-C2 compared to unconjugated ^{68}Ga-EDTA at the tumor site but not in blood, brain, spleen, lungs, kidneys, bladder or liver (Figure 4A-E; 3 animals/group; n = 2). These results are consistent with the abundance of HSP110 in the tumor microenvironment.[14]

3.5 | A-C2 reduces tumor growth in mice, which is associated with an intratumor infiltration of cytotoxic macrophages

The effect of intraperitoneally (i.p.) administered Nanofitin on tumor growth was evaluated in the CT26 colorectal cancer BALB/c mouse model. Tumor growth experiments were performed with A-C2 in three control groups: a non-HSP110 inhibiting Nanofitin (B-D1), an irrelevant Nanofitin (iNF) and the vehicle alone (Vehicle). In all cases, the samples were injected in mice bearing a 50 mm^3 tumor (n = 9 per group). In the light of our biodistribution experiments (Figure 4) and the rapid clearance of Nanofitins already described in previous in vivo PET studies,[22,29] the Nanofitins were administered every 2 days (20 mg/kg, i.p.) until the end of the experiments. For ethical reasons, this procedure was determined by the size of the tumors in the

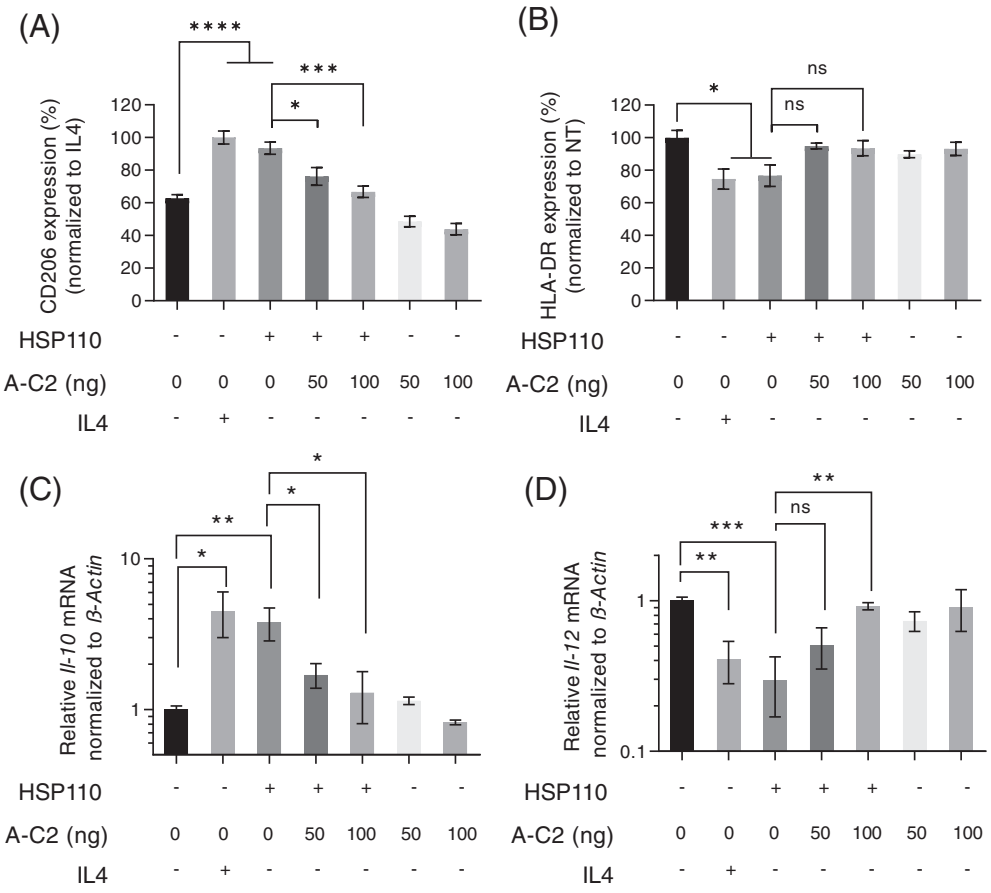

FIGURE 3 A-C2 reduces M2-like markers while increasing M-1 markers on macrophage treated with HSP110. A,B, Purified primary human macrophages were incubated with or without HSP110 in the presence or absence of A-C2. IL-4 was used as a control and inductor of macrophage polarization into an activated M2-like profile. The expression of the CD206 M2-like marker (A) and the HLA-DR M1-like marker (B) were determined by flow cytometry. C, Downregulation of the immunosuppressive cytokine IL-10 (left panel) and upregulation of the proinflammatory IL-12 (right panel) by A-C2 was determined by quantitative real-time PCR. Results are expressed as percentage of (A) CD206 cell expression normalized to 100% for control IL4-treated cells, (B) HLA-DR cell expression normalized to 100% for control untreated cells, or (C,D) as relative indicated mRNA expression normalized to 1 (arbitrary unit (A.U.) for control untreated cells. Data are shown as means ± SEM (two-tailed unpaired Student's *t*-test; ns, nonsignificant [$P > .05$]; *$P < .05$, **$P < .01$, ***$P < .001$ and ****$P < .0001$)

IJC International Journal of Cancer

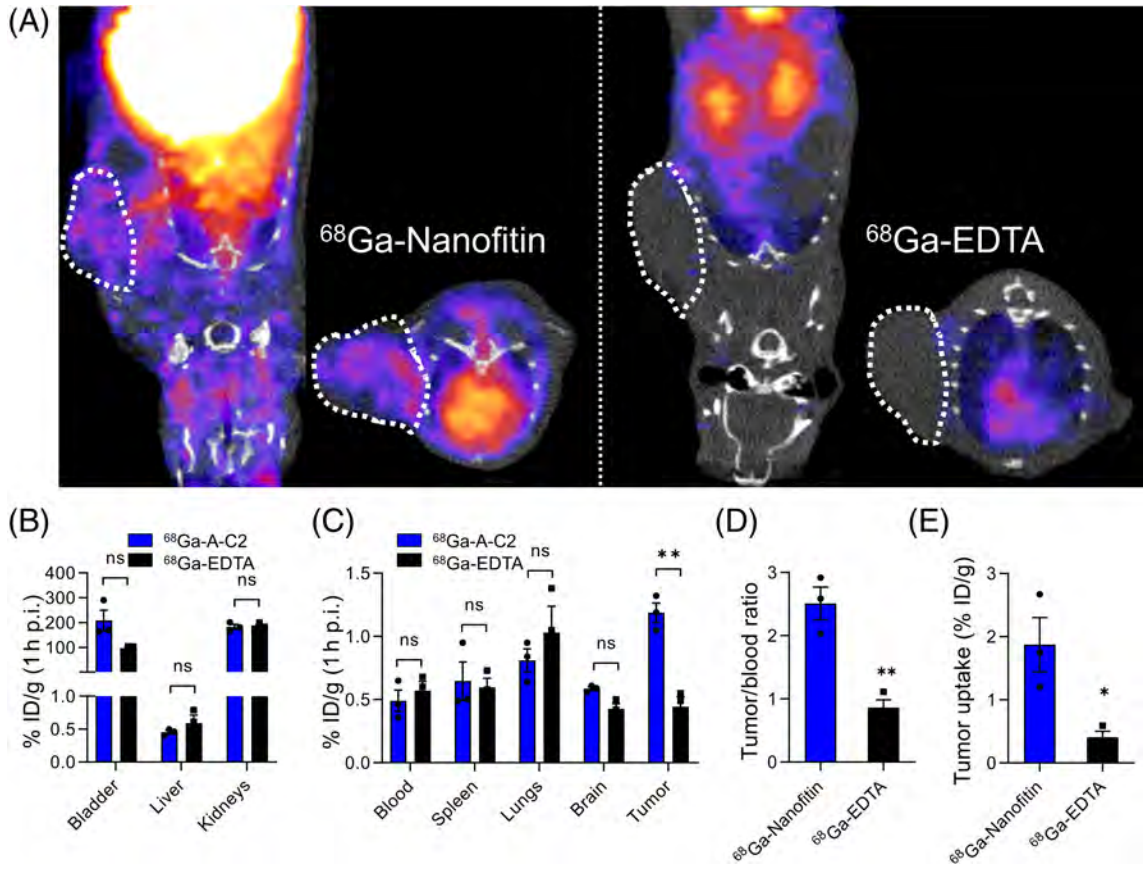

FIGURE 4 In vivo tumor targeting of HSP110 with ^{68}Ga radiolabeled Nanofitin. A, Representative coronal and transversal PET/CT images of CT26 tumor-bearing mice, 1 hour after being injected intravenously with 5 MBq of ^{68}Ga-Nanofitin (left panel) or ^{68}Ga-EDTA (control, right panel). 3 mice/group, n = 2. The tumor is highlighted by a white dotted circle. B, Global biodistribution in the main clearance organs (bladder, liver and kidneys) of ^{68}Ga-Nanofitin and ^{68}Ga-EDTA. Radioactivity was measured using a gamma counter after imaging. Results are expressed as percentage of injected dose per gram of tissue (%ID/g). C, Global biodistribution in blood, spleen, lungs, brain and tumors of ^{68}Ga-Nanofitin and ^{68}Ga-EDTA. Radioactivity was measured using a gamma counter after imaging. Results are expressed in %ID/g. D, Tumor/blood ratio measured by gamma counting of ^{68}Ga-Nanofitin and ^{68}Ga-EDTA in CT26 tumors from mice injected intravenously with 5 MBq radiolabeled compounds. Results are expressed in %ID/g. E, Tumor uptake measured on PET/CT imaging of ^{68}Ga-Nanofitin and ^{68}Ga-EDTA in CT26 tumor-bearing mice injected with the radiolabeled compounds. Results are expressed in %ID/g. One out of two independent biodistribution experiments is shown. Data are shown as means ± SEM (Mann-Whitney *t*-test; ns, nonsignificant [$P > .05$]; $^{*}P < .05$ and $^{**}P < .01$)

control groups. As shown in Figure 5, A-C2 was able to significantly reduce tumor growth as demonstrated measuring the tumors' size (Figure 5A) and weight (Figure 5B), while the control Nanofitins had no such effect. The decrease in tumor growth was associated with an increase in immune cells infiltrating the tumor and particularly cytotoxic macrophages (Figure 5C,D). Immunofluorescence analysis showed that only in the A-C2-treated tumors we observed an increase in the M1-like macrophage marker iNOS and a decrease in the M2-like macrophage marker CD206 (Figure 5C), suggesting a switch in tumor-infiltrating macrophages.

There was no apparent toxicity associated with the Nanofitins during the in vivo experiments. Treatment with both control Nanofitins and A-C2 did not modify the size of the spleen (Supplementary Figure 6A) and did not induce apoptosis (as shown by the near absence of cleaved [active] caspase 3 staining) in the epithelial cells from the intestinal crypts (Supplementary Figure 6B), which are known to be very sensitive to toxic insults. Similarly, no differences were found among the treated and control animal groups in the blood cell counts (Supplementary Figure 7).

3.6 | Combinational immunotherapeutic effects of A-C2 and an anti-PD-L1 therapy in vivo

In the light of the observed effect of A-C2, we decided to study a therapy scheme involving an immune checkpoint inhibitor targeting PD-L1. This scheme was based on either a combination therapy with the coadministration of A-C2 and an anti-PD-L1 antibody or a bispecific format involving a heterodimeric construction with A-C2 being fused to an anti-PD-L1 Nanofitin (B11). For the first approach, we used the previously described CT26 colorectal cancer BALB/c mouse model. As shown in Figure 6A,B, we observed an additive effect when combining both therapeutic modalities (anti-HSP110

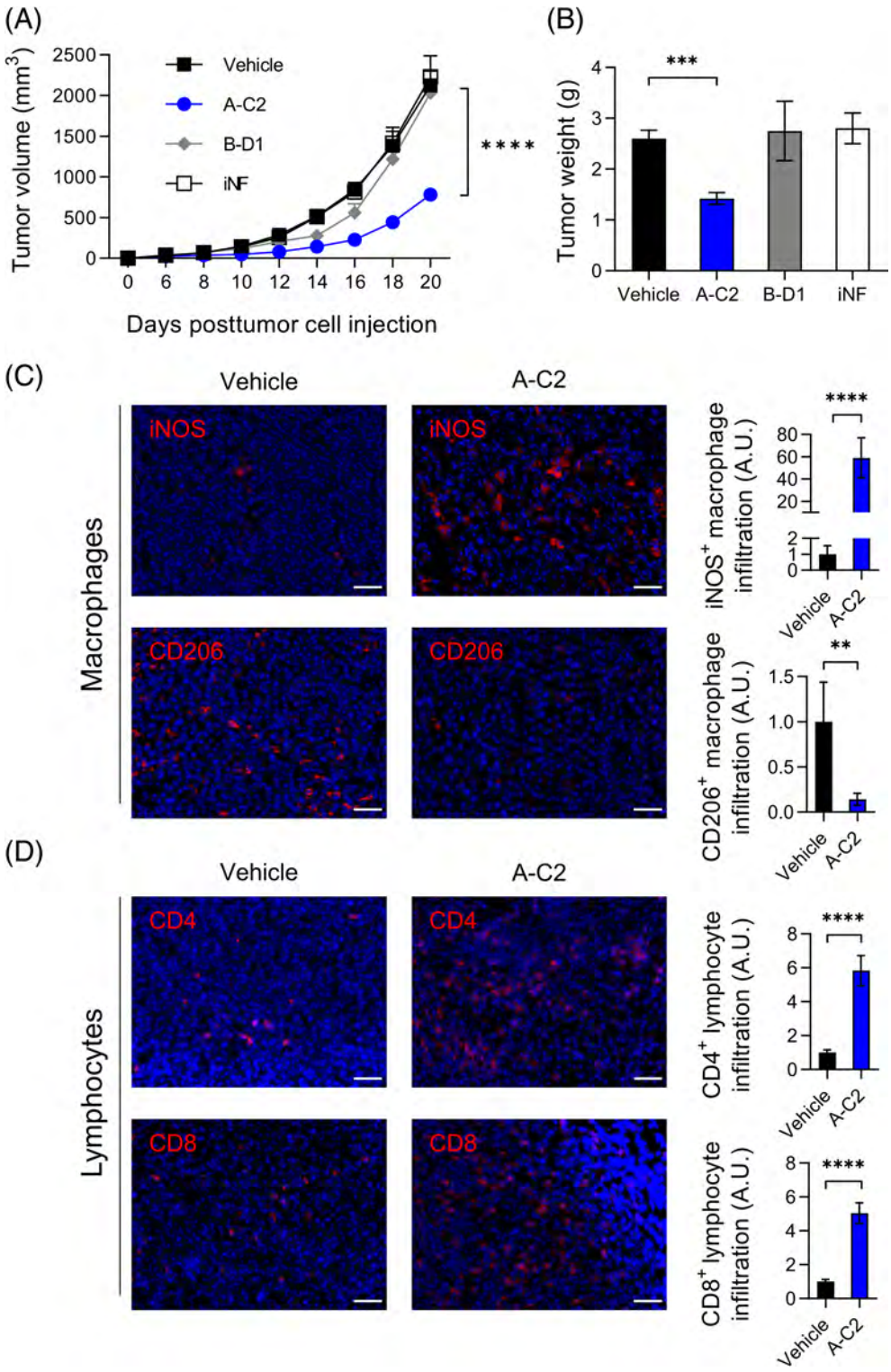

FIGURE 5 A-C2 reduces tumor growth and induces an increase in cytotoxic macrophages infiltrating the tumor. A, BALB/C mice bearing a 50 mm^3 CT26 colorectal tumor were treated every 2 days (20 mg kg^{-1} in i.p.) with Nanofitins A-C2 (—■—), H4 (iNF —●—), B-D1 (—◆—) or vehicle alone (PBS —□—). n = 9 mice/group; Data are shown as means ± SEM (two-way analysis of variance; ****P < .0001). B, Tumor weight was measured at the end of the experiment shown in (A). n = 9 mice/group; Data are expressed as means with SEM (two-tailed unpaired Student's t-test; ***P < .001). C, A-C2 antitumor effect was associated with a significant increase in well-known M1-like antitumor macrophages (iNOS—red) and a decrease in M2-like macrophages (CD206—red), as determined by immunohistochemistry. D, This infiltration was also correlated with a significant increase in $CD4^+$ and $CD8^+$ T cells within the tumors. C,D, Representative images (left panels) of tumor sections labeled with indicated antibody (red) and DAPI (blue). White scale bars represent 50 μm. Quantifications (right panels) were performed measuring the fluorescence intensity in four different randomly chosen areas. Results are expressed as relative indicated specific macrophage or lymphocyte infiltration normalized to 1 (arbitrary unit (A.U.)) in tumor collected from vehicle treated, tumor-bearing mice. Data are shown as means ± SEM (Mann-Whitney t-test; **P < .01 and ****P < .0001)

A-C2 and anti-PD-L1) in CT26-tumor-bearing mice. For the second approach, we involved a well-established chicken CAM model[30] with an engrafted MDA-MB-231 human tumor cell line. As a control, we used the therapeutically relevant benchmark Keytruda (pembrolizumab), at its maximum tolerated dose for this assay (2 mg/kg). All the constructions were found to be effective at providing tumor regression, with statistical relevance observed for the Keytruda (2 mg/kg, P < .05), A-C2 (20 mg/kg, P < .01) alone and bispecific A-C2-B11 (20 mg/kg, P < .05) (Figure 6C).

Overall, these results demonstrate the potential therapeutic interest of A-C2 in cancer through an effect involving macrophages, suggesting its complementarity with anti-PD-L1.

IJC International Journal of Cancer

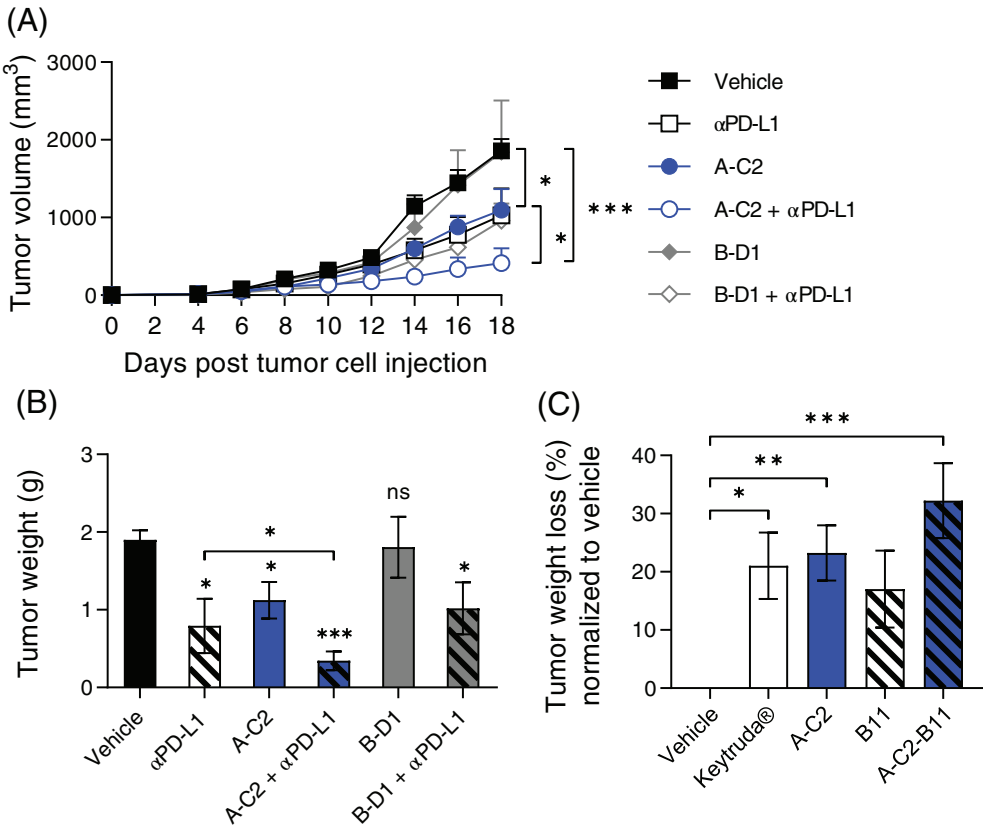

FIGURE 6 Complementary effect of A-C2 and an anti-PD-L1 therapy on tumor growth in vivo. A, BALB/C mice bearing a 50 mm^3 CT26 colorectal tumor were treated every 2 days (20 mg kg^{-1} in i.p.) with Nanofitin A-C2 (—■—) or with InVivoMAb anti-mouse PD-L1 (αPD-L1, 10 mg/kg, —□—) or with A-C2 combined with αPD-L1 (—●—). As a control, we used the same doses of Nanofitin B-D1 (—○—) alone or combined with αPD-L1 (—◆—), as well as vehicle alone (PBS —◇—). 6 mice/group; Data are shown as means ± SEM (two-way analysis of variance; *P < .05 and ***P < .001). B, Tumor weight was measured at the end of the experiment. Data are shown as means ± SEM (two-tailed unpaired Student's t-test; ns, nonsignificant [P > .05]; * P < .05 and *** P < .001). C, CAM model of tumor cell engraftment was obtained by injecting MDA-MB-231 cells (1×10^6). From Day 1 to Day 9 after graft (E10-E17 of development), chicken eggs were treated (at E10, E12, E14, E15 and E17) with A-C2 (20 mg/kg) alone or together with the anti-PD-L1 Nanofitin (B11, 20 mg/kg). As a control, eggs were also treated with Keytruda (pembrolizumab, anti-PD-1 antibody, 2 mg/kg). Tumor weight was measured at the end of the experiment (Day 9). n = 15-23 eggs/group; data are shown as means ± SEM (Student's t-test; *P < .05, **P < .01 and ***P < .001)

4 | DISCUSSION

HSP-targeting drugs have emerged as potential anticancer agents, driven by the hypothesis that HSPs have oncogene-like functions and may mediate a nononcogene addition of "stressed" tumor cells that must adapt to a hostile microenvironment.[17] With the exception of one inhibitor of HSP27,[31] only inhibitors of the abundantly expressed constitutive chaperone HSP90 are currently in clinical trials.[32] The reason is that HSP90 is a relatively easily druggable protein with a particular ATP pocket where many of its specific inhibitors bind, for instance geldanamycin-derived inhibitors.

We recently demonstrated that HSP110 might be a more relevant target in cancer therapy, particularly in colorectal cancer. It is the only HSP for which a mutation has been described and associated with cancer. We demonstrated that microsatellite instability-high colorectal cancers bear a mutation in the HSP110 gene. As a result, a truncated inactive HSP110 mutant formed to the detriment of the wild-type HSP110. Patients bearing an HSP110 inactivation (around 10% of colorectal cancers) had good prognosis (excellent response to Folfox chemotherapy).[6]

The implication of this chaperone in different cellular functions may explain its tumorigenic effect. First, HSP110 is a powerful chaperone with antiaggregation properties that is involved in double-stand break DNA repair.[33] Second, HSP110 has been shown to inhibit apoptosis, although how it happens at a molecular level remains elusive. However, in contrast to other HSPs, apoptosis inhibition does not seem to be its key role.[4] Third, HSP110 has been shown to participate in STAT3 phosphorylation and in beta-catenin pathways, thereby favoring cancer cell proliferation.[7] Last but not least, secreted HSP110 can promote an anti-inflammatory protumor environment by skewing macrophages into the M2-like phenotype.[14] This protumor anti-inflammatory function has also been described for other extracellular HSPs such as HSP70 or HSP27, which, like HSP110, are abundant in cancer microenvironment. This extracellular function contributes to the overall mechanism of defense against immune clearance.

To further demonstrate the relevance of HSP110 as a target for cancer therapy, we addressed its druggability through the custom generation of specific anti-HSP110 Nanofitins. Nanofitins are alternative scaffold proteins that can be engineered for specific and affine molecular recognition.[21-24] Originally, Nanofitins derived from the hyper-thermostable protein Sac7d isolated from the archeabacteria Sulfolobus acidocaldarius. They display drug-like attributes such as high stability to temperature and chemical stress, high manufacturing yield, and high specificity and affinity for their target. In our study, different anti-HSP110 Nanofitins were selected for their ability to bind and block HSP110 chaperone activity in vitro. HSP110 is generally described as similar to HSP70 with the duplication of a sequence contained in the substrate-binding domain.[34] We demonstrate that the Nanofitins used for our study were selective for HSP110 since no interaction was detected with HSP70.

Our screening read-out was their ability to block the effect of HSP110 on primary human macrophage polarization. The A-C2 Nanofitin was particularly effective. Interestingly, our biodistribution experiments demonstrate that ^{68}Ga-labeled A-C2, when compared to unconjugated ^{68}Ga-EDTA, accumulated within the tumor area. Although further experiments are needed, these results suggest that the Nanofitin might be used both as a probe for tumor detection purposes and as a therapeutic molecule.

It is worth noting that we used Nanofitins with a low entotoxin content in order to avoid unspecific macrophage recognition and activation. Although how the Nanofitin inhibits the effect of HSP110 on macrophage polarization remains to be studied in depth, our results suggest that it may involve HSP110 interaction with TLR4 on the differentiating macrophages.[14] Nevertheless, Nanofitins might also affect other HSP110 functions such as the ability to carry oncogenic antigens with an effect on macrophage polarization. Indeed, HSP110 is one of the chaperones most used in vaccine preparations because it can chaperone multiple peptide antigens.[35] This last hypothesis could be explained by the ability of A-C2 to bind with high affinity to the HSP110 lid which can disable the chaperone ability and induce the release of the antigenic substrates.

In conclusion, Nanofitins, which were initially developed as antibody alternatives, might be of use in cancer therapy. More specifically, A-C2, which targets HSP110, can modulate the tumor microenvironment and foster an anticancer immune response involving macrophages, leading to a decrease in tumor growth. In the present study, the decrease in tumor growth was demonstrated in an in vivo cancer mouse model but also in a well-established CAM model. This antitumor effect seems to have an additive effect with anti-PD-L1 approach. Even though the antitumor immune responses induced by this combinatory therapy needs to be explored, the fact that A-C2 increases the effect of this checkpoint inhibitor suggests that the anti-HSP110 Nanofitin modality might be used in combination with currently tested immunotherapeutics. This is of particular significance because resistance to checkpoint inhibitors has been described to involve macrophages.[36] Targeting both macrophages and T cells might be a way to overcome this resistance and provide an efficient immunotherapy.

Overall, this Nanofitin designed to target HSP110 appears to be a promising immunotheranostic lead compound.

ACKNOWLEDGEMENTS

We thank Inovotion for their advice and for performing the experiments with the CAM model. We thank Justine Picot, Anaelle Perrocheau, Harmony Gorre and Chloe Savignard from Affilogic for their contribution in the generation and characterization of the anti-HSP110 Nanofitins. We also thank Suzanne Rankin (Dijon University Hospital) for revising the manuscript.

This work was supported by a French Government grant managed by the French National Research Agency under the program "Investissements d'Avenir" with reference to ANR-11-LABX-0021 and ANR-15-IDEX-0003, the Institut National du Cancer and the Conseil Régional de Bourgogne (C. Garrido). G. Marcion had fellowships from the "Ministère de l'Enseignement Supérieur de la recherche" and the "Association pour la Recherche sur le Cancer" (ARC). F. Hermetet was supported by a fellowship from the Université Bourgogne Franche-Comté through the ISITE-BFC program and A. M. M. Dias, from La Ligue Nationale contre le Cancer. C Garrido's team is labeled by La Ligue Nationale contre le Cancer. We thank the FEDER for their financial support.

CONFLICT OF INTEREST

O. Kitten and M. Cinier have potential conflict of interest as follows: they hold employment in Affilogic SAS, Nantes, France. The Nanofitin technology described in this study, commercialized by Affilogic, the uses of the patent application owned by Institut Pasteur and Centre National de la Recherche Scientifique (CNRS): "OB-fold used as scaffold for engineering new specific binders": PCT/IB2007/004388. The remaining authors declare no conflict of interest.

DATA AVAILABILITY STATEMENT

The data that support the findings of this study are available from the corresponding author upon reasonable request.

ETHICS STATEMENT

All experiments involving mice were approved by the ethics committee for animal welfare of the University of Burgundy and the "Centre George François Leclerc" (Dijon, France) and the French Ministry of Higher Education, Research and Innovation (under reference APAFIS#25224).

ORCID

François Hermetet https://orcid.org/0000-0001-5549-1992

REFERENCES

1. Oh HJ, Easton D, Murawski M, Kaneko Y, Subjeck JR. The chaperoning activity of hsp110. Identification of functional domains by use of targeted deletions. *J Biol Chem*. 1999;274:15712-15718.
2. Bracher A, Verghese J. The nucleotide exchange factors of Hsp70 molecular chaperones. *Front Mol Biosci*. 2015;2:10.
3. Slaby O, Sobkova K, Svoboda M, et al. Significant overexpression of Hsp110 gene during colorectal cancer progression. *Oncol Rep*. 2009; 21:1235-1241.

4. Dorard C, de Thonel A, Collura A, et al. Expression of a mutant HSP110 sensitizes colorectal cancer cells to chemotherapy and improves disease prognosis. *Nat Med*. 2011;17:1283-1289.
5. Kimura A, Ogata K, Altan B, et al. Nuclear heat shock protein 110 expression is associated with poor prognosis and hyperthermo-chemotherapy resistance in gastric cancer patients with peritoneal metastasis. *World J Gastroenterol*. 2017;23:7541-7550.
6. Collura A, Lagrange A, Svrcek M, et al. Patients with colorectal tumors with microsatellite instability and large deletions in HSP110 T17 have improved response to 5-fluorouracil-based chemotherapy. *Gastroenterology*. 2014;146:401-11 e1.
7. Berthenet K, Bokhari A, Lagrange A, et al. HSP110 promotes colorectal cancer growth through STAT3 activation. *Oncogene*. 2017;36:2328-2336.
8. Yu N, Kakunda M, Pham V, et al. HSP105 recruits protein phosphatase 2A to dephosphorylate β-catenin. *Mol Cell Biol*. 2015;35:1390-1400.
9. Joly AL, Wettstein G, Mignot G, Ghiringhelli F, Garrido C. Dual role of heat shock proteins as regulators of apoptosis and innate immunity. *J Innate Immun*. 2010;2:238-247.
10. Seigneuric R, Mjahed H, Gobbo J, et al. Heat shock proteins as danger signals for cancer detection. *Front Oncol*. 2011;1:37.
11. Chalmin F, Ladoire S, Mignot G, et al. Membrane-associated Hsp72 from tumor-derived exosomes mediates STAT3-dependent immunosuppressive function of mouse and human myeloid-derived suppressor cells. *J Clin Invest*. 2010;120:457-471.
12. Banerjee S, Lin CF, Skinner KA, et al. Heat shock protein 27 differentiates tolerogenic macrophages that may support human breast cancer progression. *Cancer Res*. 2011;71:318-327.
13. Shen Y, Guo D, Weng L, et al. Tumor-derived exosomes educate dendritic cells to promote tumor metastasis via HSP72/HSP105-TLR2/TLR4 pathway. *Onco Targets Ther*. 2017;6:e1362527.
14. Berthenet K, Boudesco C, Collura A, et al. Extracellular HSP110 skews macrophage polarization in colorectal cancer. *Onco Targets Ther*. 2016;5:e1170264.
15. Biswas SK, Mantovani A. Macrophage plasticity and interaction with lymphocyte subsets: cancer as a paradigm. *Nat Immunol*. 2010;11:889-896.
16. Workman P. Combinatorial attack on multistep oncogenesis by inhibiting the Hsp90 molecular chaperone. *Cancer Lett*. 2004;206:149-157.
17. Jego G, Hazoume A, Seigneuric R, Garrido C. Targeting heat shock proteins in cancer. *Cancer Lett*. 2013;332:275-285.
18. Whitesell L, Lindquist SL. HSP90 and the chaperoning of cancer. *Nat Rev Cancer*. 2005;5:761-772.
19. Lacaná E, Amur S, Mummanneni P, Zhao H, Frueh FW. The emerging role of pharmacogenomics in biologics. *Clin Pharmacol Ther*. 2007;82:466-471.
20. Imai K, Takaoka A. Comparing antibody and small-molecule therapies for cancer. *Nat Rev Cancer*. 2006;6:714-727.
21. Huet S, Gorre H, Perrocheau A, Picot J, Cinier M. Use of the Nanofitin alternative scaffold as a GFP-ready fusion tag. *PLoS One*. 2015;10:e0142304.
22. Goux M, Becker G, Gorré H, et al. Nanofitin as a new molecular-imaging agent for the diagnosis of epidermal growth factor receptor over-expressing tumors. *Bioconjug Chem*. 2017;28:2361-2371.
23. Mouratou B, Schaeffer F, Guilvout I, et al. Remodeling a DNA-binding protein as a specific in vivo inhibitor of bacterial secretin PulD. *Proc Natl Acad Sci U S A*. 2007;104:17983-17988.
24. Mouratou B, Béhar G, Paillard-Laurance L, Colinet S, Pecorari F. Ribosome display for the selection of Sac7d scaffolds. *Methods Mol Biol*. 2012;805:315-331.
25. Gozzi GJ, Gonzalez D, Boudesco C, et al. Selecting the first chemical molecule inhibitor of HSP110 for colorectal cancer therapy. *Cell Death Differ*. 2019;27:117-129.
26. Arlet JB, Ribeil JA, Guillem F, et al. HSP70 sequestration by free α-globin promotes ineffective erythropoiesis in β-thalassaemia. *Nature*. 2014;514:242-246.
27. Gobbo J, Marcion G, Cordonnier M, et al. Restoring anticancer immune response by targeting tumor-derived exosomes with a HSP70 peptide aptamer. *J Natl Cancer Inst*. 2016;108:djv330.
28. Marcion G, Seigneuric R, Chavanne E, et al. C-terminal amino acids are essential for human heat shock protein 70 dimerization. *Cell Stress Chaperones*. 2015;20:61-72.
29. Dammicco S, Goux M, Lemaire C, et al. Regiospecific radiolabelling of Nanofitin on Ni magnetic beads with. *Nucl Med Biol*. 2017;51:33-39.
30. Komatsu A, Higashi Y, Matsumoto K. Various CAM tumor models. *Enzyme*. 2019;46:37-57.
31. Wettstein G, Bellaye PS, Kolb M, et al. Inhibition of HSP27 blocks fibrosis development and EMT features by promoting snail degradation. *FASEB J*. 2013;27:1549-1560.
32. Yuno A, Lee MJ, Lee S, et al. Clinical evaluation and biomarker profiling of Hsp90 inhibitors. *Methods Mol Biol*. 2018;1709:423-441.
33. Causse SZ, Marcion G, Chanteloup G, et al. HSP110 translocates to the nucleus upon genotoxic chemotherapy and promotes DNA repair in colorectal cancer cells. *Oncogene*. 2019;38:2767-2777.
34. Liu Q, Hendrickson WA. Insights into Hsp70 chaperone activity from a crystal structure of the yeast Hsp110 Sse1. *Cell*. 2007;131:106-120.
35. Wang XY, Kazim L, Repasky EA, Subjeck JR. Characterization of heat shock protein 110 and glucose-regulated protein 170 as cancer vaccines and the effect of fever-range hyperthermia on vaccine activity. *J Immunol*. 2001;166:490-497.
36. Herbst RS, Soria JC, Kowanetz M, et al. Predictive correlates of response to the anti-PD-L1 antibody MPDL3280A in cancer patients. *Nature*. 2014;515:563-567.

SUPPORTING INFORMATION

Additional supporting information may be found online in the Supporting Information section at the end of this article.

SARTORIUS

Application Note

February 1, 2022

Keywords or phrases:
Pharmacokinetics, preclinical PK studies, ELISA, monoclonal antibodies, immunoassay, therapeutic molecules, orientation-directed binding assay, immunogenicity, Octet, Bio-Layer Interferometry

Strategies for the Development of a High Throughput Octet® Bio-Layer Interferometry Method to Measure Pharmacokinetics of Monoclonal Antibodies in Preclinical Animal Models

Wahala M Wahala, Ph.D‡ Lori Armstrong, M.S; Susan Buist, Ph.D.
Elanco US Inc., 2500 Innovation Way, Greenfield, IN, 46140

‡**Corresponding Author:** wahala.wahala@elancoah.com
Email: octet@sartorius.com

Introduction

Therapeutic antibodies are developed to treat various diseases, including cancers, immunological disorders, and infectious diseases. The safety and efficacy of these therapeutic molecules may be influenced by the way they interact with the body. Therefore, it is vital to understand how a body reacts to a biopharmaceutical after administration. Pharmacokinetic studies (PK) measure the variations of drug levels in the body as a function of time and are an essential part of the drug development process. Properly designed PK studies facilitate the determination of the proper dosage, distribution, safety, and efficacy throughout the duration of drug treatment.

Reliable and sensitive bioanalytical methods are required to quantitate drug molecules in samples collected from PK studies. ELISA or other immunoassay formats are the commonly utilized methods to analyze samples from these studies. However, developing a conventional plate-based immunoassay requires a reasonable investment of time, and additionally these assays are not high throughput for analyzing clinical samples unless the process is automated. In this application note, we evaluated the feasibility of utilizing the Bio-Layer Interferometry (BLI) platform to rapidly design, establish, and qualify a method with which to quantitate therapeutic canine antibodies from rat PK study samples to support an urgent project request.

Find out more: www.sartorius.com/octet

Table 1
Materials and Reagents Utilized for the Development of the PK Method

Material/Reagent	Vendor	Cat. No.
Octet® High Precision Streptavidin (SAX) Biosensor	Sartorius	18-5118
Rabbit Anti-Canine IgG Fc Fragment Secondary Antibody [Biotin] (polyclonal antibody)	Novus Biologicals	NBP1-73513
Rabbit Anti-Canine IgG F(ab)2 Secondary Antibody (polyclonal antibody)	Novus Biologicals	NBP1-73923
Normal Rat Serum (NRS)	abcam	ab7488
Black 96-well plates	Greiner Bio-one	655209
Octet® R8	Sartorius	
Octet®-AS Offline Biosensor Immobilization Station	Sartorius	
20x HBS-EP Buffer	Teknova	H8022
Diluent (1x HBS-EP, 0.1% BSA)	N/A	N/A
Glycine (10 mM) pH 1.5	GE Healthcare	BR-1003-54

Method and Assay Optimization

Biosensor and Assay Format Selection

A fit-for-purpose assay design concept was used to determine the assay format and biosensor selection for a non-GLP study, which does not require a fully validated assay. Generally, IgG can be quantitated using protein A and G biosensors. However, our therapeutic antibody of interest is in a rat serum matrix consisting off-target rat IgG and other serum components that also bind to these sensors. Therefore, to minimize off-target binding, a High Precision Streptavidin SAX biosensor-based capture assay format was selected. The basic assay format is shown in Figure 1. To summarize, the biotinylated capture antibody was immobilized onto the SAX biosensors. The therapeutic antibody (drug) molecule in the serum sample was then captured. To increase the assay specificity and sensitivity, capture of the drug was confirmed by use of a detection antibody specific to the target drug molecule.

Compared to the selection of commercially available anti-human antibodies, availability of anti-species specific (canine) antibodies are limited, and most of these antibodies are not well characterized. Based on previous experience and institutional knowledge, there is a possibility of cross reactivity of the detection antibody with the capture antibody which can be minimized by selecting an antibody pair generated from the same animal species. After an initial characterization of a selection of antibodies from several vendors, a biotinylated rabbit anti-canine Fc specific antibody (polyclonal) and a rabbit anti-canine F(ab)2 specific antibody (polyclonal) were selected as the antibody pair for developing an orientation-directed binding assay. Even though biotinylated target protein could have been used to capture the target protein specific canine antibodies in rat serum samples, we decided to use the aforementioned antibody capture assay format to establish a universal assay platform with which to analyze any canine antibodies in rat sera to support any future pre-clinical PK studies conducted in rats.

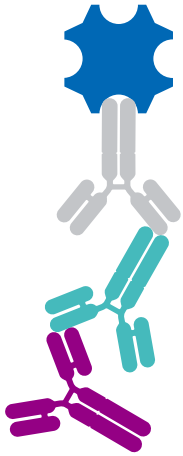

High-precision Streptavidin (SAX) Biosensor

Capture Ab immobilization
Biotinylated rabbit anti-canine Fc specific antibody (directional capture)

Capturing therapeutic mAb from Rat sera
Caninized mAb in rat serum

Detecting captured therapeutic mAb
Rabbit anti-canine F(ab)2 specific antibody

Figure 1
Assay Format
Biotinylated rabbit anti-canine Fc specific antibody was immobilized onto high precision streptavidin (SAX) biosensors. Utilizing an Fc-specific antibody allows directional capture of the Fc portion of therapeutic caninized mAb in the rat serum matrix. For additional specificity/sensitivity, the Fab portion of the therapeutic mAb was detected using a Rabbit anti-canine F(ab)2 specific antibody.

Assay Optimization

Assay optimization experiments were carried out using a standard curve spanning the expected range of the drug molecule in the serum. The standard curve was prepared by serially diluting the drug molecule in 1:10 diluted normal rat serum (matrix). All initial assay optimizations were performed in kinetic mode at a temperature of 30° C. Concentrations of spiked samples were calculated by fitting to a standard curve generated by plotting signal response (Req) levels for each standard concentration.

A. Buffer Optimization

The intended purpose of the assay is to quantitate the therapeutic antibody in a complex matrix such as serum or plasma. These complex matrices tend to produce higher background signals in an assay. So, optimization of buffer and blocking reagents are crucial steps in the assay development workflow.

Initial experiments were conducted in HBS-EP assay buffer containing 0.1% BSA. However, when testing standards diluted in rat serum, the assay produced an elevated amount of non-specific binding to the sensors. To minimize non-specific binding from rat serum samples, an additional blocking step consisting of normal rat serum diluted 1:10 in the HBS-EP assay buffer was introduced after the capture antibody immobilization step. To further aid in reducing the non-specific/off target binding, the amount of NaCl and Tween-20 was varied from 150 mM-500 mM and 0.05% or 0.09%, respectively to determine the best combination of NaCl and Tween 20 in the assay buffer.

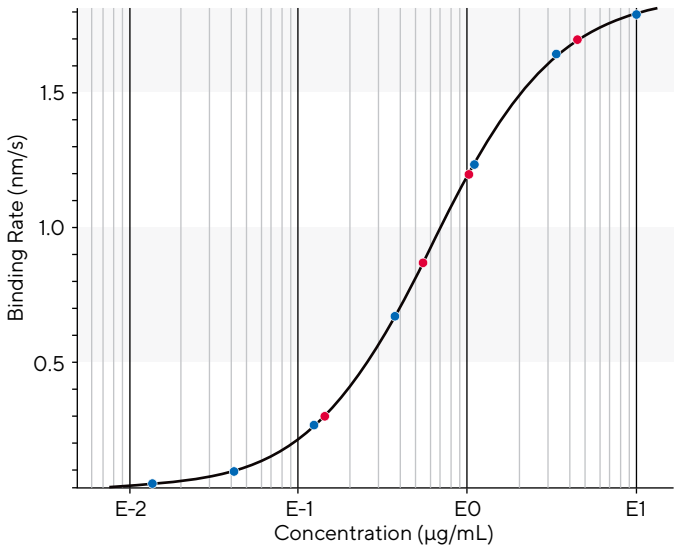

Figure 2

Octet Standard Curve

mAb standards were diluted 3-fold ranging from 10 µg/mL to 0.013 µg/mL in assay buffer. Known concentrations of mAb (4, 1, 0.5 and 0.125 µg/mL) were spiked into 1:10 diluted rat serum. Assay was performed as a kinetic assay and the data was analyzed using the quantitation module of the Octet data analysis software. Spiked samples are shown in red in the graph.

Increasing the concentrations of NaCl and Tween 20 decreased the background signal, however, the specific signal was also reduced (data not shown). Therefore, HBS-EP buffer containing NaCl (150 mM), Tween-20 (0.05%), 0.1% BSA was selected as the optimal assay buffer composition for future assays. After a few scouting experiments, 25 µg/mL and 5 µg/mL were selected as capture and detection antibody concentrations, respectively.

B. Shaking Speed Optimization

Since sensitivity is a critical parameter of a PK assay, different shaking speeds were tested to improve the assay sensitivity. The experiment was conducted in the assay buffer selected from the previous set of experiments (HBS-EP buffer containing 150 mM NaCl, 0.05% Tween-20, 0.1% BSA). SAX sensors were immobilized with 25 µg/mL of biotinylated rabbit anti-canine Fc specific antibody in the assay buffer. Rabbit anti-canine F(ab)2 specific antibody was diluted at 5 µg/mL in assay buffer and used as the final detection reagent. Octet® signals for the wells containing anti-canine F(ab)2 specific antibody were used for interpolation of the antibody concentrations. Shaking speeds of 800 and 1000 rpm were tested for the serum blocking, drug molecule capture in matrix, baseline, and detection antibody steps. Standards were diluted 3-fold ranging from 10 µg/mL to 0.013 µg/mL, and simulated spiked samples at varied concentrations were also included to calculate percent recovery at both speeds (Figure 2, standards in blue, spiked samples in red). Drug molecule at 0 µg/mL was used as a reference control. A shaking speed of 800 rpm provided the better recovery, with all samples within ±20% bias, and was selected as an assay parameter (Table 2A and 2B).

A. Shaking Speed—1000 RPM

Spiked mAb:	Spiked Conc. (µg/mL)	Calc Conc. (µg/mL)	% Bias
	4	5.73	43.25
	1	0.9944	-0.56
	0.5	0.5816	16.32
	0.125	0.1333	6.64

B. Shaking Speed—800 RPM

Spiked mAb:	Spiked Conc. (µg/mL)	Calc Conc. (µg/mL)	% Bias
	4	4.5	12.50
	1	1.02	2.00
	0.5	0.5472	9.44
	0.125	0.1425	14.00

Table 2

Shaking Speed Optimization and Percent Recoveries of Spiked mAb in Serum

Known concentrations of mAb at 4, 1, 0.5, and 0.125 µg/mL were spiked into 1:10 diluted normal rat serum. Shaking speeds of 1000 rpm (A) and 800 rpm (B) were tested. Spiked sample concentrations were interpolated, and percent bias was calculated for each shaking speed. With a shaking speed of 800 rpm, all samples were within ±20% bias. 800 rpm was selected as the optimal shaking speed parameter.

C. Assay Linearity

Using an experimental setup similar to the previous experiment, assay linearity was tested with simulated spiked drug molecule at 4, 1, 0.5, 0.125, and 0.0313 µg/mL against a standard concentration range from 10 µg/mL to 0.013 µg/mL by carrying out 3-fold dilutions. All dilutions were done using 1:10 diluted normal rat sera. Data was collected for 300 or 400 seconds for the final detection antibody binding step. Shaking speed was set at 800 rpm for serum block, drug capture, baseline, and final detection antibody steps. Shaking speed for all other steps was set at 1000 rpm. As shown below (Figure 3 and Table 3A and 3B, the quantitation assay had a very strong assay linearity (R2 > 0.99) in the range tested indicating that the Octet® based quantitation assay is suitable to test the PK study samples. Readings collected from 3 separate runs at 300 and 400 seconds both provided similar assay linearity. For both runs, recovery of all spiked samples was within ±20% bias.

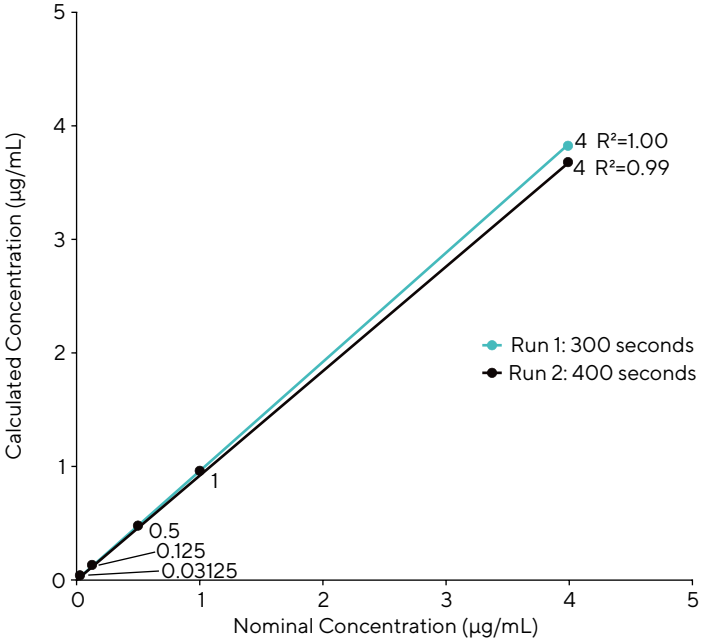

Figure 3

Assay Linearity

To test the linearity of the assay, standard mAb was spiked into 1:10 diluted serum matrix starting at 4, 1, 0.5, 0.125 and 0.03125 µg/mL. Calculated numbers were graphed against the nominal concentration of spiked amount of standard mAb to show the assay linearity.

A.300 Second Detection

Spiked mAb:	Spiked Conc. (µg/mL)	Calc Conc. (µg/mL)	% Bias
	4	3.83	-4.25
	1	0.9505	-4.95
	0.5	0.479	-4.20
	0.125	0.1273	1.84
	0.03125	0.0362	15.65

B.400 Second Detection

Spiked mAb:	Spiked Conc. (µg/mL)	Calc Conc. (µg/mL)	% Bias
	4	3.67	-8.25
	1	0.9494	-5.06
	0.5	0.4793	-4.14
	0.125	0.1268	1.44
	0.03125	0.0358	14.37

Table 3

Spike Recovery of mAb at 300 and 400 Second Detection Times

Sensor Regeneration and Initial Cycles of Regeneration Are Needed Before Analysis

Sensor regeneration is required to repeatedly use the sensors for replicate measurement of the samples. This will reduce the total assay time when testing the study materials along with decreasing the cost of consumables. Regeneration conditions at acidic pH were tested using the maximum standard concentration of 10 µg/ml with glycine-HCl solutions at pHs 1.5, 2.0, 2.5 and 3 to select the reagent that fully dissociates the analyte–ligand binding without drastically affecting the binding activity of the ligand. Sensors were neutralized in the assay buffer after the glycine-HCl regeneration step.

After each detection step in the assay, sensors underwent 3 cycles of regeneration, each consisting of a dip into the glycine solution for 5 seconds, then a dip into assay buffer for a 5 second neutralization. Signals from the rabbit anti-canine F(ab)2 specific detection step were used to calculate the binding response. The entire assay was run for 6 cycles with 5 regeneration steps total. The first run was performed with a fresh set of sensors without prior regeneration.

A. Binding Response Changes vs. Regeneration Cycle

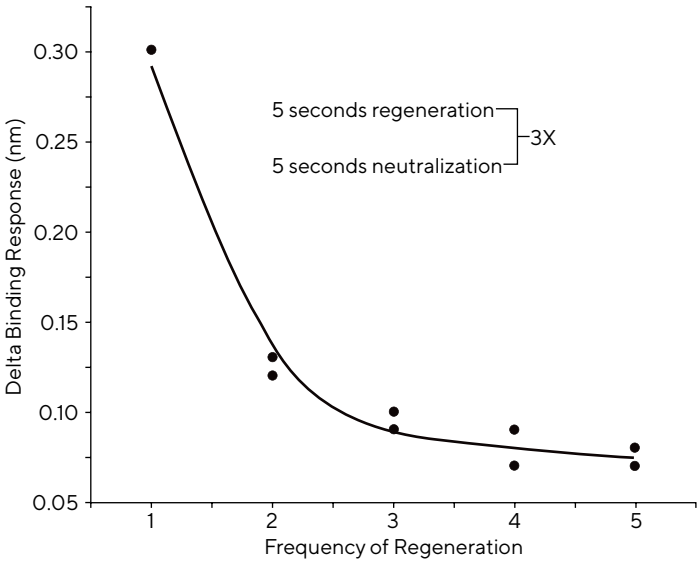

Figure 4A

Binding Response Changes Over Multiple Regeneration Cycles

Biosensors were regenerated a total of 5 times, and the change in binding response between cycles was calculated. Response decreased the greatest from regeneration 1 to 2, and response stabilized between cycles 3 and 5.

B. Glycine Biosensor Regeneration

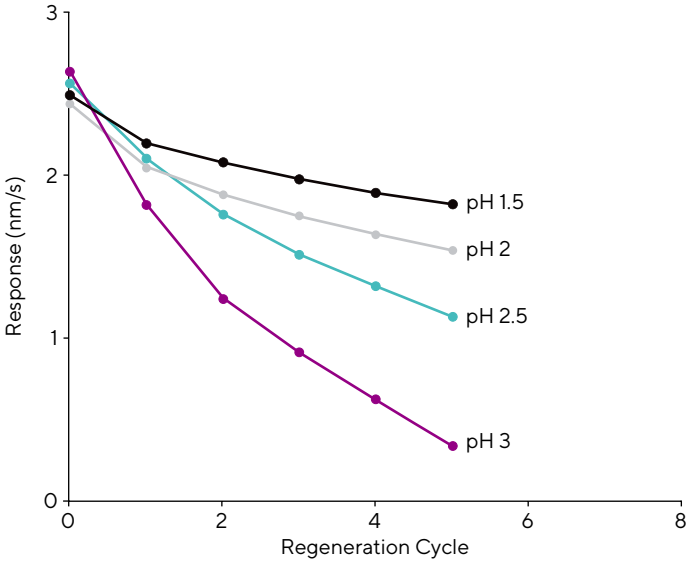

Figure 4B

Testing Biosensor Regeneration Buffers

Biosensors were regenerated for a total of 5 cycles in glycine-HCl buffer at pH 1.5, 2, 2.5, and 3, and binding response was monitored. Glycine buffer at pH 3 had the greatest binding change after regeneration, and Glycine buffer at pH 1.5 impacted binding the least.

Glycine Regeneration Buffer (pH)	1.5	2	2.5	3
Regeneration Cycle 0 Response (nm)	2.5	2.45	2.58	2.62
Regeneration Cycle 1 Response (nm)	2.2	2.05	2.1	1.81
Regeneration Cycle 2 Response (nm)	2.08	1.88	1.76	1.24
Regeneration Cycle 3 Response (nm)	1.98	1.75	1.52	0.9125
Regeneration Cycle 4 Response (nm)	1.89	1.64	1.32	0.6206
Regeneration Cycle 5 Response (nm)	1.82	1.54	1.13	0.331
Total Signal Loss from Regeneration	**0.68**	**0.91**	**1.45**	**2.29**

Table 4

Effects of Glycine Regeneration Buffer pH on mAb Binding Response (nm) Between Regeneration Cycles

Irrespective of the pH of the regeneration buffer, after each regeneration step binding rates decreased. The decrease was the most clear/ drastic between the first and second run where the first assay was run without prior sensor regeneration. This decrease was reduced between regeneration cycles 3 and 5 suggesting prior regeneration of sensors is a prerequisite before the actual sample analysis. (Table 4 and Figure 4)

As indicated by Table 4 and Figure 4A, the lowest binding response decrease (Δ binding response) after regeneration steps was observed with Glycine at pH 1.5, so this condition was selected for sensor regeneration. Data was also collected to determine the impact of acid regeneration steps on the assay dilution linearity. As depicted in Figure 5 dilution linearity was not affected even after multiple cycles of sensor regeneration. The graph below shows the assay linearity after three individual runs with regeneration steps.

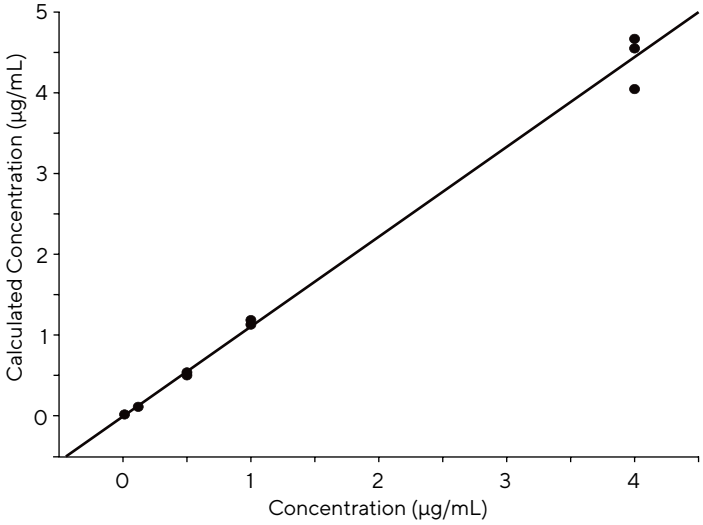

Figure 5

Assay Linearity After Three Individual Runs with Sensor Regenerations at pH 1.5: $R^2 = 0.99$

Introducing Octet® AS Offline Biosensor Immobilization Station to Improve Throughput

The final step of the assay was to introduce the Octet® AS offline biosensor immobilization station, which is capable of simultaneous and uniform reagent loading onto all 96 biosensors in a biosensor tray to increase the throughput and precision of the PK assay while also decreasing total assay handling time. Thus, the Octet® AS was used to simultaneously handle 96 biosensors to perform all offline assay steps that do not require online signal monitoring, such as initial biotinylated capture antibody loading, baseline, serum blocking, capture of the drug molecule from PK study samples, and sensor regeneration steps. Only the final detection step was monitored in real-time using the Octet® instrument.

SAX sensors were loaded with 25 µg/mL of biotinylated rabbit anti-canine Fc specific antibody in assay buffer. Drug molecule was diluted 3-fold ranging from 10 µg/mL to 0.013 µg/mL in 1:10 normal rat serum (NRS) in assay buffer to generate a standard curve. Simulated spiked samples were prepared by adding the drug molecule at 4, 2, 1, 0.5, 0.125, 0.0625, 0.031, and 0.0156, µg/mL in normal rat serum diluted 1:10 in assay buffer.

The rabbit anti-canine F(ab)2 specific antibody detection reagent concentration was increased from 5 µg/mL to 50 µg/mL to generate an equivalent signal with a decreased 60 second reaction time compared to the previous reaction time of 300 seconds. This allowed for the detection step to be completed faster for the entire plate reducing the chances for any low level capture drug dissociation from the biosensor while the detection steps are carried out one column at a time. On the other hand a Octet® RH96 system will be able to read the entire 96-well plate in a single read step.

Before the first quantitation run, biotinylated canine anti-Fc specific antibody was loaded onto the sensors and the sensors were serum blocked. After these two initial steps, sensors were regenerated with Glycine at pH 1.5. The serum blocking and regeneration steps were repeated once, for a total of 2 regeneration cycles, before the sensors were used in the quantitation assay.

Final Assay Format and Plate Map Showing Placement of Standards, Study Samples, and Quality Control Samples

Final assay setup, parameters and the plate layout is shown in Figure 6 and Tables 5A and 5B. Due to sample arrangement logistics, only four QC controls were setup at 4, 1, 0.5 and 0.125 µg/mL for samples analysis. Standard curve duplicates were setup at the beginning and the end of the plate to ensure that the sample loaded sensors remaining in the assay buffer does not impact the final quantitation due to possible reagent dissociation. All the samples collected from each animal were run using a single assay plate to maintain consistency of the data throughout the sample collection regimen. Each sample set underwent a duplicate run after sensor regeneration.

	1	2	3	4	5	6	7	8	9	10	11	12
A	10	R0001 T0	R0001 T2	R0001 T4	R0001 T6	R0001 T8	R0001 T10	R0001 T12	10			
B	3.33333	R0002 T0	R0002 T2	R0002 T4	R0002 T6	R0002 T8	R0002 T10	R0002 T12	3.33333			
C	1.11111	R0003 T0	R0003 T2	R0003 T4	R0003 T6	R0003 T8	R0003 T10	R0003 T12	1.11111			
D	0.37037	R0004 T0	R0004 T2	R0004 T4	R0004 T6	R0004 T8	R0004 T10	R0004 T12	0.37037			
E	0.12346	R0001 T1	R0001 T3	R0001 T5	R0001 T7	R0001 T9	R0001 T11	4 µg/mL	0.12346			
F	0.04115	R0002 T1	R0002 T3	R0002 T5	R0002 T7	R0002 T9	R0002 T11	1 µg/mL	0.04115			
G	0.01372	R0003 T1	R0003 T3	R0003 T5	R0003 T7	R0003 T9	R0003 T11	0.5 µg/mL	0.01372			
H	0	R0004 T1	R0004 T3	R0004 T5	R0004 T7	R0004 T9	R0004 T11	0.125 µg/mL	0			

Figure 6

Final Assay Plate Map for Standards, QC Samples, and Clinical Rat Serum Study Samples

Standard curve duplicates were placed in the 1st and last columns of the plate. All timepoints collected from a single animal were analyzed on the same plate. Samples were analyzed in a duplicate run after biosensor regeneration.

A. Initial Biosensor Regeneration

Step	Step Type	Time (sec)	Shaking Speed (RPM)	
1	Equilibration	90	1000	Octet® AS Station
2	Loading Biotin Ab	60	1000	
3	Baseline	60	1000	
4	Serum Blocking (1:10 NRS)	120	800	
5	Regeneration (3x)	5	400	
6	Neutralization (3x)	5	400	

B. Sample Analysis and Quantitation

Step	Step Type	Time (sec)	Shaking speed (RPM)	
1	Baseline	60	1000	Octet® AS Station
2	Serum Blocking (1:10 NRS)	120	800	
3	mAb Drug in Matrix Capture	150	800	
4	Baseline	60	800	
5	Baseline	30	800	Octet® R8
6	Detection Ab Association	60	800	
7	Regeneration (3x)	5	400	Octet® AS Station
8	Neutralization (3x)	5	400	

Table 5

Finalized Assay Parameters for Analyzing Canine Antibodies From Rat PK Study Samples

Table 5A: Initial Biosensor Regeneration. Biotinylated antibody loading, baseline, 1:10 diluted normal rat serum (NRS) blocking, and initial biosensor regeneration steps were performed on the AS offline biosensor immobilization station.

Table 5B: Sample Analysis and Quantitation. The AS offline biosensor immobilization station was utilized for the baseline, 1:10 NRS blocking, and mAb drug in matrix capture steps. The remainder of the assay, baseline and detection antibody association steps were performed on the Octet R8 utilizing the quantitation assay method format. The assay plate was returned to the immobilization station to regenerate the biosensors offline for the duplicate assay run.

Spiked at (µg/mL)	Calc Conc. (µg/mL)	% Bias	Standard Deviation
4	4.493	12.33	0.393
1	0.959	-4.11	0.023
0.5	0.554	10.70	0.012
0.125	0.121	-2.81	0.008

Table 6

QC Sample Percent Bias Data From 8 Individual Assay Runs

Results and Summary of Sample Analysis

Samples collected at 13 different time intervals from four groups of animals were tested. As indicated in Table 6 and Figure 7, QC samples tested showed the expected recovery (within 20%) and assay linearity indicating the samples runs were successful. The quantity of the drug molecule in all the samples, with the exception of samples collected at time 0, were within the assay linearity (between 4 µg/mL–0.0313 µg/mL) range (Figure 7) indicating accurate quantitation of drug molecule in these samples.

The data generated from this study (Figure 8A and 8B) were used for PK profile analysis of the biotherapeutic molecules. A clear immunogenic response was observed with mAbs A and B by 120 hr after administration, an expected result of administering caninized mAbs to rats. Therefore, the first 5 days of exposure were used to characterize the four mAbs of interest. The highest C_{max} and greatest exposure, based on AUC over the first 120 hr, was achieved by mAb D. The other three mAbs were comparable based on C_{max} and AUC (Table 7). While rodent PK data cannot be directly correlated to canine PK, this data suggests mAb D may have the potential for greater absorption and overall exposure in dog compared with the other mAbs. This mAb also happened to have the greatest *in vitro* potency. The potency and rodent PK were combined to drive the decision to further characterize mAb D in dogs.

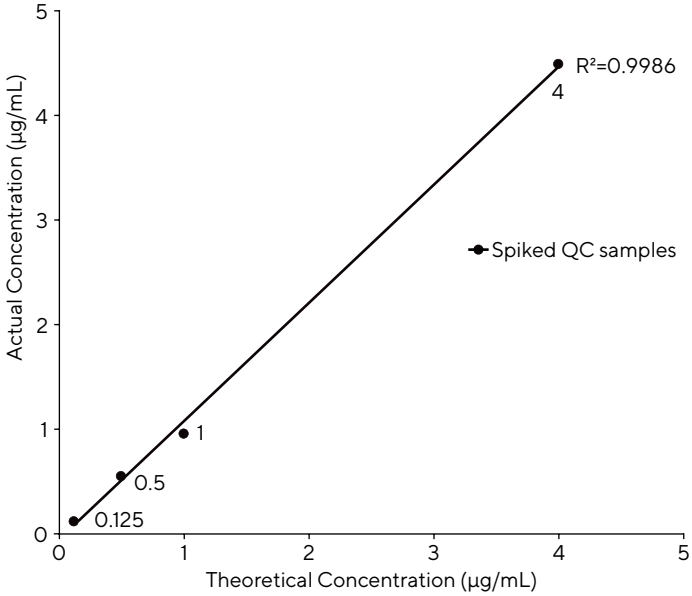

Figure 7

Assay Linearity for QC Samples From 8 Individual Assay Runs

A. Analysis of Rat Sera

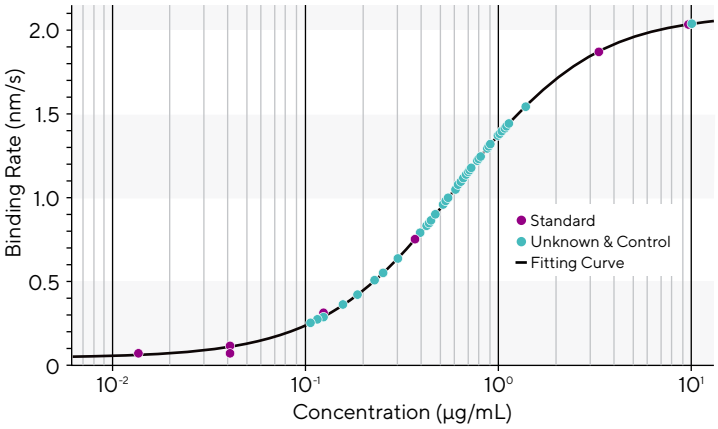

Figure 8A
Graph shows the standard curve and concentration of serum sample analyzed.

B. 336-hour Rat Exposure

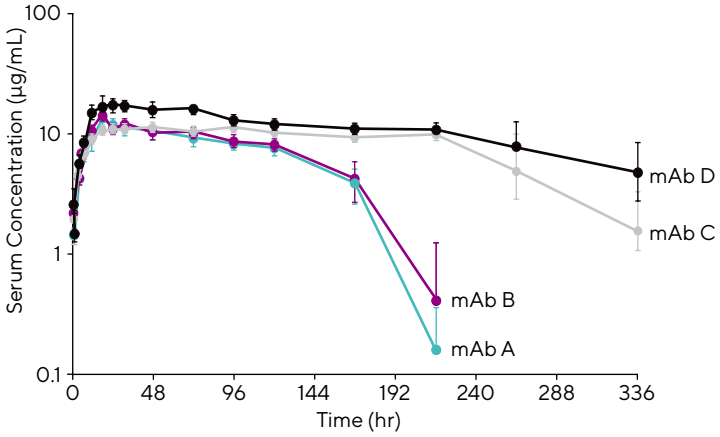

Figure 8B
Mean (±SD) serum concentration vs time profiles for mAb A (green), B (purple), C (gray), and D (black). Samples were serially collected from 4 subjects per dose group over 336 hr following subcutaneous administration of 5 mg mAb/kg body weight.

PK Parameter		mAb A	mAb B	mAb C	mAb D
C_{max}	µg/mL	13.4 (5)	14.9 (20)	12.1 (5)	19.0 (9)
T_{max}	hr	18 (0)	18 (0)	62 (45)	25 (23)
AUC_{0-120}	µg*hr/mL	1120 (12)	1190 (9)	1250 (1)	1740 (7)

Data presented as Mean (%CV)

Table 7
Mean Rat Serum PK Parameters Following Subcutaneous Administration of 5 mg mAb/kg Body Weight

Conclusions

We established an immune capture assay using the Octet® R8 platform to quantitate therapeutic molecules in serum samples collected from a pre-clinical PK study. With the combination of the off-line Octet® AS instrument, an Octet®-based PK assay was converted to a semi-automated high throughput assay. Compared to a conventional plate-based immunoassay, the assay was established in a very short time window to support an urgent PK assay need.

North America
Sartorius Corporation
565 Johnson Avenue
Bohemia, NY 11716
USA
Phone +1 888 OCTET 75
or +1 650 322 1360
Email: orders.US07@sartorius.com

Europe
Sartorius Lab Instruments GmbH & Co. KG
Otto-Brenner-Strasse 20
37079 Goettingen
Phone +49 551 308 0
Email: euorders.UK03@sartorius.com

Asia Pacific
Sartorius Japan K.K.
4th Floor, Daiwa Shinagawa North Bldg.
1-8-11, Kita-Shinagawa 1-chome
Shinagawa-Ku
Tokyo 140-0001
Japan
Phone +81 3 6478 5202
Email: orders.US07@sartorius.com

Find out more: www.sartorius.com/octet-support

For questions, email: AskAScientist@sartorius.com